UNIVERSITÀ DEGLI STUDI DI PADOVA
DIPARTIMENTO TERRITORIO E SISTEMI AGRO-FORESTALI

SCUOLA DI DOTTORATO DI RICERCA IN:
“TERRITORIO, AMBIENTE, RISORSE E SALUTE”

CICLO XXVI

Linking River Channel Forms and Processes in Gravel Bed Rivers: Time, Space, Remote Sensing and Uncertainty

Direttore della Scuola: **Ch.mo Prof. Mario Aristide Lenzi**

Supervisore: **Ch.mo Prof. Mario Aristide Lenzi**

Co-supervisore: **Prof. Luca Mao**

Dottorando: **Johnny Moretto**

Dedicated to my Family

and Stefania

Contents

Section One

State of Art

Section Two

Field Research, Materials and Methods

Section Three
Remote Sensing Analysis

Section Four
Discussions and Final Remarks

Index of Figures

Index of Tables

Abstract

The “modern” fluvial morphology, is the results of a series of events characterized by both natural and human dynamics. Recognizing the process responsible for particular morphology is not a simple analysis, it can be more difficult or impossible if the data collected have too low resolution or too high uncertainty in relation to the spatial and temporal scale assessed.

This work aims to analyse and optimize different data and collection methods, derived from different time, space and resolution scales, with a good equilibrium between time-consuming and results at low uncertainty.

Different gravel bed reaches were analysed as study area: Brenta, Piave, Tagliamento River (Italy) and Feshie River (Scotland).

Three geomorphic analyses were applied at different spatial and temporal scale. A planimetric approach through a multitemporal analysis over the last 30 years on the Brenta River. A volumetric approach through a revised colour bathymetry; hybrid digital terrain models (HDTM) building and comparison of different digital elevation models (DoD) was used to study relevant flood events that occurred in the North-East Italian rivers (Brenta, Piave and Tagliamento). A highly detailed resolution, derived from Terrestrial Laser Scanner (TLS) to study its uncertainty, was applied on the Feshie River and to some laboratory experiments.

Results show that on the Brenta River, lower active channel narrowing happened from 1981 to 1990 even if relatively important floods occurred. The active channel was likely at its minimum extent due to still relevant human impacts. Partial recovery of the active channel width was detected from 1990 to 2011 due to less gravel mining and human pressure.

The proposed methodology for producing high-resolution Digital Terrain Models (DTMs) in wet areas has an uncertainty comparable to LiDAR (Light Detection And Ranging) data in dry areas. The bathymetric model calibration only requires a dGPS survey in the wet areas contemporary to aerial images acquisition. Detailed and automatic erosion - deposition analyses starting from a DoD are possible thanks to the “principal erosion deposition analyser” script developed.

Density, angle of incidence and laser intensity seem to be the most uncertain influencing factors in DTMs building from TLS point clouds. A new TLS filter developed provides semi-automatic point cloud classifications to filter the vegetation.

The geomorphic approaches presented provide an adequate topographical description of the rivers to explore channel adjustments due to natural and human causes at different spatial and temporal scales. The study represents a valuable tool for any fluvial engineering, river topography description, river management, ecology and restoration purposes.

Riassunto

La “moderna” morfologia fluviale, è il risultato di una serie di eventi caratterizzati da differenti dinamiche, naturali ed antropiche. Riconoscere i processi responsabili di una particolare morfologia, può divenire complesso se i dati disponibili presentano bassi livelli di risoluzione o eccessiva incertezza in funzione della scala temporale e spaziale analizzata.

Questo lavoro si è focalizzato ad analizzare ed ottimizzare differenti tipi di dati e metodologie di rilievo in differenti tratti fluviali a fondo ghiaioso dell’Italia Nord-Orientale e della Scozia: Fiume Brenta, Piave e Tagliamento (Italia) e Fiume Feshie (Scozia).

Tre differenti metodologie geomorfometriche sono state applicate a diverse scale spaziali e temporali. Un approccio planimetrico attraverso un’analisi multitemporale degl’ultimi 30 anni in un tratto del Fiume Brenta. Un approccio volumetrico attraverso una rivisitata applicazione di batimetria da colore, con costruzione di modelli digitali del terreno “ibridi” (HDTM) e comparazione di modelli di elevazione (DoD) per lo studio di un intenso evento di piena, avvenuto nei fiumi italiani considerati. Rilievi in laboratorio e nel Fiume Feshie ad alta risoluzione, tramite laser scanner terrestre (TLS), sono stati eseguiti per studiarne l’incertezza ed individuare metodologie di classificazione spaziale delle nuvole di punti.

I risultati, mostrano che dal 1981 al 1990 nel Fiume Brenta persiste ancora un processo di restringimento dell’alveo attivo. L’impatto umano è ancora presente. L’alveo attivo presenta la sua minima estensione. Dal 1990 al 2011, sembra che un parziale recupero della larghezza dell’alveo attivo sia in atto. Minor pressione da estrazione di ghiaia e da impatto umano, caratterizzano questo periodo. La metodologia proposta per produrre DTM ad alta risoluzione in presenza di aree bagnate ha dimostrato un’incertezza comparabile con il LiDAR nelle aree secche. La calibrazione dei modelli batimetrici, richiede un rilievo dGPS nelle aree bagnate in “contemporaneo” con l’acquisizione delle foto aeree. Grazie allo script sviluppato (PrEDA), sono possibili più dettagliate e automatiche analisi dell’erosione e della deposizione. Densità, angolo di incidenza ed intensità laser sembrano essere i fattori che maggiormente influenzano l’incertezza nella realizzazione di modelli di elevazione da TLS. Il filtro sviluppato per nuvole TLS è in grado di fornire semi-automatici filtraggi della vegetazione.

Gli approcci geomorfometrici presentati, forniscono adeguate descrizioni topografiche dei sistemi fluviali; utili ad esplorare aggiustamenti dei canali dovuti a cause naturali o antropiche in differenti scale spaziali e temporali. Lo studio proposto, può rappresentare un valido supporto alla topografia in ambito fluviale, alla progettazione di interventi di ingegneria fluviale, ad una adeguata gestione fluviale, considerando aspetti ecologici e di riqualificazione fluviale.

Section One

State of Art

1 *Introduction*

In the last 200 years most Italian and European rivers have suffered considerable human pressures at both basin and channel scales (Liébault and Piégay, 2002; Gurnell *et al.*, 2009; Surian *et al.*, 2009a; Comiti *et al.*, 2011). Phases of deforestation and reforestation, channelization, sediment mining, urbanization, dam building, torrent-control works, water diversion for agriculture and hydroelectric power generation, and many other interventions have modified natural water and sediment fluxes and boundary conditions. The trapping of river transported sediment involves most of the hydrologic basin and can also reach 50% of the total sediment transport (Surian, 1999; Liébault and Piégay, 2001; Globevnik and Mikoš, 2009). In particular, the deficit of sediment budgets in many Italian rivers was aggravated by building material mining activities within the channel over the period 1960-1980 (Comiti *et al.*, 2011). These impacts have, as a consequence, caused the development of different morphological adjustments, which are generally greater than those expected by a natural fluvial evolutionary dynamic.

Considering Italian Alpine rivers, a common trend of considerable channel responses was recognized in the last decades, consisting of a major phase of narrowing and incision followed by more recent widening phases (Surian and Rinaldi, 2003). In the Piave River, for example, natural and artificial reforestation, mainly after the 1950s, and erosion- and torrent-control works, massively after 1970s, led to consequences on gravel supply, causing a strong narrowing of the river during the last century and the change from braided to wandering/single-thread morphology, leaving large areas available for the establishment of riparian forests (Comiti *et al.*, 2011). Bed incisions have reached 1 m and bed width has decreased by about 50% (Comiti *et al.*, 2011). The morphology of fluvial systems has changed considerably: it appears that, in the past, multi- thread channels were more common, moreover, also still braided rivers, as the piedmont reaches of Piave and Brenta rivers, today feature a braiding index clearly lower in respect to the past. Recent studies carried out on the Brenta river (Surian *et al.*, 2009b) highlighted that human interventions have strongly modified sediment regime, in particular during the second half of the 20th century. Understanding fluvial processes and channel evolution is a crucial issue for sustainable management and restoration of largely impacted rivers. An effective river restoration, as defined in the EU Water Framework Directive, is now required for most Alpine rivers that are characterized by channel instability, flood problems and biodiversity decline.

The type of fluvial islands present in a riverine system can also help to describe the river processes. Gurnell and Petts (2002) determined that most European rivers were once islands-dominated (pre-1900), but have become devoid of islands due to human interference. Away from areas of agricultural or urban development in Europe, islands remain a common feature of riverine landscapes, such as the Tagliamento River in northeast Italy (Ward *et al.*, 1999). The presence of a certain species of plant on the islands can help to determine the flow conditions in the area. Some plant species require specific growth conditions, such as inundation duration, gradient, and particle size (Picco *et al.*, 2012a, 2012b). Some large rivers are flow-regulated to some degree. This can have implications for fluvial islands development and stability.

Dams reduce flood peaks, increase base flow, and store sediments (Kondolf, 1997; Braatne *et al.*, 2003). As a result of human impacts and unwise management, most braided rivers have evolved into incised single-thread channels (Surian, 1999; Piégay *et* al., 2006) or tend toward that shape. The sediment transported downstream of a dam can only be a fraction of the normal sediment load. Flow regulation can, in fact, reduce bedload transport up to 50% (Hicks *et* al., 2003), and this leads to an armoured bed with consequent sediment supply issues on downstream reaches. This also generally reduces the biological habitat, diversity, and interactions between biotic and hydrologic processes (Poff *et al.*, 2007). While dams can reduce erosion and destruction of fluvial islands, they also promote bank attachment by decreasing the sediment supply and reducing the downstream transport capacity, which leads to deposition of tributary input sediment.

For the analysis of the magnitude of different morphological adjustments, precise quantitative approaches are needed. The development of several representation technologies, which derive their digital elevation models (DEMs) from precise acquisition data instruments, such as Light Detection and Ranging (LiDAR) and Terrestrial Laser Scanner (TLS), has allowed large areas to be characterized at finer resolutions in a very short time. Consequently the role of DEM uncertainty has become crucial, as it can strongly affect volume estimations and surface analysis (i.e. roughness mapping). The evaluation of geomorphometrical changes with Difference of DEMs methodology (DoD) is affected by multiple sources of errors and the results are often subject to significant uncertainties (Wheaton, 2008; Wheaton et al., 2010). The weakness of this approach is the correct representation of the bottom of wet channels, because the water column absorbs the signal of the sensors (active or passive) (Marcus & Fonstad, 2008). Recently developed bathymetric LiDAR sensors (ALB) still have high costs and relatively low resolution and data quality (Hilldale & Raff, 2008). Different methods to produce bathymetric data have recently been proposed. They are based on passive sensors (aerial photos) and the technique of ortho-restitution (Rinner, 1969; Fryer, 1983) or on the calibration of a depth-spectral-variation relationship of images defined according to the Beer-Lambert law (e.g. Winterbottom & Gilvear, 1997; Carbonneau et al., 2006; Marcus et al., 2003; Legleiter, 2011).

On the other hand, if we aim at highly detailed surface analysis by using TLS, such as to create the roughness map (useful in numerical modelling), precise analysis of the distributed uncertainty is needed. The TLS point cloud, collected from the instrument, is affected by a considerable number of factors that could decrease its quality. The influencing factors in quality of TLS data collection are identified as: systematic errors, instrument mechanism, atmospheric condition, object surface proprieties (surface reflectivity and surface geometry), location and orientation of scanned surface and the error due to the operator in the field (Lichti et al., 2006; Hodge, 2010; Soudarissanane et al., 2011). Other sources of errors are imaging geometry, registration errors due to the cloud matching or bundle adjustment algorithms used to register the multiple scans into the same model space. The data resolution determines the smallest detail that can be distinguished in the collected data, and it is determined by the laser footprint area and the minimum point spacing for data collection.

This work deals with linking river channel forms and processes in gravel bed rivers. Analysis and optimization of the different date derivable at different time, space and resolution scale, with a good equilibrium between time-consuming and results at low uncertainty.

The specific objectives of this PhD Thesis are:

i. *Multitemporal analysis of the Brenta River (Italy) over the last 30 years, to understand and to compare the morphological and vegetation dynamics of a typical human impacted gravel bed river;*
ii. *Development of an optimized colour bathymetry methodology applied on different gravel bed rivers (Brenta, Piave and Tagliamento Rivers) to provide accurate elevation models also in the wet areas;*
iii. *Precise digital elevation models (DTMs) and Digital Surface Models (DSM) production through LiDAR survey and colour bathymetry;*
iv. *Erosion and deposition analysis of an intense flood event (November and December 2010 floods – RI ~ 10 years) through a newly developed tool;*
v. *TLS uncertainty analysis, for the production of DTMs with the associated uncertainty map, through a developed "uncertainty tool utilities";*
vi. *Development of a new tool for the spatial point cloud classification in fluvial systems.*

2 *Fluvial Systems*

2.1 Catchment controls

Climate, geology, topography, vegetation, soil type and river management all play a role in shaping the behaviour of river channels. The change in these characteristics across the countries gives each of rivers a distinctive character. These controlling variables also change within individual catchments and determine the nature of water stored underground or occurring as surface water in waterbodies. Hydrology and the other key catchment controls listed above in turn also influence the magnitude and availability of sediment supply in rivers (Fryirs and Brierley, 2013).

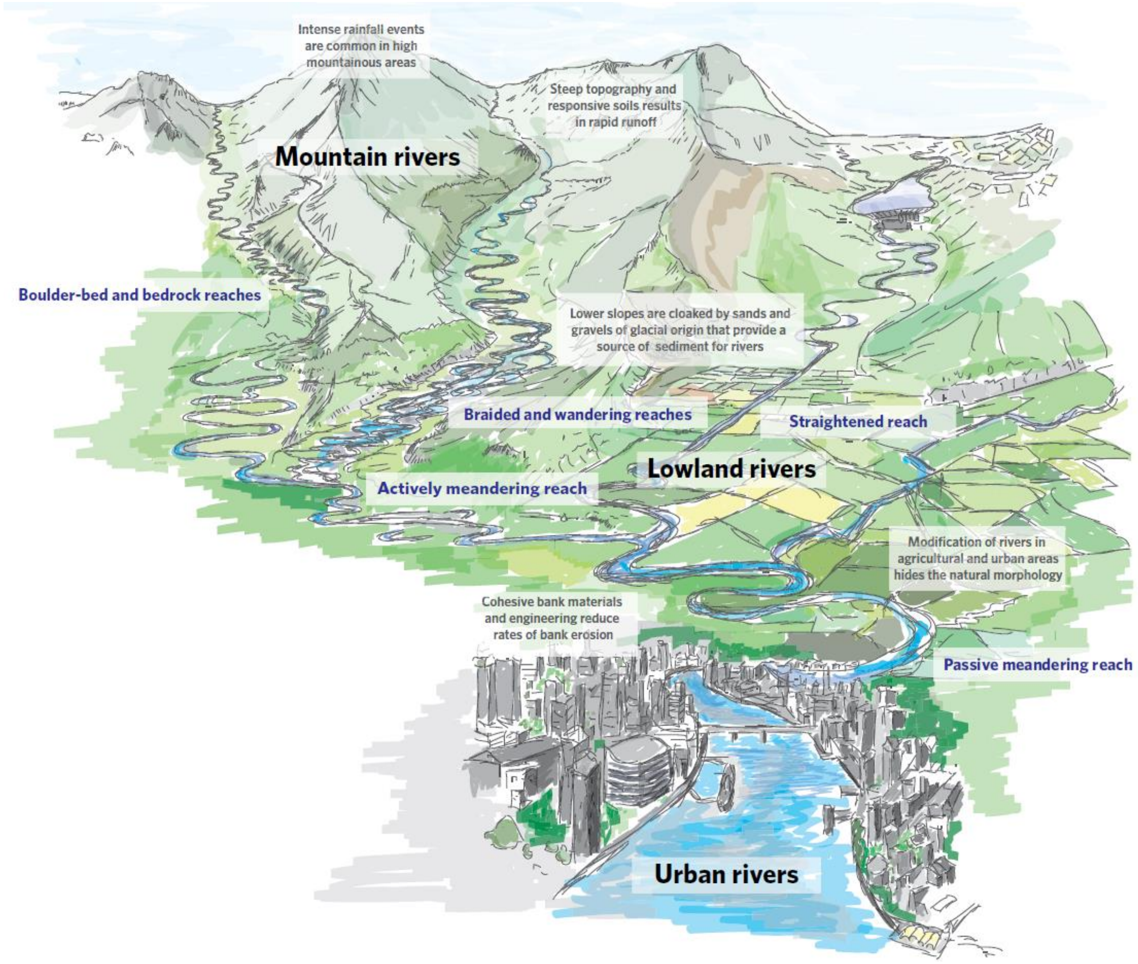

Figure 1. *River catchment.*

Geology and topography

Rainwater generally runs off rapidly from catchments with 'hard-rock' geologies or areas covered by tarmac and concrete in urban zones resulting in larger floods for a given rainfall event. The steepness of a catchment as determined by its geology and glacial history, together with land cover and land management (whether, for example, undrained moorland, drained farmland or urban areas; see below), are the most important factors that control the rate at which water runs off the land. The product of stream flow and channel slope determines the stream power available for rivers to erode, transport and deposit material. Topography also influences the availability of sediment for rivers; the lower slopes of many valleys are cloaked with a mixture of sands and gravels – a by-product of glaciation. These have been, and continue to be, reworked by rivers to produce distinctive landforms associated with specific channel types.

Vegetation and soil type

Much of the rainfall in a catchment is intercepted by vegetation before reaching the ground. The form and density of the vegetation can in turn influence the hydrology of rivers. Most vegetation types delay the time that rainfall takes to reach the river network to some degree. Woodland and dense herbaceous vegetation significantly slow the rate of surface runoff compared to heavily grazed grasslands. Across woodland areas runoff is further reduced through evaporation of rainfall to the atmosphere from the tree canopy under certain climatic conditions. Once the rainfall reaches the ground surface the structure of the soil will affect the proportion of water able to infiltrate. Poorly drained or heavily compacted soils result in higher rates of overland flow associated with rapid rises in river level. In many catchments, changes in land use have significantly altered the nature of soil and vegetation types and runoff regimes.

River types

In response to specific combinations of catchment controls, rivers have geomorphic traits that can be used to classify river types at the reach scale. Traits include the morphology of the river bed and banks, the steepness of the channel, the river planform and how dynamic the reach is. Typical locations within the catchment for each river type are shown in Figure 1, but deviation from this idealised downstream sequence is common due to variation of the landscape topography:

> *Upper catchment:* Mountain headwaters are strongly influenced by the boundary material and vegetation. In peatlands with high annual rainfall, the channels can cut

deeply into the peat, but the generally low gradients in these areas mean such channels are low energy. Where channel gradients are high or bedrock is close to the surface, high energy bedrock channels develop. Stream beds covered with boulders are associated with cascade or step-pool channel morphologies.

Mid catchment: Stream power tends to be highest in the mid catchment after the confluence of a number of tributaries but where gradient continues to be high. Under these conditions gravel-bed wandering and active meandering channels migrate across the floodplain through the processes of bank erosion and deposition of point bars. Where the valley gradient flattens out, rivers transporting a large amount of sediment develop a braided character as the transport capacity falls in response to reduced stream power. In lower sediment supply conditions or where confinement by valley sides is greater, relatively straight plane-bed and plane-riffle reaches occur.

Lower catchment: Stream power declines further when rivers reach the low gradient, wide valleys of the lowlands. As a result, the sediment load becomes increasingly finer but still dominated by gravel. Where un-cohesive banks occur the energy of the river may be sufficient for an active meandering morphology to develop and adjustment of meanders creates important river corridor habitat. Where cohesive clay banks dominate, the channel is more stable and rivers have passive meandering morphologies.

2.2 River dynamics and morphology

The diversity of rivers partly reflects the fact that three of the key controls on river form – topography, geology and climate – vary considerably. These catchment level controls determine the rate at which water and sediment are supplied to the river and in turn river form. In addition to these controls, the local channel slope, width and boundary materials further control the shape (i.e. morphology) of a river at a given location. A useful way to understand how energetic a river is, how it was formed and how it might behave in the future, is to consider its stream power. Total stream power is a statement of how much energy is contained within the volume of water flowing past a particular location as it is accelerated by gravity down the slope of the river bed. If the total stream power is then divided by the width of the river, it is possible to work out unit stream power, which reflects the actual conditions on the river bed. If the river contains little flow but is narrow, it may have a higher unit stream power than a very wide river with much more flow. The power of the river channel is counteracted by the resistance of the bed and banks to erosion. Cohesive bank material, riparian vegetation and coarse riverbeds all increase resistance, therefore reducing the influence of stream power. Different river types have different combinations of stream power and resistance factors. Along the course of a river, the relative contribution of factors that influence stream power and resistance changes. This produces different channel morphologies with varying levels of channel stability. Rivers follow a general pattern of increasing catchment area and decreasing valley slope moving from the headwaters to the estuary. The result in a simplified river catchment would be a continuum of channel morphology. However, to aid understanding and management, reaches are categorised according to their characteristic morphologies. Along the stream network, the river type may change gradually over kilometres or suddenly as a ‘step change’ over a few metres. Local topography, river confluences and boundaries between drift geologies (material overlying solid bedrock) are associated with either a change in stream power or resistance producing sudden changes in river morphology. The interaction between stream power and channel resistance changes with water discharge. The morphology of rivers is often therefore described as being in dynamic equilibrium. Material entrained and transported during periods of high stream power is replaced by deposition of transported material as floods recede and the capacity of the river to transport sediment falls. In this way, the size, number and precise location of fluvial features within a reach may fluctuate over time, while the general character of the reach is maintained. In-stream management is often undertaken in response to very large rare floods that cause significant visible changes, but it is the influence of smaller frequent floods occurring every few years that cumulatively have the greatest role in determining the size and shape of the channel. The size of these bankfull floods events, referred to as “channel forming flows”, may change over time in response to flow regulation, land management practices and climate patterns (Fryirs and Brierley, 2013).

Stream power, channel resistance and sediment transport

The balance of stream power and channel resistance shape channel morphology by influencing the size and volume of sediment that can be transported. Reaches of high stream power and low resistance tend to be a source of sediment to the stream network. Erosion processes in these reaches, excavated sands, gravels and pebbles from the river bed, banks and valley sides. There is a net movement of gravel from the river valley into the channel followed by export to the downstream river network during flood events. These reaches tend to be highly dynamic with large expanses of exposed gravel. High stream power, high resistance reaches tend to be zones of sediment transfer. The resistance of the bed and banks prevents the entrainment of new sediment and stream power remains sufficient to transport sediment out of the reach. The movement of material may be highly dynamic while the reach morphology remains stable if the input and export of sediment is balanced. The frequency of bed mobilisation in rivers relates not only to the occurrence of floods (stream power) but also the bed material size. Areas of the riverbed with larger pebbles and boulders material are relatively resistant to high stream power and are infrequently mobilised. Finer material, mobilised by smaller floods, is transported more often and moved further, with the very finest sands and silts regularly transported into the lowermost reaches of the catchment. Reaches of reduced stream power and low resistance tend to export sediment from the river channel back to the landscape.

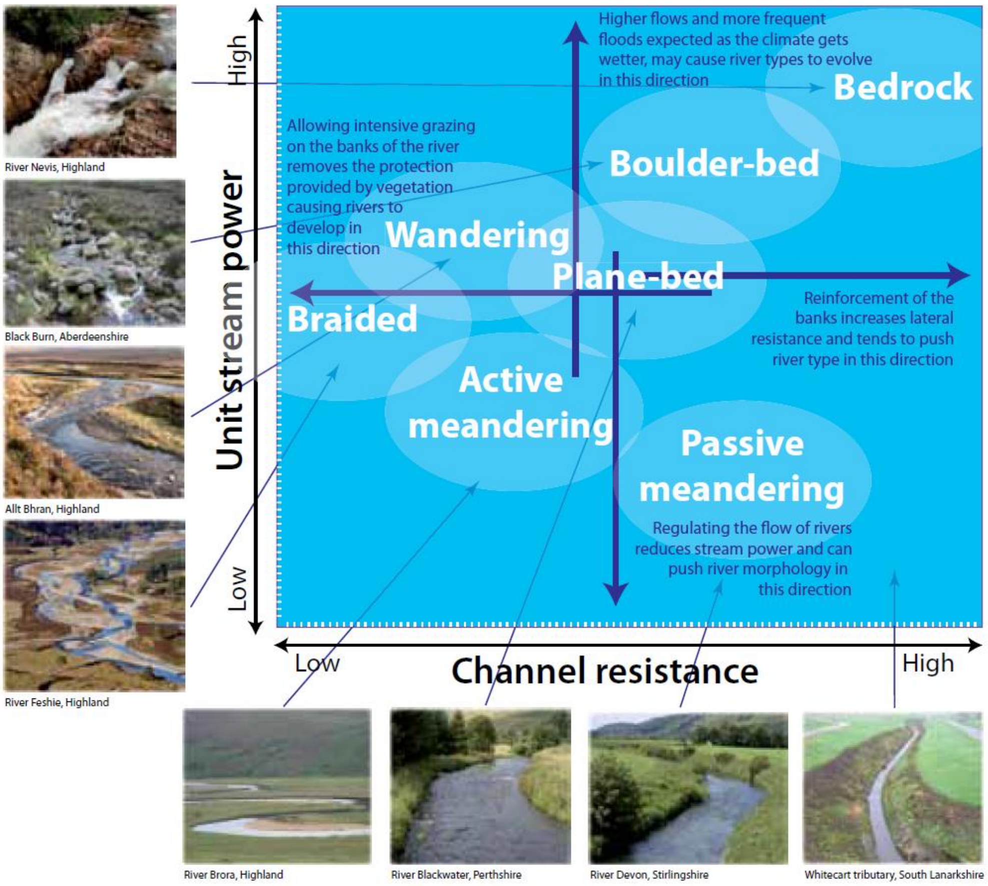

Figure 2. *River forms versus unit stream power.*

Distribution of key river types in relation to different combinations of unit stream power and channel boundary resistance can be considered as ‘sediment sinks’ and represent a net loss of sediment from the river network. Sediment is transported into the reach faster than it can be exported, leading to the accumulation of sediment over bars and islands. As these deposits rise and the influence of the river lessens, vegetation encroaches and floodplains form.

Individual reaches may fluctuate between eroding and depositing states as the stream power changes, either due to deposition of gravel changing the channel slope or changes in discharge due to climatic variation. The influence of low stream power during low flow and drought periods may be less obvious but is still important. Finer sediments may still be gradually reworked and deposited and the low levels of disturbance can give vegetation an opportunity to establish, reducing erosion and channel size. Plants play an important role in stabilising stream features and can significantly alter the morphological response to large floods (Fryirs and Brierley, 2013).

Changing the stream power

Widening: Increasing channel width, with the aim of accommodating larger floods, causes a reduction in unit stream power. This is likely to result in deposition of material and aggradation of the riverbed. As the channel reverts back to its natural width, the development of mid-channel gravel bars can deflect water towards riverbanks creating localised erosion in locations that were previously stable. This in turn is likely to increase processes of channel movement and adjustment.

Narrowing and deepening: Increasing the depth of a channel by dredging or reducing its width, increases the unit stream power as more water is conveyed per metre width of channel. The increase in stream power is likely to lead to further deepening and increased sediment transport. Problems associated with aggradation may develop at locations downstream where the sediment is redeposited.

Straightening: Straightening a channel by cutting off meanders increases the channel slope. This raises the stream power and can result in the export of sediment, deepening of the channel and increased riverbank slumping. Within the straightened channel, the natural tendency of flow to follow a sinuous course will trigger erosion and deposition processes and over time the channel will start to regain some of its natural planform. The transported sediment may be deposited downstream causing further issues associated with aggradation.

Alteration of discharge: Flow regulation associated with dams and abstraction reduce the magnitude of flow, which in turn can reduce stream power. This can lead to reduced sediment transport capacity and competence. Over time this may lead to a gradual stabilisation of dynamic river features such as bars and eroding banks as they are colonised by vegetation. The opposite effect may occur where land use changes create a more responsive catchment system that increases run-off and in turn boosts stream power, leading to increased channel activity.

Changing the channel resistance: Reinforcing the riverbanks of meandering channels increases lateral resistance to erosion. Depositional processes will continue on the inner bank with the effect of narrowing the channel and increasing unit stream power. This causes excessive scour and deepening on the outer bend potentially undermining the bank reinforcements. The effect can continue downstream, causing lateral erosion where it did not previously occur.

Removal of bankside vegetation: Tree and shrub vegetation bind river bank soils, increasing their resistance to erosion. When vegetation is removed or heavily grazed and trampled, the resistance properties are reduced leading to greater vulnerability to erosion. Bank erosion can cause river widening. The increased width is likely to result in the deposition of gravel bars and aggradation of the riverbed as the stream power is reduced. The development of mid-channel bars can divert water towards riverbanks creating localised erosion in locations that were previously stable.

2.3 Time scale

Implicit in the dynamic nature of rivers is the fact that their morphology responds to environmental fluctuations. Rivers are constantly responding to the changing input of water and sediment from year to year and from decade to decade. Over a defined period of time, if the inflow and outflow of sediment into a reach are in balance, the result is an equilibrium condition whereby the basic morphology is maintained. Over long timescales, their may be an imbalance of these processes resulting in a gradual change of morphology that may not be easily noticeable. In contrast, a major flood or input of sediment may lead to a geomorphic threshold being crossed and a rapid, obvious shift in morphology. Because of the complexity involved, separating temporary adjustments from changes related to long-term trends can be difficult. Consideration of timescales is therefore fundamental to understanding river ecosystems. Thus the river, which becomes to us a living force, spreading its influence from side to side of its valley never at rest, but ever at work preparing a fertile soil for the vegetation, which is at once the glory and protection of the valley floor, and the main source of subsistence for man and beast" (Fryirs and Brierley, 2013).

Timescales of adjustment

Months (0 - 1 year): The geomorphic response to frequent high-flow events tends to be restricted to in-channel habitats. These flows may occur every month or so and tend to be concentrated in the spring and autumn months. They scour and sculpt fluvial features, altering their shape and size from month to month. Over many millennia, riverine plants and animals have developed both morphological and behavioural adaption. Many organisms have life cycle stages linked to these events, such as salmonids that use the more frequent high-flow events to get past obstacles in order to reach the shallow burns and rivers in the upper catchment to spawn.

Years (1 - 10 years): In unregulated rivers the highest flow of the year will vary from one year to the next. In some years it will be contained within the channel, while in others it will inundate the full extent of the floodplain. The mean annual flood describes the average across a number of years. A flow event approximating the size of the mean annual flood is expected to return every few years (1.5 - 2 years on average). On natural rivers it is these relatively frequent events that determine the size of the channel (Bankfull discharge). During these events, erosion of a riverbank may be balanced by deposition during the same or subsequent floods, resulting in minor adjustments to the course and a redistribution of sediment, while overall maintaining channel size and form. Very active river forms such as dynamic braided reaches, may change course a number of times within this timescale. Colonisation by terrestrial vegetation, which requires a period of substrate stability, is prevented by the rapid adjustments, adding to the mobile character of the reach. Smaller changes to the course of a river through meander migration may be seen on moderately active types.

Decades (10 - 100 years): Even under stable climatic conditions it is typical for the frequency of large floods to vary from one decade to the next. This can result in adjustments to river size and morphology. As the river enters a flood-rich period, the size of the mean annual flood will increase. The balance between erosion and deposition will tip in favour of erosion, adjusting the channel size to accommodate the increased flows. As flood frequency falls after a flood-rich period, vegetation encroachment and deposition processes begin to dominate. Smaller floods provide an opportunity for terrestrial plants to recolonise flood deposits, reducing channel width until the erosion-deposition balance is restored. This variability is independent of long-term trends in climate, despite appearing to be new over the timescales that river management is undertaken. Flood-rich periods may be separated by a number of decades. Visible adjustment to the course of moderately active rivers, such as active meandering and wandering channel types, may also occur within this timescale.

Significant changes tend to be linked to large floods expected only a few times each century. In-channel features for example, jams of dead woody material, may be transient when considered over the timescale of 10–100 years. A jam may persist for several years providing habitat to a range of species, before eventually breaking up. The amount of dead woody material in a reach and its persistence depends on the rate of decay and replenishment of material. Where extensive riparian woodland is present, a high density of such accumulations can occur.

Centuries (100 - 1000 years): The largest floods are separated by hundreds of years of lower flows and smaller floods. Very large or extreme floods can significantly alter the character of a river, even those sections that have been stable for several lifetimes. These rare events can result in disturbance to habitats, realignment of planform and transport of vast volumes of sediment. As discussed at the beginning of the book, river type is generally controlled by catchment scale factors, which include climate. A shift from one river type to another therefore often occurs over similar timeframes to climatic changes (Fryirs and Brierley, 2013).

3 Linking River Channel Forms with processes in Gravel Bed Rivers

3.1 Gravel Bed Rivers

Great efforts were made to classify gravel bed rivers from the scientists. Three principal planform features characterize the gravel-bed rivers: straight wandering and braided streams (Leopold et al, 1964).

Different kind of classification systems focusses on bed form as a distinctive feature, that is the system proposed by Montgomery and Buffington’s (1997). They cleared the relation between bed form and flow pattern, especially in mountain environment systems.

This classification method born in the Pacific Northwest of U.S.A., and it has also been applied with success in the Italian Alps (Lenzi et al, 2000). Rivers are classified into five categories; two of them apply to gravel-bed rivers, called plane-bed and pool-riffle forms.

A plane-bed forms can be recognized in the field thanks to its lack of bed forms. Usually, they consist of straight reaches with no bars, therefore the longitudinal profile can be a straight line (Figure 3).

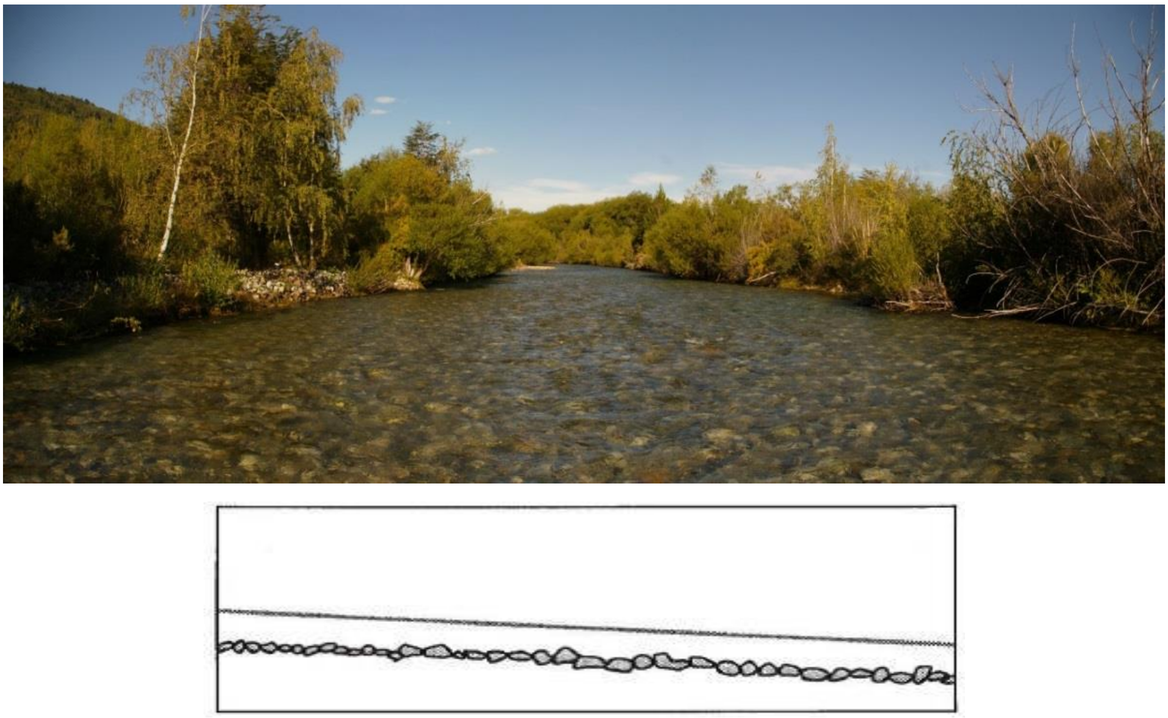

Figure 3. *Plane-bed form of Epuyen River in Chubut Province, Argentina and a typical longitudinal profile.*

A cross section of a plane-bed has a low width/depth ratio and the presence of large gravel and pebbles on the bottom that gives low values of relative submergence (water depth to grain size ratio). These geometric and sediment size characteristics are related to a specific flow pattern. A uniform flow with a lack of convergent – divergent lateral flow sequences. The low aspect ratio and greater relative roughness may decompose lateral flow into smaller circulation cells (Montgomery and Buffington, 1997).

When roughness is sufficiently low the velocity of the vertical distribution can be considered with a logarithmic law. On the other hand, when roughness is very high we cannot apply this law because the distribution is greatly disturbed by the presence of large particles. Nonetheless, in both cases the grain roughness is the primary source of flow resistance. A typical feature of plane-bed channels is the presence of a mobile armoured bed surface at near bankfull discharge (Buffington, 1995). Parker (1990) shown that a mobile armour layer indicates a balance between mean annual sediment supply and transport capacity for gravel bed rivers where the bankfull shear stress just exceeds the threshold value.

Riffle-pool forms have a rhythmic sequence of lateral bars and an undulating bed with shallow and deep areas (Figure 4). At low flow bars emerge from the water and the bed pattern can be recognized.

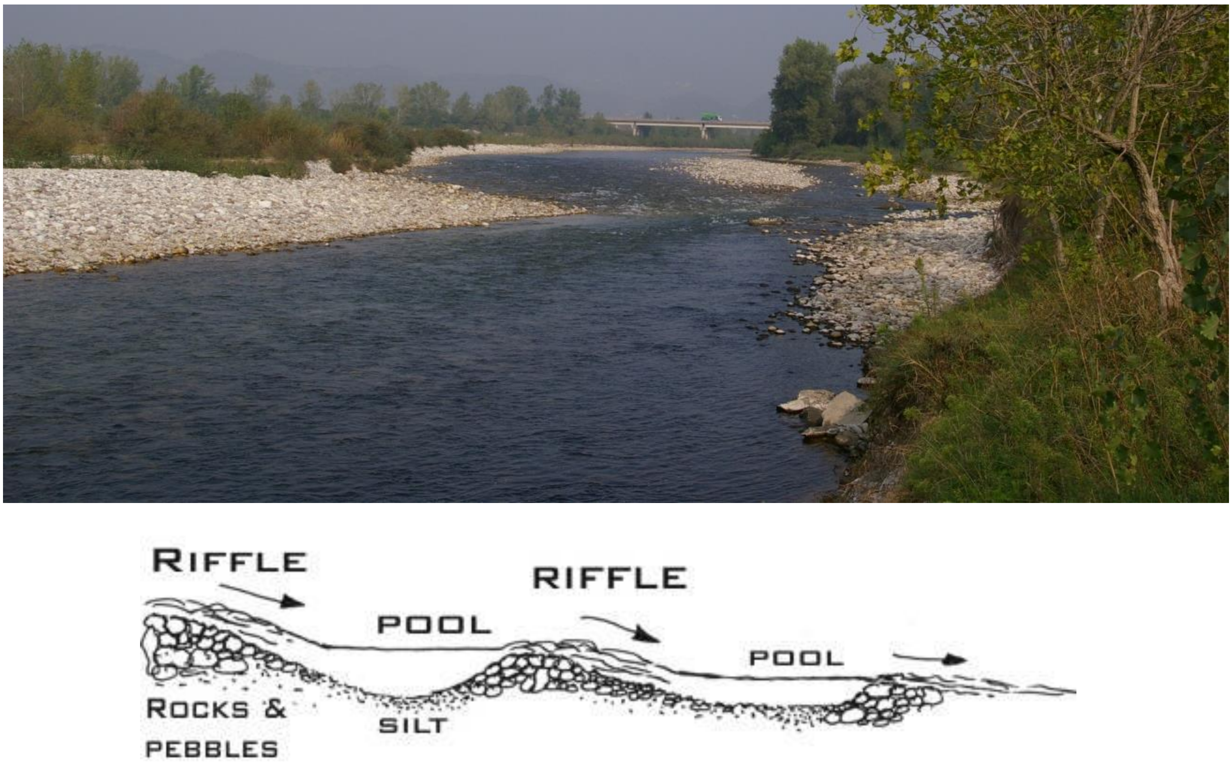

Figure 4. *Riffle-pool form of Brenta River, Italy and its typical longitudinal profile.*

Lateral bars alternate making the low flow to describe a sinuous trajectory (sinuosity between 1.3 and 1.5). The highest point in the bar corresponds with the maximum depression in the channel, which is the pool. At the head of a bar the flow passes from one side to the other of the channel. This sector with a low water depth is called a riffle. Field observations evidence that these features are spaced evenly along the channel with a separation about five to seven channels width (Leopold et al, 1964; Hey and Thorne, 1986).

The development of the alluvial bars requires a sufficiently large width to depth ratio and small grain sizes that are easily mobilized and stacked by the flow (Church and Jones, 1982). Surface grain size is variable with the courser sizes in riffles and generally finer sizes in pools. Substrate size in riffle-pool streams varies from sand to pebble, but is typically is gravel sized. It is common to observe an armour layer with finer size in the substrate and coarser size on the surface (Kaless, 2013).

This bed undulating produce a no uniform flow. Thompson (1986) has presented a description of the flow along a riffle-pool sequence. At the upstream of a riffle surface, the flow passes obliquely, and is directed towards the outer bank, creating the “talweg line” (Figure 5).

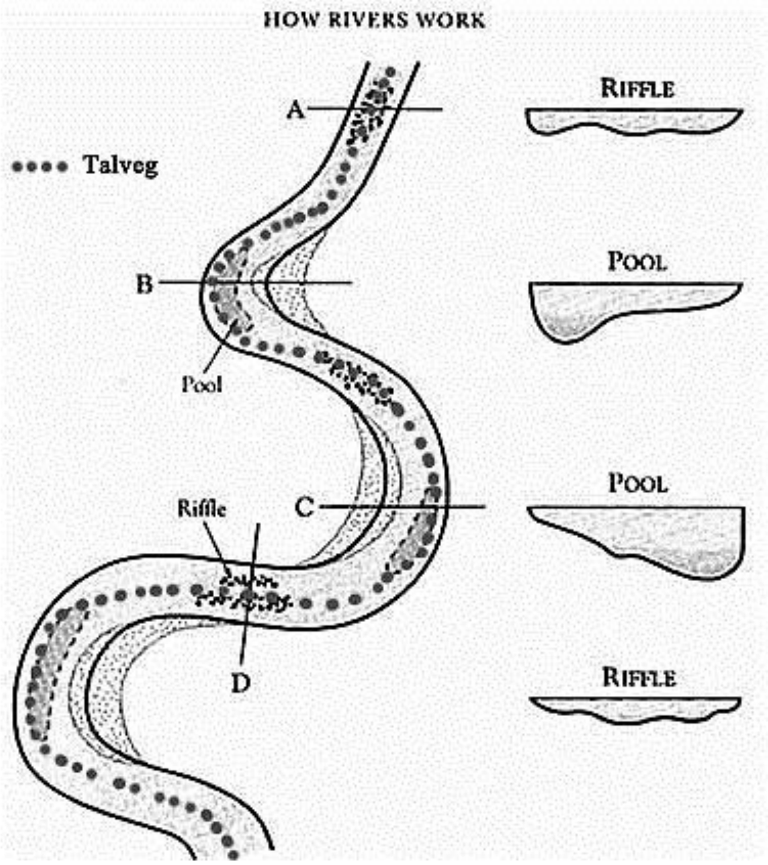

Figure 5. *Riffle-pool sequence: depth, talweg and typical cross-sections.*

At the outer bank there is a zone of upwelling and a strong inward movement of surface water towards a zone of convergence over the deepest part of the pool.

Near the river bed the current flow diverges and divides making two opposite secondary flow cells. The helix flow decays as the depth decreases downstream. At the crest of the depositional front, on the riffle, the flow diverges passing obliquely to the other bank and then starting the sequence again. The presence of secondary flow is not exclusively associated to the presence of alternating bars. They have also been observed in straight reaches (Leopold, 1982) suggesting that they could be a consequence of instability in turbulent flow. In fact, Einstein and Shen (1964) demonstrated that a meandering talweg could be produced on the bed of a straight laboratory channel by the action of twin surface-convergent cells of secondary flow induced purely by wall turbulence. Although secondary currents are present in both straight channels and sinuous channels, the intensity and origin in each case is different. In a straight channel the secondary flow is due to instabilities in turbulent flow and has a very low intensity (2% of the principal current). On the other hand, a change in direction can create a secondary current, but this time with a higher intensity, that is the case of the riffle-pool sequence (Kaless, 2013).

Several theories proposed the development of riffle-pool sequences. Langbein and Leopold (1968) proposed the kinematic wave theory that gives the interesting result of a static plan form for the maximum transport rate capacity. According to Yang (1971) riffle formation is the result of the combination of two processes: dispersion stresses acts over the potential riffle resulting in the sorting of the bed material. Keller and Melhorn (1973) invoked the alternating divergent-convergent flow with secondary flow pattern (as described later by Thompson, 1986) as the main mechanism for the development of scour and depositional patterns.

From a planimetric point of view the riffle-pool bed forms can be divided into two morphological categories, braided and wandering, as reported from Billi classification 1994.

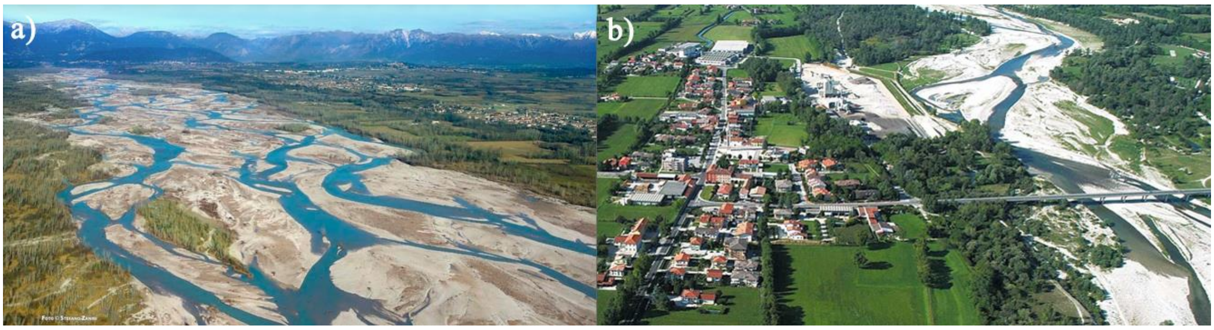

Figure 6. *Typical braided reach (a) of the Tagliamento River (Italy) and typical wandering reach (b) of the Brenta River (Italy).*

Braided rivers forms are favoured by high energy conditions, a very variable water discharge, abundant supply and availability of sediments, relevant quantities of bed load transport and non-cohesive banks. They are characterized by wide active channel usually composed of two or more channels similar in size, and showing riffle-pool bed-forms. Their length-depth ratio is usually higher than 40 (it can reach even 300) and their solps is lower than 4%. Two bar type characterize braided rivers, different in altitude. Lower bars are continuously subjected to submersion and erosion phenomena, while higher ones, which are also more stable, are reached by water only during severe flood events. The main distinguishing characteristics of these two bars are referred to the particle size distribution and the presence of vegetation.

Bars, which are frequently submerged, are characterized by coarse-grained sediments and lack of vegetation (or poor presence). In more stable bars, which are also higher, finer surface sediments are more abundant, thus favouring the spread of vegetation. The Vegetation effects it’s a helps to stabilise the bar by increasing its resistance to motion, thus lowering the current velocity above it and favouring in this way further deposition of finer sediments, according to a positive feedback process. Braided rivers are characterized by high dynamicity with a continuous displacement of bars and channels during flood events. A further peculiarity of this morphological typology is the difference between low-flow and ordinary overflow channels. During low flow, few channels are filled with water, whereas by an increasing discharge rate more and more channels collect water until filling the entire flood channel, reaching a sinuosity values close to unity.

In the other hand, Wandering rivers (Figure 6b) are characterized by a low or medium sinuosity (1.3 – 1.5) and they belong to the intermediate shape between braided and meandering rivers.

They are usually composed of alternate lateral bars, usually half-moon shapeand by one single active channel. There could be also a secondary channel, which can be active (shear channel) or inactive (dead channel) and with a variable width, but not exceeding that of the main channel. Furthermore there are also secondary transverse channels on the bars. The shear channel forms during strong floods due to the cross shear of lateral bar; it can subsequently obstruct or be abandoned, or, on the contrary, even widen and become the main channel. The dead channel, instead, is the final part of a no-longer-active channel, which is supplied only during floods with stagnant water. The main characteristic of these fluvial systems is the sinuosity variation by changing water discharge.

During low or moderate flow, bars emerge and the stream takes on a meandering shape (sinuosity equal to 1.5), which fades during bigger floods that provide an increment in water depth to cover a large part of the lateral bars, reaching a sinuosity level close to unity.

Wandering rivers are considered as the evolution of braided rivers determined by the anthropic influences. They are very common in Italy and in many mountain areas (Picco, 2010).

3.2 Linking channel forms with processes

A common problem in fluvial geomorphology is identify the dominant process responsible for creation of a particular form. If we really want to connect a process with a change is necessary reconstruct it at a specific time and temporal scale. The observation as they happened can resolve controversies over, for instance, which process or event (e.g. discharge) is dominant (Richards, 1982). This problem is correlated by the interaction of discharge and sediment supply fluctuation in causing channel changes at the study site. Figure 7 (Lane and Richards, 1997), show the effects of changes in discharge on net volume of morphological change, derived by difference of DEMs linked with its hydrological data. The Figure 7 highlight that there is a close correlation between the magnitude and the volume of erosion and of deposition; with larger discharge increase, the volume of erosion is greater. Despite this general trend, closer inspection reveals a more complicated pattern. Indeed as shown in the Figure 7 similar level of change in discharge do not produce in every case similar results. Lane *et al.*, 1996 has confirm that when observations between volumetric and discharge changes show that there is no significant correlation between these two variables, for determinate range of changes, its depend on the sediment supply. This observation emphasizes that discharge and sediment supply act together to control river channel changes.

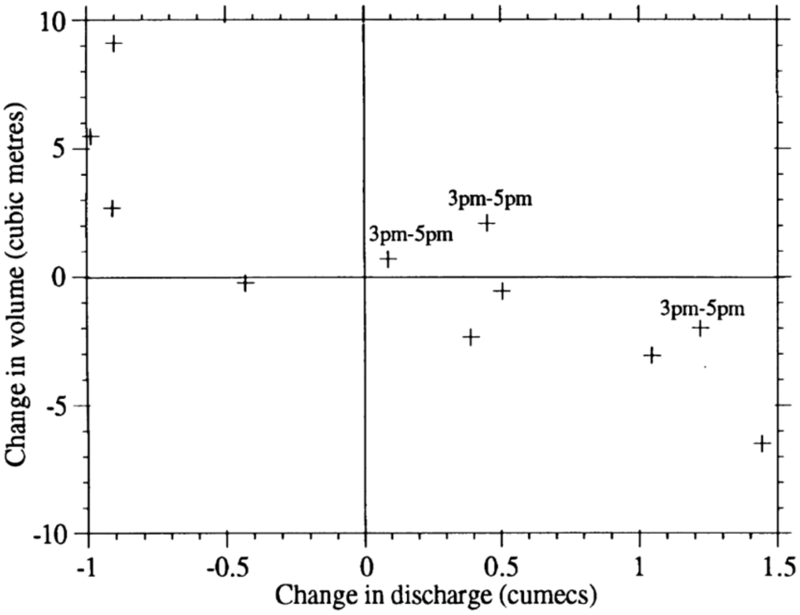

Figure 7. *Plot of volume erosion (negative change in volume) or deposition (positive) versus the associated change in discharge (Lane and Richards, 1997).*

Sediment supply is determined both by patterns of erosion and deposition upstream, and more local supply of sediment from eroding banks within the reach. Sediment supply from upstream reflects the interaction of daily discharge fluctuations with the availability of transportable sediment in the reach. This conclusion as confirmed by Bathurst, 1987 implies that both bed sediment availability and upstream supply affect the sediment transport rate.

The dynamics of a river reach can be conceived in terms of interacting waves of discharge and sediment, moving at different velocities through the catchment; as append during a flood events (Figure 8). These interactions creates temporary zones of both sediment storage and sediment erosion, determining future patterns of storage and erosion. The behaviour observed in a study reach reflects its position in the catchment, and the local interaction of externally imposed discharge fluctuation with internally driven controls on sediment supply. Understanding the behaviour of the reach cannot be divorced from consideration of its position in the catchment (Lane and Richards, 1997). An implication of the above discussion is that the response of a system to an imposed process event depends on the "conditioning" effects of previous events (Newson, 1980), which define the context that determines the systems response. This conditioning has a spatial and a temporal scale, both because processes patterns depend on a three-dimensional morphological initial condition and the spatial distribution of a transportable sediment, and because the effects are closely related with the time taken for the event to be propagated through the system.

Figure 8. *Relevant flood event of November 2010 (RI > 8 years) Brenta River (Italy).*

4 Remote Sensing in Gravel Bed Rivers

The study of river morphology and dynamics is essential to understand the factors determining sediment erosion, transport and deposition processes. Natural (e.g. climatic and hydrologic variations) and anthropic factors (e.g. water captures, grade-control works, gravel mining, deforestation) can act at both reach- and basin-scales to change the degree or timing of these processes (Buffington, 2012). The reach geomorphic variations are a direct consequence of sediment erosion and deposition, which are influenced by the size and volume of the sediment supply, the transport capacity of the flow, and by local topographic constraints. The quantification of the interaction of these processes is limited by the difficulty of collecting high spatial resolution data in river environments. Traditional approaches based on the application of hydraulic formulas at cross-sections fail when aiming at describing non-uniform natural conditions. Three-dimensional and high-resolution representations of river bed morphology are used in many applications: hydraulic and cellular modeling (e.g. Rumsby *et al.*, 2008); impact of climate change evaluation (eg. Barbata et al., 2006); and flood risk management (Rumsby *et al.*, 2001; Macklin and Rumsby, 2007); defining hazardous areas which also involves an assessment of erosion and deposition areas along the river corridor (Stover and Montgomery, 2001; Lane *et al.*, 2007). Calculating sediment budgets and estimating sediment transport rates are also fundamental to quantify geomorphological changes due to flood events and changes in flow regime (Ashmore and Church, 1998).

The traditional techniques of terrain survey (e.g. total station devices, dGPS) for evaluating morphological changes in large areas have been demonstrated as being expensive, time-consuming and difficult to apply to less accessible areas. Some innovative methods have shown a good ability in the production of high-resolution Digital Terrain Model (DTM) of fluvial systems. Recent studies on morphological channel changes have used passive remote sensing techniques such as digital image processing (e.g. Forward Image Model, Legleiter and Roberts, 2009), digital photogrammetry (Dixon *et al.*, 1998; Heritage *et al.*, 1998; Lane *et al.*, 2010), active sensors including Light Detection And Ranging (LiDAR) (e.g. Hicks *et al.*, 2002; 2006; Kinzel *et al.*, 2007; Hicks, 2012), Terrestrial Laser Scanner (TLS) (eg. Brasington et al., 2012; Picco et al., 2012c) and acoustic methods (eg. Muste *et al.*, 2012; Rennie, 2012).

The main problem related to the production of precise DTMs with non-bathymetric sensors is due to the absorption of natural (solar) or artificial (LiDAR) electromagnetic radiation in the wet channel. The capacity of the electromagnetic signal to pass through water, reflect from the bed and reach a sensor depends on the water surface texture (pleating, reflexes, etc.), the water column (depth and turbidity) and some bed (substrate type and algae presence) characteristics (Marcus, 2012; Marcus and Fonstad, 2008).

Only few tools have proved to be able to provide an accurate and high-resolution measure of the submerged bed surface, and survey precision decreases with the increasing of the water depth. Bathymetric LiDAR sensors have recently been developed and should enable the survey of underwater bed surfaces. Nevertheless, they feature high costs, relatively low resolutions, and data quality comparable to photogrammetric techniques (Hilldale and Raff, 2008). Many progress in the LiDAR acquisition of topographic information from submerged areas, have been made with a new technology: Experimental Advanced Airborne Research LiDAR system (EAARL) that records the full waveform of returning laser pulse. This system is affected by environmental conditions (such as, e.g. the turbulence in the pool, bubbles in the water column, turbidities, and low-bottom albedo) and post-processing algorithms even if the accuracy appears comparable to that of airborne terrestrial near-infrared LiDARs (Kinzel et al., 2012; McKean et al., 2009).

The survey of wet areas can be thus approached using two photogrammetric techniques (manual or automatic) which are able to produce a cloud of elevation points (Rinner, 1969; Fryer, 1983), or with a technique based on the calibration of a depth-reflectance relationship of images, which can be in greyscale (e.g. Winterbottom and Gilvear, 1997), coloured (e.g. Carbonneau *et al.*, 2006) or multispectral (Marcus *et al.*, 2003; Legleiter, 2011). Both solutions need a field survey, contemporary to the flight, to allow the availability of calibration depth points. The depth-reflectance relationship can be defined using an empirical relationship, using one or more bands (e.g. Legleiter *et al.*, 2009 - Figure 9), or according to the Beer-Lambert law. In the last case the amount of light absorbed by a transparent material is proportional to the distance of the light travelling through that material (Carbonneau *et al.*, 2006):

$$I_{out} = I_{in}\, e^{-cx} \tag{1}$$

Where l_{in} is the incoming intensity, l_{out} the outgoing intensity, c is the rate of light absorption, and x the distance. Once reliable digital elevation models (DEMs) are obtained, it is possible to detect and interpret, in a quantitative way, geomorphic changes in river systems (e.g. Lane *et al.*, 1994). An important component to be evaluated on DEMs is the uncertainty, which can be influenced by a large number of factors. The most decisive error sources include survey point quality, sampling strategy, surface topographic complexity and interpolation methods (Panissod et al., 2009; Milan *et al.*, 2011). Total uncertainty is usually derived from the classical statistical theory of errors (Taylor, 1997) where an estimation of DEM accuracy based on survey data is used as a surrogate of DEM quality (Milan *et al.*, 2007).

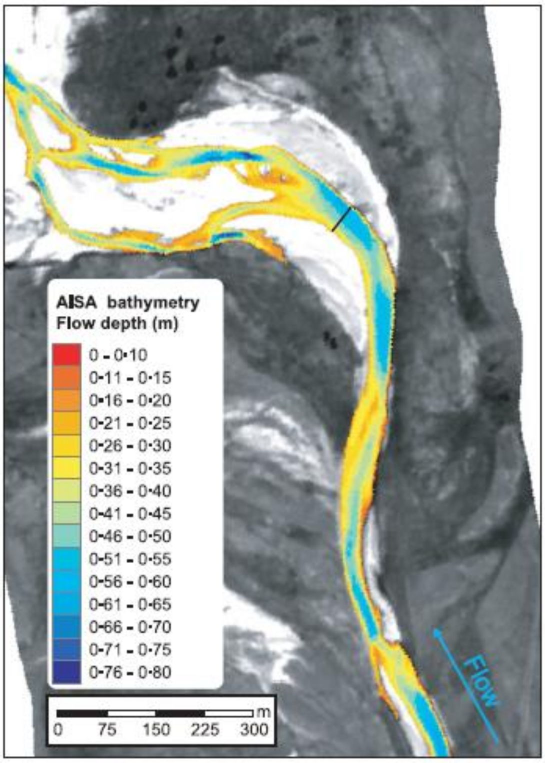

Figure 9. *Spectrally based bathymetric map of the Lamar River (Legleiter et al., 2009).*

If reliable depth estimates could be made with the images used to measure grain size, a very powerful tool capable of automated measurements of both depth and grain size could be developed. Such a remote sensing approach to river characterization could have a major impact on future research in all fields interested in fluvial environments and in addition the bathymetric methods.

The use of high resolution imagery for automated depth measurement has specific difficulties:

- If centimeter resolution airborne imagery is collected at the catchment scale, this necessarily implies that a very large number of photographs, will be necessary to cover the whole study area;
- Each images must have a perfect georeferencing to predict in a reliable manner the depth of the channel;
- The use of digital images to measure light intensity value can be problematic. As described by Fonstad and Marcus (2005), when applying bathymetric models to

imagery, it is necessary to measure the light intensity with the digital number of each image pixel.

Therefore, photography principles such as aperture and exposure times should be considered, since these factors control the conversion of actual light intensity in the field to digital image numbers. Of particular importance is the case where camera exposure and aperture settings are variable within the image data set since the conversion from light intensity to digital numbers will vary accordingly. In the case of large image data sets, this variability can be problematic since identical lighting conditions in the field may not be represented by identical digital image numbers in the imagery. There is a significant body of literature describing the physics of bathymetric mapping (Lyon *et al.*, 1992; Lyon and Hutchinson, 1995; Legleiter *et al.*, 2004). However, these methods all assume that identical light conditions in the field will produce identical image brightness levels. Therefore, the issues of variable camera apertures and exposures leading to variable image illumination must be addressed separately. This specific problem is discussed in the literature owing to the recent availability of high resolution with image data sets comprised of thousands of images (Carbonneau *et al.*, 2006).

5 Uncertainty among Methodologies, Time and Spatial Scales in Fluvial Geomorphology

5.1 Multitemporal analysis uncertainty

A study of planform changes of a gravel bed rivers over the last 200 years was performed on Piave River (Comiti et al., 2011). They analyzed features on three historical maps (1805, 1890, and 1926), seven (1960, 1970, 1982, 1991, 1999, 2003, and 2006) aerial photos (Figure 10) and an historical flood data series. The maps range in scale from 1:25,000 to 1:26,000, whereas the aerial photos range from 1:8000 to 1:33,000. Photos scanned at a resolution of 600 dpi in order to obtain an average virtual resolution of 1 m or smaller.

Digital maps and aerial photographs rectified and coregistered to a common mapping base at 1:5000 by GIS software (Esri ArcGIS 9.2). Approximately in this study were used 30 ground-control points to rectify each single frame, and second-order polynomial transformations were then applied, obtaining root mean square errors (RMSE) ranging from 2 to 4 m. The higher RMSE are for historical maps, particularly for the oldest map (1805, scale 1:26,000).

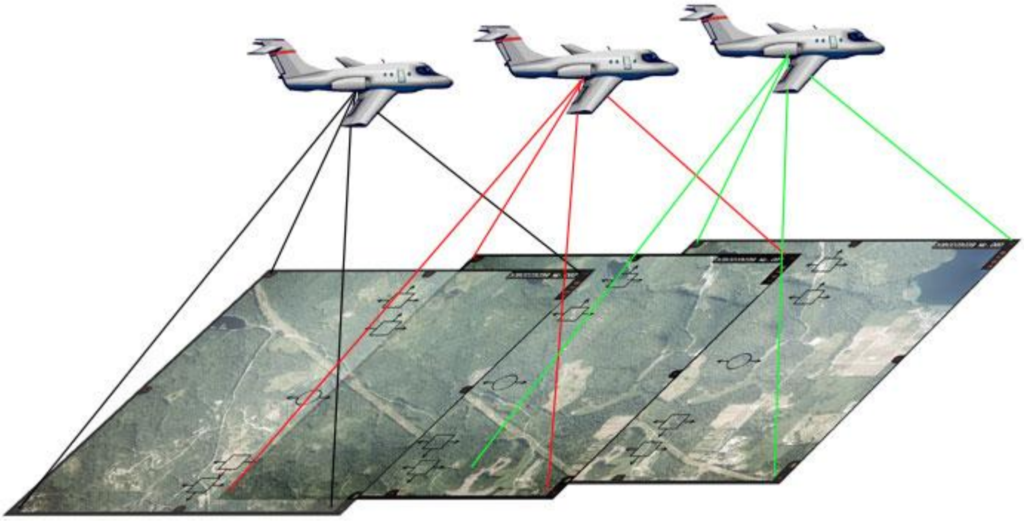

Figure 10. *Aerial photo survey.*

Significant planform features were digitized on rectified maps and photos in order to derive land use for each image. Measurements are affected by uncertainty due to errors from rectification and digitization processes. To estimate the uncertainty in these analysis previous studies that took into account:

- RMSE values, which can be an acceptable proxy of the average error of georectification (Hughes et al., 2006);
- Both georectification and digitization errors (e.g., Gurnell, 1997; Winterbottom, 2000; Mount et al., 2003; Zanoni et al., 2008);
- Some field measurements with dGPS to assess the position of digitized features.

In the research of Comiti el. al. 2011 the uncertainty analysis has revealed maximum errors of about 15–20 m and 6 m for measurements on maps and aerial photographs, respectively.
Historical maps were important in this study to distinguish the boundaries of three basic fluvial features lying within the fluvial corridor (i.e., the area bordered by hillslopes and ancient terraces and thus including active channel, floodplains, and recent terraces): unvegetated active channel, vegetated islands (i.e., shrubby/arboreal vegetation within the active channel), and marginal woody vegetation (i.e., shrubby/arboreal vegetation at the channel margins). Aerial photos allow the identification of more vegetation classes: islands with arboreal vegetation, islands with shrubby vegetation, arboreal marginal vegetation, shrubby marginal vegetation, and herbaceousmarginal vegetation (example in Figure 11). Furthermore, three additional classes related to human use of the river corridor were adopted: urban areas, cultivated areas, and gravel mines. All aerial photos must be taken during low flow conditions. Following these rules it’s possible use the entire unvegetated active channel class to describe areas occupied by flowing water during low flows (main and secondary channels) and exposed and unvegetated surfaces (i.e. bars) next to the channels, i.e., to represent the whole area inundated and subject to bed mobilization during frequent floods (RI=1–2 years). Bars covered with herbaceous vegetation were thus assigned to this active channel category. In the aerial photos, evidence of canopy texture, shape, and shadows are useful to estimate vegetation height and thus to differentiate between arboreal and shrubby vegetation classes. A height of about 4–5 m is necessary to separate the two classes. An arboreal island is defined as (Gurnell, 1997) a distinct vegetated area surrounded by the active channel having at least 60% of its surface occupied by arboreal vegetation (i.e., an arboreal island can include portions of herbaceous or shrubby vegetation). If the surface covered by trees is 60%, the area was classified as a shrubby island.

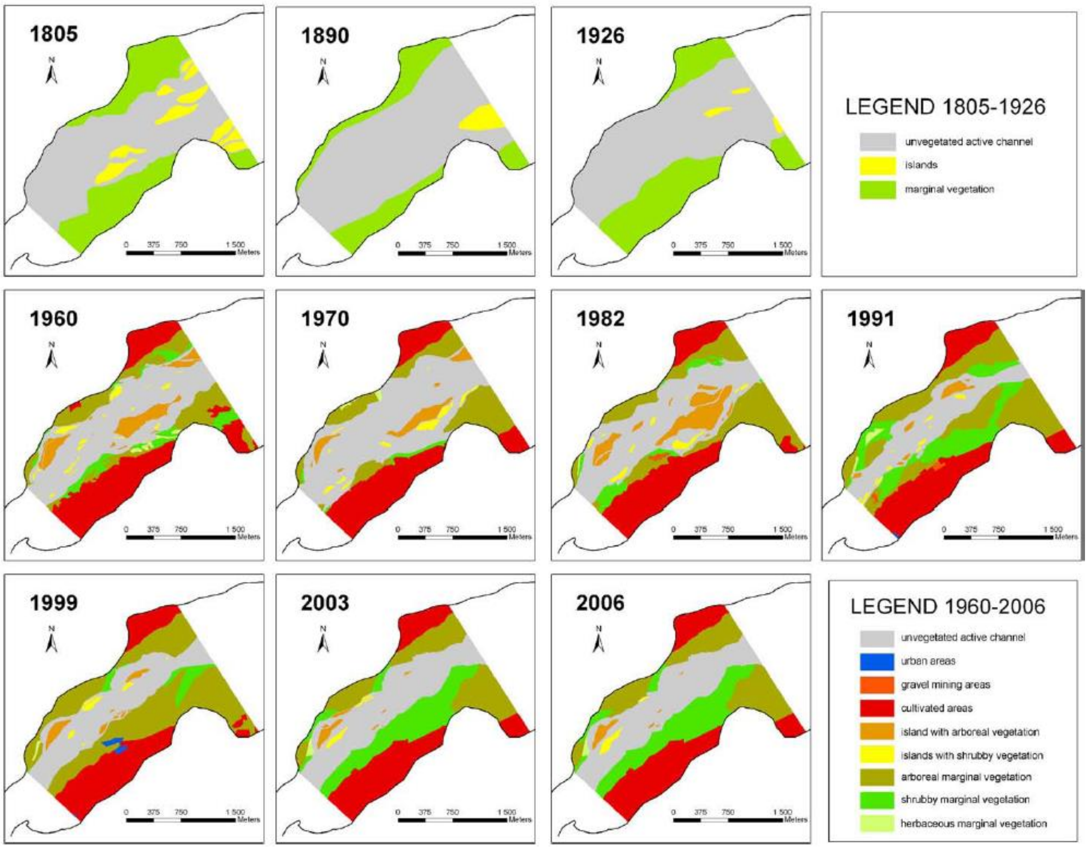

Figure 11. *Planform evolution of sub-reach 9 of Piave River from 1805 to 2006 (Comiti et al., 2011). The classification of fluvial features is simplified in 1805, 1890, and 1926 because it is derived from the analysis of historical maps. Aerial photographs, which allow more detailed interpretation of vegetation and land use, have been used in the subsequent years from 1960 to 2006 .*

5.2 Airborne LiDAR

The transition from point data to spatial data, was started with the development of airborne laser scanning goes back to the 1970s with early NASA systems. Although expensive, cumbersome and limited to specific applications, these early systems demonstrated the value of the technology and your possible applications. These systems operate by emitting laser pulses. Through measuring the return time of a laser pulse, the “range” calculated using the speed of light, it’s possible define the coordinates x, y and z of areas concerned (Figure 12). This is similar to using a total station surveying instrument but with very more points surveyed even if with less precision. The advent of GPS technology in the late-80s provided the necessary positioning accuracy required for high resolution LiDAR. It wasn’t long until rapid pulsing laser scanners were developed and linked to the GPS system. The systems became complete with ultra accurate clocks for timing the LiDAR return and Inertial Measurement Units (IMU) for capturing the orientation parameters (pitch, roll, and heading angles) of the scanner. A modern LiDAR system has a rapid pulsing laser scanner (with continuous wave lasers which obtain range values by phase measurements), precise kinematic GPS positioning, orientation parameters from the IMU, a timing device (clock) capable of recording travel times to within 0.2 of a nanosecond, a suite of robust portable computers, and substantial data storage (100 GB per mission). From the earliest applications of airborne laser scanning, the mapping community was aware that vertical accuracies of 15 - 20 cm Root Mean Square Error (RMSE) were possible, with horizontal accuracies of about 1/1000 flying height of fly. Maximizing this technology greatly reduces the time and fieldwork required by most traditional methods such as surveys in mountain basins. (Picco, 2010)

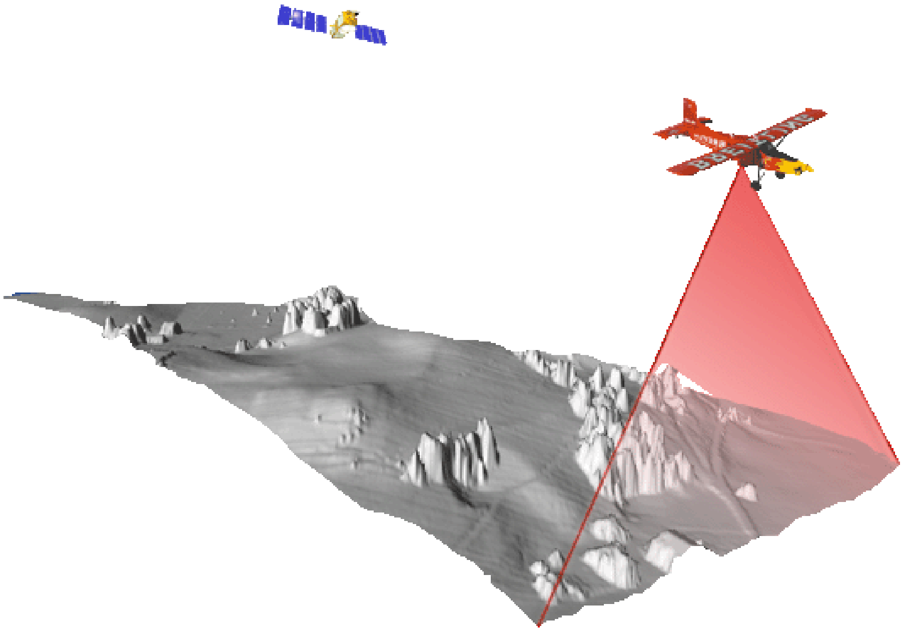

Figure 12. LiDAR survey and DTM production.

Starts with a well-defined flight plan for meeting the project's requirements. The average post-spacing of the points must be at a density to support the level required for a Digital Surface Model (DSM). An important point is the flying height. In fact, changing the flight altitude of the aircraft or the scan angle of the scanner allows for modifying the density of the post-spacing. Urban areas with tall buildings and steep terrain require special consideration to avoid holes in the data. The density of cloud of points is an important parameter to define the cells size. For the differential correction of coordinates LiDAR points, a base station of known location with a multi-channel GPS must be initialized with the GPS receiver on-board the aircraft. This initialization lock must remain in place during the entire flight. LiDAR data may be acquired quite rapidly: a system emitting 15,000 pulses per second with the capability to record 5 returns per pulse could potentially capture 75,000 values per second. The number of returns from such a system collecting data for a forest is closer to 35,000 values per second (for 3-hour of LiDAR survey with 900,000 pulses per minute, the database has collected 162 million of pulses). Since LiDAR is an active illumination system, data can be captured in all conditions (day or night). This factor is useful in taking advantage of good weather conditions and the opportunity to capture data at night in busy air space around airports. As mentioned, most terrain mapping LiDAR systems use a near infrared laser, so pulses hitting standing water are completely absorbed. In the last year, there is the possibility of using a "green laser" capable of providing pulse of return also on water surfaces, but is still a so much expensive system, with too much uncertainty.

After mission each point collected is georeferenced and it can be viewed in-situ using GIS software to verify coverage of the site. Also, to validate the accuracy of the collection, known survey data and a check of the bore site should be completed in-situ (Picco, 2010).

5.2.1 Airborne LiDAR data processing and uncertainty evaluation

LiDAR data processing is composed of two phases. First, from the available LiDAR data formed by a rough cloud of points (Figure 13), filter automatically the points in order to classify them into classes and to obtain the ground layer for study reach, then proceed with manual filtering to control errors due to automatic filtering. A typical LiDAR dataset has a file of about 80 - 100 MB per square kilometer with 2 – 3 ground points per square meter. Therefore is necessary a very robust data processing software and hardware to work with data sets of this size. The second phase is interpolate the points to derive the final products: DTM, DSM, or intermediate return information. These surfaces are derived using modeling software such as (ArcGis, Matlab, etc.). To realize in correct manner this step is necessary choose the right interpolation algorithm and right parameters.

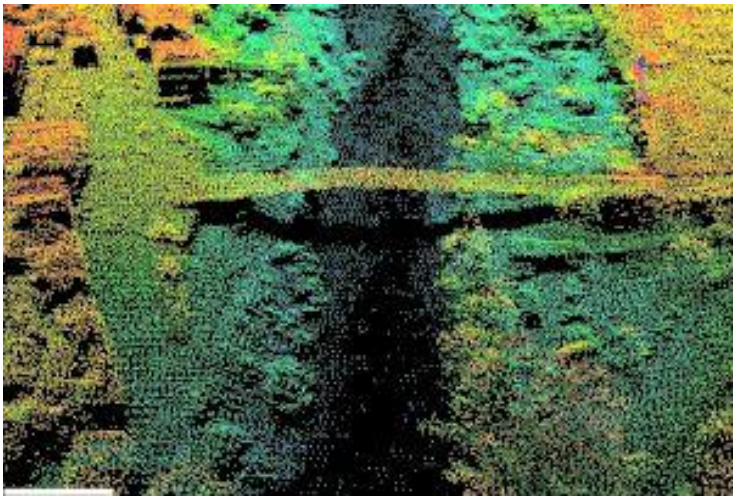

Figure 13. *Typical LiDAR point cloud.*

5.2.2 Interpolation methods

Theissen Polygons

This method is appropriate if we wish to define the "region of influence" of a point or line. The region of influence is based on "nearest neighbours" to the point or line. The region of influence for a series of points is represented by a set of polygons encoded with the nominal value for each point. These polygons are referred to as Thiessen Polygons or collectively as a proximal map. Theissen (1911) came up with the first technique to estimate areal average precipitation. Theissen polygons are probably the most common approach for modeling the spatial distribution of rainfall. The approach is based on defining the area closer to a gage then any alternate gage and the assumption that the best estimate of rainfall on that area is represented by the point measurement at the gage. Because the basis of the model is geometry and gage location, implementation of Theissen polygons in a GIS environment is not difficult. However, one impact of the use of Theissen polygons is the development of discontinuous surfaces defining the rainfall depth over the area under study. This effect arises at the boundaries of the polygons where a discrete change in rainfall depth occurs (Ball and Luk, 1998).

Spline (Regularized & Tension)

Spline interpolation consists of the approximation of a function by means of series of polynomials over adjacent intervals with continuous derivatives at the end-point of the intervals. Smoothing spline interpolation enables to control the variance of the residuals over the data set. The solution is estimated by an iterative process. It is also referred to as the basic minimum curvature technique or thin plate interpolation as it possesses two main features: (a) the surface must pass exactly through the data points, and (b) the surface must have minimum curvature (Franke, 1982 and Mitas and Mitasova, 1988).

Inverse Distance Weighting (IDW)

Inverse Distance Weighting (IDW) is an interpolation technique in which interpolated estimates are made based on values at nearby locations weighted only by distance from the interpolation location. IDW does not make assumptions about spatial relationships except the basic assumption that nearby points ought to be more closely related than distant points to the value at the interpolate location. This technique determines cell values using a linearly weighted combination of a set of sample points. The weight is a function of inverse distance.

IDW allows the user to control the significance of known points upon the interpolated values, based upon their distance from the output point (Tung, 1983 and Watson and Philip, 1985).

Trend Surface

The linear trend surface interpolator creates a floating-point grid. It uses a polynomial regression to fit a least-squares surface to the input points. It allows the user to control the order of the polynomial used to fit the surface. Trend interpolation is easy to understand by considering a first-order polynomial. A first-order linear trend surface interpolation simply performs a least squares fit of a plane to the set of input points. Trend surface interpolation creates smooth surfaces. The surface generated will seldom pass through the original data points since it performs a best fit for the entire surface. When an order higher than 1 is used, the interpolator may generate a grid whose minimum and maximum might exceed the minimum and maximum of the input points. The most common order of polynomials is 1 through 3 (Kruizinga and Yperlaan, 1978).

Natural Neighbour Interpolation

Natural neighbor interpolation (Figure 14) is a method of spatial interpolation, developed by Robin Sibson. The method is based on Voronoi tessellation of a discrete set of spatial points. This has advantages over simpler methods of interpolation, such as nearest neighbor, in that it provides a more smooth approximation to the underlying "true" function. The basic equation in 2D is:

$$G(x, y) = \sum_{i=1}^{n} w_i \, f(x_i, y_i) \tag{2}$$

where $G(x, y)$ is the estimate at (x, y), w_i are the weights and $f(x_i, y_i)$ are the known data at (x_i, y_i). The natural neighbour method proposes a measure for the computation of the weights, and the selection of the interpolating neighbors. The natural neighbor method utilizes the change to the Voronoi tessellation to compute weights. The weights, w_i, are by utilization of the area "stolen" from the surrounding points when inserting a new point into the tessellation. Each weight may be computed by dividing the section of the new tessellated region that lies within the tessellated region of each original neighboring tessellated polygon (Sibson, 1981).

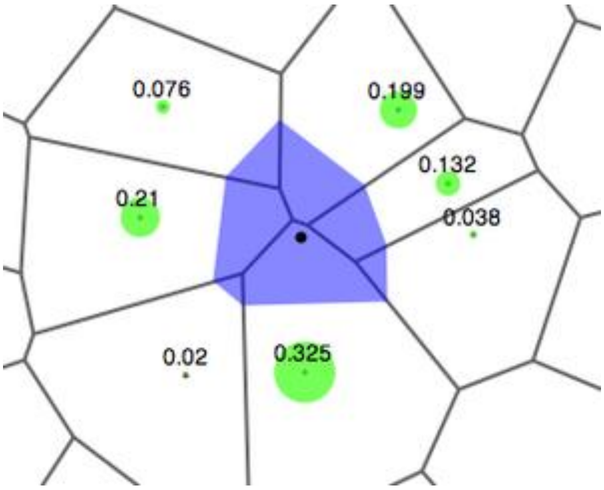

Figure 14. *Natural Neighbour Interpolation*

Kriging

Kriging provides a means of interpolating values for points not physically sampled using knowledge about the underlying spatial relationships in a data set to do so. Variograms provide this knowledge. Kriging is based on regionalized variable theory which provides an optimal interpolation estimate for a given coordinate location, as well as a variance estimate for the interpolation value. It involves an interactive investigation of the spatial behavior of the phenomenon before generating the output surface. It is based on the regionalized variable theory, which assumes that the spatial variation in the phenomenon is statistically homogeneous throughout the surface; that is, the same pattern of variation can be observed at all locations on the surface. This hypothesis of spatial homogeneity is fundamental to the regionalized variable theory. Data sets known to have spikes or abrupt changes are not appropriate for the Kriging technique. In some cases, the data can be pre-stratified into regions of uniform surface behavior for separate analysis (Royle et al.,1981; Press, 1988 and Oliver, 1990).

DTM and DSM surface

Unlike a DTM, in which a cell coincides with a unit numerical value defining an altitude, in a DSM (*Digital Surface Model*) the altitude can either indicate the effective altitude in a terrain or the height of either a tree or a building.

DTM is the acronym of Digital Terrain Model (Figure 15), and unlike DSM it exclusively relates to terrain, to be more precise it only represents those surfaces lacking in vegetation. It is a static representation of a continuous surface of terrain through an elevated number of known points in coordinates x, y, z related to a reference arbitrary system, a model allowing to represent details such as rivers and lakes. DTM is the base element to the numerical representation of terrain morphology and it is probably the most commonly used starting point to the measurement, analysis and modeling of slope hydrologic processes (Cavalli, 2006).

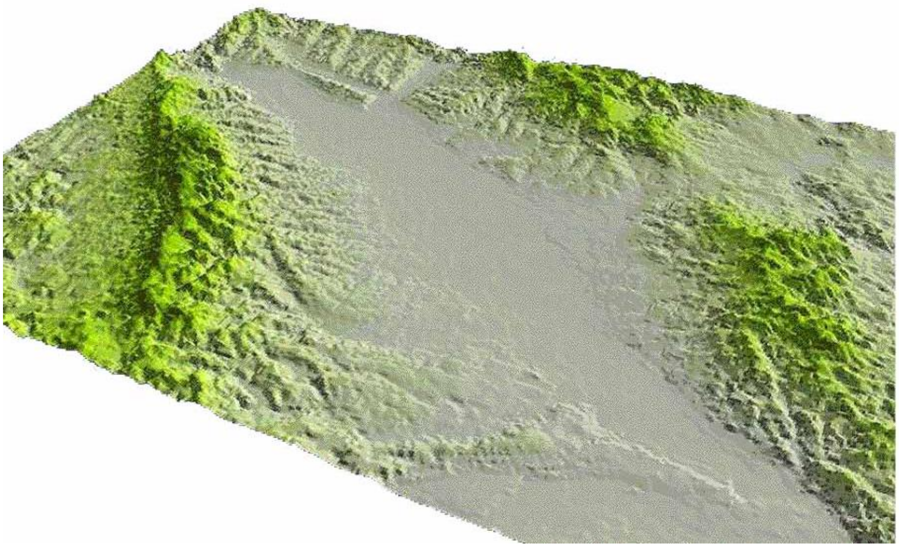

Figure 15. *Example of Digital Terrain Model (DTM).*

Such representation models besides describing terrain course, they enable to calculate several parameters such as area, volume, altitude, gradient, lines of maximum surface flow etc. It is clear that the characteristics of used starting points and interpolation methods determine the level of detail and the level of accuracy in resultant model.

5.2.3 DTM Uncertainty

The write approach to quantifying the influence of surface representation uncertainty when we aim at sediment budgets derived from DTM differencing consistent in a progression through three steps (Wheaton *et a*l., 2010):

1. quantifying the surface representation uncertainty in the individual DTM surfaces that are being compared;
2. propagating the identified uncertainties into the DoD maps;
3. assessing the significance of the propagated uncertainty.

There are a variety of ways to quantify uncertainties in the vector topographic survey data (i.e. x,y,z point clouds) manifest in DTMs. This uncertainty will be denoted as δz. The horizontal components of this positional error depend on the flying height, in some cases they have a similar magnitude to the vertical components, but they have negligible influence on vertical surface differences in low slope areas (i.e. most fluvial environments). Treating the horizontal components as negligible, δz is related to the actual elevation Z_{Actual} as follows:

$$Z_{Actual} = Z_{DTM} \pm \delta z \tag{3}$$

where Z_{Actual} is the true value of elevation, and Z_{DTM}, the spatially-paired DTM elevation.
Approaches for approximating δz range from adopting a manufacturer reported instrument precision to attempts at composing complete error budgets (Lichti *et al.*, 2005). In fact, manufacturer reported precision is only one of many components of δz, which include measurement errors, sampling bias (density and sampling patterns) and interpolation methods. By contrast, complete error budgets require data collection and testing protocols that go beyond typical survey practice. Other techniques for estimating δz include repeat observation of control points (Brasington *et al.*, 2000), repeat surveys of unchanging surfaces (Wheaton, 2008), fuzzy terrain models (Lodwick and Santos, 2003) and more traditional geostatistical techniques like surface interpolation with Kriging surfaces (Chappell *et al.*, 2003).

Brasington *et al.* (2003) showed the individual errors in the DTMs can be propagated into the DoD as:

$$\delta u_{DoD} = \sqrt{(\delta z_{new})^2 + (\delta z_{old})^2} \tag{4}$$

where δu_{DoD} is the propagated error in the DoD, and $\delta znew$ and $\delta zold$ are the individual errors in DTMnew and DTMold, respectively.

This method assumes that errors in each cell are random and independent. The combined error can be calculated as a single value for the entire DoD if spatially-explicit estimates of $\delta znew$ and $\delta zold$ do not exist. Alternatively, spatial variability in δz can be considered for both DTMs independently and $\delta uDoD$ can be calculated on a region by region (Lane *et al.*, 2003; Westaway *et al.*, 2003) or cell-by-cell basis (Wheaton, 2008). While in submerged regions versus un-submerged areas, are possible to apply, objective techniques for a more detailed and cell-by-cell estimate of δz have been lacking.

5.2.4 Assessing the significance of DoD uncertainty

There are two primary ways in which the significance of uncertainties in DoD predicted elevation changes are typically expressed. Both rely on thresholding the DoD and discarding or applying a lower weighting to elevation changes below some detection limit (i.e. $_{min}$LoD). In the first approach, the propagated uncertainties (i.e. δu_{DoD}) are used to define a threshold elevation change, or $_{min}$LoD (with dimensions of length; e.g. +/−10 cm). For example, a $_{min}$LoD of 10 cm could correspond to two DTMs with equal δz of 7.07 cm using Equation (4). More uncertain is the DTM (and hence the higher the minLoD threshold), more information are lost from the budget. Thus, the significance of the uncertainty manifested in δu_{DoD} is the inability to reliably detect elevation changes below the $_{min}$LoD threshold. As an alternative, Brasington *et al.* (2003) and Lane *et al.*(2003) draw on Taylor (1997) to show how probabilistic thresholding can be carried out with a user defined confidence interval. If the estimate of δz is a reasonable approximation of the standard deviation of error (*SDE*), Equation (4) can be modified to:

$$U_{crit} = t\left(\sqrt{SDE_{new}^2 + SDE_{old}^2}\right) \tag{5}$$

where U_{crit} is the critical threshold error, based on a critical student's *t*-value at a chosen confidence interval where

$$t = \frac{\left|z_{DTM_{new}} - z_{DTM_{old}}\right|}{\delta u_{DoD}} \tag{6}$$

In Equation (6), $\left|Z_{DTM_{new}} - Z_{DTM_{old}}\right|$ is the absolute value of the DoD. The probability of a DoD predicted elevation change occurring purely due to chance measurement error can then be calculated by relating the *t*-statistic to its cumulative distribution function (CDF). Wheaton *et a*l., 2010, show an example of this approach.

Following this method, an error-reduced DoD can then be obtained by discarding all changes with probability values less than the chosen threshold. In practice it is possible to apply a confidence-interval based threshold from spatially uniform versus spatially variable estimates of δz. However, objectively estimating a spatially variable δz is the major challenge.

5.3 Terrestrial Laser Scanner

The Terrestrial Laser Scanner (Figure 16) is an active laser imaging systems that combine high frequency laser range observations with precision angular sampling to generate spatially-dense point cloud data (Lichti et al., 2008; Petrie and Toth, 2008). Designed originally for applications in civil and structural engineering, TLS have since been enthusiastically adopted within a range of fields, including architecture, transport, heritage, archaeology, mining and forensic science (Vosselmann and Mass, 2010). Applications across the geosciences are now beginning to emerge rapidly as instrumentation costs fall and awareness of the capability of TLS grows (see Buckley et al., 2008; Heritage et al., 2009 for recent reviews).

Figure 16. *Terrestrial laser scanner Leica HDS 6200.*

While prototype TLS were first developed in the 1990s, fast, ruggedized instrumentation suitable for field-based geophysical survey has only become available in the last 3-4 years. In these systems, 3 dimensional measurements are facilitated by a sensor head comprising rotating mirrors, servo motors and accurate radial encoders that enable fine angular measurement (rad - mrad) and dense spatial sampling across a wide field of view Brasington *et al.*, 2012). The measure of distance is based on reflections from natural objects without the need for retro reflectors and uses either time-of-flight or continuous-wave (phase-difference) ranging (Wehr and Lohr, 1999). Time-of-flight scanners operate typically over longer distances (10-4000 m) but at significantly reduced measurement frequencies (2-50 kHz). Continuous-wave devices can be acquire data at very fast rates and therefore at high densities, but generally only over short ranges (typically < 40-180 m). Until recently most scanners returned single range-estimates along a given bearing, based on the last significant reflector (or last pulse). The next generation of scanners now coming to market, however, offer the capacity to discretize, such as with the airborne LiDAR, the returned waveform into multiple reflections providing information on the opacity of the scene. For both approaches, range errors are strongly linked to divergence of the laser beam and (without secondary compensation) verticality of the sensor head, so that point accuracy deteriorates with distance (Lichti and Jamtsho, 2006).

A trade-off between data quality (spatial density and point accuracy) and range emerges that must be tailored to the particular application and field logistics. Currently available instruments operate over ranges of tens of metres to > 4 km and at measurement frequencies of between 1-1000 kHz (1,000-1,000,000 points s^{-1}). Most scanners also record the intensity of the reflected laser beam, which although strongly influenced by distance, incidence angle and surface moisture, may also provide information on surface mineralogy and roughness (Lichti, 2005; Francheschi et al., 2009, Nield and Wiggs, 2011). Additionally, some instruments incorporate high-resolution digital cameras, enabling the true-colour pixel values to be remapped directly onto each survey observation to produce photo-realistic 3d renderings. Further technical details on the principles of TLS are available elsewhere (e.g., Wehr and Lohr, 1999; Lichti et al., 2002; Brasington et al., 2012).

5.3.1 Data Acquisition with TLS

Terrestrial laser scanners are generally deployed on a tripod, held stationary for the duration of measurements at a fixed position. Most scanners have rotating sensor heads and scanning mirrors that create a 360° horizontal field of view.

Despite this large sampling window, data acquisition remains limited by line-of-sight, so that surveys of complex objects typically require multiple setups to ensure adequate overlap and coverage (Figure 17). The observables from each position are a set of measurements of range, horizontal and vertical angles and intensity. These are converted directly to local Cartesian coordinates (X, Y, Z) where the origin and orientation are defined relative to an internal scanner coordinate system (scanner space).

Figure 17. *Field data acquisition with Terrestrial Laser Scanner on Feshie River (Scotland).*

Two important steps are thus required for the production of data deliverables; registration and geo referencing. Registration refers to the merging of multiple scans into a common reference space, but relative coordinate system, whereas geo-referencing involves the transformation of scans to an established local, national or global coordinate system (object space). These two processes are often referred to synonymously, but represent important distinct processes which incorporate different sets of errors.

The registration process of multiple scans can be achieved using either or a combination of two approaches; (i) a rigid body similarity (conformal) transformation from scanner-space to object-space based on common, observed control points identified by reflective targets (e.g., Horn, 1987) or; (ii) cloud-to cloud registration which involves identifying tie-points between overlapping point clouds on the basis of local matching geometry. This latter approach utilizes the large redundancy that exists in dense scan data and a variety of methods have been developed to solve this complex problem (e.g., the iterative closest point algorithm of Besl and McKay, 1992; see also Lichti and Skaloud, 2010).

As a good practice these two approaches are often best used in combination, whereby a 3 dimensional similarity transformation based on known targets is used to provide the initial orientation of the point clouds, then cloud-to-cloud registration employed to maximise the fit. Registration is also best undertaken as a global transformation problem, where multiple overlapping scans are orientated simultaneously and global least-squares metrics used to ensure the isotropy of the solution.

While registration of scan data to a common, relative coordinate system may be sufficient to generate products suitable for characterizing a particular object, it is often desirable to tie these data to a recognized frame of reference. This step facilitates the integration of additional data, such as airborne LiDAR or ground-observations positioned by GPS and importantly, also enables the comparison of datasets over time. Geo-referencing is usually undertaken during post-processing as part of registration, where control points measured on national or global mapping system are used to define the principal similarity transformation. During data collection a direct geo-referencing is possible is also possible when the location and orientation of the sensor head are prescribed *a priori* and the scan observables (range and angles) are transformed directly. This approach is likely to become more popular as new instruments directly incorporate GPS and inertial measurement units, so enabling the collection of real-world coordinates in real-time. Finally, it is important to recognize that geo-referencing inevitably introduces uncertainties associated with the accuracy of the positional data used to define transformations and that care should be taken to work within a consistent

3D Cartesian framework to avoid incorporating distortion associated with map projections (Brasington *et al*., 2012).

5.3.2 Uncertainty in DEMs surface analysis at highly detailed scale by using TLS

Terrestrial Laser Scanners (TLS) allows to realize detailed Digital Elevation Models (DEMs) starting from a point cloud with spatial information (XYZ) for each point. A very high point density allow to generate highly detailed DEMs where is possible a surface roughness analysis. The general workflow to create a Digital Terrain Model (DTM) by using the TLS can be described as (Buckley et al. 2008):

- *Field Locality;*
- *Reconnaissance:* identification the best positions and the amount of necessary scans.
- *Data collection:*
    - Scans: relative x, y, z and intensity data;
    - Images: true-colour information for LiDAR points;
    - GPS: Absolute position in LiDAR points;
- *Scan registration of TLS clouds:*
    - Relative orientation: with targets or without targets (cloud-to-cloud registration);
    - Absolute orientation: with GPS points;
- *Extra image registration (optional):* for adding more detailed true colour information with high resolution camera;
- *Point cloud editing and decimation:*
    - Error points filtering; (Hodge et al., 2009);
- *Vegetation, debris and Structures filtering;*
- *Points interpolation;*
- *Grid model filtering;*
- *Model interpretation and visualization.*

The TLS point cloud collected from the instrument is subjected from a considerable number of factors that could decrease the quality of them. The influencing factors in quality of TLS data collection are identified as (Lichti et al. 2006, and Hodge 2010, Soudarissanane et al. 2011):

- *Systematic errors:* common to total station;
- *Instrument mechanism* - hardware, calibration setting and mechanisms of TLS can produce:

  Physical error: range finder additive constant, collimation and trunnion, axis errors (in function of horizontal direction), vertical circle index error, eccentricity, etc.;
  Empirical Error: geometric defects in construction, electrical cross-talk;
- *Atmospheric condition:* humidity, temperature that can also influence the time-of-flight of the laser pulse;
- *Object surface proprieties:*
  Surface reflectivity: with a more surface reflectivity, the detector in an artificially shorter time-of-flight and range measurement;
  Surface geometry: determines the amount of scans to the total cover;
- *Scan geometry:* location and orientation of scanned surface. The principal parameters of local scan geometry are the range (distance from the object and the scanner) and the angle of incidence (between incoming laser beam and the local surface normal). The received signal level of the measurements decrease with increasing incidence angle and range whereas the footprint of the laser beams increase. A more large footprint equal to a lower intensity of received signal, lower intensity equal to more noise. The received signal level influence the precision of the distance determination;
- *Operator in filed:* instrument levelling and centring, back sight target centring;
- *Imaging geometry:* mixed pixel, angular displacement errors:
- *Registration Errors:* due to the cloud matching or bundle adjustment algorithms used to register the multiple scans into the same model space;
- *Data resolution:* it determines the smallest detail that can be distinguished in the collected data, and is determined by the laser footprint area and the minimum point spacing for data collection.

Section Two

Fields Research, Materials and Methods

6 Study Rivers

6.1 Brenta River

6.1.1 Climatic, geological and morphological setting of the Brenta River basin

The Brenta River is one of the most important rivers of the Southern Alps (Italy) flowing into the upper Adriatic sea (Figure 18).

The mountain drainage basin covers a surface of 1567 km^2. The river length is 174 km and can be divided into two main reaches: an upper 70 km long stretch flowing within the mountain basin, and a 104 km long stretch flowing within the Venetian floodplain area (Surian and Cisotto, 2007). The upper basin features a typical continental-Alpine climate with annual rainfall of about 1500 mm (Giuliacci *et al.*, 2001).

At Bassano del Grappa the river abandons the mountain valley and flows into the plain. Therefore, the course of the river can be divided into two reaches: an upper reach, 70 km long, within the mountain area, and a lower reach, 104 km long, in the Venetian Plain. The principal valley divides the moutain basin in two unequal parts, been the biggest placed on the left side and hence, it contains most of the tributaries, such as, the Cismon Torrent the main one, and others smaller, the Ceggro Torrent, The Maso Torrent and Grigno Torrent. From the right side the Brenta River receives the discharges of Cesa Torrent.

The mountain basin has a humid temperate-continental climate. The mean annual precipitation is 1313 mm but the runoff at the basin outlet is 105%. Such a high value of runoff is due to the contribution of karst springs which are located in the lower part of the drainage basin (Prealps). The rainy seasons have the maximum precipitations during the months of May-June and October- November. The landscape is very different in the upper and lower part of the basin. In the upper part the river flows through a typical glacial-fluvial valley (U-shaped), the Valsugana Valley, from the Caldonazzo Plain up to the Primolano gorge. In the lower part, the Venetian Plain can be divided into an old deposition plain (alluvial fan of Bassano, Upper Pleistocene) placed on the left side of the Brenta River, and a more modern plain, the current Brenta River floodplain (Holocene).

The geological setting is rather complex and includes limestone, dolomite, gneiss, phyllite, granite and volcanic rocks. Regarding its morphology, the river exits from the Caldonazzo lake as a straight channel, and then evolves in a braided-wandering pattern in the piedmont area (Surian and Cisotto, 2007), before becoming meandering and then heavily rectified in its lower course.

6.1.2. Human impacts within the Brenta River basin

During the past centuries, the Brenta River has been affected by multi-spatial and temporal human interventions (Surian and Cisotto, 2007) which have heavily modified its natural characteristics. The magnitude and consequences of such disturbances have increased during the last 100 years. The human impacts consist mostly of direct interventions, such as channelization, gravel mining and dam, levees and groins construction, but also of indirect effects on river dynamics, such as reforestation (Surian *et al.*, 2009b). In particular, gravel mining has been recognized as the human intervention with the greatest impact on channel morphology. This activity, which has mostly occurred in the lower reaches especially between 1950 and 1980, removed a large volume of sediments, exceeding replenishment rates and producing a significant alteration in sediment fluxes (Surian and Cisotto, 2007). Indeed, official estimates set volumes of extracted sediment to around 6-8 million m^3 from 1953 to 1977. However, these values are most likely to be far underestimated (Castiglioni and Pellegrini, 2001). The second most important human disturbance has been the construction of several dams which have reduced both flow and sediment discharges. The largest dam, built in 1954 for hydroelectric power generation and irrigation purposes, is the Corlo dam, in the Cismon torrent, with its 42 million m^3 reservoir (the main tributary of Brenta River). It is also worth mentioning the impacts of torrent-control works in the low-order mountain streams and the last trend of basin natural reforestation, which have reduced the sediment yield at the basin scale contributing to channel incision. These impacts resulted in the narrowing of the average river bed width from around 440 m at the beginning of the 1800s to around 220 m in 2003 and the remarkable channel incision of up to 7 m (Surian and Cisotto, 2007).

6.1.3 Study reach

The Brenta River’s reach considered in the present study is approximately 20 km long and is located in the piedmont area of the basin (area of about 1567 km^2) between the cities of Bassano Del Grappa and Piazzola sul Brenta (Figure 18a). The upper part of the reach, located immediately downstream of the mountain area, features a fairly straight channel and a narrow alluvial plain. In its middle portion the river widens, the slope is lower (about 0.3 %) and the river features a braided pattern with islands. In its lower part, the river exhibits a wandering pattern with higher sinuosity (≈ 1.12) and the presence of extensive riparian vegetation on floodplains. Within the study reach there is a wide range of human infrastructures such as embankments, bridges, and transversal works such as the Carturo transverse (located at the very end of the study reach). Also, the floodplains are characterized by the presence of urbanized areas, and much of the discharge is diverted for irrigation and hydroelectric purposes.

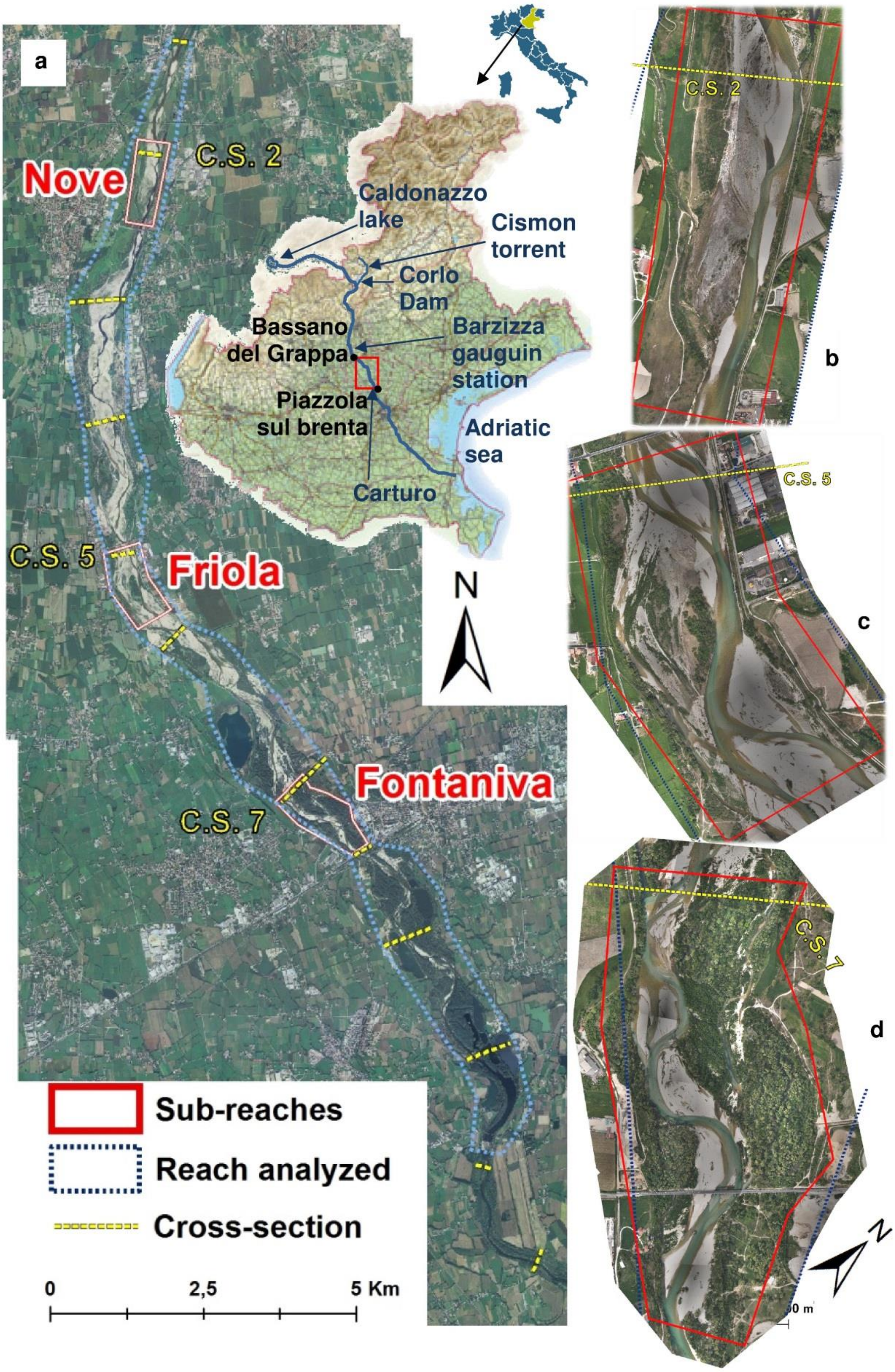

Figure 18. *General view of the Brenta River context, the study reach and cross-sections.*

Within this study reach, three sub-reaches 1.5 km long and 5 km apart were selected as representative of the upper- middle- and down-stream part of the study area and named according to the nearby villages: Nove, Friola and Fontaniva (Figure 18b, c and d). The upstream sub-reach (Nove) has a single straightened channel morphology with an average width of around 300 m. By contrast, Friola shows a more complex morphological pattern, with the braided channel accounting for high levels of vegetation density and an average width of 500 m. In the downstream sub-reach, Fontaniva, the braided trend is more marked, with the formation of many fluvial islands and the 800 m wide channel divides into several branches.

6.2 Piave River

6.2.1 Climatic, geological and morphological setting of the Piave River basin

The basin of Piave River extends over 4500 km^2 in the Veneto Region (Italy) territory. The main fluvial stem has a length of 220 km starting near Peralba Mount at an elevation of 2030 m a.s.l. (Belluno Province) and finishing in the Adriatic Sea (Venezia Province). The basin is placed mainly in the mountain region (3900 km^2) and less on the Venetian plain.

The hydrographic network is developed mainly along the right side of the river. There are three principal tributaries; two of them, the Boite River near Perarolo di Cadore and the Mae River near Longarone are placed at the northern side of basin, and the third, the Cordervole River, collects water from the western region. The basin has a humid temperate-continental climate, which is common in the entire eastern Alps region. Precipitation has a wide spatial variability due to the complex topography. The mean precipitation is 1350 mm, with a minimum of 1000 mm in the north-western side (it includes the basin of Cordevole River) and higher values in the central-eastern corner (near the Vajont basin). Autumn is the rainiest season followed by the spring, been November and June the months that concentrate most of the annual rainfall. Summers are hot (frequent maximum temperatures of 33-35 °C) and humid, while winters are cold (mean temperature of 2-3 °C) and also humid.

At the headwater torrents have high slope and flow along very narrow valleys. At high elevations typical structures due to glacial processes can be identified, such as glacial circus and big pools, mainly in the high flat lands. Besides, valleys have the typical U-shape associated with glaciers erosion. The Valley of the upper Piave River is narrow and deep, and cuts the stratified rocks that constitute the basement of the region. At Ponte nelle Alpi the characteristics of the landscape change dramatically. At this place the river arrives to a former synclinal that directs the flow towards Feltre. This reach is characterized by a wide valley with a flat bottom and gentle sides, the so-called “Vallone Bellunese” (Bellunese Valley, hereafter). Six levels of terraces have been recognized that are associated with the recent geological history (Late Pleistocene - Holocene). After Feltre, the river enters into a narrower valley that cuts the Grappa-Tomatico-Cesen-Visentin mountain range, which stratification constitutes a long anticline arc. Finally, the river flows through a zone with a syncline disposition arriving to the deep gorge at Nervesa. This point constitutes the end of the mountain basin, and following the river flows along the Venetian plain. The mountain area of the basin is occupied by tows of median to small dimensions. In the Piave River basin several and different rock types crop out with a variety of origin, composition and age: Schist-phyllite rocks (Paleozoic), Sandstone, marlstone, argillite and sedimentary rocks (limestone and dolomite). The most diffused rocks within the Piave River basin are limestone and dolomite (Kaless, 2013).

6.2.2. Human impacts within the Piave River basin

During the first years of the 20th century it was evident the need of electric energy generation and the development of irrigation systems. Since the ‘30s until the ‘60s all the current dams were constructed. Although the area subject to dam regulation is large, the storage capacity is rather low, only the 4% of the annual precipitation is storage in dams within Piave River basin. Then, dams have a scarce capacity for storing volumes during flood events and hence to reduce peak discharge. But, actually dams were not design with that scope; instead, the complex network of dams and conducts was thought looking for the optimization in the use of water for energy generation and irrigation scopes. On the contrary, the main effect of dams has been on the regime of sediment delivery. The presence of artificial reservoirs has stopped the natural sediment flow during floods affecting the sediment balance in the fluvial network placed downstream. The decrease of sediment supply has also been a consequence of other human interventions: bank protection occurring mainly during the 19th century and the implementation of torrent control works from the 20s, both promoted channel stability due to the increase of bank strength and fixing the stream bottom bed. More recently, another human activity has altered the dynamic of these fluvial systems. Between the ‘60s and ‘90s intense gravel mining was carried out in the main channel and its main tributaries. Official records, which are presumably underestimation of actual values, indicate that in Piave River 170,000 m^3 were excavated in the upper basin in 1973, 303000 m^3 in 1993 and 348000 m^3 in 1995 (Surian, 1999). However, a recent study based on detail topography of a long Piave River reach indicates that the total extracted volume may be in the order of 6 million cubic meters (Comiti et al., 2011).

6.2.3 Study reach

The study reach of Piave River (Figure 19) is located between Ponte delle Alpi and Busche (BL) and features a length of approximately 30km. The drainage area at Busche is 3174 km^2 and the dominant morphological patterns of the channel in this area are braided and wandering, even though narrower reaches present an alternate bars structure. The average slope is approximately 0.45% and the median surface grain size is comprised between 20mm and 50mm (Surian, 2002). The width of the fluvial corridor ranges between 100m and 2000m depending on the presence of geological constrains, such as terraces or hillslopes (Surian, 1998). Within the study reach, two sub-reaches have been identified basing the selection on the homogeneity in river corridor width, presence of artificial elements (i.e. groynes, bank protections) and historical and morphological patterns.

The first one, Belluno, features a length of about 2.2 km, whereas the second, Praloran, 3.2 km. The river morphology in the study sub-reaches is dominated by braided and wandering channel patterns, the slope is around 0.45%, and the D_{50} ranges between 20 and 50 mm.

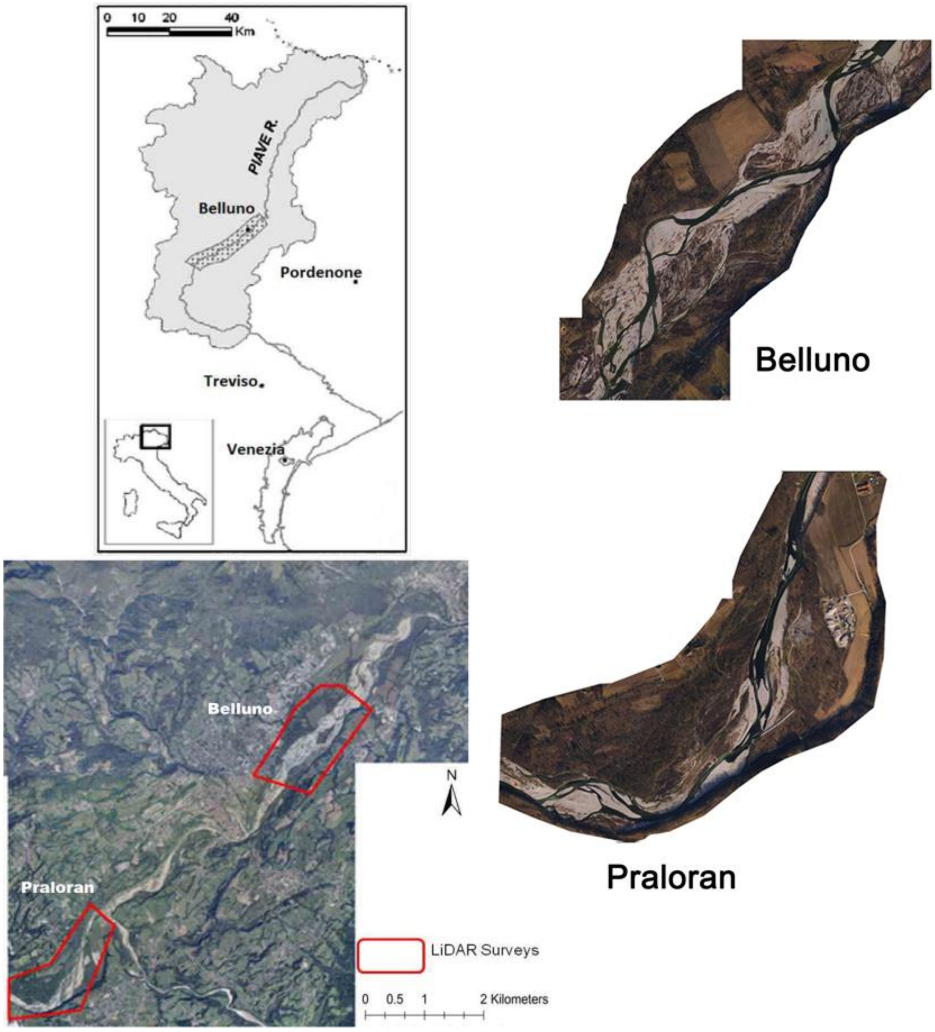

Figure 19. *The Piave River basin and the two study sub-reaches, Belluno and Praloran.*

6.3 Tagliamento River

6.3.1 Climatic, geological and morphological setting of the Tagliamneto River basin

The Tagliamento River, one of the last European rivers still maintaining a high degree of naturalness and representing an important bio-geographical corridor with a strong longitudinal, lateral and vertical connectivity, high habitat heterogeneity, a characteristic sequence of geomorphic types and very high biodiversity (Tockner et al., 2003).

The Tagliamento River is a gravel-bed river located in the Southern Alps in North-Eastern Italy (Friuli Venezia Giulia region). It originates at 1195 m a.s.l. and flows for 178 km to the north Adriatic Sea, thereby forming a link corridor between the Alps and the Mediterranean zones. Its drainage basin covers 2871 km^2 (Figure 18). The catchment is limited by the Carnic Alps (North); by Piave, Livenza and Meduna basins to the West; and by Isonzo and Torre basins to the East. The river has a straight course in the upper part, while the most of its path is braided shifting to meandering in the lower part, where dykes have constrained the last 30 km (it features the characteristics of an artificial channel with a width of about 175 m). However, the upper reaches are more or less intact, thus the basic river processes, such as flooding, and sediment transport, take place under near-natural conditions.

The hydraulic regime of the Tagliamento River is characterized by an irregular discharge and a high sedimentation load; due to the climatic and geological conditions of the upper part (annual precipitation can reach 3100 mm). The catchment is mainly mountainous and the slopes are very steep, leading to high peak flows and sediment loads in the central and lower part of the basin. The climatic characteristics of the catchment area result in a bi-modal pluvial flow regime. As all braided river channels, also the Tagliamento is characterized by a marked instability due to easily erodable banks, high sediment transport rates and considerable width of the valley (Picco 2010). This in turn leads to a frequent remodeling of the morphological elements. The large size of the floodplain and the rapid morphological variation are the main reasons accounting for the absence of a good stage-discharge relationship. In the present study, we refer to the water stage level recorded at the Venzone gauging Station (Figure 20).

The alpine area of Friuli mainly consists of limestone, with a spatial sequence of Silurian, Devonian, Triassic, Jurassic and Cretaceous formations north to south. Limestone is occasionally intermixed with layers of gypsum that lead to high sulphate concentrations in the Tagliamento (Arscott et al., 2000). The catchment is tectonically active, continuously developing faults and overthrusts. Many tributary streams, like the Fella, have sharp bends following the direction of these faults (Figure 20).

Flooding represents the major physical disturbance along river corridors. Rivers also experience frequent but smaller water level fluctuations (“flow pulses”; Tockner et al., 2000) that occur well below bankfull discharge. Although not responsible for rapid morphological restructuring, these flow pulses are important for creating and maintaining habitat heterogeneity and for ecosystem processes (Picco, 2010). Complete inundation of the active flood plain occurred 3 - 4 times per year; however, the degree of inundation was highly dynamic during most of the year.

6.3.2. Human impacts within the Tagliamento River basin

Although the Tagliamento is considered to be the most natural river system in the Alps, it is not without human impacts. Major human influences on the main river corridor are (i) water abstraction in the upper Tagliamento valley, (ii) organic pollution, and (iii) gravel exploitation. Many small tributaries contain drop structures to inhibit erosion and channel incision. Water is abstracted for hydropower generation in the upper area, altering the flow regimes of the Degano, the Lumiei, and sections of the main stem Tagliamento. The Tagliamento frequently loses surface flow, that is 23 m^3 s^{-1} is abstracted for irrigation purposes. Nevertheless, large tributaries like the Fella, But and Arzino are characterised by a natural flow regime. In addition, the flood dynamics of the main stem of the Tagliamento is largely unaffected by water abstraction. The Tagliamento suffers from organic pollution between Tolmezzo and its confluence with the Fella, and in the channelized section downstream of Latisana; however, water quality has improved considerably in recent years. There are lateral dams along some sections (e.g. between Pioverno and Pinzano; and downstream of Dignano). However, they are far outside the active corridor and primarily used to protect agricultural land. The river corridor, which is morphologically intact along virtually its entire length, is the feature that makes the Tagliamento unique in the Alps. The corridor has escaped massive river engineering and floodplain development schemes, thus retaining the functional characteristics of a near-pristine system: strong longitudinal, lateral and vertical connectivity, high habitat heterogeneity, and a characteristic sequence of geomorphic types (Picco, 2010).

6.3.3 Study reach

The LiDAR survey and analysis were performed in two sub-reaches located near to the village of Forgaria nel Friuli, in Friuli, Venezia Giulia Region.

The upstream sub-reach (Figure 20), called "Cornino", shows a predominant braided morphology, channels are separated by vegetated islands and gravel bars. The length is about

3 km and the active channel width ranges from a maximum of 1 km to a minimum of 700 m with a slope of around 0.35%. This sub-reach is characterized by a heterogeneous sediment size composition ranging from medium-fine sand to coarse gravel.

The lower, called Flagogna sub-reach has a predominant wandering morphology with central bars and dead channels. As shown in the Figure 20, the main channel flows almost exclusively through the left bank and, as in Cornino sub-reach, there is a large number of longitudinal and lateral bars and river islands mostly located in the right side. The length is about 3.5 km and the active channel width is between 300 and 800 m, with a slope of around 0.30%.

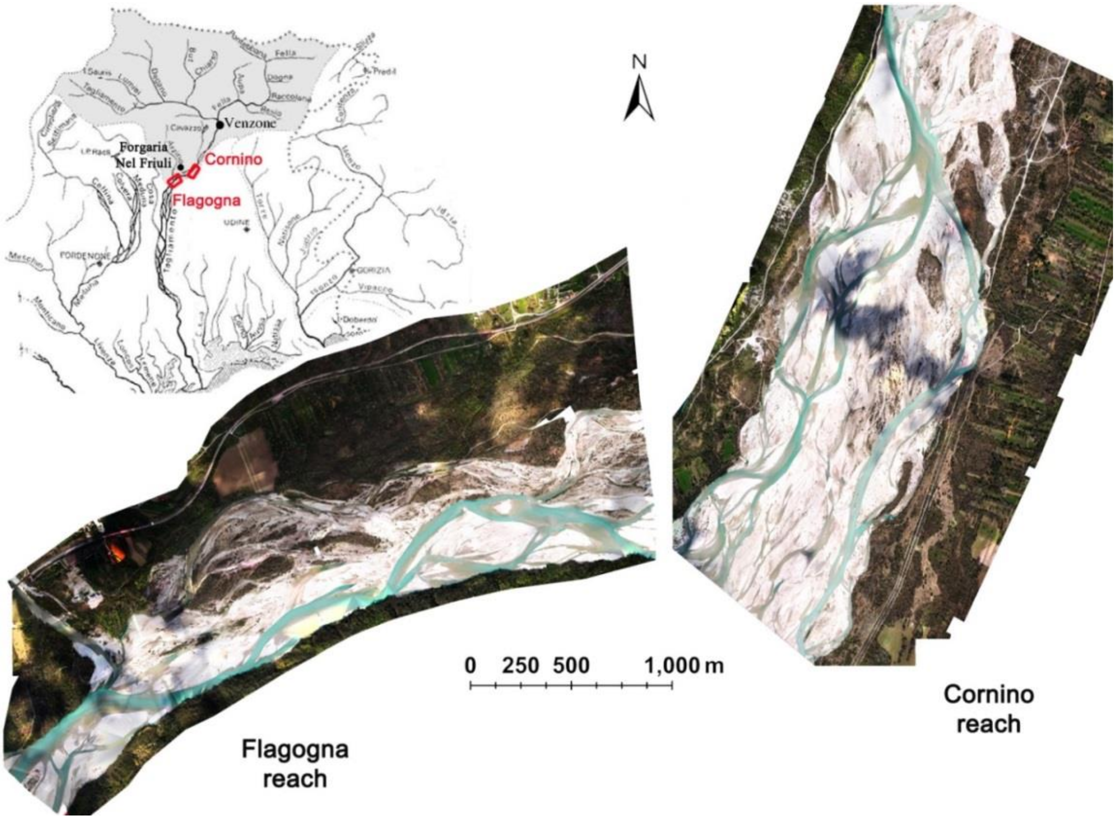

Figure 20. *The Tagliamento River catchment and Cornino and Flagogna sub-reaches.*

6.4 Feshie River

6.4.1 Climatic, geological and morphological setting of the Feshie River basin

The River Feshie is situated in the Cairngorm Mts. of Scotland, which belong to the paleozoic system of the Grampians. The river is the right−bank tributary of the River Spey, which flows north−east to the North Sea (Figure 21). The climate of the area is strongly oceanic. The annual totals of precipitation are high (from 830 mm to 2050 mm) and air temperatures mild. The bedrock geology of the drainage basin consists in 80 per cent of paleozoic metamorphic schists (Moinian schists). The rest is underlain by granite outcrops (Cairngorm granite) from the local batholits. These granites occur in marginal fragments of the basin and do not underlain the channel of the main river. The River Feshie valley has been remodelled by Pleistocene glaciers. It cuts the high elevated Gaick Plateau (700−1000 m a.s.l.) and its north−western slope. Except the uppermost fragment which cuts the Gaick Plateau, the upper part of the valley is narrow and features a typical glacial trough. In the middle and the lower parts (below 400 m a.s.l.) the valley is getting wider. Its bottom is covered with alluvial deposits and flanked with morainic and fluvioglacial material which forms five, well expressed late−glacial and Holocene terraces (Young 1976). Before the late Pleistocene the upper part of today's Feshie valley belonged to the river system of Geldie. Then the low watershed between the two valleys was cut by transfluencing glacier and next by proglacial waters. As a result of this the upper part of the River Geldie was captured by the River Feshie (Linton 1949). This has caused the rapid growth of the drainage area of the River Feshie by about 30 per cent. Glen Feshie is mostly deforested. Scots pine clusters (*Pinus silvestris*) being the remnants of the ancient Caledonian forest occupy the fragments of the valley bottom. Most of the area is covered by heath (*Calluna−Empetrum*). At the highest elevations the typical mountain meadow communities dominate. Due to the steep valley slopes, poor bedrock permeability and well saturation of peat the infiltration of water is limited. This favours easy formation of overland flow, which results in rapid response of the river to rainfall events. Floods usually follow the intensive summer rainfalls of a convectional origin and autumn or winter ones of a frontal origin. The role of snowmelt in flood formation is minor (Werritty 1984). The lag between rainfall and flow peaks is short; thus the River Feshie is considered one of the flashiest rivers in Britain (Ferguson, Werritty 1983).

6.4.2. Human impacts within the Feshie River basin

During the late 18th and early 19th centuries, land drainage, construction of flood embankments, dredging and channelization significantly affected the middle and lower courses of many Scottish rivers. Towards the late 19th century, water supply schemes and early hydroelectric power generation schemes also resulted in significant changes to river flow. During much of the 20th century, there was a continuation of some of the early trends. River flow regulation and water abstraction increased markedly as a result of the development of large hydroelectric power and water supply schemes. More recently, smaller 'run-of the river' hydropower schemes have been developed under the Scottish Renewables Order. Surface water is also abstracted by freshwater fish farms, distilleries, paper mills and other industries, and for potato irrigation in eastern Scotland. Catchments with hydropower schemes cover 20% of the area of mainland Scotland. Hydropower schemes involve not only direct impoundment of the main rivers, but also substantial cross-catchment transfer, using an estimated 1000 off-takes to divert discharge from smaller rivers. In addition, there are over 400 groundwater abstraction boreholes of more than 15 m depth and many more small private abstractions, which may have indirect effects on river discharge through the depletion of baseflows (Robins, 1990). These modifications have been to the benefit of water supply for domestic, industrial and agricultural use, and hydropower production. There is little doubt that historical changes in Scottish rivers were accompanied by changes in hydrology, geomorphology, water quality and ecological quality, yet there are few data with which to quantify change.

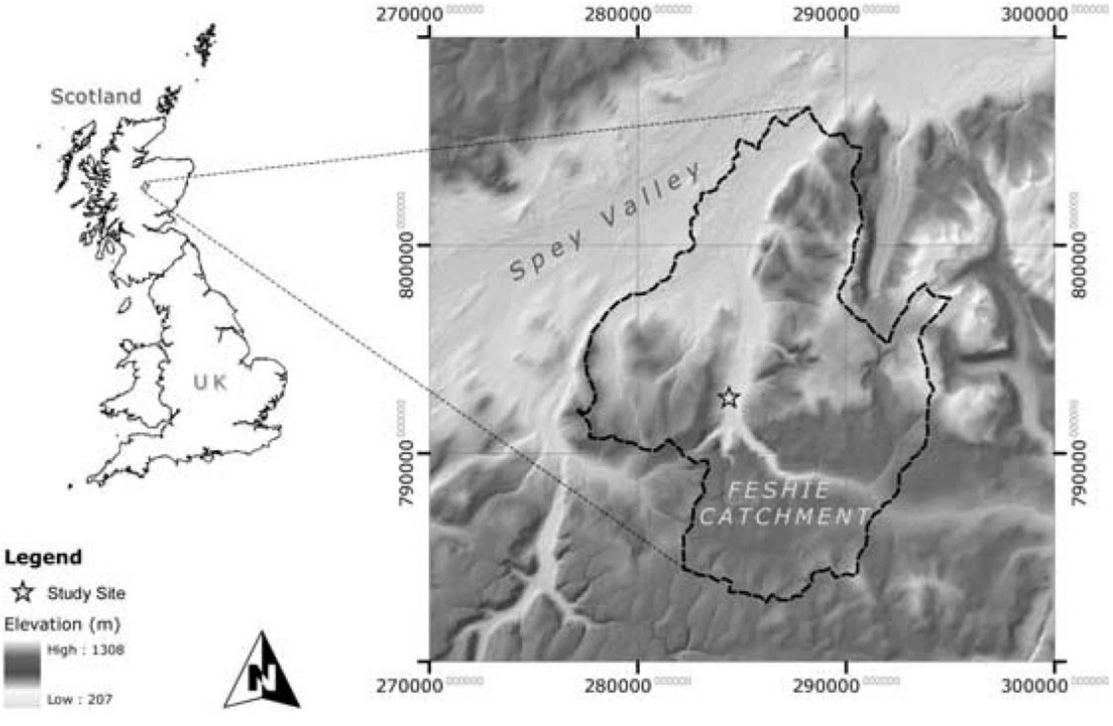

__Figure 21.__ The Feshie River catchment.

6.4.3 Study reach

The study reach lies within the uppermost braided section where the valley widens downstream of a deep glacial trough and braiding is extensive for over 2 km downstream. This reach has an upstream drainage area of 80 km^2 and is underlain predominantly by schists which dominate the coarse bedload, and a small proportion of granite of the Cairngorm batholith. Average valley width varies between 200 and 500 m, the gradient in the study area is 1.5% and the median surface grain diameter (D_{50}) is 65 mm. No contemporary flow record is available for the reach, but a gauge 14 km downstream at Feshie bridge, which drains an area of 235 km^2, reveals a highly variable flow regime. Instantaneous peak flows at Feshie bridge exceeded 100 m^3 s^{-1} six times between 1998 and 1999, while the 50% exceedance percentile 1992–1999 is just 5.2 m^3 s^{-1}. The major flood events occur mainly during October-January with a smaller number in late spring resulting from a combination of snowmelt and rain on snow. Downscaling by area is difficult, however, this regime is consistent with records from a gauge 2 km downstream of the study reach maintained in the late 1970 which recorded a mean flow of 3 m^3 s^{-1} and a mean annual flood of 70 m^3 s^{-1} (Brasington et *al.*, 2012).

Figure 22. *The study area of the Feshie River.*

7 Geomorphic Analysis: Planimetric Approach

7.1 Cross-sections and longitudinal profile

Twelve historical cross-sections described in detail by Surian and Cisotto (2007) lie within the study reach (Figure 18a). They were first surveyed in 1932, and then in 1997 with a total-station device. In 2010, the first 10 cross-sections were re-surveyed with a dGPS with a maximum vertical error of ± 0.03 m. Two Light Detection and Ranging (LiDAR) surveys taken in 2010 and 2011 are available for the study area. Further re-surveys of the study cross-sections were derived from these data, taking advantage of the ground points of the filtered LiDAR data and the underwater points obtained by an image analysis of coloured aerial photos taken during the same flight (Moretto *et al.*, 2012a). The vertical error of these cross-sections was estimated to be around ± 0.15 m. The longitudinal profile along the river reach was derived from an averaged cross-section elevation, calculated using all points within the active channel (i.e. excluding banks and floodplains).

7.2 Flow regime

The Flow regime was measured at the basin outlet, Barzizza gauging station, by the former Italian National Hydrographical and Hydrological Agency from 1924 to 1996, and by ARPAV (Environment Protection Agency of Veneto Region), from 1997 to 2010. The station is located 5 km upstream of the analyzed reach (see Figure 18). Mean daily discharges (Q) were available for two periods: 1924-1996 and 2005-2011. From 1997 to 2004, Q was obtained through the application of the stage-discharge rating curve validated by ARPAV for the period 2005-2011. All values of the two series of data were checked and original missing data were calculated by cross-correlation and interpolation techniques (Kaless *et al*., 2011; Lenzi *et al*., 2010).

Nevertheless, values of water levels recorded at the Barzizza station, were not available for most part of the years 1942, 1943, 1944, 1945, 1946, 1967, 1968 and 1984 and was thus not possible to estimate mean daily water discharges by interpolation techniques (Figure 18).

A comparison between maximum instantaneous peak water discharge, maximum hourly daily water discharge and maximum main daily discharge, was carried out for 24 floods events measured in the field by the ARPAV, and occurred in the period 2004-2009. Flood events were chosen with the criteria of guaranteeing both the non-dependency between two consecutive floods (on the value of the peak discharge for each event) and to cover a large range of water discharge peak values. A very good correlation was obtained (Kaless *et al.*, 2011) between the values of maximum hourly daily and maximum main daily water discharge ($r^2 = 0.96$). Extending this analysis to the entire available data set, a total of seventy nine (79) flood events were chosen, checked and considered for testing different probability distribution functions and for the flood frequency-return time estimations (Kaless, 2013).

7.3 Identification of geomorphological and island features from aerial photos

The evolution of islands and bed river morphologies over the last 30 years was analyzed taking advantage of nine series of aerial photos, acquired always during low-water level conditions (see details of the photos in Table 1). Aerial photographs were rectified and co-registered to a common datum base at 1:5000 using a GIS software (ESRI® ArcGIS 10). Approximately 40 ground-control points were used to rectify each single frame, and third-order polynomial transformations were then applied, obtaining root mean square errors (RMSE) ranging from 0.3 to 1 m. The higher RMSE are for 1981, 1990 and 1999 (1 m of pixel size).

Table 1. *Technical specifications of aerial image series used in the study. Px: pixel size; Hf: height of flight; Fcl: focal, Q: Daily discharges ($m^3 s^{-1}$).*

Year	Px (m)	Aprox. Scale	Hf (m)	Fcl (mm)	Date flight	Company	Q ($m^3 s^{-1}$)
1981	1.00	1:17000	2600	153.13	April 15	CGR Parma	38
1990	1.00	1:20000	3000	152.82	April 15	CGR Parma	31
1994*	0.35	1:20000	8000	305.38	20 Sept.	CGR Parma	88
1999	1.00	1:16000	2500	153.26	July 23	CGR Parma	36
2003	0.50	1:10000	5400	150.00	May - Nov.	CGR Parma	62
2006	0.50	1:10000	5400	150.00	May - Nov.	CGR Parma	69
2008 A	0.40	1:8000	1250	153.64	July 15	Rossi -	75
2008 B	0.75	1:16000	2400	153.64	July	CGR Parma	85
2010	0.15	1:12000	2000	100.47	August 30	CGR Parma	55
2011	0.15	1:12000	2000	50 - 35	April 12	OGS	69

**1994 flight does not include the upper part of the study reach.*

These photos were analyzed using the same method described in Comiti *et al*. (2011), in order to identify the active channel and islands extents along the whole 20 km-long study reach. The active channel is defined as the area without shrub vegetation, thus including unvegetated bars and active and inactive channels, while the fluvial islands class include pioneer, young and stable islands according to Gurnell and Petts (2002) classification. In order to analyze morphological changes along the study reach, active channel and islands widths were taken in 85 position, 250 m apart in transects perpendicular to the river axis which were created in GIS environment.

7.4 Photo-interpretation errors

The errors related to the photo-interpretation assessment were performed using the Mount *et al*. (2003) method. This procedure consists of the estimation of two independent errors, the first represents the operator error associated with the bankline digitalization, while the second defines the uncertainty deriving from the air images. Considering the first type, we multiplied the pixel resolution (R) by the mean of the maximum number of pixels (p) of repeated right and left delineations of the bankline. Given that the error range was below 2 m (among all photo sets), we decided to group together the offset data for each set, reaching one average pixel error value (p). The distortion degree within each air image was assessed by comparing positions (i.e. building corners) easily identifiable on all photo sets with the same ones found on the 2006 ortho-photographs. Finally the quantification of the distance difference was carried out. Thus, the photo distortion error considering each image set (θ), represents the mean distance difference between points. Concluding the process of error identification, the total error in width (E_w) was assessed by Mount *et al*. (2003) equation:

$$E_w = 2^{1/2}pR + 2\theta \tag{7}$$

Accounting for the polygonal areal error (erosion, channel, islands), we needed to set two assumptions: (1) the constancy (no error) of eroded bank segments, channel length or islands and (2) the rectangular form of the polygons describing these areas. In this sense, the assessment error related to the area was equal to the product between the polygon length and the width error (Mount *et al.,* 2003).

8 Geomorphic Analysis: Volumetric approach

8.1 Colour bathymetry and Hybrid Digital Elevation Models

To create an accurate digital terrain model, a regression model was calibrated between the water depth and the Red, Green and Blue (RGB) bands values deriving from aerial images acquired during the LiDAR survey. The water depth was estimated indirectly as the difference between the water surface (estimated from interpolation of selected LiDAR points; see details in section 8.1.2) and bed elevation (measured with dGPS in the field). Hybrid digital terrain models (HDTM) were then created, derived from the interpolation of LiDAR (section 8.1.4) points for dry areas and colour bathymetry derived points for wet areas. A total of three HDTMs were developed for each considered year referring to the three sub-reaches (Nove, Friola and Fontaniva).

This process (Figure 23) was divided into five principal steps: (A) LiDAR data and field survey, (B) dataset preparation, (C) bathymetric model determination, (D) HDTMs creation and (E) HDTMs validation. At the end, three DEMs of difference (DoDs - one for each sub-reach) were produced for each year, and the volumetric surface change and relative uncertainty calculated. The details of this process are explained in the sub-sections below.

The novel contribution of this approach mainly regards four aspects:

I) The field of application involves complex depth and colour characteristics (due to high periphyton loads on the channel bottom);

II) A revised methodology to estimate the water depths to associate with the colour bands (depths of calibrations), thanks to the difference between the elevation of the water surface (derived from selected LiDAR points) and that of the channel bottom (derived from a dGPS survey performed contemporarily with the LiDAR survey). In this way the application of the approach is also possible without direct water depth measures;

III) The search for the best depth-colour model, testing existing physical models (based on Beer Lambert law formula - Equation 1) and empirical models through different statistical regression methods;

IV) The application of filters, based on colour variability analysis, to reduce the errors of the bathymetric models (presence of pheriphyton, light reflections, exposed sediment, shadows, suspended load and water turbulence).

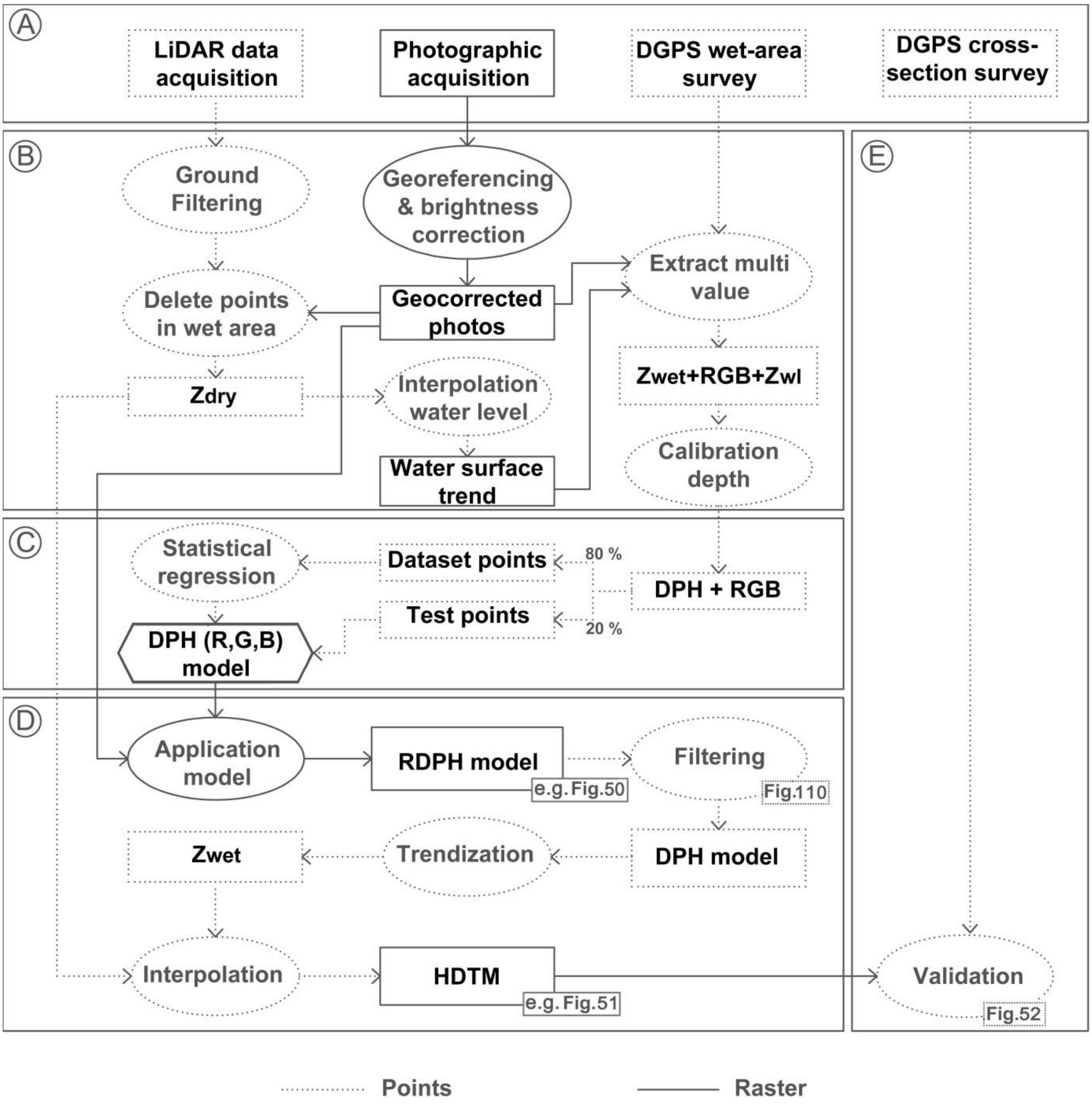

Figure 23. *HDTM building process: (A) LiDAR data and field survey, (B) data preparation for process application, (C) bathymetric model determination, (D) hybrid DTM building, (E) DTM validation.*

8.1.1 LiDAR data and field survey

Two LiDAR surveys were commissioned: the first in 2010 and the second in 2011 after the significant floods registered on November and December 2010. The two company that have flight for these surveys were the Blom GCR Spa through an OPTECH ALTM Gemini sensor and OGS Company through a RIEGL LMS-Q560 sensor (flying height ~ 850 m). For each LiDAR survey a point density able to generate digital terrain models with 0.5 m of resolution (at least 2 ground points per square meter) was required. LiDAR data were taken together with a series of RGB aerial photos with 0.15 m pixel resolution. The average vertical error of LiDAR was evaluated trough dGPS points on the final elevation model. The survey was carried out with the best weather conditions and low hydraulic channel levels. In-channel dGPS points acquisition was performed, taking different depth levels in a wide range of morphological units. Overall, 399 (2010) and 1421 (2011) points for the Brenta River, 337 (2010) and 2301 (2011) points for the Piave River, 1107 (2010) and 9366 (2011) points for the Tagliamento River were acquired. Finally, two cross-sections for each sub-reach, were surveyed through dGPS (average vertical error ± 0.025 m). It is important to note that the dGPS survey was performed contemporary with the LiDAR data to avoid the introduction of additional stochastic components.

8.1.2 Dataset preparing and automatic wet area extraction

The raw LiDAR point cloud was analyzed and the ground surface was identified through an automatic filtering algorithm (TerraScan, Microstation Application®) and, in occasion of critical areas, using manual checks (such as near bridges). The aerial photos were georeferenced and corrected by applying a brightness analysis using the appropriate tool within the semi-automatic framework TerraPhoto (Microstation application®). The corrected photos were joined (ESRI® ArcGIS 10) and the pixel size was resampled from 0.15 m to 0.5 m to minimize the georeferenziation error and decrease the possible strong colour variation due to light reflection, sediment exposed, periphyton, shadows and suspened load. This represents a crucial point because a bad photo georeferentiation can significantly increase the error due to an erroneous association between water depth and colour intensity. The choice of improving the pixel size exactly to 0.5 is also in relation to the resolution of the final elevation model (value derived from point density analysis).

A revised approach proposed by Antonarakis et al. (2008), regarding the determination of the wet areas through a combination of a canopy surface model (CSM; difference between digital surface model and digital terrain model) and the intensity of the LiDAR signal (Figure 24), was carried out. To estimate wet areas we have used a combination of LiDAR intensity, CSM and a detrended DTM (without slope). The purpose of each component was: a) to divide the zone with very low intensity (as water and vegetation) from the zone with high intensity (as gravel) as shown in Figure 24; b) to divide vegetation from the water; c) to divide artificial pool-lakes and channels (with different “altitude elevation level”) from the river channels. Wet areas were defined with a LiDAR intensity lower than 55 (as in Antonarakis et al., 2008), and a CSM elevation lower than 0.5 m. The “natural wet area” from artificial pool-lakes or channels on the detrended DTM was extracted with a “threshold elevation” in function of the study area. This assumption was made because the fluvial channels of the Tagliamento River are always below artificial (pool-lakes) wet areas.

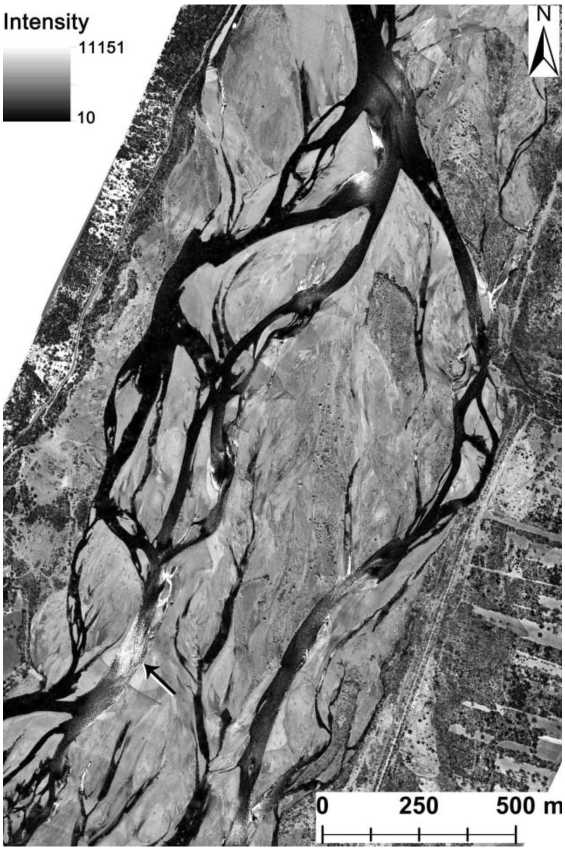

Figure 24. *LiDAR intensity raster of Cornino sub-reach in 2011. The arrow indicates an area with anomalous intensity values.*

Elaborations have been performed in ArcGIS 10® using a macro-utility, starting from LiDAR intensity, CSM and detrended DTM rasters. The results can be viewed as an output representing, with a shape file, the wet area. This approach, applied to a large river with braided morphology such as the Tagliamento, significantly decreases the time employed for extracting the wet areas of the active natural channel. In addition, the resulting shape file can be easily modified, in the case of anomalous intensity values that produce uncertainty detection of the real wet areas (see arrow in the Figure 24).

Along the edges of "wet area" shape polygons, LiDAR points able to represent the water surface elevation (*Zwl*) were selected and used to create a water surface elevation raster (Kriging interpolation).

Corresponding colour bands intensities and *Zwl* were added to the points acquired in the wet areas (dGPS wet-area survey) obtaining a shape file of points containing five fields (in addition to the spatial coordinates x and y): intensity of the three colour bands, Red (*R*), Green (*G*), Blue (*B*), elevation of the channel bed (*Zwet*) and *Zwl*. Finally, channel depth was calculated as $Dph = Zwl - Zwet$. A similar method has been used by Legleiter (2013) using the difference between the mean water surface elevation and the bed elevation, both derived from GPS survey.

8.1.3 Determination of the best bathymetric model

Starting from the obtained dataset, the water depth (estimated indirectly) was considered as the dependent variable, with the three intensity colour bands (R, G and B) as independent variables. 80% of the dataset was used for calibrating the depth-colour model and the remaining 20% to verify the efficiency and choose the best model. Physical models based on the Beer Lambert law (Eq. 1) were tested first.

A ratio-based method was employed to detect changes in depth and filter out the effect of changes in bottom albedo (e.g., Dierssen *et al*., 2003). Legleiter *et al*. (2004) and Marcus and Fonstad (2008) demonstrated that the log-transformation of the red-over-green band ratio correlates linearly with water depth across a wide range of substrate types:

$$DPH = \alpha + \beta_0 ln\ (R/\ G) \tag{8}$$

where DPH is the water depth, α and β_x are the calibration coefficient, and R and G are the intensities of the red and green bands.

An empirical linear model evaluating all the colour bands, the possible interactions and the square and cubic terms were then tested:

$$DPH = \alpha + \beta_0 R + \beta_1 G + \beta_2 B + \beta_3 RB + \beta_4 RG + \beta_5 GB + \beta_6 RGB + \beta_7 R^2 + \beta_8 G^2 + \beta_9 B^2 + \beta_{10} R^3 + \beta_{11} G^3 + \beta_{12} B^3 \tag{9}$$

Where α and β_x are the calibration coefficients in the depth colour regression. In this model the significance of each component was tested and deleted when the statistical test adopted (explained below) resulted as negative.

The statistical regressions were performed in R® environment using two methods: the traditional regression method based on statistical significance testing of each variable (p-value < 0.05), and the AICc index (Burnham and Anderson, 2002). The second approach estimates all the significant models, forming a ranking founded on the AICc value (the lower value represents the best model), starting from the most complex plausible model. The AICc method automatically deletes the non-significant variables while the deleting process in the first method is manual. The model featuring the lower error was used to build the "raw channel depth raster" (RDPH).

8.1.4 Hybrid DTM creation and validation

The best bathymetric model was applied to the georeferenced images (raster calculator) to determine the “raw channel depth raster” (RDPH). The RDPH was then transformed into points (2 points/m^2) and filtered in order to delete wrong or suspicious points, mainly due to sunlight reflection, turbulence, and elements (wood or sediment) above the water surface.

The proposed methodology used for filtering possible wrong points is characterized by an analysis of slope changes in neighbouring cells. When there are very strong slope changes between neighbouring cells, a potential error of depth estimation exists. We could analyse these variations through a semi-automatic method that forecasts the creation of a “curvature raster” (ESRI® ArcGIS 10), obtaining a value of curvature (slope derivative) for each cell. The “range” of curvature to consider a difference of depth between two cells “real” (with our pixel resolution of 0.5 m) was identified as $-600 < x < 700$. The cell values outside this range were removed, as in this case the “gap” between two cells is greater than 0.6 m. In addition, the upper and lower implausible limits (outliers; < 5% of total points distribution) were deleted.

On the corrected points (*DPH* model), the corresponding *Zwl* was subtracted to obtain, for each point, the estimated elevation of river bed ($Zwet = Zwl - DPH$). Hybrid DTMs (HDTM) were built up with natural neighbour interpolator, integrating Zdry points (by LiDAR) in the dry areas and Zwet points (by colour bathymetry) in the wet areas.

The final step was the validation of the HDTM models which was carried out by comparison with random dGPS surveys (1841 points on Brenta River, 2638 points on Piave River, and 10473 points on Tagliamento River) and dGPS cross-sections. The error of each “control point” was derived considering the difference between the elevation of the HDTM and the corresponding elevation of dGPS control point.

The accuracy of the hybrid DTMs was estimated separately for wetted and dry areas, taking into account also the dGPS error (available from the instrument for each point). The wet areas accurancy of the hybrid DTMs was estimated considering colour bathymetry errors at different water stage levels grouped in classes incremented of 20 cm.

8.2 Principal Erosion-Deposition analysis

8.2.1 Difference of DEMs production

In Matlab environment (Fuzzy Logic application) an "ad hoc" FIS file considering as inputs slope, point density and bathymetric points quality and as output elevation uncertainty was edited. Slope and point density categorical limits (i.e. low, medium, high) were chosen taking into consideration the literature values (Wheaton *et al.*, 2010) and our fluvial environments (gravel-bed rivers) and related field experience. The third input variable, the bathymetric points quality, represents an innovation inasmuch the colour bathymetry derived points (Moretto *et al.*, 2012a) that were used to interpolate the wet areas of the DTMs were also evaluated in their accuracy (Delai *et al.*, 2013). The achievement of reliable final geomorphic estimates considering the precision of in-channel depths was here considered as fundamental since the most significant scour and fill processes occur in the wet areas. For this input variable, we needed to consider only in-channel elevations so that, beside the common low, medium and high categories, a fourth "out channel" category including all the points elevation of the dry areas was added. The categorical limits of this bathymetric accuracy input feature small differences among the considered years and rivers (Table 1) depending on the number of dGPS points used to calibrate the model (Moretto *et al.*, 2013a). Finally, 36 FIS rules were edited, setting the output qualities of the elevation uncertainty according to Wheaton et al. (2010) as low, average, high and extreme. For details on the FIS logic and procedure we refer to Wheaton et al. (2010).

In ArcGIS® 10 (ESRI) environment the three DTMs associated to the input variables (slope, point density and bathymetric points quality) were then created for each sub-reach and year (2010 and 2011) using, as basis source, the hybrid DTMs. The slope and point density DTM were interpolated using the correspondent ArcGIS® tools. Concerning the "bathymetric points quality" DTM, a surface interpolating in the wet areas the points (increased by 10) derived by the Moretto et al. (2012a) procedure and in the dry areas a unique value of 11 m to include all the outer channel surface was finally built (Delai *et al.*, 2013).

At this point, the basic hybrid DTMs, the FIS files ("Piave", "Tagliamento 2010" and "Tagliamento 2011" differing only in the class limits of the input variable "bathymetric points quality") and the associated input DTMs (slope, point density and bathymetric points quality) were ready to be run in the Geomorphic Change Detection 5.0 (GCD) software (Wheaton *et al.*, 2010; http://gcd.joewheaton.org). Through the creation of associated uncertainty surfaces derived by the combination of the input DTMs and FIS rules, the basic hybrid DTMs and the error rasters were differenced producing reliable DoDs. Geomorphic changes were calculated, following literature (Wheaton *et al.*, 2010), by using a spatially variable uncertainty thresholded at 95% C.I. and the Bayesian updating method which accounts for spatial coherent erosion and deposition units (5x5 mobile windows) (Delai et al., 2013).

8.2.2 Principal Erosion – Deposition Analyser (PrEDA)

Thanks the colour bathymetry able to provide precise DTMs also in the wet areas, and the calibrated GCD tool able to delete erroneous areas on the final DoD (Figure 25), it is possible to conduct an accurate erosion-deposition analysis. A new tool developed in this work was implemented in Matlab® environment: Principal Erosion-Deposition Analyser (PrEDA).

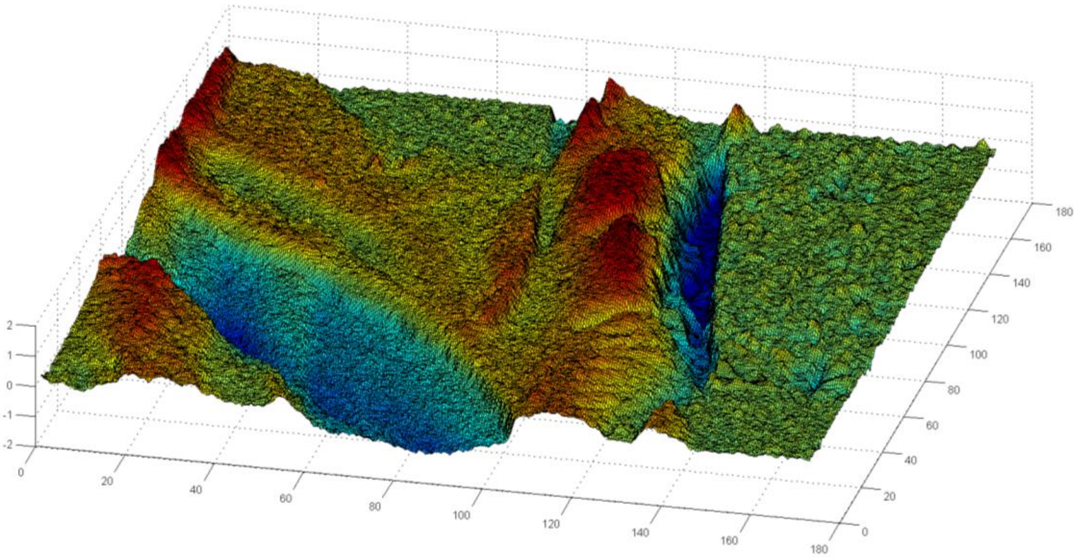

Figure 25. *Difference of DEMs (DoD) – Matlab 3D Output.*

Starting from an exported raster DoD (Ascii format), PrEDA requires as input a DoD ascii file (the same file exported from ArcGIS®), the cell size value (m) and two parameters to lead the analysis: the area limits (m^2) and a "delta" of variation (m). The area limits and the delta of variation allow to detect and split homogeneous patches of erosion and deposition with at least an imposed threshold continuous surface and a depth of erosion or deposition.

This tool checks for each cell, when it satisfies the delta of variation, its boundary and if neighbouring cell is found that satisfies the "delta" condition they will be written in a temporary list (Figure 26 – 3). This list will be used to identify the cells to check their boundary. During this process this list can increase, therefore increasing the number of cells to check. Once no more neighbouring cells to check are present, we have a continuous surface of erosion or deposition with a specified minimum "delta of variation". If the patch has a surface greater than the area limits, it will be plotted on a map and the "patches parameters" will be calculated (Figure 27).

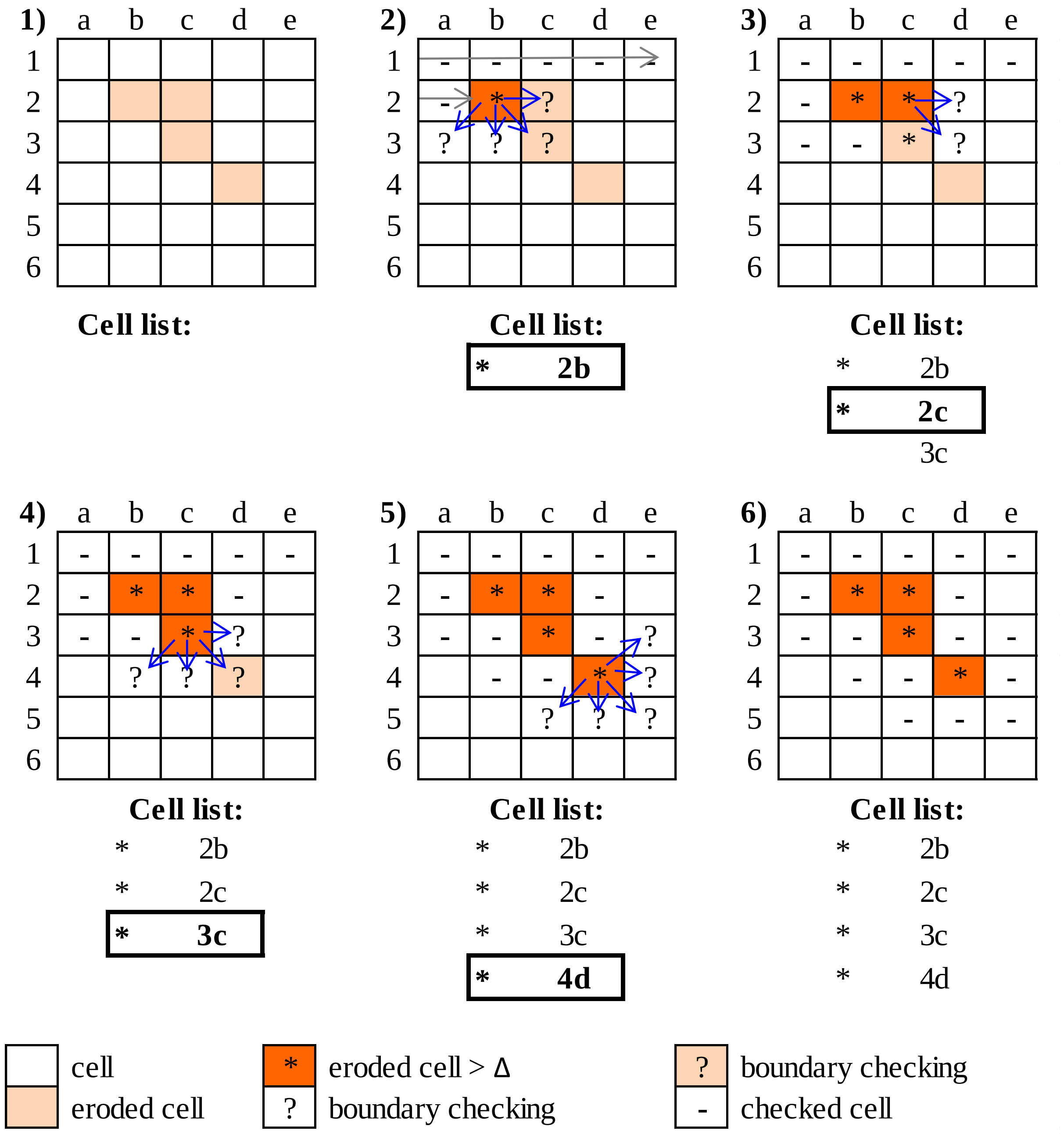

Figure 26. *PrEDA grid workflow.*

During the neighbour checking, the already checked cell will be marked to avoid subsequent checking that increases the computing time. The statistics that this tool is able to provide for each patch of erosion and deposition are: surface of erosion or deposition (m^2), volume (m^3), mean depth of variation (m), maximum depth of variation (m), standard deviation of variation (m) and two geometrical parameters regarding the extension in X and Y coordinate (m). With these pieces of information for each patch (Figure 28) we have the total amount of erosion and deposition with the imposed characteristics and a 2D and 3D plot of the DoD and a 2D plot of the erosion and deposition patches extracted. The advantage of this tool is that it is easily modifiable to allow the computing of different or more required statistics.

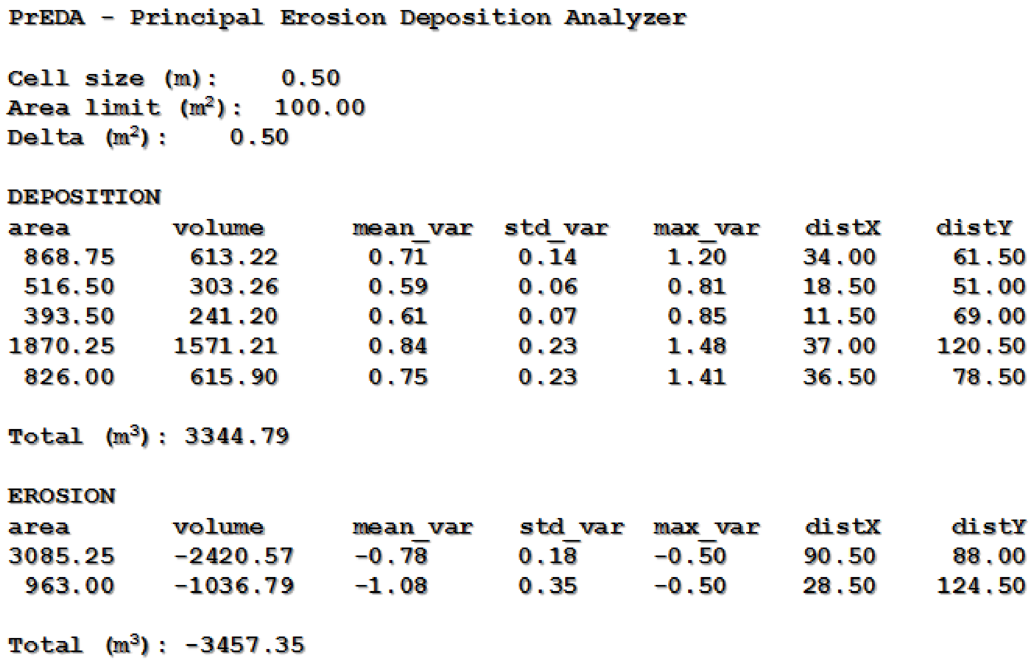

```
PrEDA - Principal Erosion Deposition Analyzer

Cell size (m):     0.50
Area limit (m²):  100.00
Delta (m²):     0.50

DEPOSITION
area        volume       mean_var  std_var   max_var   distX    distY
 868.75      613.22      0.71      0.14      1.20      34.00     61.50
 516.50      303.26      0.59      0.06      0.81      18.50     51.00
 393.50      241.20      0.61      0.07      0.85      11.50     69.00
1870.25     1571.21      0.84      0.23      1.48      37.00    120.50
 826.00      615.90      0.75      0.23      1.41      36.50     78.50

Total (m³): 3344.79

EROSION
area        volume       mean_var   std_var  max_var   distX     distY
3085.25     -2420.57     -0.78      0.18     -0.50     90.50     88.00
 963.00     -1036.79     -1.08      0.35     -0.50     28.50    124.50

Total (m³): -3457.35
```

Figure 27. *Analytic output of PrEDA.*

PrEDA could be a support to understand different patterns of morphometrical changes such as to divide reaches with more concentrated or more distributed erosion or deposition. In addition different characteristics can be analysed and compared among the patches, to better understand different reach behaviours. All the DoD produced were analysed and compared with this tool.

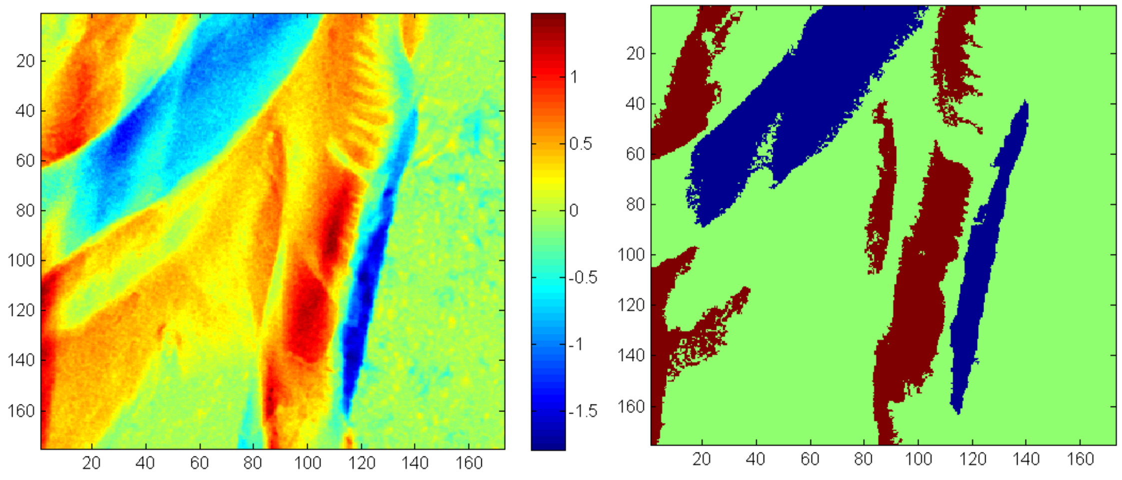

Figure 28. *Two dimensional DoD and Erosion-Deposition patches extracted.*

8.2.3 Analysis of riffle-pool behavior

Thanks to the HDTMs obtained with a precise definition in both dry and wet areas, we were able to explore the effects of severe floods. HDTMs comparison, analysing the dynamics of the bed forms (riffle - pool) as a consequence of flood events and natural and artificial “constrictions”, was performed in order to integrate the erosion-deposition patterns analysis described in Moretto *et al*. 2012a for the same study area.

Canopy surface models (CSM), derived from difference between digital surface models (DSM) and DTMs, were produced to identify the natural (fluvial islands) and artificial (embankments and bridges) vertical construction in the analysed sub-reaches. In addition to the bathymetric rasters, three water depth classes (0 – 0.5m; 0.5 – 1m and > 1 m) were applied to identify the different bed forms.

9 Geomorphic Analysis: Highly Detailed Resolution

The aims of this section are to quantify different types of errors (exposed in sub-chapter 5.3) on TLS surveys, and provide a "use protocol" as a function of the degree of detail desired, with a good awareness of the limitations and uncertainty committed, are. The new approach was used to make a proper uncertainty analysis able to be used in research and technical application. New Matlab tool utilities were made to make possible, easily and rapidly, the analysis among repeated TLS scans and a distributed uncertainty quantification on the final DEM.

In order to do an uncertainty analysis, if we aim at DTM building starting from raw clouds another new tool was needed to allow the vegetation filtering with TLS clouds.

9.1 Terrestrial Laser Scanner Uncertainty Analysis

9.1.1 TLS survey

Two kinds of survey were done: Lab Survey and Field Survey. In the lab survey three different surfaces were scanned: flat (black and white poster), spheres (50 mm diameter) and gravel (40 mm to 60 mm of average diameter - D_{50}). The laboratory "study area" was inside a tray 1 m x 1 m able to contain gravel or artificial spheres. The tray was scanned for each sample and subsequently, through Cyclone software a square of 0.80 m x 0.80 m was extracted and subsequently analysed. This reduction in the area of analysis was necessary to avoid boundary influence (of the tray) in the final results. The field surveys were on two different patches 1m x 1m of the Feshie River. As for the lab experiment the patches were reduced to 0.80m x 0.80 m. A geo-orientation of each TLS scan was introduced to allow the comparison of the same surface among the different scan repetitions. Targets and an Imaging Station were used to allow the geo-orientation of the TLS clouds.

The TLS experiments are divided into two main types: range experiments and moving experiments. The first kind compares the DEMs of the same surface derived from different scan distances, whereas the second one compares the results of the same surface from different scanner and control targets dislocation.

RANGE EXPERIMENTS

The range experiments are divided into vertical and horizontal experiments. In this analysis the scanner and the control targets were fixed, whereas the angle of incidence changed from normal to oblique from the first to the second kind of survey.

FIXED SCANNER, FIXED CONTROL TARGETS, NORMAL ANGLE OF INCIDENCE

Flat and sphere surface: 10 scans of the same patch at different distance: 10 m, 15 m, 20 m
The results of this experiment are useful to analyse the loss of detail in relation to the distance and identify a threshold distance to have a good roughness estimation. The maximum distance to use depends on the type of TLS used (short or long range). The vertical disposition of the surface allows not to have effects of the angle of incidence.

The flat surface used was 1/2 black and 1/2 white to verify the effects of different colour intensity (Figure 29).

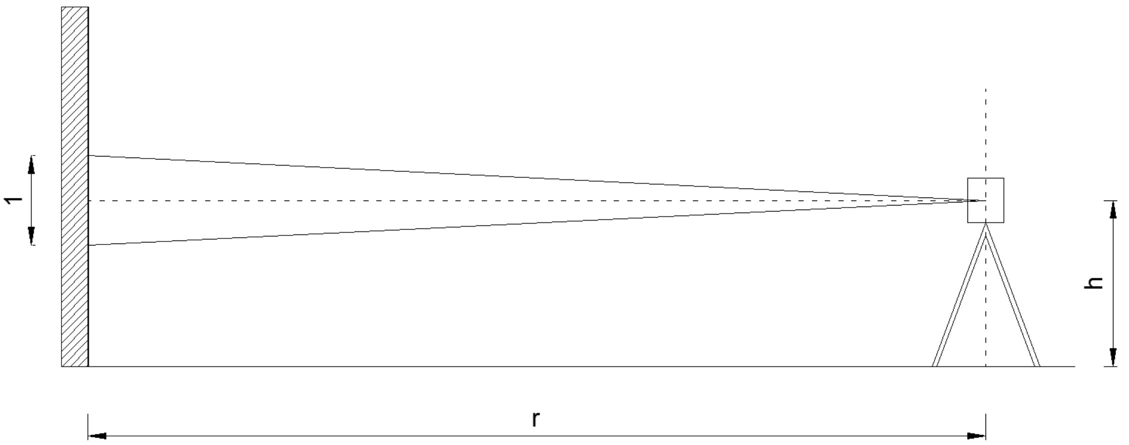

Figure 29. *Normal range experiments.*

FIXED SCANNER, FIXED CONTROL TARGETS, OBLIQUE ANGLE OF INCIDENCE

Flat, spheres, gravel surface and Feshie patches: 10 scans of the same patch at different distance: 5, 10, 15 m, 20 m. The results of this experiment could be useful to analyse the loss of detail in relation to the distance and identify a threshold distance to have a good estimate of roughness. The maximum distance to use depends on the TLS model (short or long range). The horizontal disposition of the surface allows to quantify the effects of the angle of incidence through comparison with the scan of the same surface in a vertical disposition (normal angle of incidence). The flat surface used was 1/2 black and 1/2 white to verify the effects of different colour intensity (Figure 30).

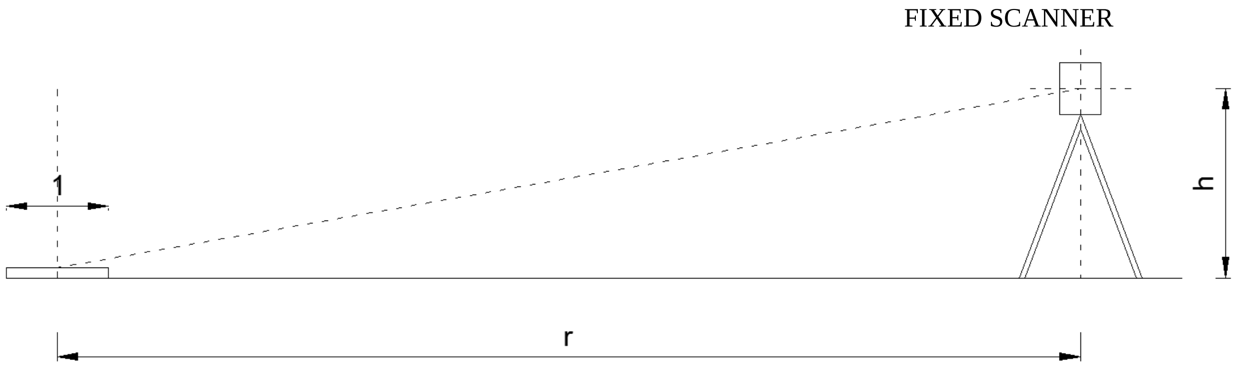

Figure 30. *Oblique range experiments.*

*M*OVING EXPERIMENTS

The moving experiments are divided divided into moving targets, moving TLS and moving both. In this experiment the scanner and the control targets were moved whereas the range and the angle of incidence was fixed.

RANDOM ERROR : *F*IXED SCANNER, *M*OVED CONTROL TARGETS

Flat, spheres, gravel surface and Feshie patches: 9 TLS surveys at 10 m of horizontal distance. The TLS was in the same positions, but the control targets relocated randomly and the scans registered individually before comparison (Figure 31).

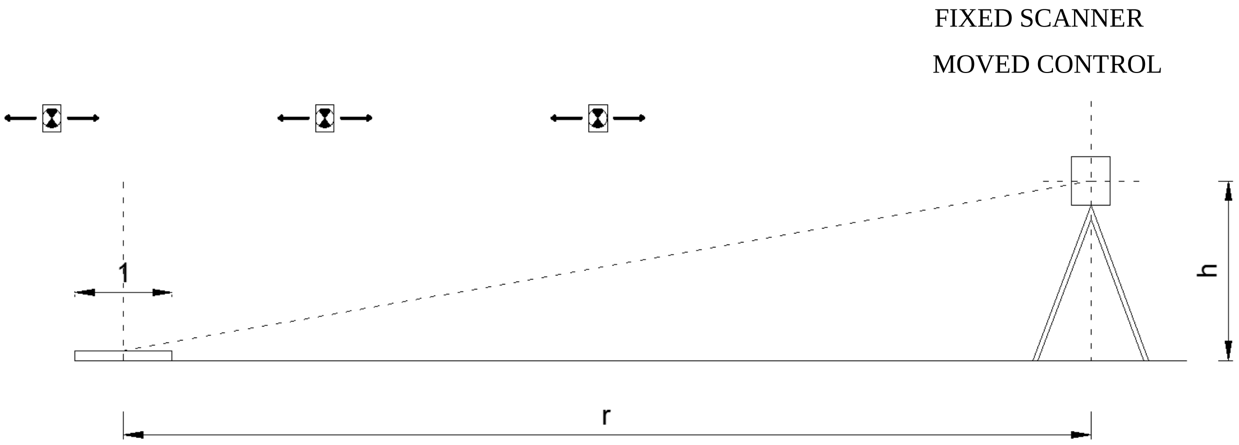

Figure 31. *Targets moving experiments.*

These experiments, could be useful to quantify the random errors due to relocating the scanner, the control targets and the registration process.

SCENE ERROR : MOVED SCANNER, FIXED CONTROLS

Flat, spheres and gravel surface: 10 TLS surveys at 10 m of horizontal distance. The TLS was in a random position, the control targets in the same positions and the scans registered individually before comparison (Figure 32).

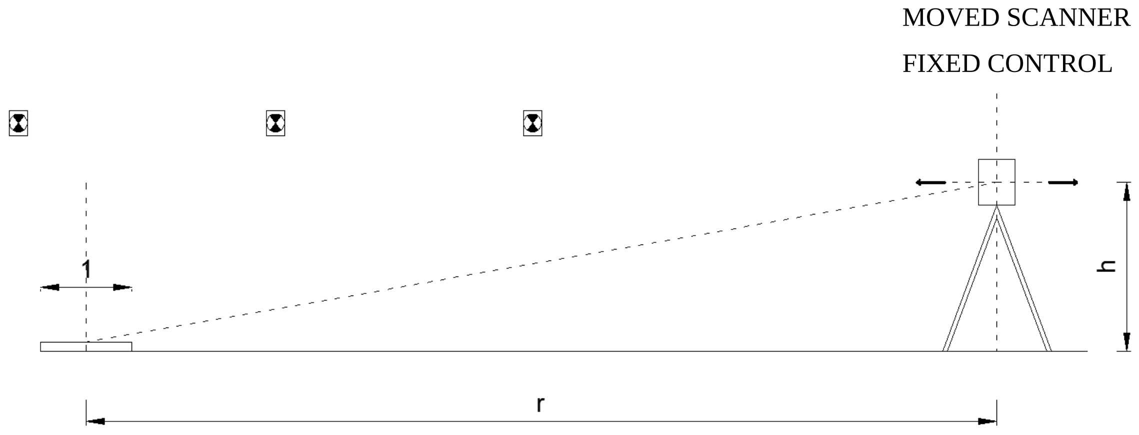

Figure 32. *Scanner moving experiments.*

The use these types of surface, it is important to analyse errors on different degree of roughness. This experiment can be useful to identify some rules of TLS positioning in relation to the roughness degree.

RANDOM AND SCENE ERROR: MOVED SCANNER, MOVED CONTROLS

Flat, spheres, gravel surface and Feshie patches: 10 TLS surveys at 10 m of horizontal distance. The TLS was in a random position and also the control targets in a random position for each scan. Individual scans registration before comparison (Figure 33).

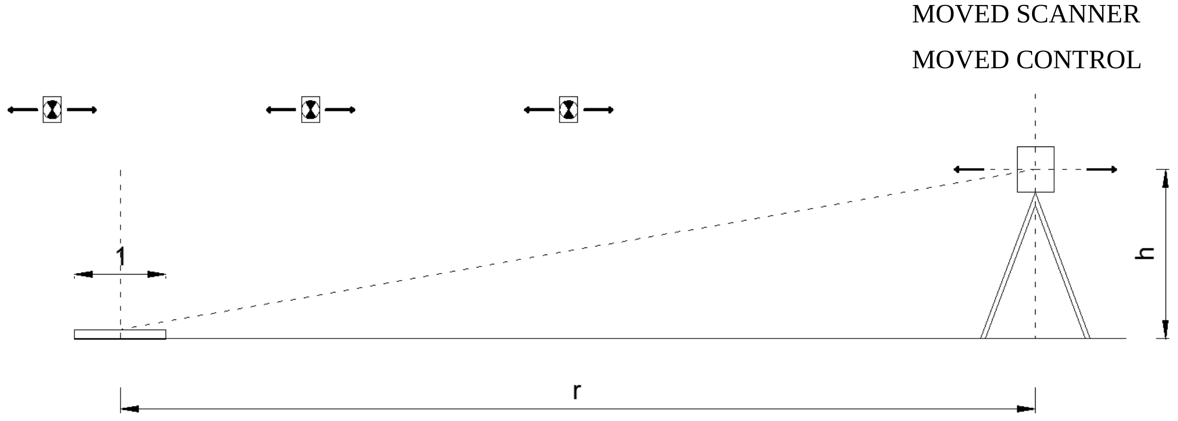

Figure 33. *Scanner and targets moving experiments.*

N.B. The internal set up (density, speed, etc.) of the TLS must be the same for all the experiments.

EXPERIMENTS SUMMARY

The different experiments carried out can be summarized as shown in table 2, while Figure 34 shows the different kinds of surfaces.

Table 2. *Different kind of experiment carried out with different surface: Flat, spheres, gravel, Feshie patch 1 and Feshie patch 2.*

EXPERIMENTS		**SURFACE**					**TOTAL**
		FLAT	SPHERES	GRAVEL	FESCHIE P1	FECHIE P2	
RANGE EXPERIMENTS	10m NORMAL ANGLE OF INCIDENCE	20	10	-	-	-	30
	15m NORMAL ANGLE OF INCIDENCE	10	10	-	-	-	20
	20m NORMAL ANGLE OF INCIDENCE	10	10	-	-	-	20
	5m OBLIQUE ANGLE OF INCIDENCE	-	-	-	10	10	20
	10m OBLIQUE ANGLE OF INCIDENCE	10	10	10	10	10	50
	15m OBLIQUE ANGLE OF INCIDENCE	10	10	10	10	10	50
	20m OBLIQUE ANGLE OF INCIDENCE	10	10	10	10	10	50
MOVING EXPERIMENTS	FIXED SCANNER, MOVED TARGETS	10	-	9	-	-	19
	MOVED SCANNER, FIXED TARGETS	-	-	9	-	-	9
	MOVED SCANNER, MOVED TARGETS	-	-	9	10	10	29
TOTAL		80	60	57	50	50	297

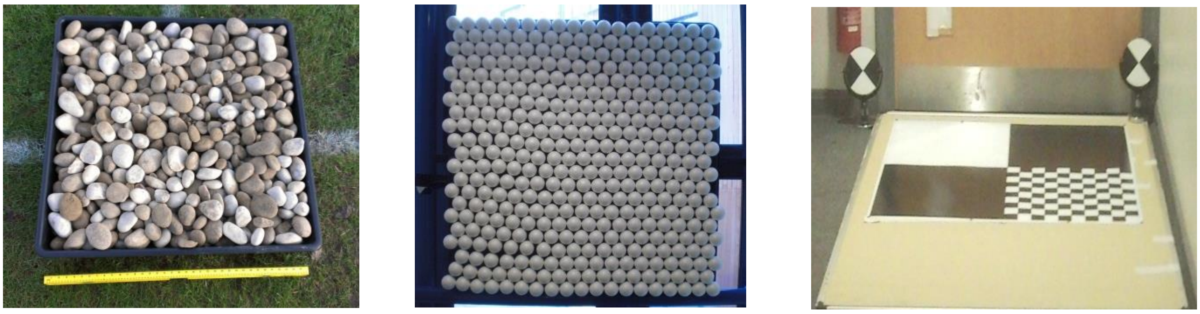

Gravel *Spheres* *Flat*

Range Feshie *Patch 1 Feshie* *Patch 2 Feshie*

Figure 34. *Surfaces scanned.*

9.1.2 Cyclone elaboration

The elaborations with Cyclone® software are divided into 5 steps:

- Data importing;
- Registration;
- Export TLS registered coordinate (tools>info>object info>point cloud info);
- Create fixed BOX to define a common study area;
- Export TLS point inside the BOX.

9.1.3 TLS tool box

A TLS tool box was created in Matlab to simplify and allow all the elaborations. Parameters for each TLS point, different statistics at different scale (whole scan and for each dimensioned cell), variability for each repeated scan, uncertainty analysis at cell scale and colour maps are the utilities of those scripts. There are nine tools in total: *Range_Angle, Columns_unifier, Cell Analyzer (CeA), CeA_b, CeA_STAT_diff_TREND, CeA_ERROR_dataset, Interpolator, CeA_colour_maps* and *CeA_Fuzzy*.

CeA Range and Angle of incidence calculation

2D Range (horizontal distance), 3D Range (real distance) and the angle of incidence with TLS registered coordinate for each scan are calculated as below, using “Range_Angle” Matlab script and then this information is added for each point (as new columns in the text matrix) with “Columns_unifier Matlab” script. The final input matrix will be used as input for CeA. Starting from a TLS xyzi text file (with scans not registered) and another text file with the TLS coordinate, the program calculates:

- $Range\_2D = \sqrt{(x_0 - x_i)^2 + (y_0 - y_i)^2}$ *(10)*
- $Range\_3D = \sqrt{(x_0 - x_i)^2 + (y_0 - y_i)^2 + (z_0 - z_i)^2}$ *(11)*
- *Angle of incidence:* $\theta = \arcsin\left({}^{Range\_2D}/_{Range\_3D}\right)$ *(12)*

Where x_0, y_0 and z_0 are the coordinates of the TLS whereas x_i, y_i and z_i are the coordinates of a TLS point. The program adds this information for each TLS point to be used in the subsequent elaborations.

Cell Analyzer

Cell Analyzer (CeA) program is a Matlab script that starting from a TLS point cloud is able to divide it in defined cells. Basic statistics, outlier point deleting, point detrending and detrended statistics for each cell are the outputs of this program.

CeA requires as input a text file (in the same folder of the program) with the following information: X, Y, Z, and Intensity. If we are also interested in verifying the range and angle of incidence, another text file is required (named TLSxyz in a folder named "TLScoord") with the XYZ coordinates of the centre of the TLS to be elaborated with "Range_Angle" Matlab script. Is important that in this file, each line must have the name of the reference scan (same name as the TLS point cloud file) and in the following columns the corresponding X, Y and Z coordinates.

A cell size and the amount of cells to cluster in temporary files to not load all the TLS points at the same time are required in CeA program. Indeed, this program splits the TLS cloud input file into a lot of small files depending on the number of cells to cluster (4, 9, 16 or 25). This function will be useful with a very large input dataset.

A points filter has been implemented in the code to delete possible "outliers" outside the range between the 5th and 95th percentiles.

CeA Rastering process

The grid creation process is shown in Figure 35. After finding the spatial limits in the point cloud and an imposed cell size, the point cloud splitting into cells is possible.

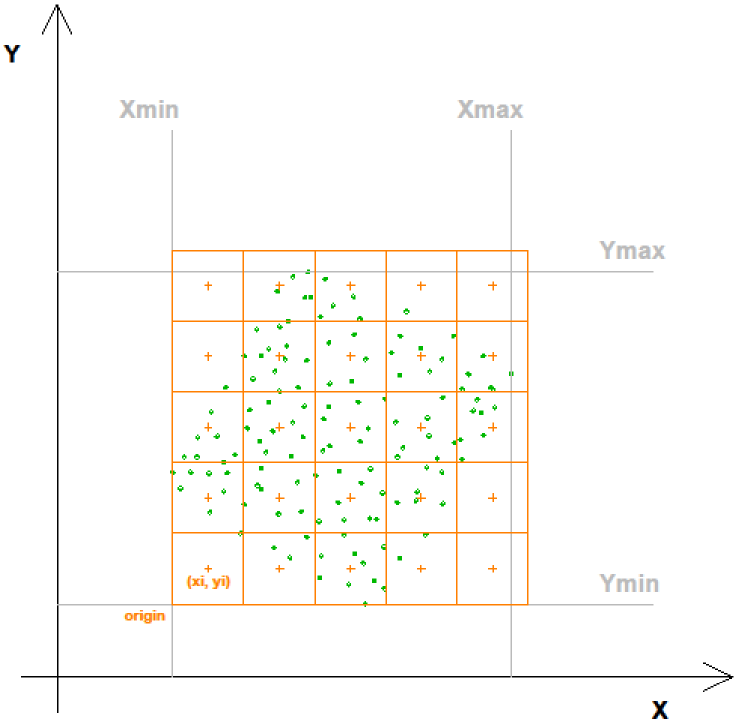

Figure 35. *Cell grid creation.*

CeA Point cloud detrending method

The detrending method of the first version of this program is the same used in ToPCAT program as explained in Brasington *et al.* (2012). For each cell, flat surfaces derived from exact interpolation of the average cell elevation, positioned in the centre of the cell, with the corresponding average elevation of the two boundary cells aligned with the axes, were estimated. Consequently, four surfaces could be estimated for each cell, and used to subtract the elevation trend derived from the slope and the "macro-morphology" (Figure 36).

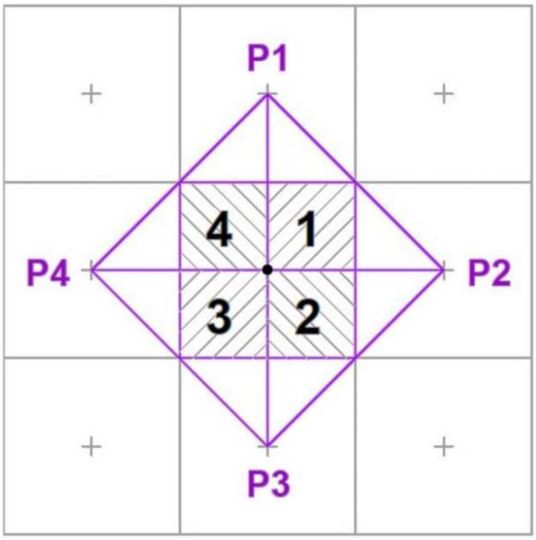

Figure 36. *Trend surface estimation.*

To estimate a plane passing through 3 points and use it to calculate the spatial coordinates (x, y, z) of the projection of a TLS point above it in a generic position, it is necessary to estimate its function and subsequently solve it with respect to the x and y coordinates of the TLS points. In this way the comparison between the "Z" elevation of the TLS points and the corresponding "Z" elevation (projection of the TLS point) of the low mean TIN is made possible. If P (x, y, z) is a generic point to calculate the "Z" coordinate on the plan, and supposing that:

$$P_0 = (1, 0, 2)$$
$$P_1 = (1, 1, 0)$$
$$P_2 = (2, 1, 1)$$

are the three points passing throughout the plan (that are the centre of the cell and two of its neighbouring cells P1, P2, P3 or P4) we can calculate the corresponding vectors:

$$P_0P_1 = P_1 - P_0 = (0, 1, -2)$$
$$P_0P_2 = P_2 - P_0 = (1, 1, -1)$$
$$P_0P = P - P_0 = (x-1, y, z-2)$$

Building a matrix with these three vector we obtain:

$$\begin{vmatrix} 0 & 1 & -2 \\ 1 & 1 & -1 \\ x-1 & y & z-2 \end{vmatrix} = 0$$

Calculating the matrix determinant we obtain the plan surface function passing through our three points:

$$z = x - 2y + 1 \qquad (13)$$

Applying this method in the Matlab code we can easily estimate all the surface functions to use as TIN of reference.

The “b” version (CeA_B) of this program, instead used a moving window 3x3 cell to delete the trend elevation. The results of the different detrending methods were compared.
The output of CeA.m (ToPCAT detrending method) and CeA_B.m (3x3 moving window detrending method) were respectively:

- *ROW CELLS* (for each cell): ID, Xi, Yi, mean Z, Standard deviation, mean Intensity, Density, mean Range2D, mean Range3D, mean angle of incidence;
- *DETRENDED CELLS* (for each cell): ID, Xi, Yi, mean Z, Density, number filtered points, XGr, YGr. Where XGr and YGr are the relative barycentre (Figure 37) of TLS cloud inside the cell (relative from Xi min and Yi min);

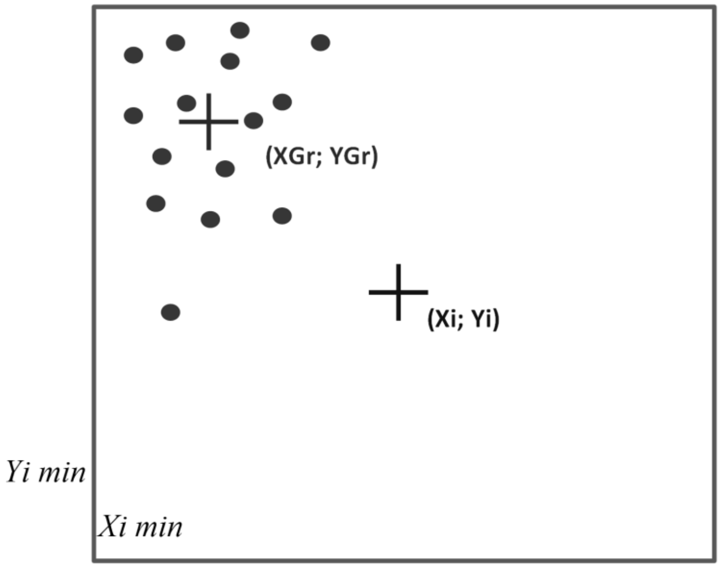

Figure 37. *Relative barycentre of the TLS cell cloud.*

- *DETRENDED STATISTICS* (for each cell): ID, Xi, Yi, Zmin, Z_{Q5}, mean Z, Z_{Q95}, Zmax, Standard deviation, Zcurtosis, Zskewness, Final density. Where:

  Z_{Q5}: 5th percentile of detrended Z;

  Z_{Q95}: 95th percentile of detrended Z;

  Z_{Kurt}: Kurtosis of detrended Z;

  Z_{Skew}: Skewness of detrended Z;

  Dif_{min}: Filter parameter that is |Z_min – Z_Q5| if greater than 1 filter the TLS points;

  Dif_{max}: Filter parameter that is |Z_max – Z_Q95| if greater than 1 filter the TLS points.
- *SUMMARY STATISTICS* (for each scan): min, mean, max and standard deviation values for: Density, Range_3D, Roughness, Intensity, Angle of incidence;
- *xERROR_DATASET* (for each cell – to use in the error dataset tool): ID, Xi, Yi, mean Z, standard deviation, mean Intensity, Density, mean Range3D, mean angle of incidence.

Cell Analyzer program workflow:

```
• Input TLS point cloud;
• Input cell size;
• Ask how many TLS sub-folder create;

------- For each text file
    • Find limits XY min/max TLS cloud;
    • Initialize grid origin and create "cell grid";
    • Decomposition TLS cloud in more folders to not upload all the points in the memory;

        For each line of cell matrix
            • Extract TLS points inside cell i;
            • Desired operation(without detrending): ID Zmean, dev_st, Intensity_mean, density, range_2D mean, range_3D mean and angle of incidence mean;
            • Fill in line output matrix;
        Parallel computing

    • Create a non-detrended results matrix;

        For each line of non-detrended results matrix
            • Find P1, P2, P3 and P4 (Figure 36);
            • Calculate sub-cell limits;
            • Estimate the triangular flat surface function for each sub-cell (if possible);
            • Extract TLS points for each sub-cell as 4 matrices (from TLS sub-folders);
            • TLS points Detrending with our "triangular" sub-cell function;
            • Write X, Y, Zdet_tr, Zdet_sq. in a matrix for each sub-cell;
            • Unify the sub-cell matrix (to have all detrended TLS points in their cell);
            • Calculate the Zdet_tr. distribution for each cell and delete outlier;
            • Remaining operations: avg_Zdet avg_Zdet final_dens N_pp_FILT XGr YG Z_Min Z_Q5 Z_Median Z_Q95 Z_Max avg_Zstd Z_Kurt Z_Skew difmin difmax f_dens;
            • D:\CeA_OUTPUT\ROW_CELL
            • D:\CeA_OUTPUT\DETRENDED_CELL
            • D:\CeA_OUTPUT\DETRENDED_STAT
            • D:\CeA_OUTPUT\xERR_DATASET
        Parallel computing

    • Display output matrix results;
    • Calculate summary statistics;
    • D:\CeA_OUTPUT\SUMMARY_STAT
    • Text file output of the matrix results;
    • Display output time of elaboration;

-------- Loop
```

The program can also work in “parallel”; this function allows computing time to be saved. To work with this option, before running the code it is necessary to add “workers” (Matlab sessions) with this code in the command window of Matlab:

```
Matlabpool local 8
```

Where 8 is the number of workers (maximum 12 with the last version of Matlab® R2012b); the number of workers to use depends on the CPU owned.

Detrending method comparison

CeA_STAT_diff_TREND.m allow, after applying CeA.m and CeA_B.m, the difference to be known for each cell due to the different detrending methods.

Outputs for each scan, for Z_Curtosis, Zmax, Zmean, Zmin, Z_skewness, Roughness: minimum value of each detrending method and difference, mean value of each detrending method and difference, maximum value of each detrending method and difference, standard deviation value of each detrending method and difference.

In addition, at the end of each text report, there are the average values for each component of each scan group.

Error dataset

With more scan repetitions of the same “object”, CeA_ERROR_dataset uses one of them, indicated as scan of reference and the other scans to evaluate for each cell in common are the standard deviation (representing the variation in value of each cell in common). Therefore the error in this application is the standard deviation of the Z detrended, evaluated for each cell in common. The aim of this tool is to provide a help to write the rules to use in the fuzzy analysis. The variables considered are: Density, Roughness, Range_3D, Intensity, Angle of Incidence, Move_TLS (put 1 if it is moving or 0 if it is still) and Move_Target (put 1 if it is moving or 0 if it is still).

Output: Zdet (of reference scan), error (comparing all the scans), Density (of reference scan), density_STD (comparing all the scans), Roughness (of reference scan), Roughness _STD (comparing all the scans), Range (of reference scan), Range_STD (comparing all the scans), Angle of incidence (of reference scan), Angle of incidence _STD (comparing all the scans), Intensity (of reference scan), Intensity_STD (comparing all the scans), Move_TLS, Move_targets.

CeA Fuzzy

To create a reliable uncertainty model the “fuzzy inference logic” can be a solution.

Whereas probabilistic models primarily describe *random variability* in parameters, fuzzy models primarily deal with *vagueness* in parameters (Chen *et al.*, 1999). Although the assumptions on the nature of the statistics (e.g. independence of variables, errors being random) underlying probabilistic models of uncertainty can be stretched in order to apply them, such applications may lead to serious errors (Chen *et al.*, 1999). By contrast, fuzzy models require very few assumptions and can be applied when relatively little is known about the uncertainty, or what is known can only be articulated in less precise linguistic terms (Bandemer and Gottwald, 1995; Klir and Yuan, 1995). One of the subsets of fuzzy set theory is fuzzy logic, and one of the tools that grows out of fuzzy logic is the fuzzy inference system (Klir and Yuan, 1995). Fuzzy logic is often described as a trade-off between significance and precision (Jang and Gulley, 2007). This is important as the geomorphologist may not necessarily need to know the precise magnitude of elevation uncertainty in each component of the error budget (e.g. errors due to slightly tilted survey pole) rather, the significance of the total uncertainty on the geomorphic interpretation. Fuzzy inference systems are convenient frameworks for taking the information that is known (inputs) and producing an appropriate output (Jang and Gulley, 2007). In the case of topographic surveys (Wheaton et al., 2010), something is always known about the survey sampling (e.g. point density) and the morphology (slope), and in some cases there may be additional information (e.g. roughness from facies maps, point quality from GPS).

Here, a fuzzy inference system (FIS) was developed that accepts the inputs that are readily available and produces a δz output that is calibrated to the range of empirically determined values. Matlab’s Fuzzy Logic Toolbox, developed by Jang and Gulley (2009), was used to implement this FIS. The fuzzy inference system consists of four components:

1. Specification of FIS type, fuzzy operation methods, rule implication method (and vs. or), aggregation method (min vs. max) and defuzzification method (if applicable);
2. Definition of fuzzy membership functions for the inputs;
3. Definition of rules relating inputs to outputs;
4. Definition of fuzzy membership function for the output; The most common default specifications suggested by Jang and Gulley (2007) were used for FIS type *Mamandi*. The fuzzy operation methods refer to how inputs for rules are combined (using Boolean operators), whereas the rule implication method refers to how an output membership function is arrived at for each rule (minimum method used). The aggregation method refers to how the outputs from all applicable rules are combined into a single output membership function

(maximum method used). Finally the defuzzification method refers to how the fuzzy number output (a membership function), can be converted into a crisp, single-value number (centroid method used).

Fuzzy inputs and output although fuzzy membership functions come in a wide array of forms, the most common are triangular and trapezoidal membership functions (Wheaton et al., 2010). Although FIS outputs tend not to show significant sensitivity to membership function shape (Klir and Yuan, 1995). The process of defining (density, range, roughness, angle of incidence, intensity and instrument mobility), the simple adjectives ‘high’, ‘medium’ and ‘low’ were deemed adequate. The second part consists of defining the membership function that describes the range of values covered by each adjective. An example of membership functions in a “FIS Editor” of Matlab are shown in Figure 38.

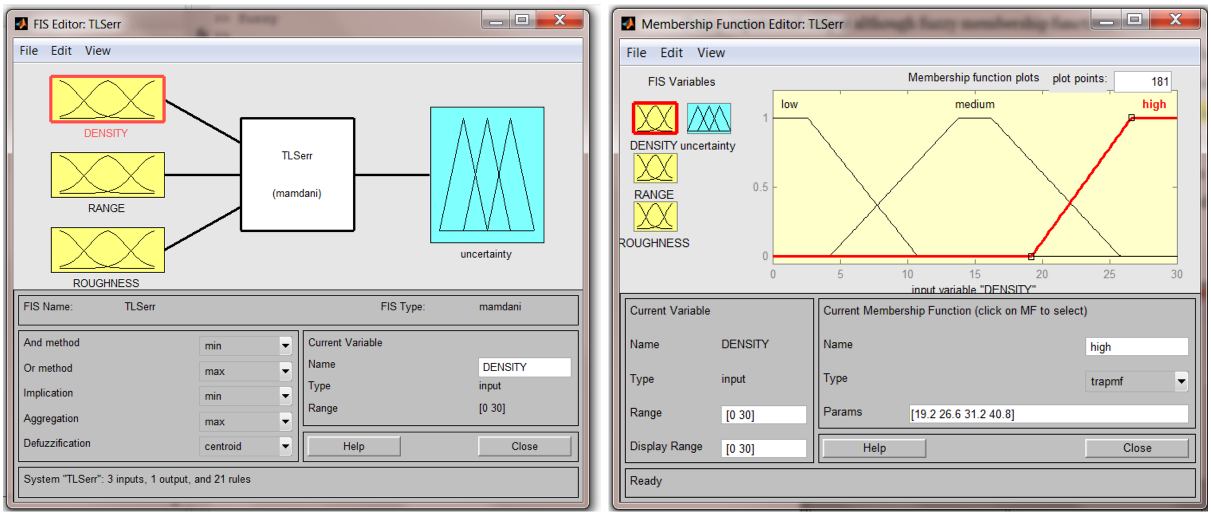

FIS Name: TLSerr
FIS Type: mamdani
And method: min
Or method: max
Implication: min
Aggregation: max
Defuzzification: centroid
Current Variable
Name: DENSITY
Type: input
Range: [0 30]
System "TLSerr": 3 inputs, 1 output, and 21 rules

plot points: 181
Current Variable
Name: DENSITY
Type: input
Range: [0 30]
Display Range: [0 30]
Current Membership Function (click on MF to select)
Name: high
Type: trapmf
Params: [19.2 26.6 31.2 40.8]
Ready

Figure 38. *Matlab fuzzy application.*

For the input variables, so long as the membership functions span the range of encountered values for that variable, the exact specification of their membership function is not critical (Jang and Gulley, 2007; Klir and Yuan, 1995). What is more important is that the expert defining the rule system knows what values the adjectives correspond to and develops rules in accordance with those perceptions. For the output variable (δz in this case), the output membership functions must correspond to realistic output values. Outputs from the FIS were calibrated to values found in empirical experiments conducted as described above in the laboratory and on the Feshie River (sub-chapter 9.1.1).

FIS rules: Rule definition for the FIS is a process of linguistically relating the inputs (using their different adjectives defined above) to a single adjective for the output. For example, as described in Wheathon et al. (2010), if 3D point quality is high, slope is low, and point density is high, then elevation uncertainty is low. By contrast if 3D point quality is low, slope is high, and point density is low, then elevation uncertainty is extreme.

After creating the fuzzy rules with the FIS editor of matlbal, the matlab code “CeA_Fuzzy”, applies for each cell in the fuzzy analysis to estimate their uncertainty. The cell coordinate, roughness, intensity, density, range, angle of incidence and the uncertainty were provided as results.

WORK FLOW SUMMARY ADOPTED

The work flow adopted to quantify the TLS uncertainty is divided into three main steps:

A) Scans;

B) Cyclone elaborations;

1. Import data;
2. Registration;
3. TLS registered coordinate (tools>info>object info>point cloud info);
4. Create fixed BOX;
5. Export TLS point inside the BOX.

C) TLS toolbox elaborations.

1. *Range_Angle.m and Columns_unifier.m* to calculate Range_2D, Range_3D and angle of Incidence with TLS registered coordinate for each scan.
2. *CeA.m* (ToPCAT detrending method – Brasington et al., 2012) or *CeA_B.m* (3x3 moving window detrending method) output:
    - ROW_CELL (for each cell): ID, Xi, Yi, avg_Z, Std., avg_Intensity, Density, avg_Range2D, avg_Range3D, avg_angle of incidence;
    - DETRENDED_CELL (for each cell): ID, Xi, Yi, avg_Z, Density, number filtered points, XGr, YGr;
    - DETRENDED_STATISTICS (for each cell): ID, Xi, Yi, Zmin, Z_{Q5}, avg_Z, Z_{Q95}, Zmax, Std., Zcurtosis, Zskewness, Final density;
    - SUMMARY_STATISTICS (for each scan): min, mean, max and standard deviation values for: Density, Range_3D, Roughness, Intensity, Angle of incidence;
    - xERROR_DATASET (for each cell): ID, Xi, Yi, avg_Z, Std., avg_Intensity, Density, avg_Range3D, avg_angle of incidence;

CeA_STAT_diff_TREND.m: Apply it after *CeA.m* and *CeA_B.m* to know the difference for each cell due to the different detrending methods.

Outputs for each scan, for Z_Curtosis, Zmax, Zmean, Zmin, Z_skewness, Roughness: minimum value of each detrending method and difference, mean value of each detrending method and difference, maximum value of each detrending method and difference, standard deviation value of each detrending method and difference.

In addition, at the end of each text report, there are the average values for each component of each scan group.

2. *CeA_ERROR_DATASET.m:* with more scan repetitions of the same "object", it uses one indicated scan as reference and the other scans to evaluate for each cell in common the standard deviation (representing the variation of each component wanted). The error in this application is the standard deviation of the Z detrended, evaluated for each cell. The aim of this tool is to provide a help to write the rules to use in the fuzzy analysis. The variables considered are: Density, Roughness, Range_3D, Intensity, Angle of Incidence, and a Moving factor (that checks the differences of scanning the same surface from the same position, by changing the target or the TLS position and by changing both).

Output: Zdet (of reference scan), error (comparing all the scans), Density (of reference scan), density_STD (comparing all the scans), Roughness (of reference scan), Roughness _STD (comparing all the scans), Range (of reference scan), Range_STD (comparing all the scans), Angle of incidence (of reference scan), Angle of incidence _STD (comparing all the scans), Intensity (of reference scan), Intensity_STD (comparing all the scans), Move_TLS (0 fixed, 1 moved), Move_targets (0 fixed, 1 moved).

3. *Fuzzy rules:* Create "TLSerr.fis" file with all the rules to apply the Fuzzy analysis.

4. *CeA_FUZZY.m* (for each cell) it applies the fuzzy analysis to estimate the uncertainty. Output: ID, Xi, Yi, avg_Z, avg_Roughness, avg_Intensity, Density, avg_RANGE_3D, avg_Ang_inc and Z_uncertainy.

5. *CeA_colour_maps. m, CeA_Fuzzy.m* to generate the DTMs and uncertainty colour maps.

9.2 Fluvial point clouds classifications

The use of high resolution TLS would therefore be highly beneficial both to provide an effective way of monitoring the evolution of tidal landforms and to provide a detailed and accurate basis for intertidal geomorphic studies. Channels or elevation features occurring over scales smaller than a few meters, in fact, cannot be detected using traditional topographic techniques over the entire marsh scale (size in the order of kilometers) nor through airborne LiDAR data, which are characterized by relatively sparse (as compared to TLS) laser return distributions (in the order of ten returns per square meter, many of which, as seen in the following, are reflected by the canopy rather than by the soil surface) and by a large beam size (with respect to canopy elements sizes) (e.g. Montané and Torres, 2006). The dense and accurate recording of surface points allowed by Terrestrial Laser Scanning (TLS) has recently motivated several research efforts towards the development of automated or semiautomated methods for feature extraction, object recognition and object reconstruction (Guarnieri et al., 2009).

In this section a new tool is presented named “VegFILTER (Vegetation Filter) applied to TLS point cloud. VegFILTER aims at an automatic vegetation point erasing from the raw TLS point cloud.

9.2.1 Projected vegetation filter

Vegetation Filter (VegFILTER) is a Matlab® script that starting from a TLS point cloud is able to extract the ground points.

The program has implemented three internal filters that work in “chain”:

- Colour filter;
- Outlier filter;
- Geometrical filter.

Colour filter

The colour filter is the first one that VegFILTER applies. This filter needs as input a vegetation and a sediment point sampling to define the different colour range of the different materials. Using a vegetation and a sediment text file as calibration points, the code computes the colour distributions for each colour band (R, G and B), for each material: vegetation and sediment (Figure 39). At this stage distribution parameters will be computed: the mean and imposed percentages (e.g. 5th and 95th). These descriptive statistics are used to define the lower and upper colour limits of each colour distribution. For each colour band, the lower and upper limits of the vegetation and the sediment are compared. Different cases can be possible, as reported in Figure 39, and for each of these the applicability of this filter and plausible vegetation band (not overlapped with the sediment band) are defined. The colour filter needs (for an imposed constriction), at least two vegetation colour bands distribution that present a not complete overlap with the correspondent sediment colour bands distribution. In the negative case, this filter cannot be used for a not objective colour separability between the vegetation and the sediment. In this case, or with a very small separability, a re-extraction of the calibration files is suggested.

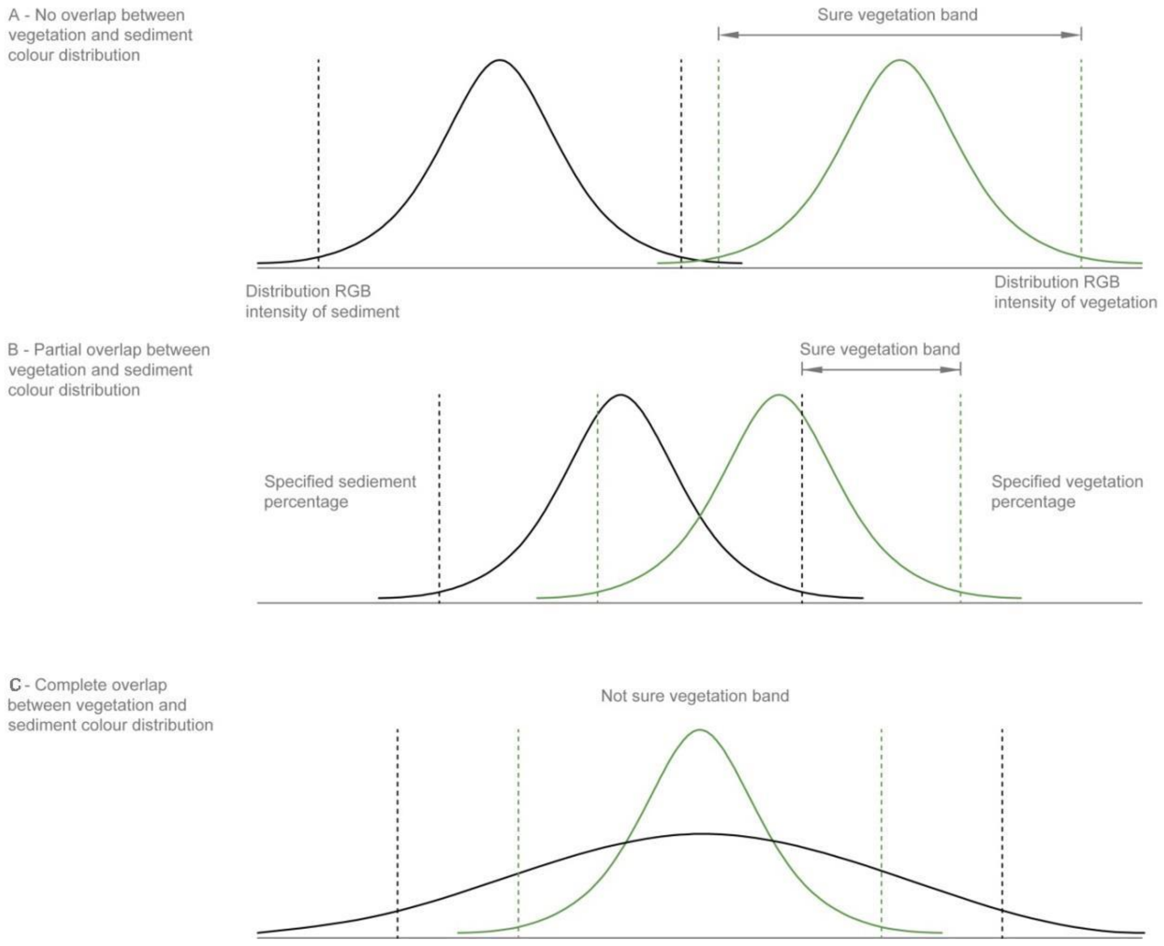

Figure 39. *Overlap checking of vegetation (grey line) and sediments colour function (black line).*

Outlier filter

A points filter to delete the possible “outliers” (Figure 40) outside the range between the 5th and 95th percentiles has been implemented. This filter is the same implemented in the CeA program (see Sub-chapter 9.1.3)

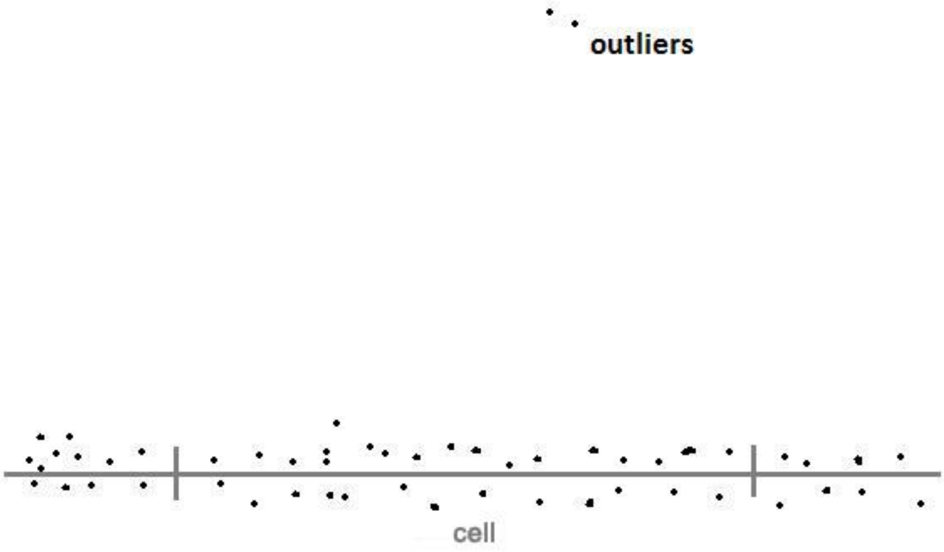

Figure 40. *Cell outliers.*

Geometrical filter

For each cell, four flat surfaces derived from exact interpolation of the average cell elevation, with the corresponding average elevation of the four boundary cells alineated with the axes, were estimated (same principle as the CeA program – sub-chapter 9.1.3). In this case the surface represents a mean low TIN (Triangular Irregular Network), where its “vertexes extension” is in relation to the cell resolution and the vertex elevation is defined by averaging the lowest TLS point inside every cell. The number of the lowest points to average to define each TIN vertex is imposed before running the code. An additional parameter is implemented, that allows in low TIN computing the lowest point (or more) to be excluded.

Four surfaces could be estimated for each cell, and used to estimate the “point delta distances”, derived by subtracting each Z points elevation with its correspondent low TIN elevation (Figure 36). Each distance estimated for each TLS point will be compared with an imposed threshold elevation (“delta distance”). If the delta distance is lower than the point delta distance, the point will be considered vegetation (Figure 41).

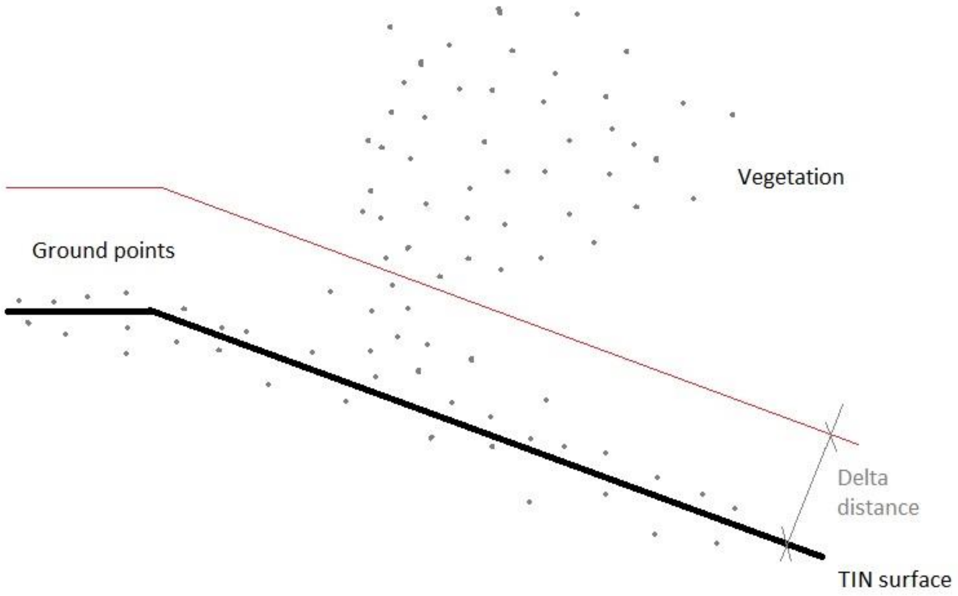

Figure 41. *Geometrical filter.*

This kind of geometrical filter allows to have a better filtering result also in presence of an irregular ground surface. Indeed the low mean surface realized with a TIN, allows the local ground tendency to be followed; in this sense the delta distance will be more representative respect a low mean surface derived from a grid representation (Figure 42).

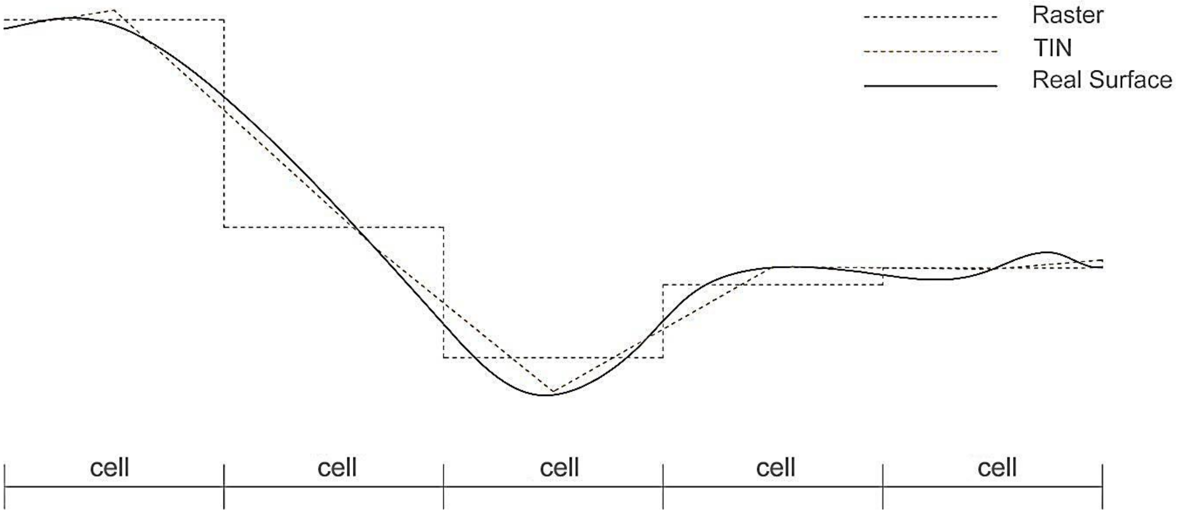

Figure 42. *Raster versus TIN representation of a real surface.*

9.2.2 Proposed vegetation filter work flow

VegFILTER requires a text file as input (in the same folder as the program) with the information: X, Y, Z, Intensity, Red, Green and Blue (bands). To use the colour filter two more text files (X, Y, Z, intensity, R, G and B) of calibration are required. As explained in the sub-chapter above the two files have to be a cloud extraction of a “well-defined” vegetation and sediment TLS point.

The parameters to provide and “play” to reach the best filtering results are:

- *Cell size of analysis:* after a geomorphometrical surface analysis the right cell size should be with the same width of the smallest channel and/or the lateral banks, but generally bigger than the average granulometry (D_{50}). A good cell size definition allows a good geometrical filtering and erroneous ground deleting to be avoided (Figure 35 and 38).
- *Number of points per cell to interpolate as mean low TIN:* joined with the cell size the mean low TIN has “vertexes extension” as a function of the cell resolution and a vertex elevation defined by averaging the lowest TLS point inside every cell. This parameter allows to choose from 1 to 5 points to average as a vertex of the mean low TIN. This parameter uses the indicated number to average the lowest points (inside the cell) and in addition allows some of the lowest points to be excluded from the low TIN computing if required.
- *Delta distance:* is a threshold elevation to compare the difference in elevation between each TLS point with its mean low TIN. If the delta distance is lower than the last one the point will be considered vegetation (Figure 41).
- *Colour calibration files:* these files allow the colour filter calibration. If at least two vegetation colour distributions do not present a complete overlap with the correspondent sediment colour distribution, this filter can work as explained above. The purer the vegetation and sand extraction are (only vegetation or sand/gravel points) the better the separability of the corresponding colour bands will be. If at least two colour bands don't present a complete overlap, this filter can work and be very useful to filter very densely vegetated areas. Indeed, some of these areas cannot be well filtered with the geometrical filter because a lot of cells have no ground points to build a reliable low mean TIN.

As output, VegFILTER provides colour distribution of the calibration files, filtering details (number of filtered points by each filter) and a text file with the ground points extracted.

Section Three

Remote Sensing Analysis

10 Medium Term Fluvial Dynamics of a Regulated Gravel Bed River (Brenta River, Italy)

10.1 Flow regime analysis

The RI of each flood was estimated from the maximum annual values of the mean daily water discharge (Qd) over 79 considered hydrological years. Various functions of the hydrological probability distribution were tested and the Gumbel distribution (OLS) was chosen, due to the best performance of the Kolmogoroff test. The bankfull discharge (RI ~ 1.5 years) was calculated around 350 m^3 s^{-1} ($Q_{1.5}$), which is exceeded 2.4 days per year, and the discharge with RI of 10 years was estimated to about 750 m^3 s^{-1} (Q_{10}). The largest flood event was registered on the 4th of November 1966, with 1330 m^3 s^{-1} as mean daily discharge (RI ~ 200 years).

The flow regime of the Brenta River is characterized by rainfall and snowmelt contributions in spring and by autumn rainfall (Lenzi *et al.*, 2010; Kaless *et al.*, 2011). Also, flood events tend to occur in May, October and November, when more than 50% of all flood events recorded from 1924 to 2011 occurred (Lenzi *et al.*, 2010; Kaless *et al.*, 2011).

Over the last thirty years, four flood events with RI equal or greater than 10 (Figure 43) years were registered (1980, 1996, 2002 and 2010). Two severe flood events occurred in November and December 2010. The first flood, caused by prolonged and extended rainfall , lasted from 31st October to 2nd November 2010, with peak discharge of about 720 m^3 s^{-1} (RI ~ 8 years). The second flood, originated by intense precipitations occurred between 21st and 26th December 2010 and peaked at 759 m^3 s^{-1}.

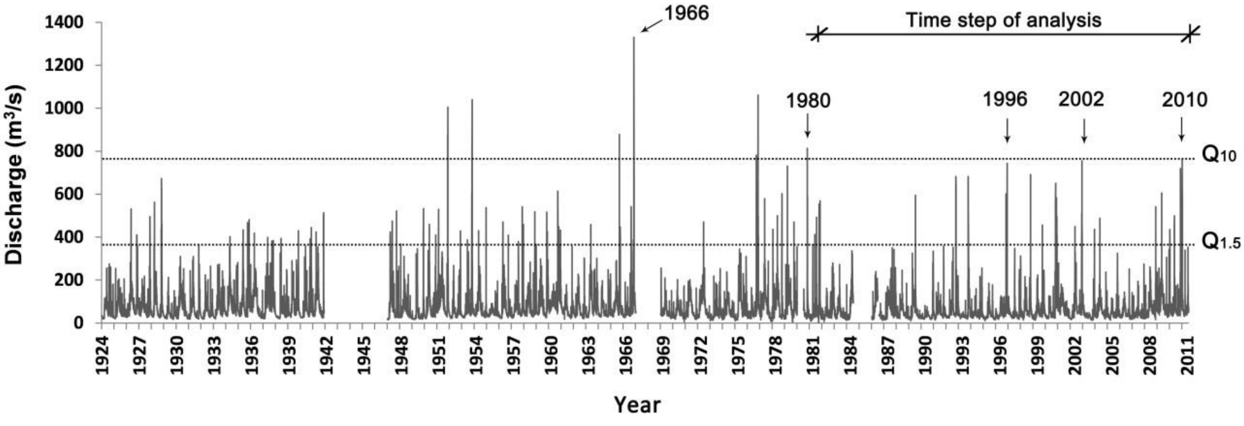

Figure 43. *Water discharges (mean daily) at the Barzizza gauging station (Bassano del Grappa, drainage area = 1567 km^2), from 1924 until June 2011; Flow discharges featuring RI = 1.5 years ($Q_{1.5}$), and RI = 10 years (Q_{10}) are also shown.*

10.2 Bed-level changes along the study reach

The vertical adjustment of the river bed was analyzed using the 10 historical cross-sections measured from 1932 to 2010, along with results coming from LiDAR analysis carried out by Moretto *et al.* (2012a, b; 2013b). If compared with the profile of 1932 (Figure 44) it appears that, as already highlighted by Surian and Cisotto (2007), the river experienced incision up to 5-8 meters except for section 1, where vertical adjustments were lower than -0.35 m.

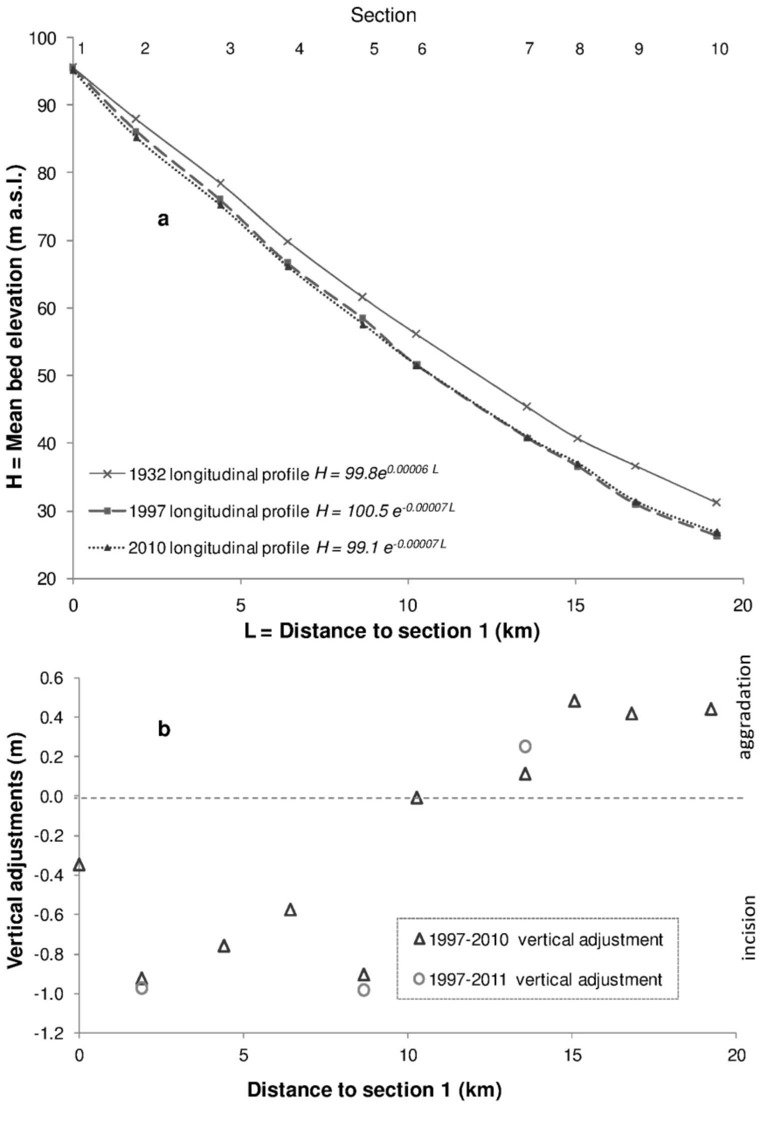

Figure 44. *(a) Longitudinal profiles of the Brenta River from 1932 and 1997 survey (Surian and Cisotto, 2007) and 2010. Best equations (exponentials) of the longitudinal profiles are reported (all three profiles* $r^2 > 0.95$*); (b) variation of average bed elevation as derived from the comparison of cross-sections along the study reach from section 1 to 10 are shown: negative values of vertical adjustments indicate an incision of streambed whereas positive values indicate an aggradation. 2011 sections are derived from LiDAR survey (Moretto et al., 2012a, b) and are available only for sections 2, 5, and 7.*

Instead, over the last 13 years (1997-2010), the river bed experienced a general incision of around 0.2 m. However, significant differences in vertical adjustments appear along the reach. In fact, in the upstream portion of the study reach, from section 1 to 5, average vertical adjustments of the active-channel during the last thirteen years range from -0.35 m (section 1) to -0.92 m (section 2), with an average of -0.7 m (average level of the active channel).

If the talweg line is considered (table 2), the largest incision of the river is equal to 1.78 m in correspondence of section 1. The middle portion of the study reach seems to be in an equilibrium condition since a vertical variation of only -0.01 m and 0.11 m occurred on section 6 and 7, respectively. Conversely, the lower portion of the study reach has been aggrading from 1997 to 2010, since the mean level of the last three historical sections (8, 9, and 10) has raised between 0.42 m and 0.48 m. The largest aggradation of the river along the talweg (table 3) in the period 1997-2010 was reached by section 7 with 0.69 m. The channel slope of the whole study reach remained virtually constant from 1997 to 2010, passing from 0.0036 m m^{-1} to 0.00356 m m^{-1} with a relative variation of only 1%.

Table 3. *Temporal variation of the active channel (AC) width (m) and the talweg (Tw) elevation (m a.s.l.) in the cross-sections (CS). It 'also shows the lateral (ΔAC) and vertical adjustments (ΔTw).*

	1923		1997		2010		1997-1923		2010-1997	
	AC (m)	Tw (m a.s.l.)	AC (m)	Tw (m a.s.l.)	AC (m)	Tw (m a.s.l.)	ΔAC (m)	ΔTw (m)	ΔAC (m)	ΔTw (m)
CS 1	248	91.6	87	92.2	90	90.4	-161	0.6	3	-1.8
CS 2	401	85.1	158	83.9	230	82.6	-243	-1.2	72	-1.3
CS 3	838	75.1	427	73.3	572	72.6	-411	-1.8	145	-0.7
CS 4	699	67.6	413	63.8	506	63.4	-286	-3.8	93	-0.4
CS 5	409	59.8	263	56.0	310	55.0	-146	-3.8	47	-1.0
CS 6	541	54.6	514	50.0	520	49.1	-27	-4.6	6	-0.9
CS 7	752	43.9	479	37.6	480	38.3	-273	-6.3	1	0.7
CS 8	303	37.9	258	33.6	242	33.4	-45	-4.3	-16	-0.2
CS 9	744	34.7	482	24.6	477	24.8	-262	-10.1	-5	0.2
CS 10	409	29.9	359	22.1	361	22.1	-50	-7.8	2	0.0

The analysis of the cross-sections derived from the 2011 LiDAR survey (Moretto *et al.*, *2012a, b; 2013b*) confirmed the vertical adjustment trends from 1997 to 2010 (Figure 44). The mean elevation of sections 2 and 5 experienced a further reduction (5 and 8 cm, respectively), and section 7 increased its elevation of 14 cm, if compared to 2010. However, it should be noted that the 2011 cross-sections could be affected by a greater error in respect to those of 2010 since they are derived from the LiDAR survey. In Figure 45, sections 2, 5, and 7 (as representative of the upper, middle and down-stream part of the study reach) are shown, and the horizontal line represents the bankfull level as surveyed in the field in 2010. Incision and narrowing tendencies are evident in the three cross-sections. In section 5 (Figure 45b), the main channel shifted progressively leftwards and reached the main embankment. A different behavior in the lower portion of the reach is evidenced by the fact that section 7 (Figure 45c) remained fairly unchanged over the last 13 years.

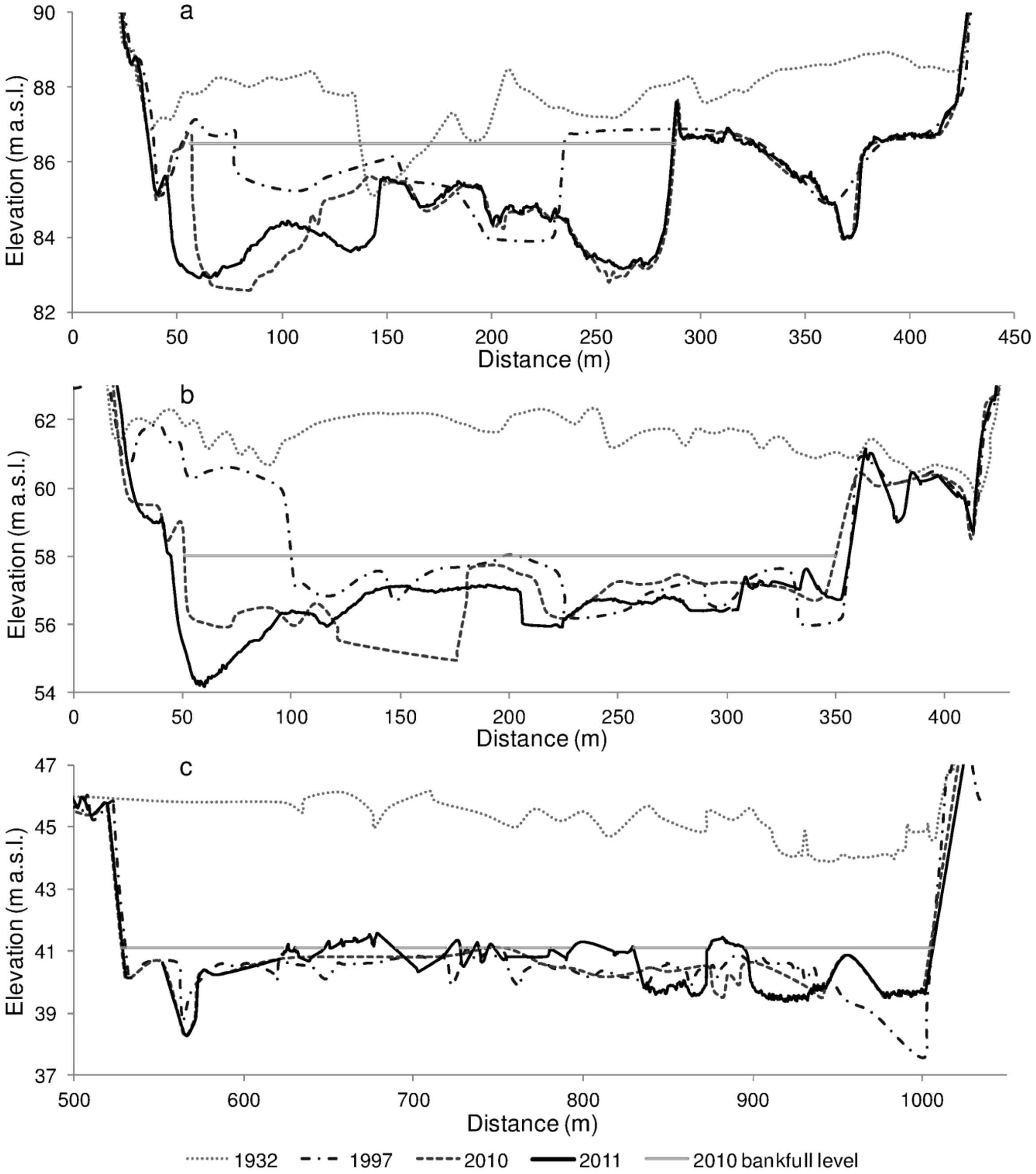

Figure 45. *Evolution of historical cross sections 2, 5, and 7 for the years 1932, 1997, 2010, and 2011. The horizontal line represents the bankfull stage for the sections measured in 2010.*

10.3 Changes of active channel area and width along the study reach

The analysis of the extent of active channel conducted by using aerial photos has confirmed remarkable fluctuations during the last 30 years (Figure 46). Five significant periods characterized by different dynamics of active channel changes could be identified: 1981-1990, 1990-2003, 2003-2008, 2008-2010 and 2010-2011. The first and third periods are characterized by a decrease of active channel surface (-148 ha and -70 ha, respectively), whereas the second, the fourth, and the fifth periods are characterized by an increase of the active channel surface (135 ha, 10 ha and 41 ha, respectively).

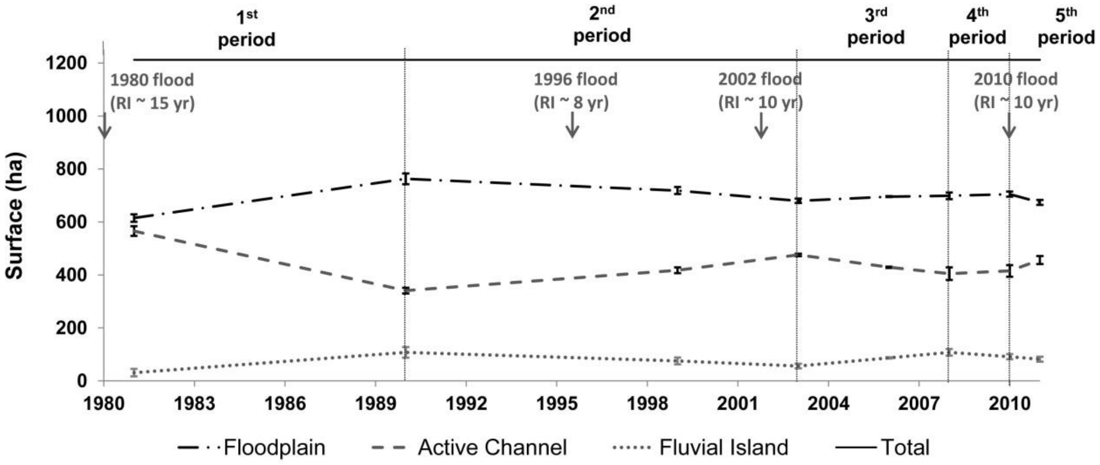

Figure 46. *Temporal variation with error bars of the surface of the active channel, floodplain and islands in the analyzed reach of Brenta River.*

Figure 47 depicts the longitudinal variation of active channel width within the 5 identified periods of different morphological behavior. The average values of channel width for the entire analyzed reach in 1981, 1990, 1999, 2003, 2006, 2008, 2010 and 2011 have respectively the following values: 266, 181, 197, 226, 225, 200, 196 and 215 m. During the first nine years of the analyzed period (1981-1990), the average active channel width decreased from 266 m to 181 m (9.44 m year^{-1}). The active channel narrowing seems to have occurred along the whole river reach, except for a rather marked enlargement occurred near the 7th section (Figure 47). In the period 1990-2003 there was an inverse tendency, characterized by an increase of the average width, up to 16 m (from 1990 to 1999, at the rate of 1.78 m year^{-1}) and then of a further 29 m from 1999 to 2003 (7.25 m year^{-1}). The average widening trend was not uniformly distributed along the reach, but appears to be more concentrated between the fourth and thirteenth km. In the most recent years (2003-2008) the active channel width reduced again from 226 m to 200 m (5.2 m year^{-1}). This average trend is mainly due to intense localized narrowing processes occurred around the thirteenth km, while in the rest of the channel the width remained fairly constant. During the period 2008-2010, there was a slight narrowing concentrated at about the thirteenth and eighteenth km along the studied reach from 200 m to 196 m (2 m year^{-1}), followed by a very recent enlargement phase between 2010 and 2011 from 196 m to 215 m, respectively, with a rate equal to 19 m year^{-1} which is the largest variation registered in the last thirty years. Overall, the active channel width reduced by 51 m from 1981 to 2011, even if different temporal trends are observed during the studied period and along the reach. It is worth noticing the effect of November and December 2010 floods (RI = 8 and 10 years, Lenzi *et al.,* 2010), which caused channel widening fairly distributed along the whole reach (Figure 47).

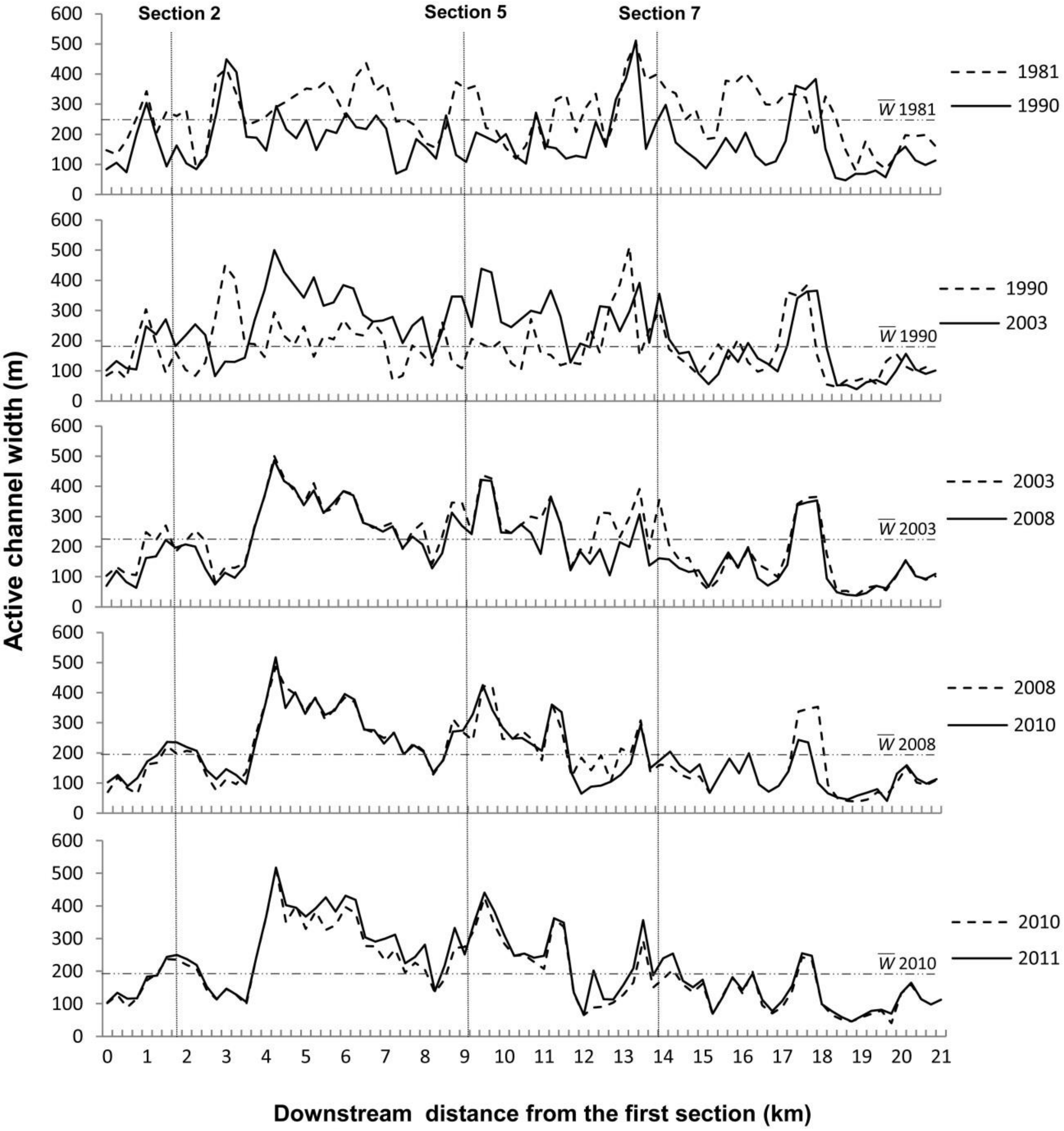

Figure 47. *Active channel evolution over the last 30 years divided in five significant periods characterized by different morphological trends.*

10.4 Changes of islands area and width along the study reach

The extension of islands within the entire reach (Figure 46 and 48) was calculated, as for the active channel area, by photo-interpretation from the historical series of aerial photos from 1981 to 2011. Changes in island area reflect the trend of the active channel area (Figure 46) but it is not uniform along the whole reach (Figure 48).

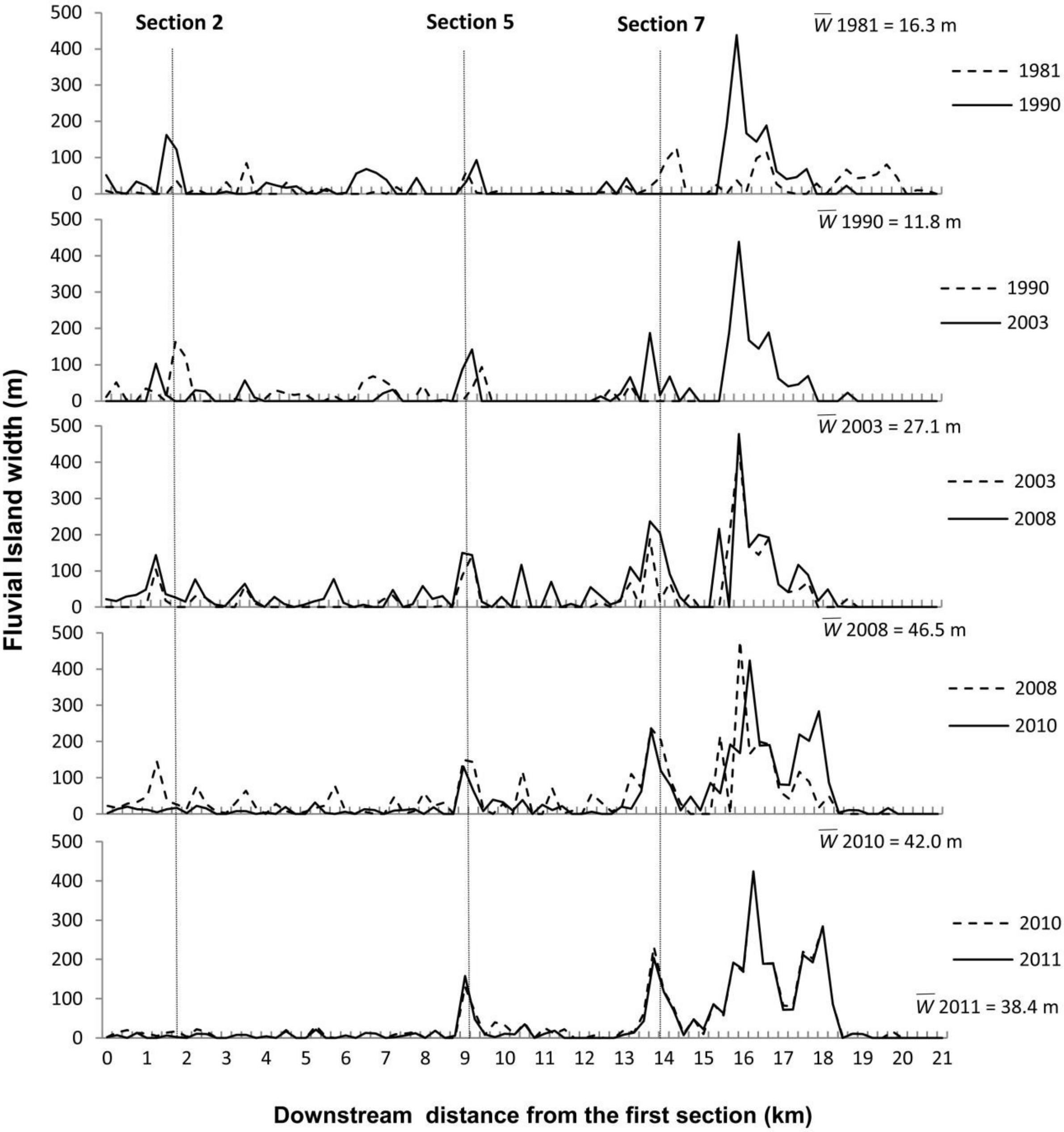

Figure 48. *Fluvial island evolution over the last 30 years divided in five significant periods characterized by different morphological trends of active channel.*

The first phase from 1981 to 1990 is characterized by an increase of 77 ha of islands and a decrease of the active channel. This appears to be more concentrated around sections 2 and 5 and below section 7. The second phase from 1990 to 2003 is characterized by 14 over-bankfull floods (with one > 10 years RI in 2002), and features a marked decrease of islands area (-52 ha). Afterwards, due to the lack of high-magnitude floods from 2003 to 2008, the areal extent of islands increased (52 ha), being this expansion relatively uniform in whole reach. The phase from 2008 to 2010 is characterized by a reduction of 17 ha of islands area, bringing the overall distribution of them in a similar situation as in 2003. The only exception is for a new relevant island area between the 17th and 18th km from section 1 (Figure 48 - 2008 *vs.* 2010). Subsequently, another decrease phase of about 10 ha from 2010 to 2011, more marked from the beginning of the study reach to the 7th cross-section.

Major island extension values (108 ha in 1990 and in 2008) are associated with the major narrowing of the active channel (341 ha in 1990 and 405 ha in 2008). On the opposite, the minimum islands extension coincides with the maximum extent of the active area (1981), equal to 51% of the entire area of the river corridor.

11 Erosion Deposition Analysis on Gravel Bed Rivers (Brenta, Piave and Tagliamento River, Italy)

11.1 Colour bathymetry, HDTMs and Principal Erosion Deposition Analysis of Brenta River

11.1.1 Colour bathymetry models

To understand the variability and the average depth of the channel, before calibrating the model regression, the average, the standard deviation and the maximum depth of 2010 and 2011 wet channels were estimated. 2010 was characterized by an average depth of 0.53 m, a standard deviation of 0.34 m and a maximum known depth of 1.62 m. 2011 was characterized by an average depth higher than 2010 and equal to 0.63 m, a standard deviation of 0.28 m and a maximum known depth of 1.63 m.

The research of the best depth-colour model has started by testing a physical model, based on the Beer Lambert law (equation 1) for each year (2010 and 2011) and with the two statistical regression methods (traditional regression and AICc index; Section 8.1.3).

The application of the traditional regression method and the AICc index have produced the same depth colour model for the 2010:

$$DPH = -0.119 + 2.725 \ln(R/G) \tag{14}$$

Where DPH is the water depth and ln(R/G) are the colour bands arranged according to the Beer Lambert law.

This model have a statistical significative p-value << 0.05, r^2 equal to 0.34 and an average error derived from the test points equal to ± 0.27 m.

A similar result was obtained in 2011 model, also in this case the two statistical regression methods have produced the same result:

$$DPH = -0.73 + 2.043 \ln(R/G) \tag{15}$$

This model have a statistical significative p-value << 0.05, r^2 equal to 0.25 and an average error derived from the test points equal to ± 0.20 m.

The *depth-colour (RGB)* statistical regressions performed in the empirical model with the two different approaches allowed to obtain two bathymetric models for each year (2010 and 2011). The average errors, detected in the two models by comparing the test points of 2010, are equal to ± 0.26 m and have highlighted negligible differences accounting for the same magnitude of the estimation errors (0.003 m of difference of average error). Therefore, the model resulting from the traditional method (reported below; with verified p-value) was preferred because of its simpler structure with fewer factors if compared to the AICc model:

$$\begin{aligned} DPH &= 5.31 + 0.07513\,R - 0.1869\,G - 0.01475\,B - 0.0004582\,RB \\ &+ 0.001056\,G^2 + 0.0003352\,B^2 - 0.000002142\,G^3 \end{aligned} \tag{16}$$

Where *DPH* is the estimated water depth and R, G, and B are the red, green and blue bands, respectively. The model presents an r^2 equal to 0.46, 12 percentage points more than the 2010 physical model.

In 2011, on the other hand, the two different methodologies (traditional and AICc index) of statistical regression have generated the same model:

$$\begin{aligned} DPH &= -0.607 + 0.03508\,R - 0.06376\,G - 0.1377\,B + 0.002257\,RG - 0.001096\,RB + 0.002303\,GB \\ &- 0.0007273\,R^2 - 0.002956\,G^2 + 0.0009993\,B^2 + 0.000002837\,G^3 - 0.00000685\,B^3 \end{aligned} \tag{17}$$

In this case, r^2 is equal to 38 %, 13 percentage points more than the physical model, whereas the estimated depth average error, resulting by the test points, accounts for ± 0.19 m. Both models, proved to be statistically significant ($p\text{-value} << 0.05$), but the empirical models seem to have more predictive capacity than the physical models. In addition, all the three colour bands significantly contribute to depth estimation and the presence of interactions between the colour bands as reported in Figure 49 should be taken into consideration (as done in the empirical models) in the used models.

Therefore, we have decided to use the empirical models because, despite the similar average errors on the test points, they feature a more predictive capacity than the physicals and they take into consideration also the interactions (correlations) between the colour bands.

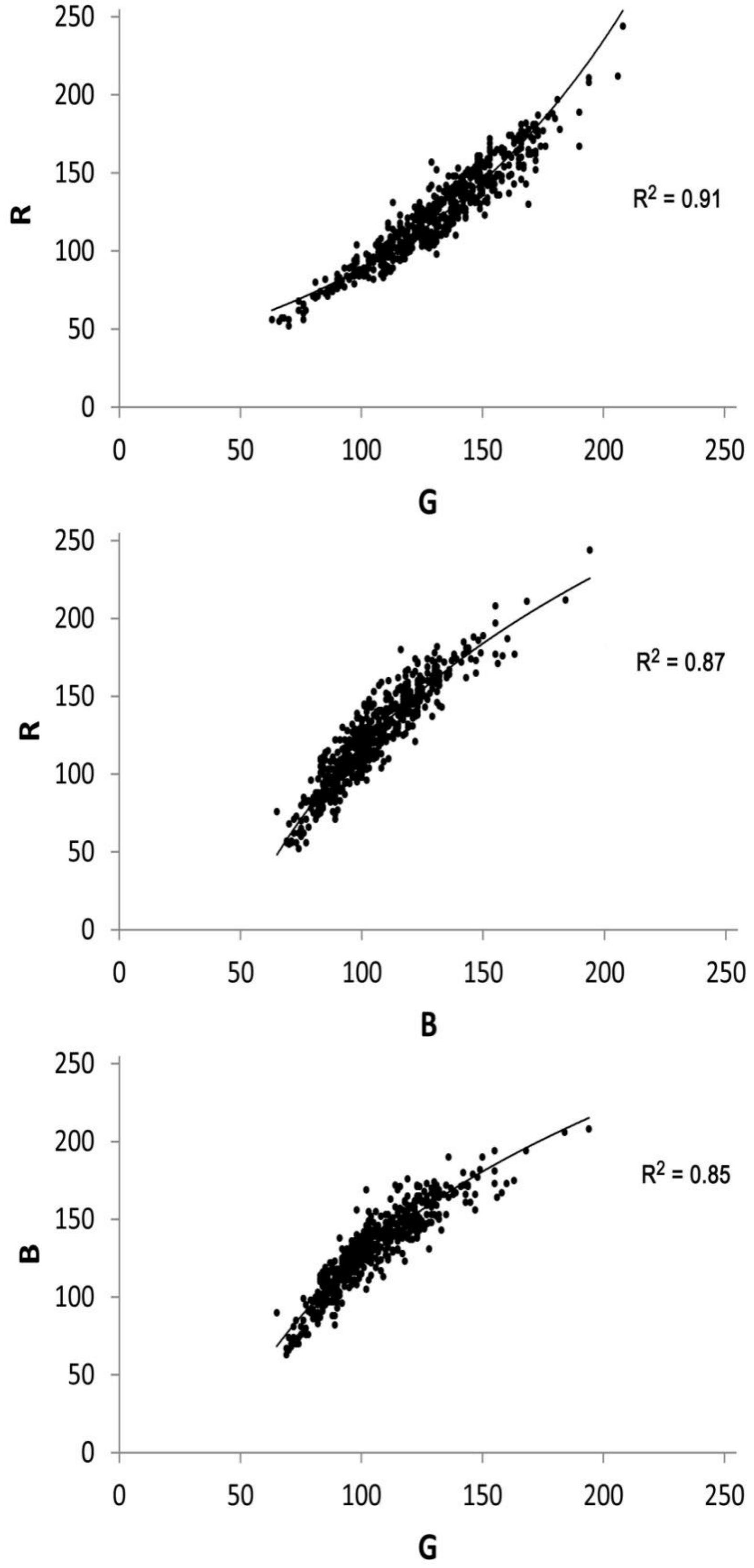

Figure 49. *Correlation between Red, Green and Blue colour bands.*

Figure 50 shows one of the outputs deriving from the model application (Eq. 17) at the Friola sub-reach. It appears that depth variations are generally respected, and variations in the colour tone, due for example to the presence of periphyton in these areas joined to lower flow velocity, do not seem to strongly influence the estimation of water depth. In this sub-reach, the maximum estimated depth from the models is up to 2 m.

Is important to note that the model error reported above was evaluated comparing the test points, the 20 % of the dataset that we have not used for the statistical regressions. Therefore this is not the final error, indeed in the next paragraph have been describing the effects of the filters (as described in 8.1.4 paragraph) to delete the major part of these errors.

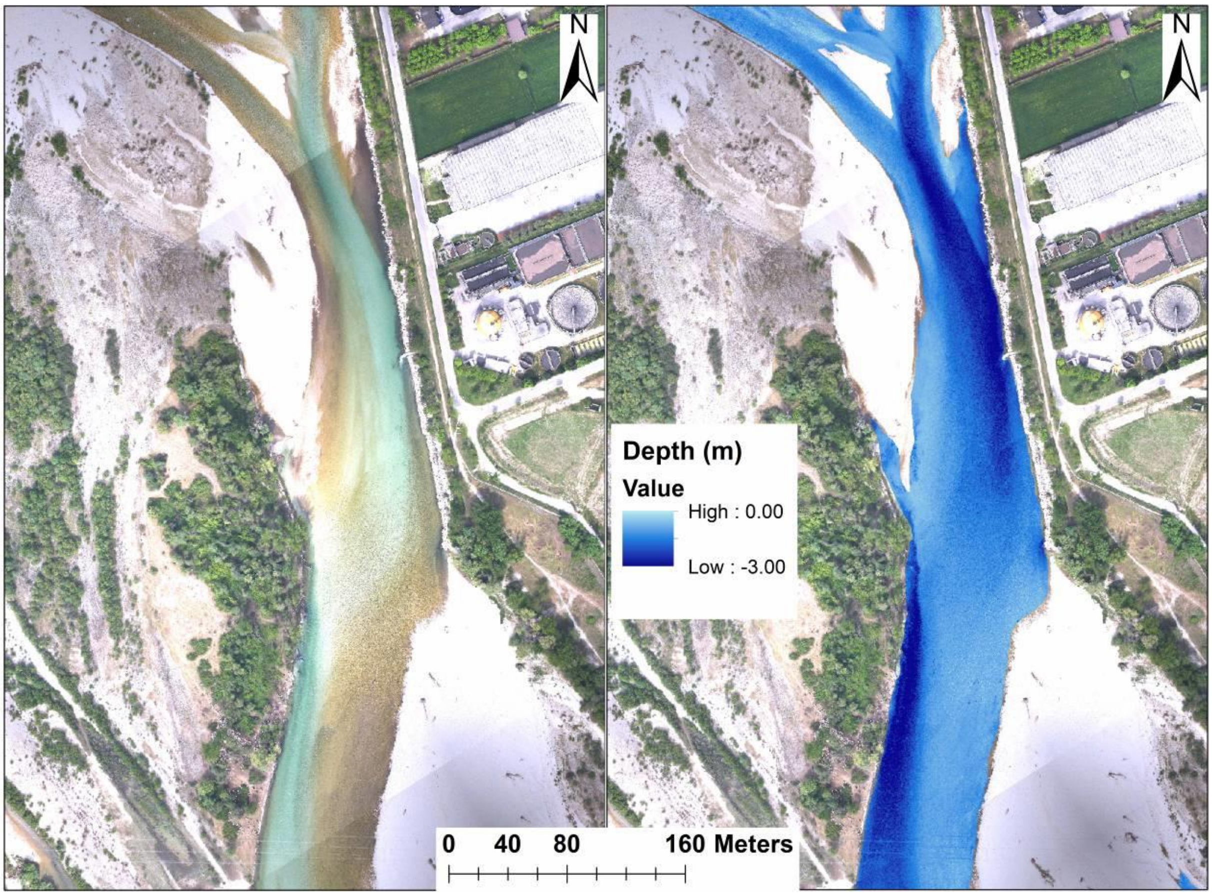

Figure 50. *Model application (2) at Friola sub-reach (2011). The brown zones on the left side are due to the presence of periphyton at the channel bottom.*

11.1.2 HDTM production and validation

After filtering raw depth points deemed wrong due to the model application on the altered pixel colour value (caused by river bed colour, turbulence, light reflections, shadows, suspended load, exposed sediment), dry areas were integrated using the LiDAR flight. The LiDAR points cloud (excluding wet areas) featured an average density equal to 2.07 points/m^2 for 2010 and 2.64 points/m^2 for 2011; the final HDTMs were generated using a 0.5 x 0.5 m cell size. The final HDTMs, three for 2010 and other three for 2011 (Nove, Friola and

Fontaniva sub-reaches) are reported in Figure 51. It is worth noting the accuracy in the bed-forms definition (riffle and pool) within the wet channels estimated through the bathymetric process.

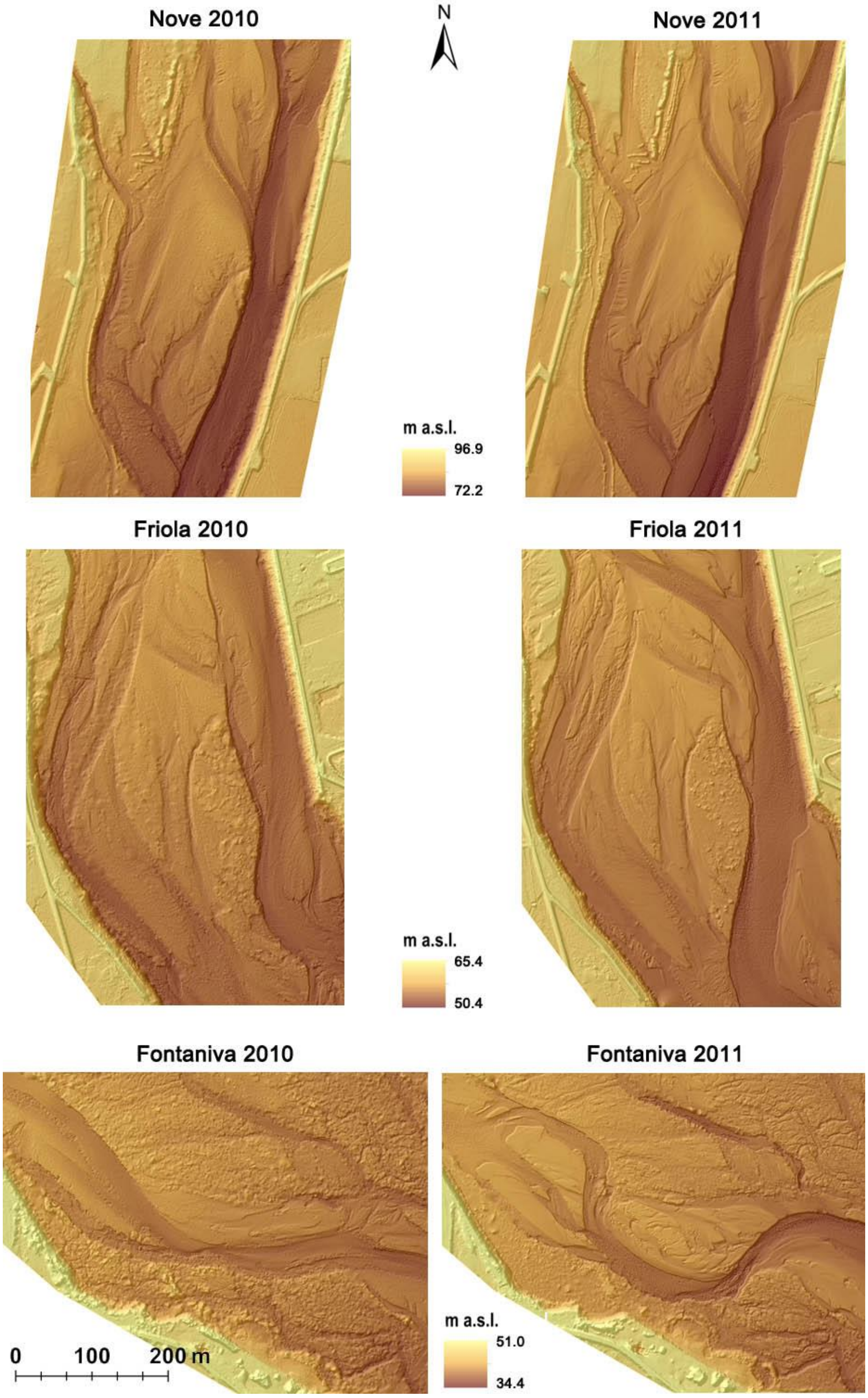

Figure 51. *Hybrid Digital Terrain Models (HDTM) of Nove, Friola and Fontaniva sub-reaches 2010 and 2011. 0.5 x 0.5 m of cell size.*

The data validation (Table 4) was carried out separately for both wet and dry areas, obtaining average uncertainty values (by field survey comparison) for each HDTM which include dGPS, LiDAR and DPH estimated errors.

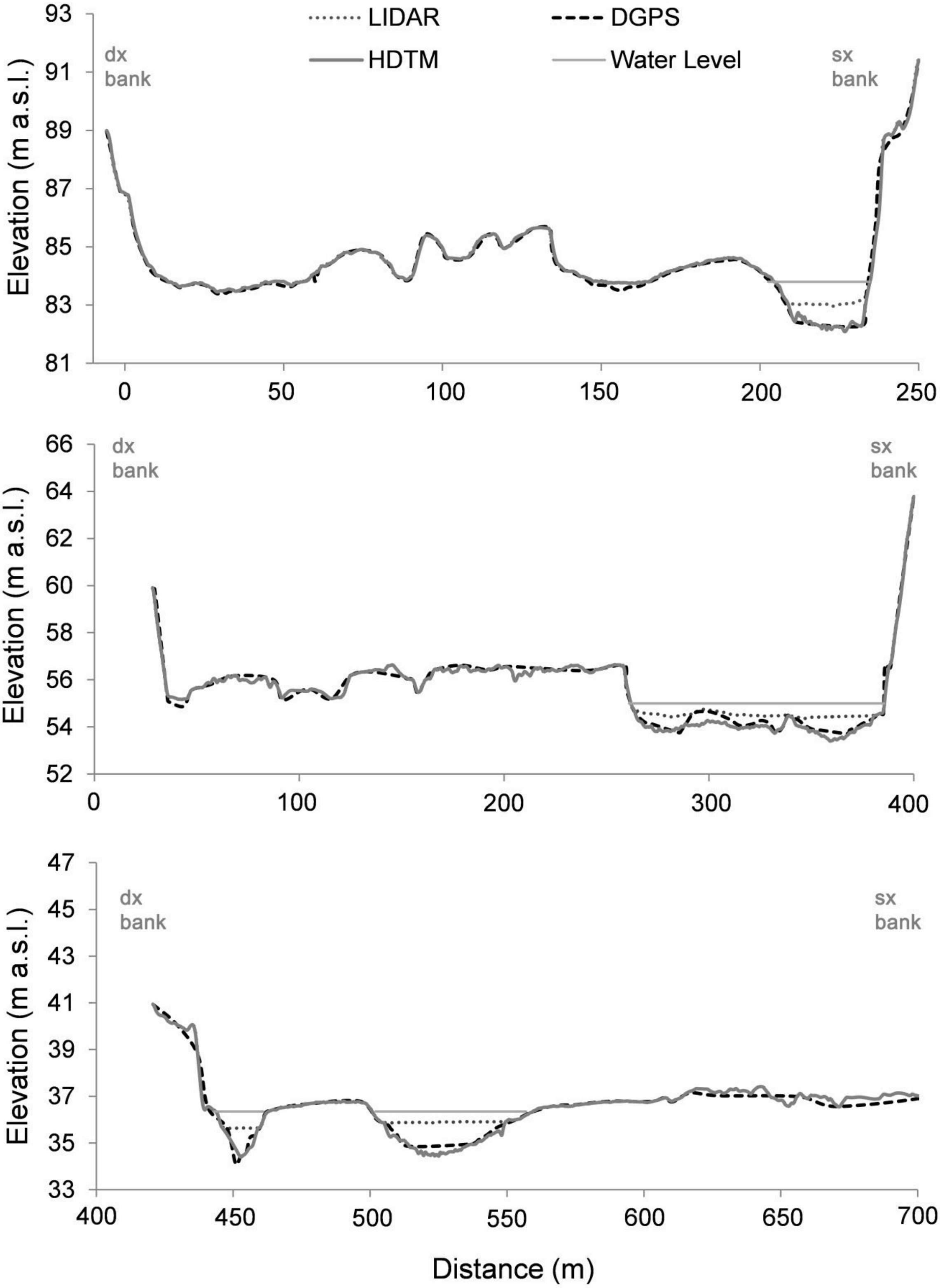

Figure 52. *Cross-section comparison between dGPS, HDTM and LiDAR profile on Nove (a), Friola (b) and Fontaniva (c) 2011.*

The average uncertainty associated to wet areas accounts from a minimum of ± 0.19 m (Friola 2011) to a maximum of ± 0.26 m (Nove - Fontaniva 2010 and 2011), whereas in the dry areas the average uncertainty ranges from a minimum of ± 0.14 m (Nove 2010) to a maximum of ± 0.26 m (Fontaniva 2010). The chosen colour bathymetric models (empirical depth-RGB) have generated similar error levels both for 2010 and for 2011. Moreover, the average weighted uncertainty was calculated in the final HDTMs, that is it ranges from ± 0.16 m (Nove 2010 – 2011 and Friola 2011) to ± 0.26 m (Fontaniva 2010).

The last phase of the HDTM production process consists in the model validation with dGPS cross-sections. Figure 52 shows an example of comparison of three cross-sections on 2011, obtained with three different types of data (dGPS survey, LiDAR, and HDTM). The section reference is the dGPS, in which the measured points have an average error of about 0.025 m. The main topographical variations result faithfully reproduced, except for the thalweg, which was impossible to detect with dGPS survey. Comparing dGPS and LiDAR profiles, the inability of LiDAR signal to penetrate the wet areas of more than 20 cm was confirmed (with consequent underestimation of calculated volumes). Instead, comparing dGPS and HDTM profiles, it appears that, overall, the ground points are fairly well replicated**.**

Table 4. *Estimated uncertainty for HDTM and for DoD models.*

		NOVE		FRIOLA		FONTANIVA	
		2010	2011	2010	2011	2010	2011
HDTM area	(m^2)	566916	566916	836967	836967	627049	627049
Wet area	(m^2)	76463	76526	108265	119497	75545	97407
Wet area/HDTM area		0.13	0.13	0.13	0.14	0.12	0.16
N° dGPS point for test DTM_{BTH}		192	408	279	821	204	283
Average uncertainty DTM_{BTH} + dGPS	(m)	0.26	0.26	0.25	0.19	0.26	0.26
N° dGPS point for test DTM_{LD}		72	132	98	155	53	64
Average uncertainty DTM_{LD} + dGPS	(m)	0.14	0.15	0.24	0.15	0.26	0.16
TOTAL average uncertainty	(m)	0.16	0.16	0.24	0.16	0.26	0.17
Volume loss without colur bathymetry	(m^3)	917559	529812	1206848	397470	4386814	4743783

DTM_{BTH}: Part of Digital Elevation Model derived by Bathymetry; DTM_{LD}: Part of Digital Elevation Model derived by Light Detection And Ranging; dGPS: Differential Global Positioning System.

11.1.3 Morphological change detection using PrEDA

Nove sub-reach

Starting from the depurated DoD (from the erroneous areas – Figure 53) using the Wheathon et al. (2010) methodology we can observe the effects of the November and December 2010 floods on Nove sub-reach (Brenta River). From a general point of view the erosion process in this reach is predominant and equal to 122 498 m^3, whereas the deposition process is 18 416 m^3.

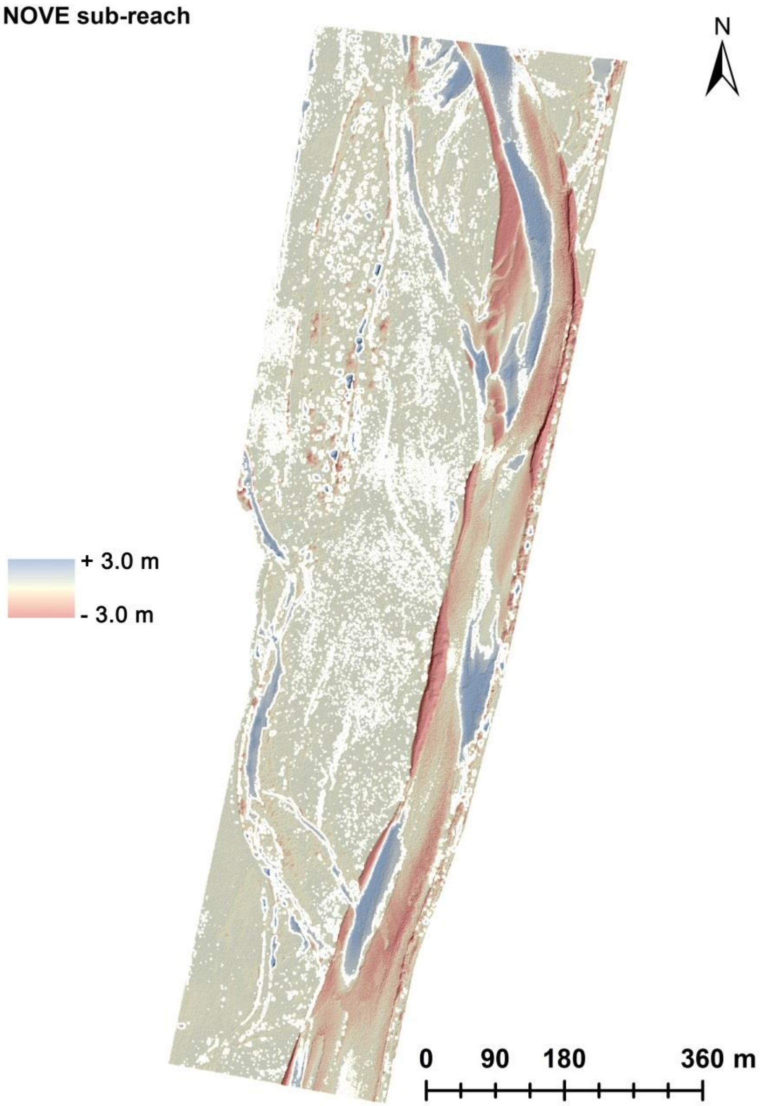

Figure 53. *Depured difference of DEMs (DoD) of Nove sub-reach.*

Thanks to the developed PrEDA tool we can analyze the distribution of these two volumes more deeply. Figure 54 shows different PrEDA applications. Erosion and deposition patches from 50 m^2, 100 m^2, 200 m^2, 500 and 1000 m^2 of threshold area with ± 0.20 m, ± 0.50 m and ± 1.00 m of depth of change were extracted. The figure shows the two extremes of these extractions, while Figure 55 shows the associated surface and the volume for each patch with the most significant variation (> 1000 m^2 and > ± 1.00 m of depth for each patch).

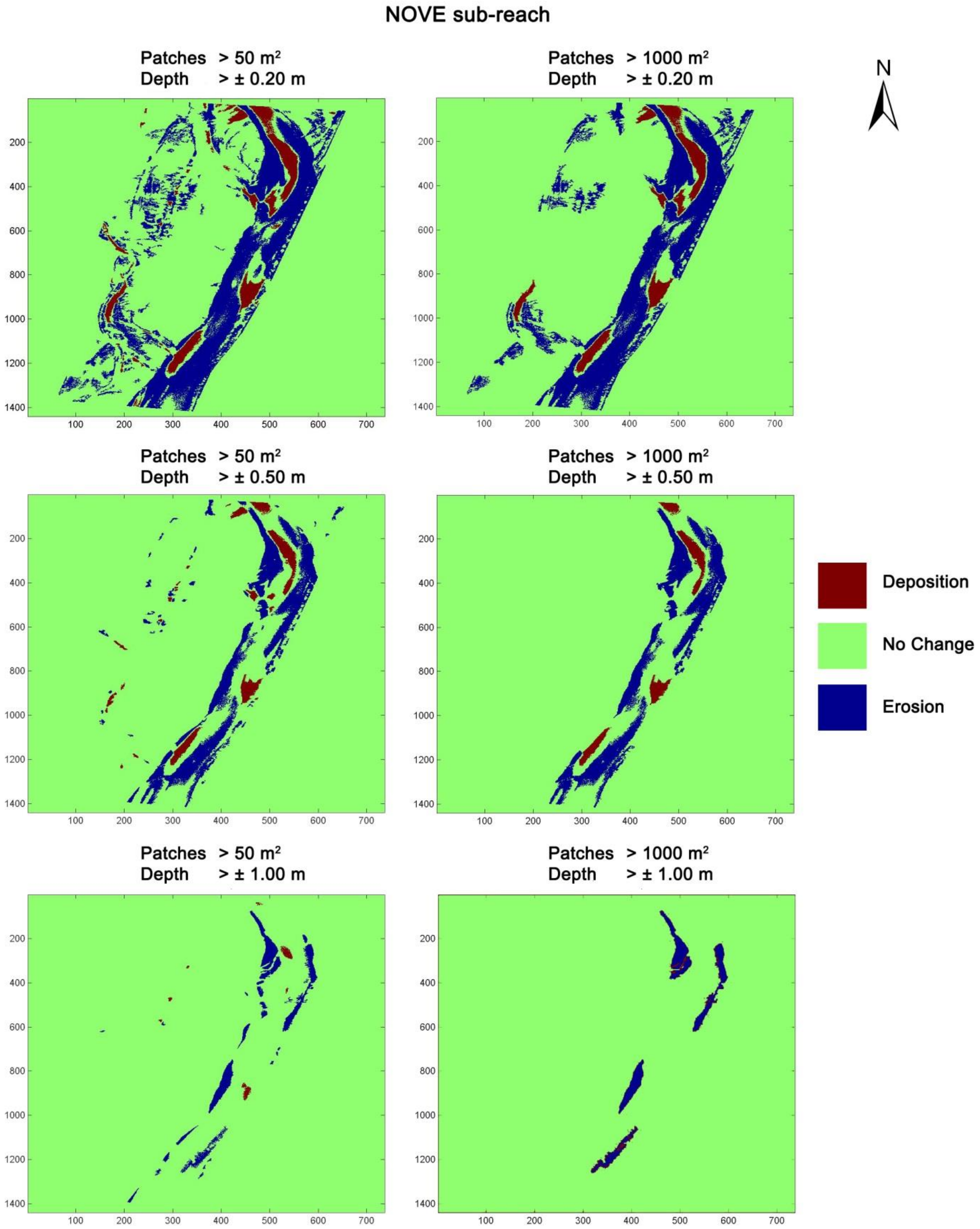

Figure 54. *Principal erosion-deposition extraction by PrEDA of Nove sub-reach. Different minimum threshold of surface and depth of erosion or deposition characterizes the different sub-figures.*

The reach shows that the majority of the erosions and depositions are located along the main channel. The deposition does not reach significant patches with more than 0.50 m of deposited material and it is mainly dislocated on 4 patches (> 1000 m^2 and > ± 0.50 m). The erosion process has a continuous layer along the main channel with at least 0.20 – 0.50 m depth of material eroded. The most significant erosion (> 1000 m^2 and > ± 1.00 m) is represented with 5 patches. Analysing Figure 55 we can note that patches 1, 2 and 4 have a ratio surface/volume around 1:1 – 1:1.2 while the 3rd and the 5th have a ratio around 1:2, this means that each 1 m^2 of erosion corresponds meanly to 2 m depth.

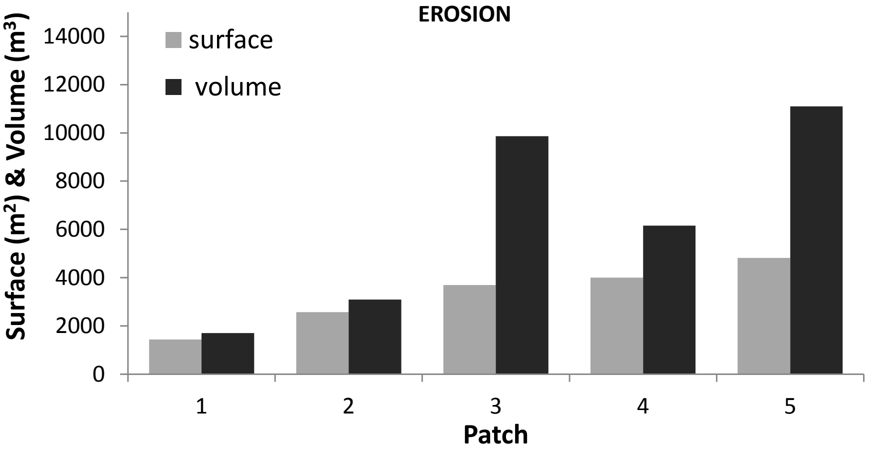

Figure 55. *Surface and volume of erosion (> 1000 m2 and > ± 1.00 m) among the different patches of Nove sub-reach.*

Friola sub-reach

Figure 56 shows the effects of the November and December 2010 floods on Friola sub-reach (Brenta River). From a general point of view the erosion and deposition process is more balanced than Nove and equal to 177 951 m^3 and 95 030 m^3 respectively. In this case the allocation of the changes seems to be developed more in a multichannel form, probably favoured by a wider active channel.

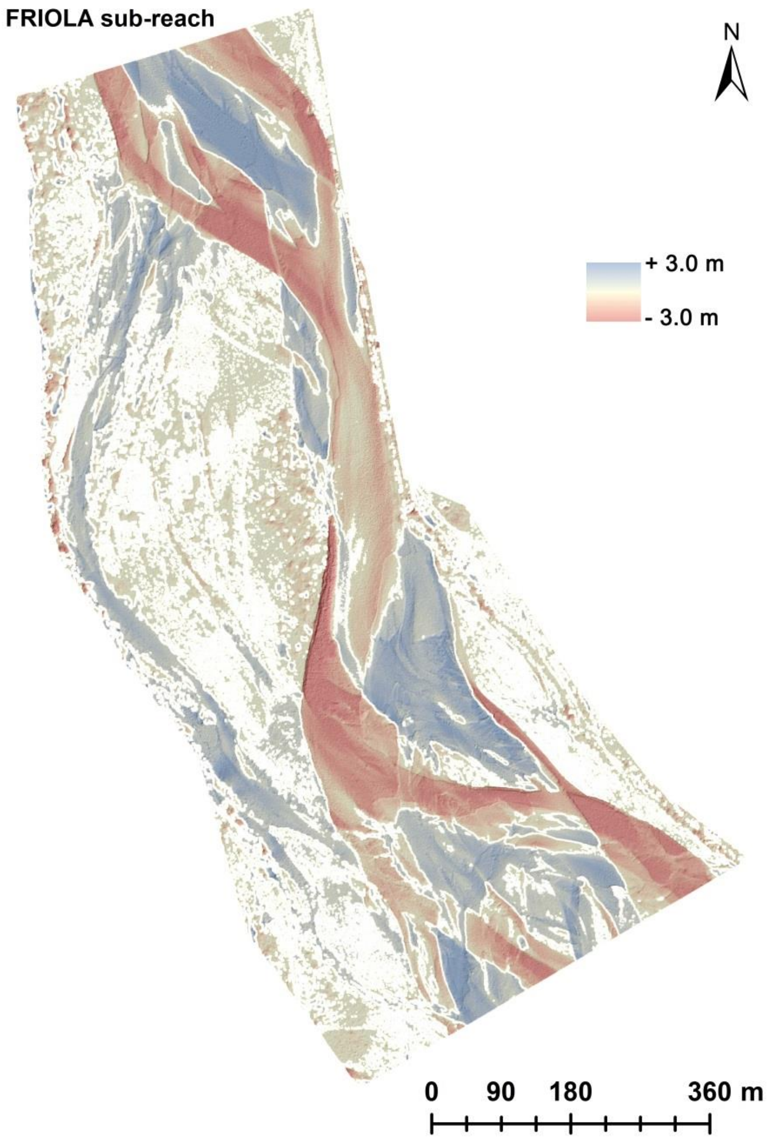

Figure 56. *Depured difference of DEMs (DoD) of Friola sub-reach.*

Thanks to the developed PrEDA tool we can analyse the distribution of these two volumes more deeply. Figure 57 shows different applications of PrEDA. Erosion and deposition patches from 50 m^2, 100 m^2, 200 m^2, 500 and 1000 m^2 of threshold area with ± 0.20 m, ± 0.50 m and ± 1.00 m of depth of change were extracted. Figure 57 shows the two extremes of the patches extracted at different depths, while Figure 58 show the associated surface and volume for each patch with the most significant variation (> 1000 m^2 and > ± 1.00 m of depth for each patch).

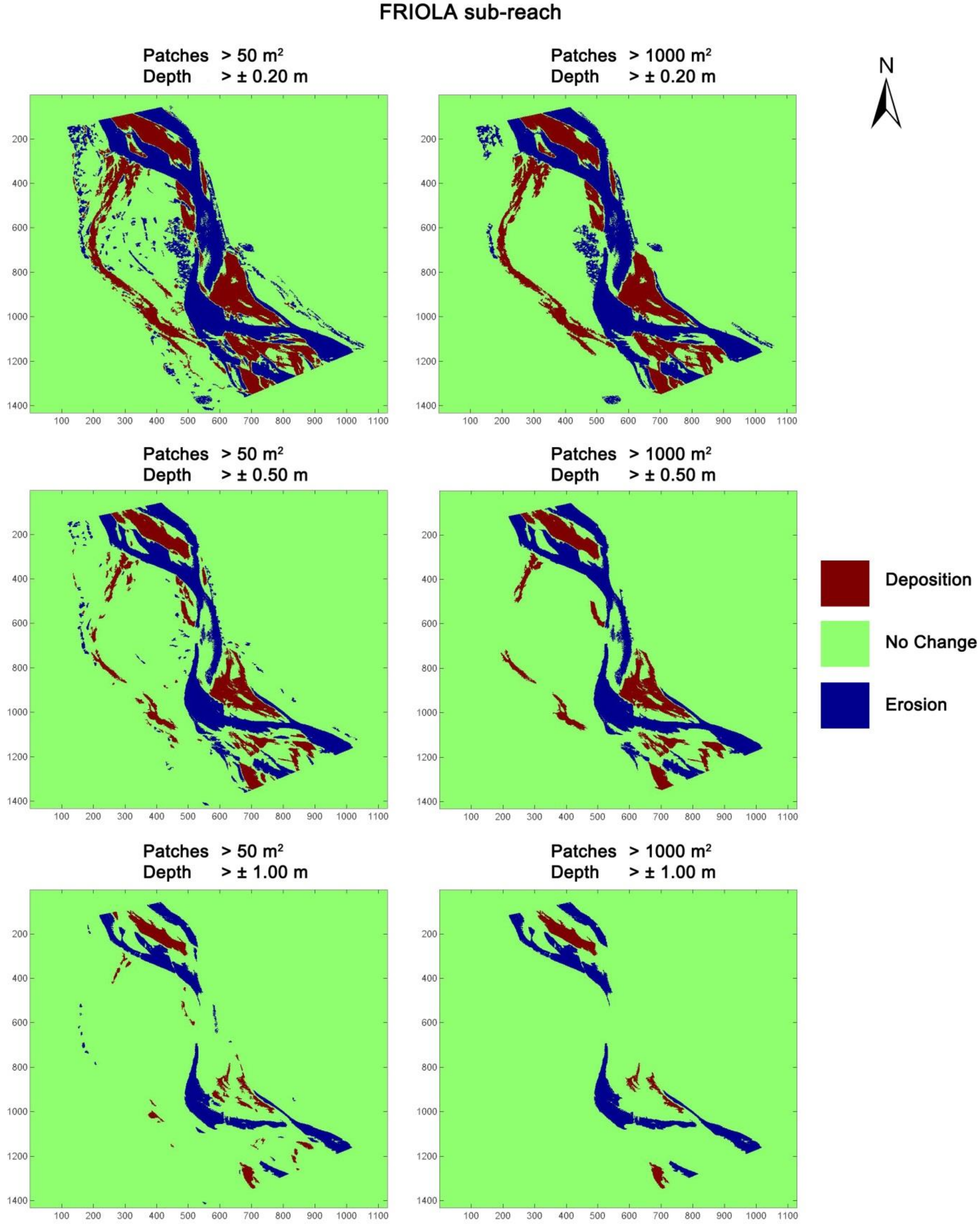

Figure 57. *Principal erosion-deposition extraction by PrEDA of Friola sub-reach. Different minimum threshold of surface and depth of erosion or deposition characterizes the different sub-figures.*

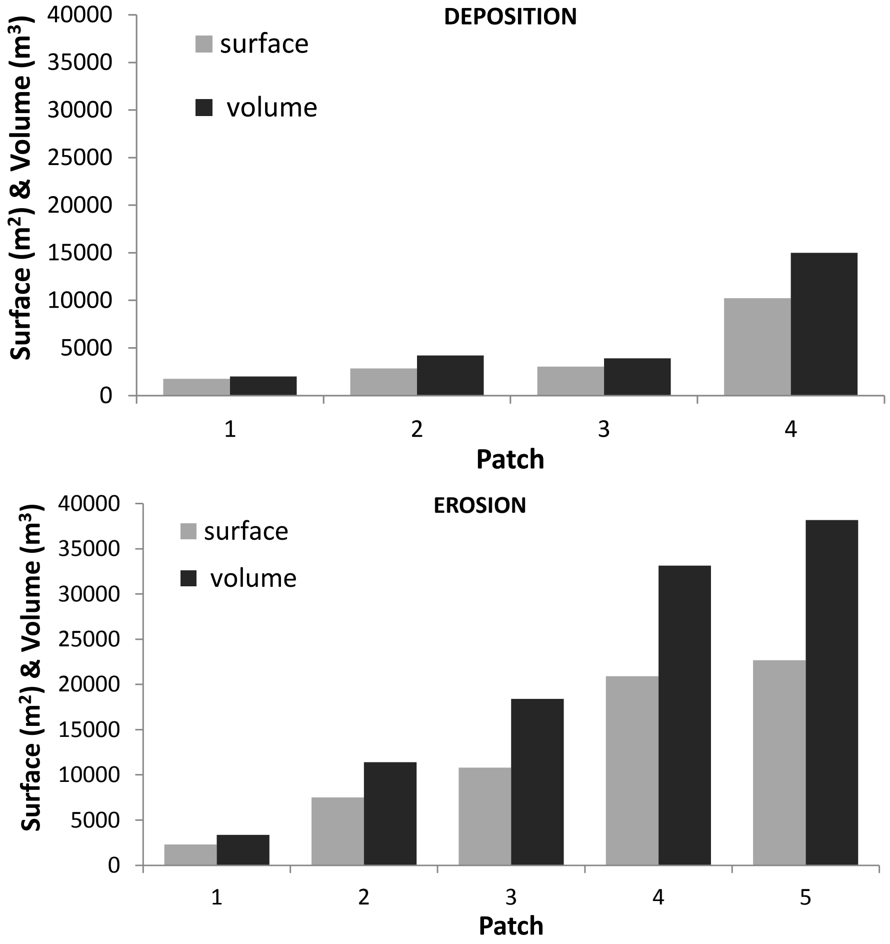

Figure 58. *Surface and volume of deposition and erosion among the different patches of Friola sub-reach.*

The reach shows that the erosions and depositions are distributed over a wider area than Nove along the active channel. Analysing Figure 59 we can note that the erosion is more concentrated along the curvature of the channels, whereas the deposition is more in the internal part of the channel curve. The erosion process has a continuous layer along the main channels with at least 0.20 – 0.50 m of material eroded. The most significant deposition (> 1000 m^2 and > ± 1.00 m – Figure 58) is represented by 4 patches with a balanced ratio of surface/volume around 1:1 – 1:1.2. The most significant erosion is represented by 5 patches. Analysing Figure 55 we can note that the bigger the patches considered the bigger the ratio surface/volume becomes. This means that for Friola sub-reach the hardest erosion is more concentrated in the major patches.

Fontaniva sub-reach

Figure 59 shows the effects of the November and December 2010 floods on Fontaniva sub-reach (Brenta River). From a general point of view, it seems that the further downstream we go the deposition process increases. Indeed the erosion and deposition in this reach are equal to 158 359 m^3 and 113 127 m^3 respectively. The allocation of the changes in this case seems be conditioned by the strongly vegetated and constricted (artificial banks and bridges) active channel and floodplain area.

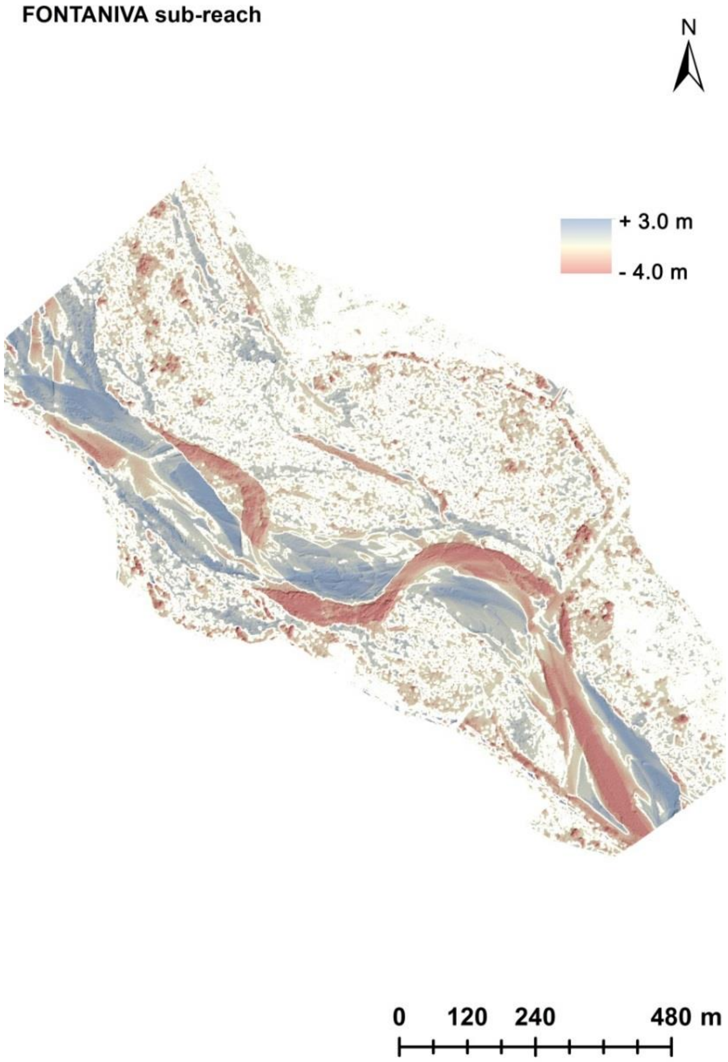
FONTANIVA sub-reach

Figure 59. *Depured difference of DEMs (DoD) of Fontaniva sub-reach.*

Also in this case we can analyse the distribution of these two volumes more deeply. Figure 60 shows different applications of PrEDA. Erosion and deposition patches from 50 m^2, 100 m^2, 200 m^2, 500 and 1000 m^2 of threshold area and ± 0.20 m, ± 0.50 m and ± 1.00 m of depth of change were extracted. Figure 60 shows the two extremes of threshold area at different depth, while Figure 61 shows the associated surface and volume for each patch with the most significant variations (> 1000 m^2 and > ± 1.00 m of depth for each patch).

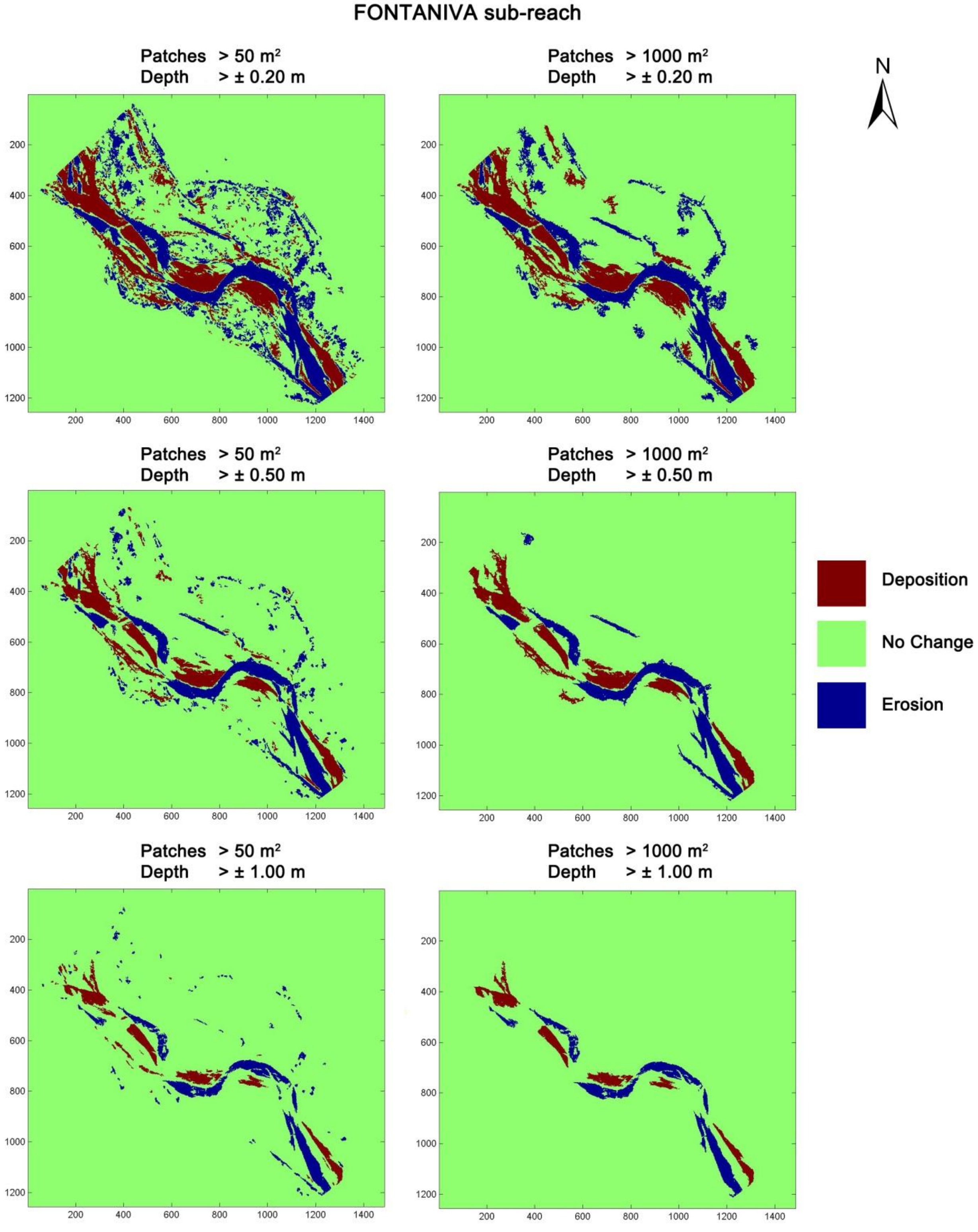

Figure 60. *Principal erosion-deposition extraction by PrEDA of Fontaniva sub-reach. Different minimum threshold of surface and depth of erosion or deposition characterizes the different sub-figures.*

The reach shows that the erosions and depositions are more located around the main channel except for some erosion on the left hand side. Analysing Figure 60 we can note, as for Friola, that the erosion is more concentrated along the curvature of the channels, whereas the deposition is more in the internal part of the channel curve. The erosion process is not in a continuous layer along the main channels as for Nove and Friola, but has a more complex pattern. Two different parts are recognizable, in the upper part we can notice a predominant deposition process, whereas in the lower part a predominant erosion process.

The most significant deposition (> 1000 m^2 and > ± 1.00 m – Figure 58) is represented by 5 patches with a less balanced surface/volume ratio of around 1:1.2 – 1:1.3, that means more concentrated deposition in this reach than the other one. The most significant erosion is represented by 6 patches. Analysing Figure 61 we can note, also in this case, that the bigger the patches considered the bigger the ratio surface/volume becomes.

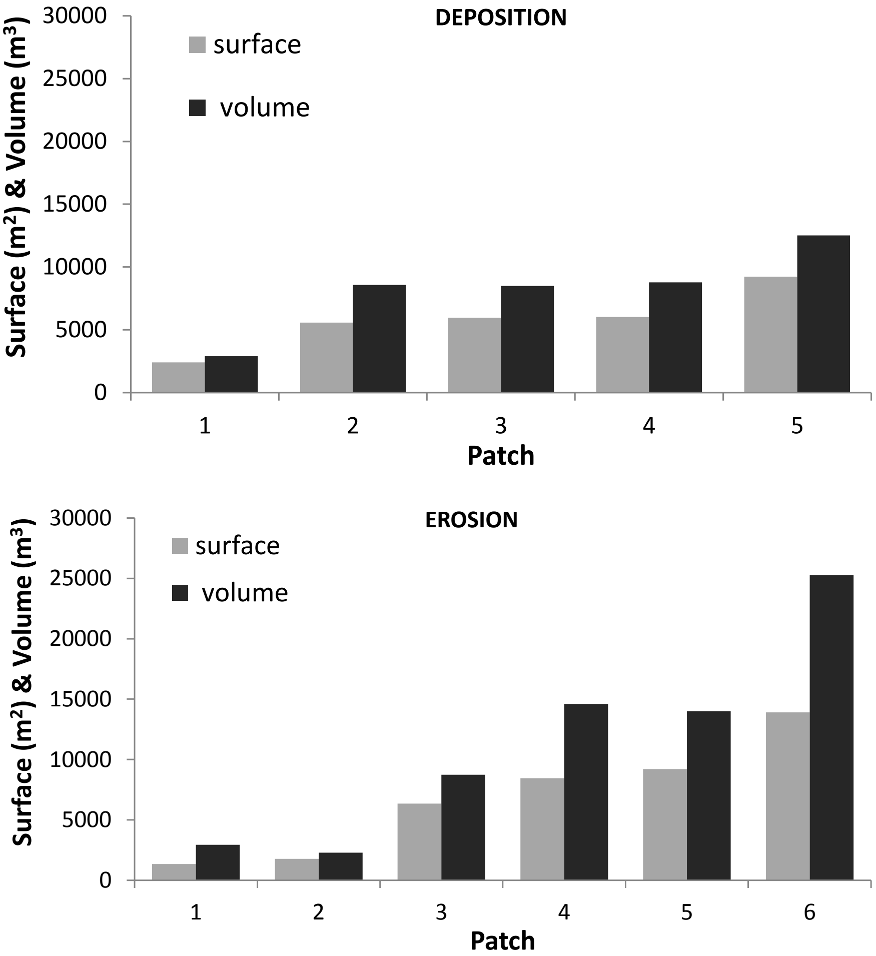

Figure 61. *Surface and volume of deposition and erosion among the different patches of Fontaniva sub-reach.*

11.1.4 Riffle-pool behavior of the Brenta River

From Figure 50 reporting the HDTMs comparison, an interesting change after the floods can be noted: where the main channel had less lateral constriction, it seems to have an increased sinuosity. Indeed, Nove sub-reach is the most constrained laterally due to artificial left enbarkments and also presents the highest incision degree. It therefore has less increase of sinuosity than Friola and Fontaniva sub-reaches. Comparing these two reaches, Friola presents less change in sinuosity than Fontaniva, probably due to the position next to the artificial banks (on the left side) of the main 2010 channel.

Figure 62 shows the CSMs with pool locations (e.g. P1, P2) on the wet areas of Nove, Friola and Fontaniva sub-reaches in 2010 and 2011. Pools are identified as dark areas, i.e. the zones with the higher water depth with respect to the riffles. It is noteworthy that after the floods, the old pools are longer on average. This phenomenon is particularly evident in Friola sub-reach (pool P3 and P4 2011) and Fontaniva (pool P4 2011). Observing the models, the new pools and the old one still presents do not seem to have formed and evolved in casual positions. The embankments and fluvial islands appear to have played an important role in the bed-form dynamics during the floods. Indeed, the pools in each 2011 sub-reach are located mainly on the side of the wet area with a more compact lateral surface with embankments and/or vegetated bars. On the other hand, riffles are mainly located where no significant “constrictions” were present on either side of the wet areas. The dislocation of the 2010 bed forms does not seem to follow the same principles.

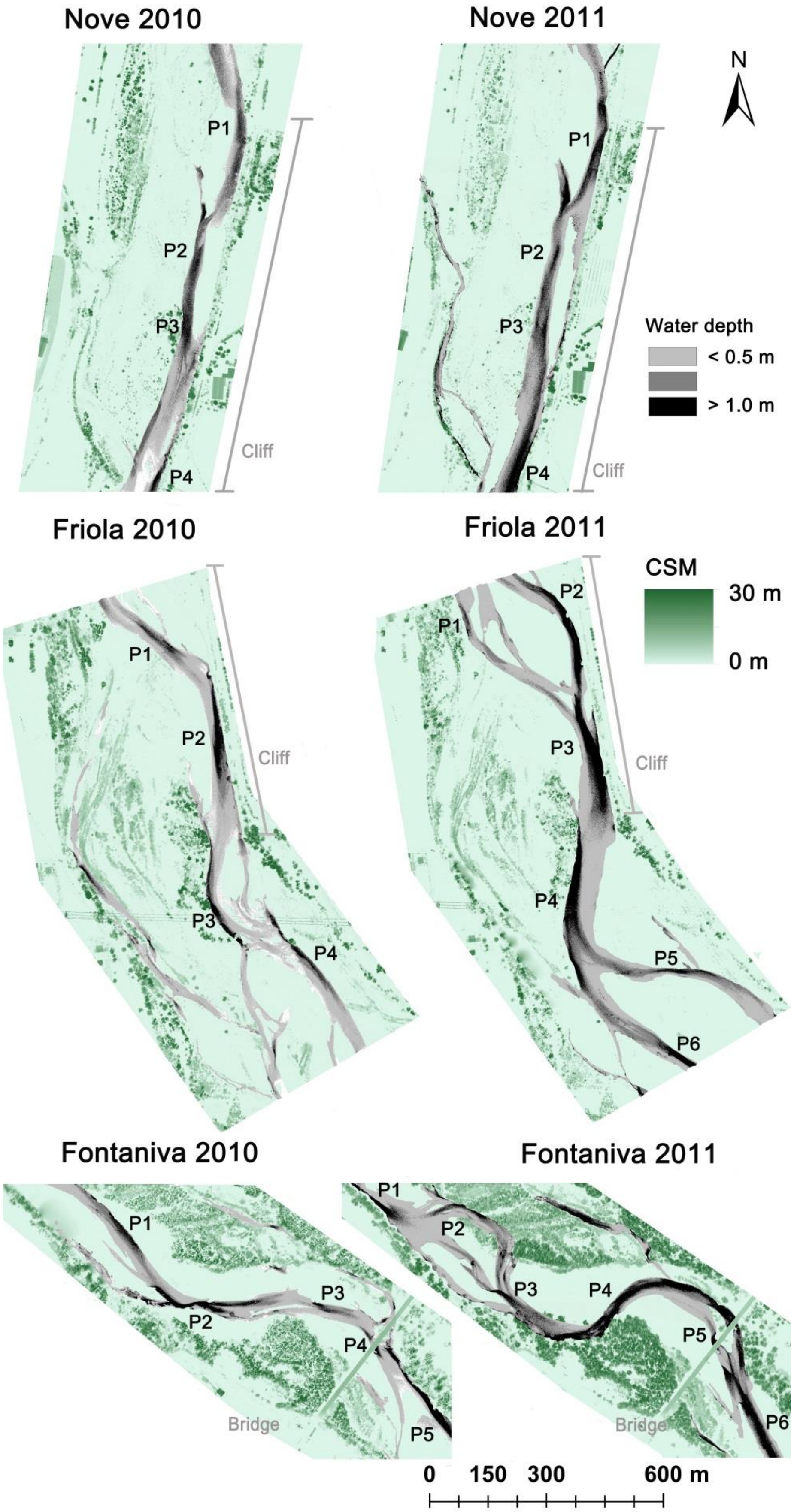

Figure 62. *Canopy surface models (CSM) with pools individuation (P1, P2, etc.) through standard deviation on wet areas of Nove, Friola and Fontaniva sub-reaches 2010 and 2011.*

11.2 Colour bathymetry, HDTMs and Principal Erosion Deposition Analysis of Piave River

11.2.1 Production of bathymetric models from colour bands

From the statistical regressions performed using the two previously described methods (traditional regression and AICc), two bathymetric models for each inter-flood period were obtained. All the three colour bands, as in the Brenta and Piave River have proved to be significantly correlated with the water depth; also interactions and square and cubic terms were considered meaningful elements of the equation (for the presence of a non-linear regression in the correlation).

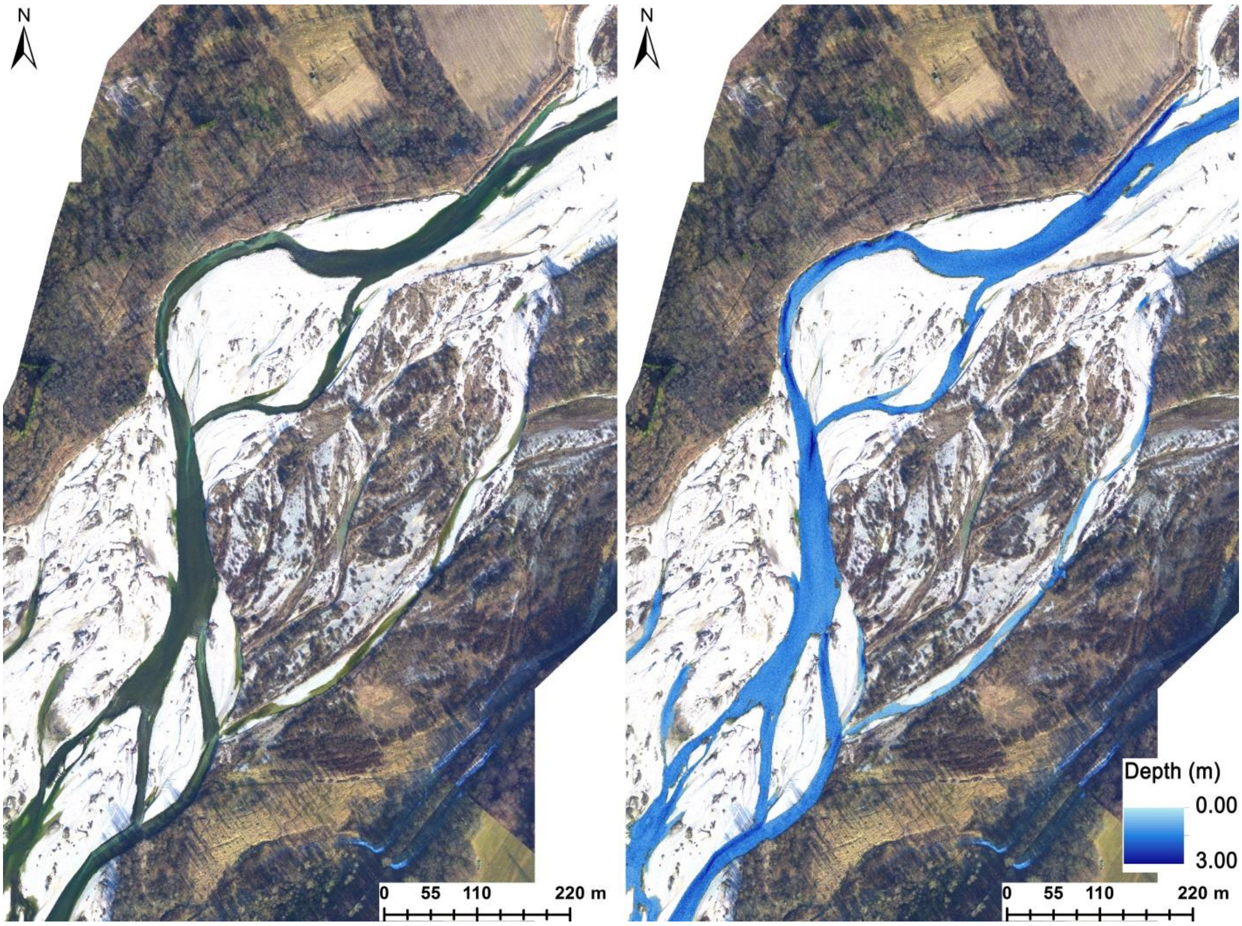

Figure 63. *Comparison between the aerial image (a) and the correspondent colour bathymetry output (b).*

In 2010 the traditional regression procedure has performed a slightly better output model in respect to the AICc:

$$Dph = 6.96 + 0.06222\,R - 0.01419\,G - 0.2581\,B - 0.0001518\,R^2 + 0.002002\,B^2 - 0.000005091\,B^3 \qquad (18)$$

Where *Dph* is the water depth and R, G and B the red, green and blue colour bands, respectively. The control operated comparing the remaining 20% dGPS points has highlighted a weighted vertical error of ± 0.18 m and a related standard deviation of ± 0.17 m for Belluno sub-reach and ± 0.28 m and ± 0.22 m for Praloran sub-reach in 2010. This model reaches 1.40 m of water depth, with an error lesser than ± 0.20 m .

Similarly, a regression model for 2011 was performed, meeting the most reliable results in the traditional method:

$$Dph = 0.83 - 0.004607\,R + 0.009665\,G - 0.04102\,B - 0.000205\,R^2 - 0.0006412\,G^2 + 0.0002062\,B^2 + 0.000002987\,G^3 + 0.0005447\,RG + 0.0005339\,RB - 0.000004473\,RGB \qquad (19)$$

In this case, the weighted vertical error accounts for ± 0.20 m and the correlated standard deviation for ± 0.15 m in Belluno sub-reach, while Praloran sub-reach features values of ± 0.19 m and ± 0.15 m, respectively.

The two models proved to be statistically significant (p-value <0.05), highlighting the important contribution of all the three colour bands to channel depth estimations. In Figure 63, a comparison between the aerial image and the related bathymetric output of Belluno sub-reach is presented. In-channel depth variations appear to be respected by the model that produces well-proportioned and fluid depth transitions. In this case, the maximum reached depth with an error lesser than ± 0.20 m is equal to 0.60 m (Table 5).

11.2.2 Accurate Hybrid DTMs creation

After the filtering process eliminating implausible wet points, LiDAR and bathymetric-derived surveys were integrated to create Hybrid DTMs featuring a cell size of 0.5 m and a "natural neighbor" interpolation.

Figure 64. *Hybrid DTM of Belluno sub-reach (2010).*

In Figure 64, an example of HDTM (Belluno sub-reach, 2010) is reported: the clear alternation of in-channel landforms (riffle-pool) can be appreciated. The accuracy of river-bed surfaces represents a helpful amelioration for geomorphic change detection.

11.2.3 *Morphological change detection using PrEDA*

Belluno sub-reach

Figure 65 shows the effects of the November and December 2010 floods on Belluno sub-reach (Piave River). From a general point of view it seems that the changes are more located in the active wet channel. The erosion and deposition in this reach are equal to 183 362 m^3 and 107 320 m^3 respectively. The allocation of the changes in this case seems to be favoured by an increase of the sinuosity degree as the erosion is located more in the external part of the channel curves.

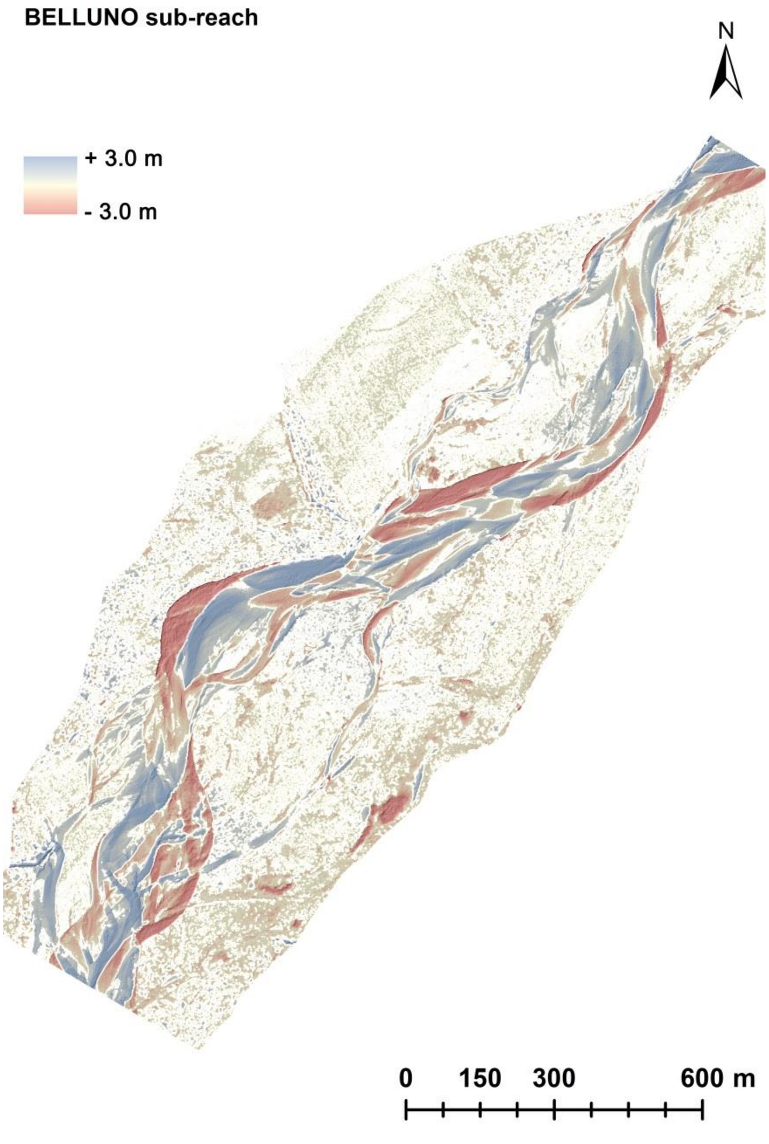

Figure 65. *Depured difference of DEMs (DoD) of Belluno sub-reach.*

We can now analyse the distribution of these two volumes more deeply. Figure 66 shows different applications of PrEDA. Erosion and deposition patches from 50 m^2, 100 m^2, 200 m^2, 500 and 1000 m^2 of threshold area and ± 0.20 m, ± 0.50 m and ± 1.00 m depth of change were extracted. Figure 66 shows the two extremes of the extracted patches at different depths, while Figure 67 shows the associated surface and volume for each patch with the most significant variations (> 1000 m^2 and > ± 1.00 m of depth for each patch).

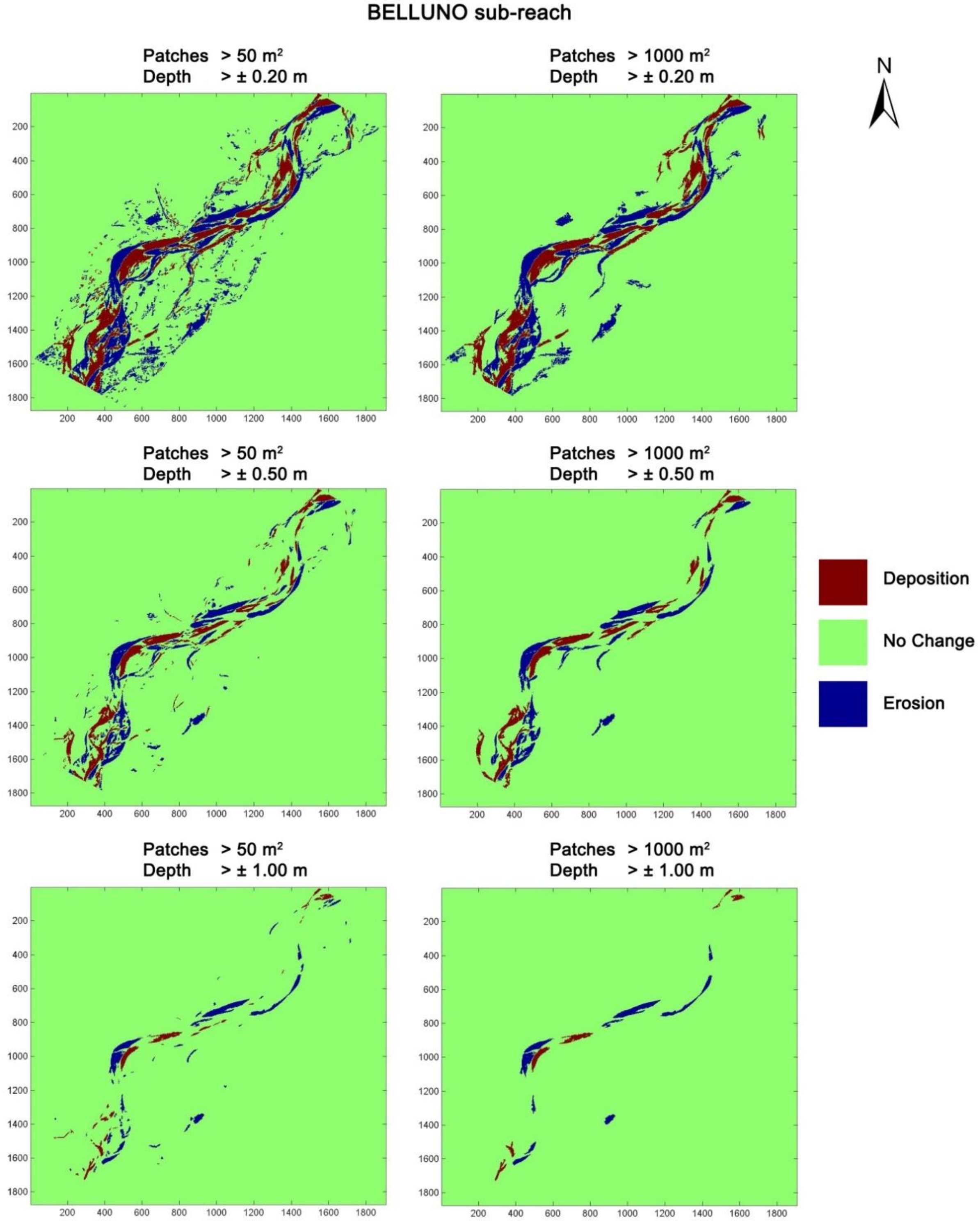

Figure 66. *Principal erosion-deposition extraction by PrEDA of Belluno sub-reach. Different minimum threshold of surface and depth of erosion or deposition characterizes the different sub-figures.*

Analysing Figure 66 we can note that the erosion is more concentrated along the curvature of the channels, whereas the deposition is more in the internal part of the channel curve.

Analysing the principal erosion and deposition we can confirm that erosion is the predominant process. The most significant deposition (> 1000 m^2 and > ± 1.00 m – Figure 67) is represented with 6 patches with a more balanced ratio than the erosion of surface/volume around 1:1.2 – 1:1.3. The most significant erosions are represented with 9 patches. Analysing Figure 67 we can note, as for the Brenta River, that the bigger the patches considered the bigger surface/volume ratio becomes.

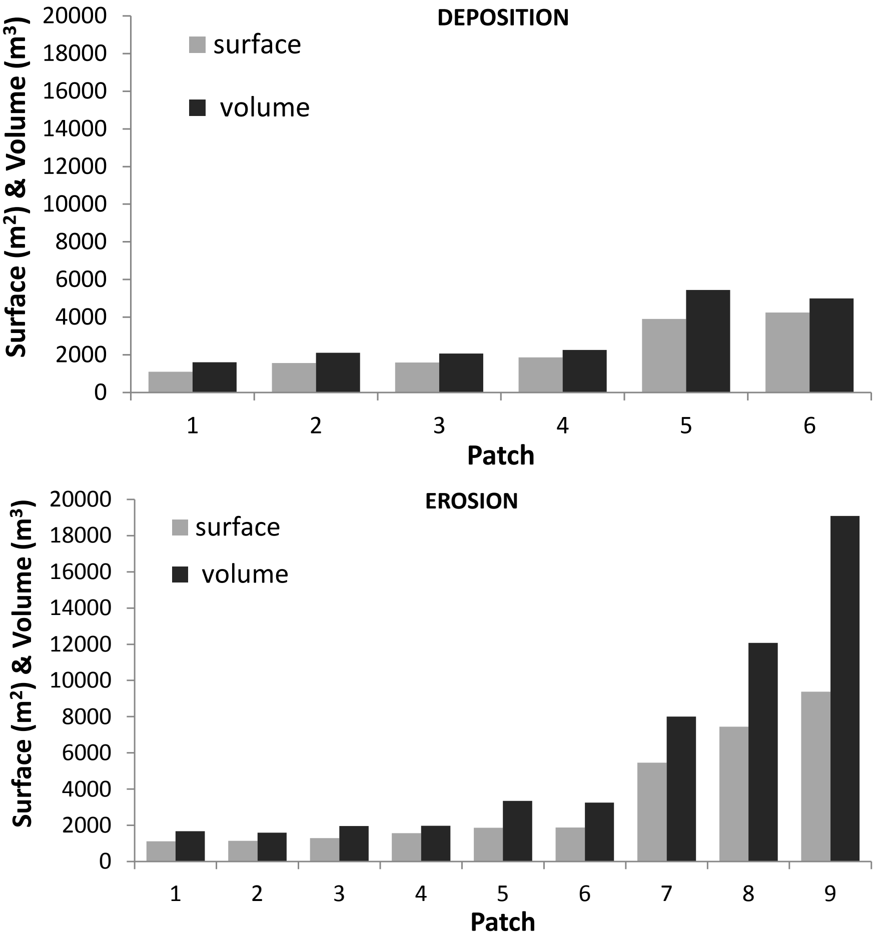

Figure 67. *Surface and volume of deposition and erosion among the different patches of Belluno sub-reach.*

Praloran sub-reach

Figure 68 shows the effects of the November and December 2010 floods on Praloran sub-reach (Piave River). From a general point of view, as for Belluno, seems that the changes are more located in the active wet channel. The erosion and deposition in this reach are equal to 190 254 m^3 and 130 179 m^3 respectively. The allocation of the deposition seems to be more in the middle part of the active channel, whereas the erosion, except for the upper parts, is located in the active area sides.

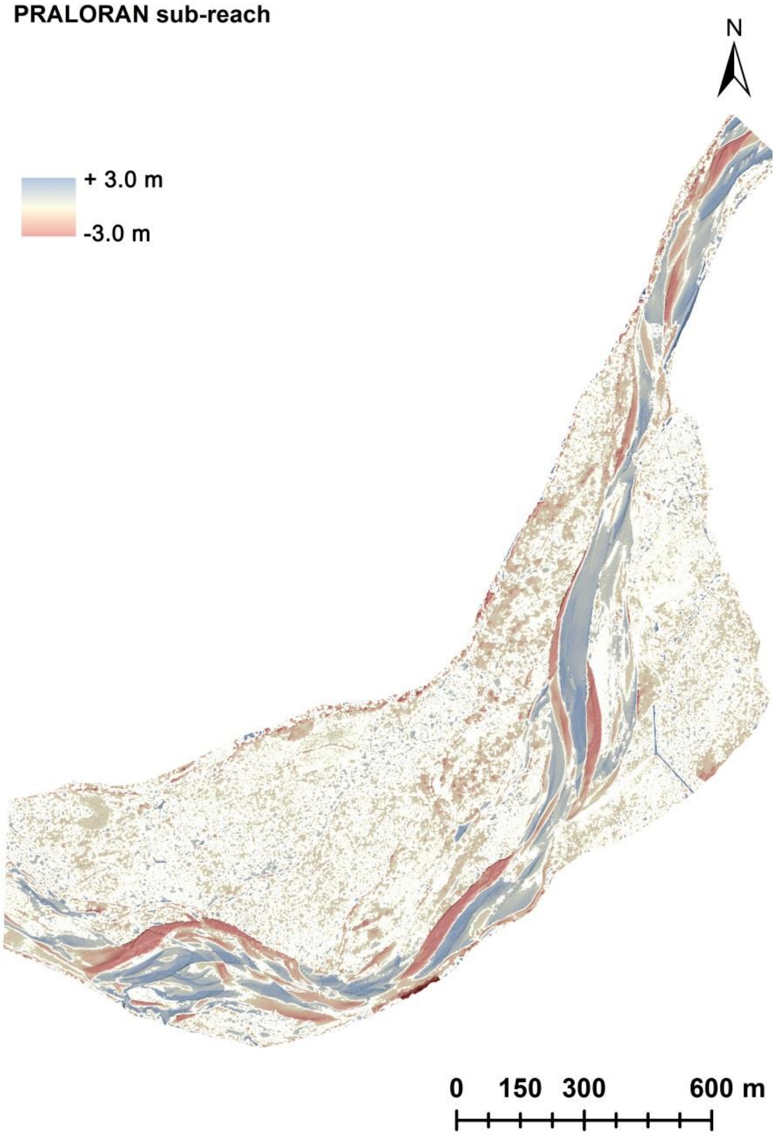

Figure 68. *Depured difference of DEMs (DoD) of Praloran sub-reach.*

To better analyse the DoD Figure 66 shows different applications of PrEDA. Erosion and deposition patches from 50 m^2, 100 m^2, 200 m^2, 500 and 1000 m^2 of threshold area and ± 0.20 m, ± 0.50 m and ± 1.00 m depth of change were extracted. Figure 69 shows the two extremes of extracted areas at different depths, while Figure 70 shows the associated surface and volume for each patch with the most significant variations (> 1000 m^2 and > ± 1.00 m of depth for each patch).

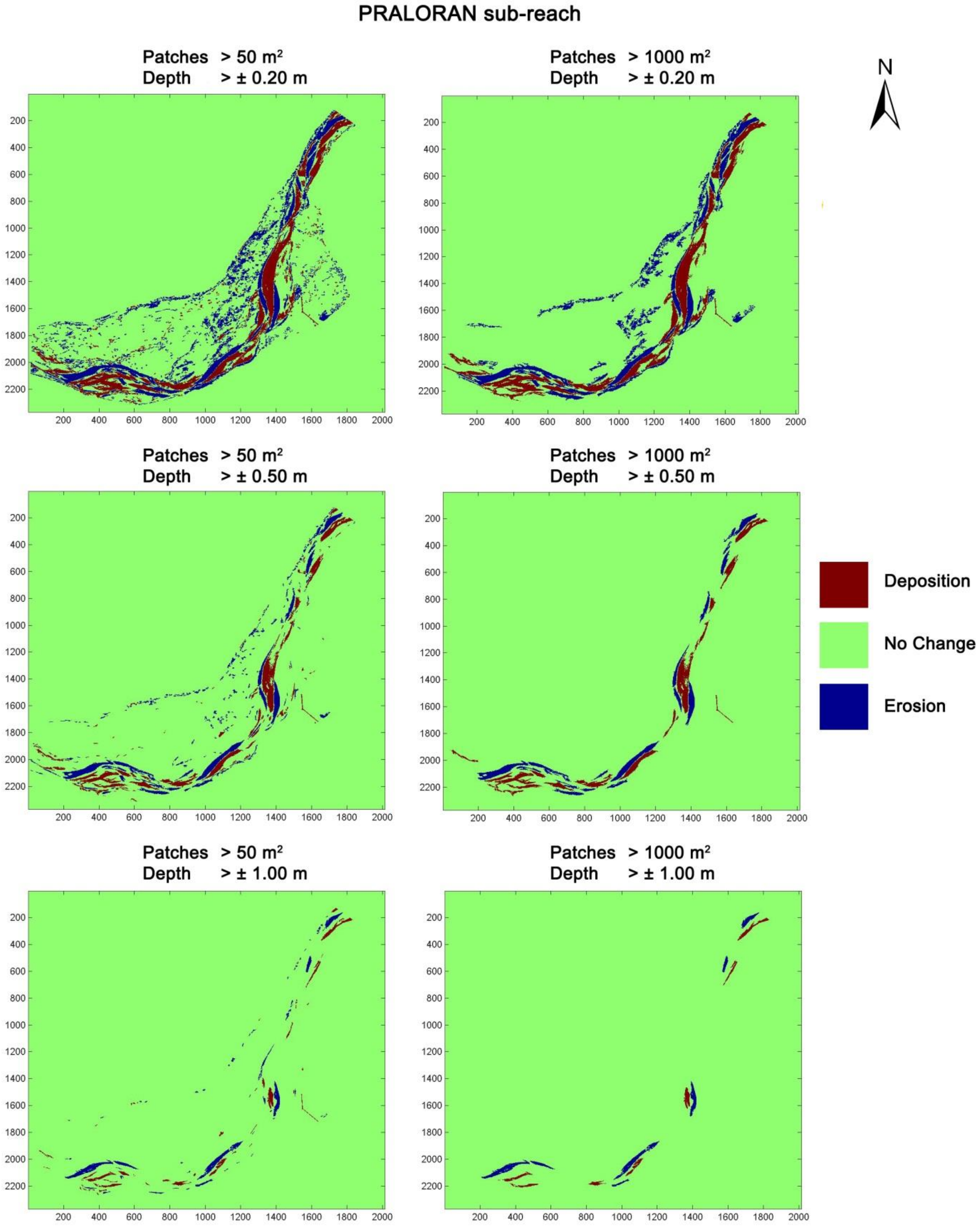

Figure 69. *Principal erosion-deposition extraction by PrEDA of Praloran sub-reach. Different minimum threshold of surface and depth of erosion or deposition characterizes the different sub-figures.*

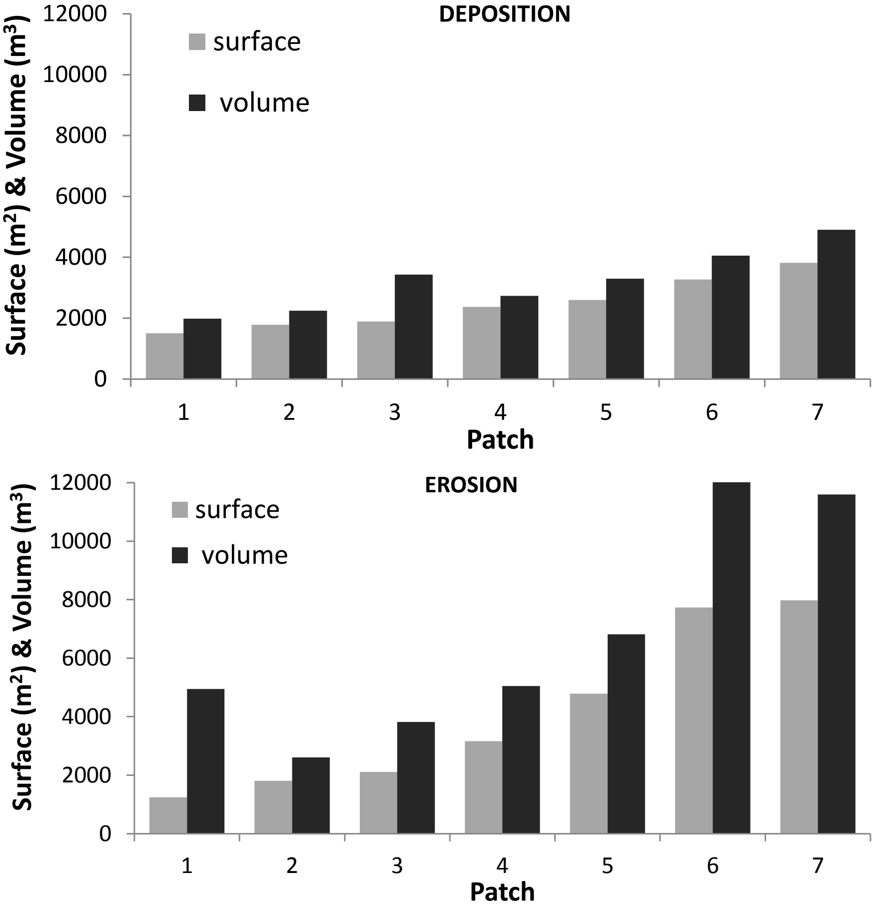

Figure 70. *Surface and volume of deposition and erosion among the different patches of Praloran sub-reach.*

Analysing Figure 69 we can confirm that deposition seems be allocated more in the middle part of the active channel, whereas the erosion, except for the upper parts is located at the sides of the active area.

Analysing the principal erosion and deposition we can confirm that erosion is the predominant process. The most significant deposition (> 1000 m^2 and > ± 1.00 m – Figure 67) is represented by 7 patches with a more balanced surface/volume ratio of around 1:1.1 – 1:1.2, than the erosion. The most significant erosions are represented by 7 patches. Analysing Figure 70 we can note, as for the Brenta River, that the bigger the patches considered the greater the ratio surface/volume becomes, but with an exception. Indeed, in this case we have an erosion patch of 1246 m^2 and 4944 m^3 of material eroded. The surface-volume ratio is equal to 1:3.9, meaning that for each 1 m^2 of erosion there is on average 3.9 m of eroded depth.

11.3 Colour bathymetry, HDTMs and Principal Erosion Deposition Analysis of Tagliamento River

11.3.1 Wet area extraction

The revised method to automatically extract wet areas has demonstrated a very good performance as reported in Figure 71a. The strong difference in LiDAR intensity between water and gravel has allowed to achieve a good edge definition. The associated rasters (CSM, and detrended DTM) have allowed to delete the dry areas featuring a similar intensity. Therefore the resulting shape files can be used to divide the wet from the dry areas.

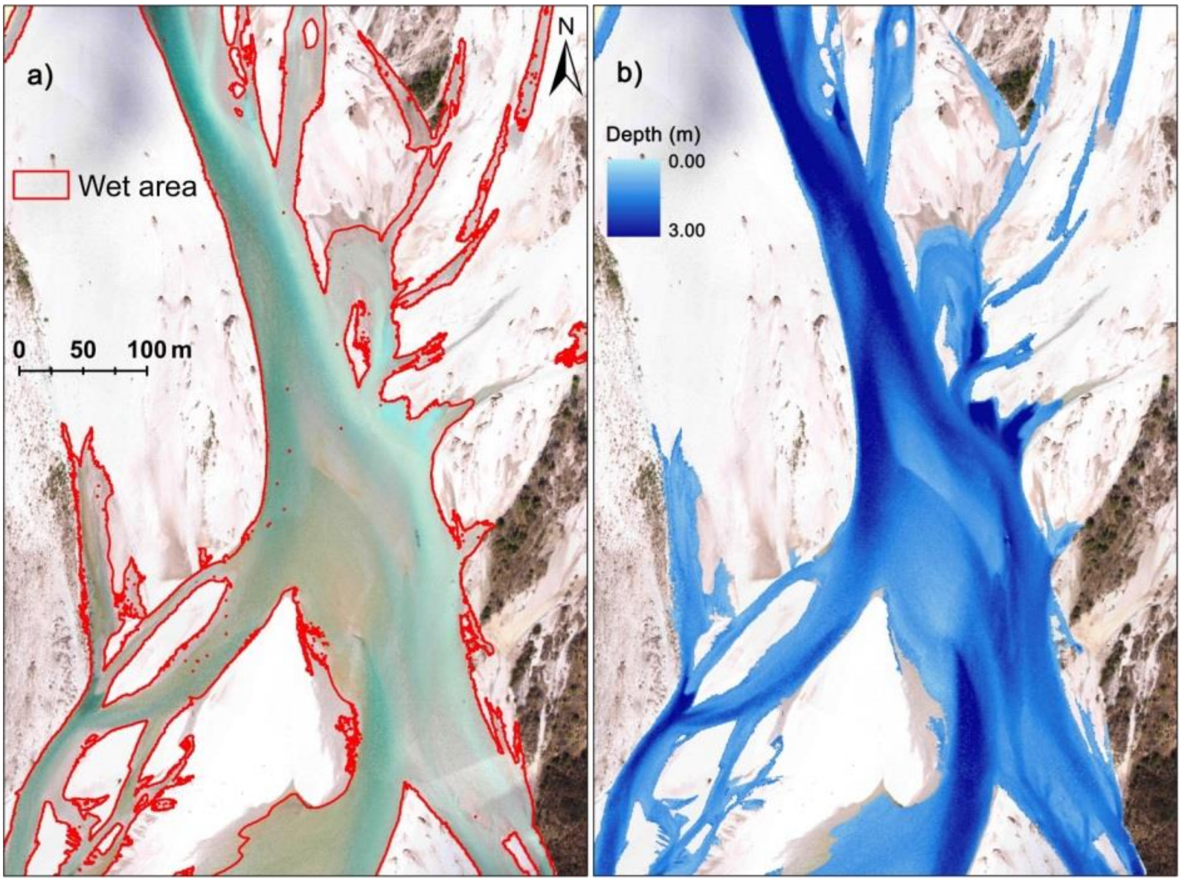

Figure 71. *Automatic wet area extraction a) and colour bathymetry application b) of Cornino sub-reach in 2011.*

11.3.2 Colour bathymetry models

The statistical regressions performed with the two different approaches (traditional regression and AICc) have produced two bathymetric models for each inter-flood period.

For 2010, both statistical regression methods have demonstrated that all the colour bands are significantly correlated with the water depth. In addition to the presence of correlation between the colour bands and a nonlinear regression, we have also found that the interactions and the square and cubic terms are all significant. The traditional regression methods have demonstrated a little better performance than the AICc:

$$\begin{gathered} Dph = -0.207 + 0.09R + 0.1151G + 0.007827B + 0.001573G^2 + 0.0006577B^2 - \\ 0.000005273G^3 - 0.000002425B^3 - 0.0006273RG - 0.0008327RB - \\ 0.0004865GB + 0.00000649RGB \end{gathered} \tag{20}$$

Where *Dph* is the estimated water depth and R, G and B the red, green and blue intensity bands, respectively. This model, if compared with the final HDTM, estimates the wet area with ± 0.13 m of weighted error (with the area of influence of each band on the water depth) and a standard deviation error of ± 0.10 m (Table 5).

Similar results are featured for 2011, but in this case the AICc method has demonstrated the best results:

$$\begin{gathered} Dph = -0.69 + 0.0235R - 0.02822G + 0.008599B + 0.000061G^2 + 0.00009621B^2 - \\ 0.00000006799R^3 - 0.0000004239B^3 - 0.00009157RG - 0.00004429RB \\ -0.00004228GB + 0.0000005079 \end{gathered} \tag{21}$$

All the terms in these models are statistically significant; a small scale (Figure 71b) and two large scales (Figure 72 and Figure 73) examples regarding the results of the model application are shown.

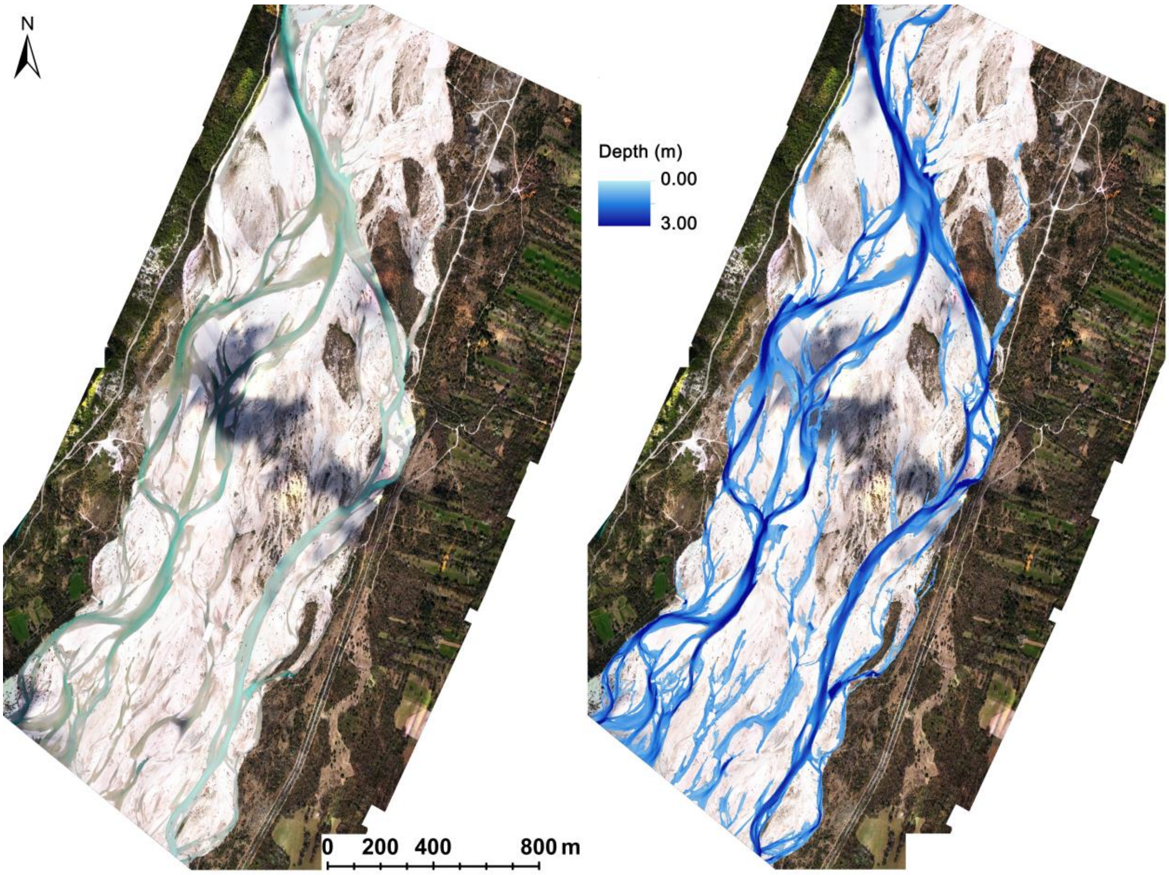

Figure 72. *Bathymetric model application on all wet areas of Cornino 2011 sub-reach.*

From a general point of view the model seems to be able to produce a good water depth estimation if compared to the aerial photos, as in Figure 71a. This model, compared with the final HDTM, estimates the wet area with ± 0.15 m of weighted error (with the area of influence of each band on the water depth) and a standard deviation of ± 0.11 m (Table 5).

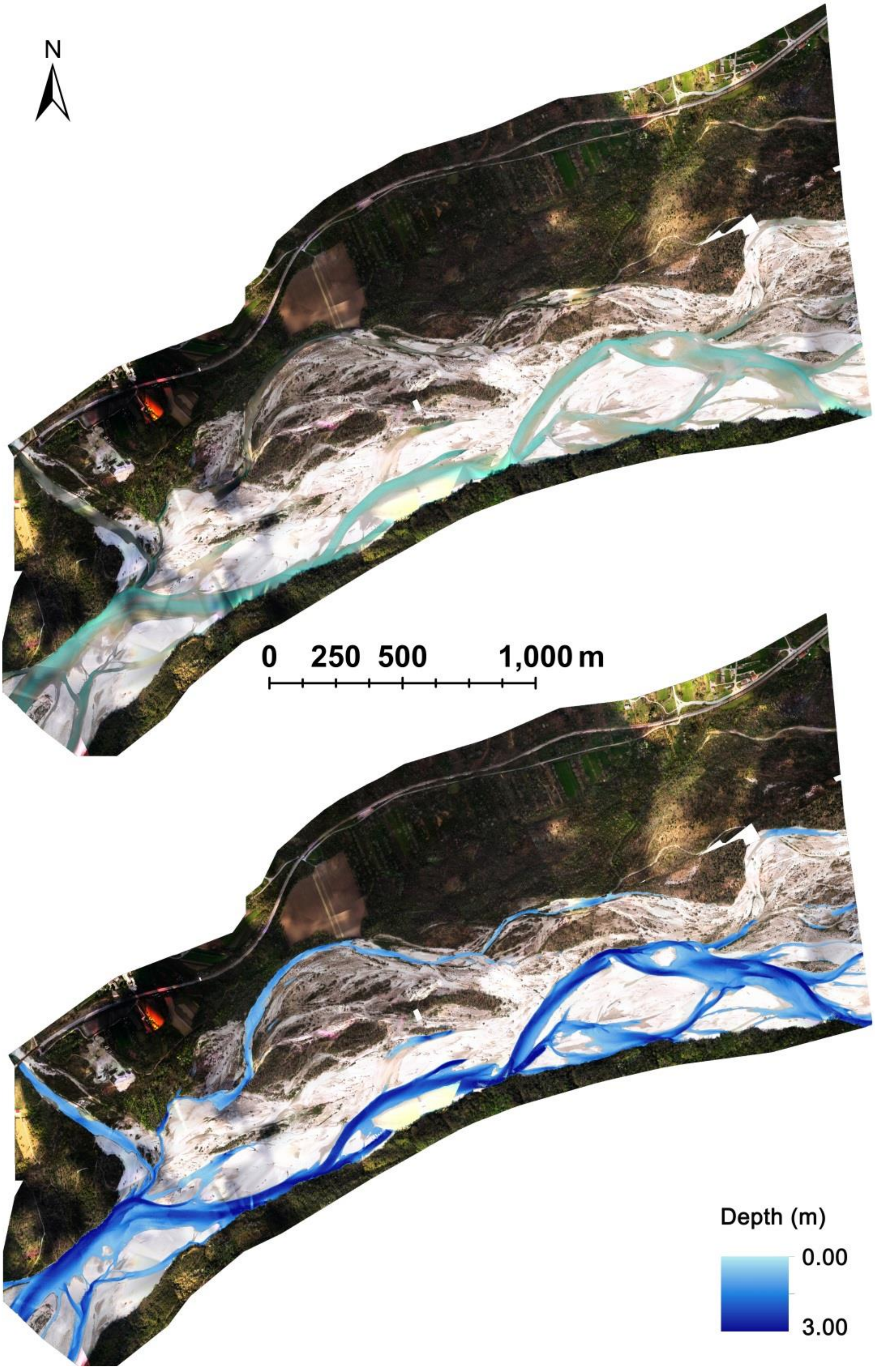

__Figure 73.__ Bathymetric model application on all wet areas of Flagogna 2011 sub-reach.

Table 5. *Error analysis of depth-colour models applied at different water stages for 2010 and 2011 on Brenta, Piave and Tagliamento River.*

REACH	**Brenta 2010**			**Piave 2010**			**Tagliamento 2010**		
Depth (m)	**Dph (R, G, B)**		**Calib. points**	**Dph (R, G, B)**		**Calib. points**	**Dph (R, G, B)**		**Calib. points**
	error (m)	**dev. St. (m)**		**error (m)**	**dev. St. (m)**		**error (m)**	**dev. St. (m)**	
0.00 - 0.19	0.26	0.22	107	0.43	0.28	7	0.15	0.11	232
0.20 - 0.39	0.26	0.24	87	0.21	0.16	42	0.10	0.09	327
0.40 - 0.59	0.21	0.20	75	0.08	0.15	81	0.10	0.09	275
0.60 - 0.79	0.22	0.18	59	0.00	0.17	70	0.18	0.13	184
0.80 - 0.99	0.26	0.15	32	0.08	0.18	50	0.32	0.19	64
1.00 - 1.19	0.51	0.21	20	0.20	0.23	38	0.54	0.22	15
1.20 - 1.39	0.69	0.14	13	0.11	0.22	27	0.46	0.21	9
1.40 - 1.59				0.29	0.23	11	-	-	1
1.60 - 1.79				0.13	0.13	8			
1.80 - 1.99				0.25	0.33	3			
> 2.00									
TOTAL			**393**			**337**			**1107**

REACH	**Brenta 2011**			**Piave 2011**			**Tagliamento 2011**		
Depth (m)	**Dph (R, G, B)**		**Calib. points**	**Dph (R, G, B)**		**Calib. points**	**Dph (R, G, B)**		**Calib. points**
	error (m)	**dev. St. (m)**		**error (m)**	**dev. St. (m)**		**error (m)**	**dev. St. (m)**	
0.00 - 0.19	0.27	0.11	61	0.05	0.09	221	0.37	0.11	127
0.20 - 0.39	0.18	0.11	248	0.04	0.11	967	0.21	0.11	599
0.40 - 0.59	0.13	0.11	427	0.19	0.11	628	0.14	0.11	1631
0.60 - 0.79	0.14	0.13	343	0.31	0.13	301	0.12	0.10	2233
0.80 - 0.99	0.24	0.19	187	0.45	0.18	123	0.13	0.10	2089
1.00 - 1.19	0.32	0.19	100	0.51	0.29	36	0.15	0.13	1419
1.20 - 1.39	0.40	0.13	35	0.62	0.30	8	0.18	0.16	755
1.40 - 1.59	0.56	0.10	20	0.69	0.56	4	0.26	0.18	341
1.60 - 1.79				0.59	0.70	7	0.38	0.21	123
1.80 - 1.99				1.08	0.54	6	0.49	0.19	39
> 2.00							0.61	0.12	10
TOTAL			**1421**			**2301**			**9366**

11.3.3 Morphological change detection using PrEDA

Cornino sub-reach

Figure 74 shows the effects of the November and December 2010 floods on Cornino sub-reach (Tagliamento River). In contrast to the other reaches this is a marked braided reach, and observing the changes we can also confirm this morphology after these intense floods. The erosion and deposition in this reach are equal to 726 083 m^3 and 490 039 m^3 respectively. The allocation of the changes in this case seems be favoured by the wide active channel.

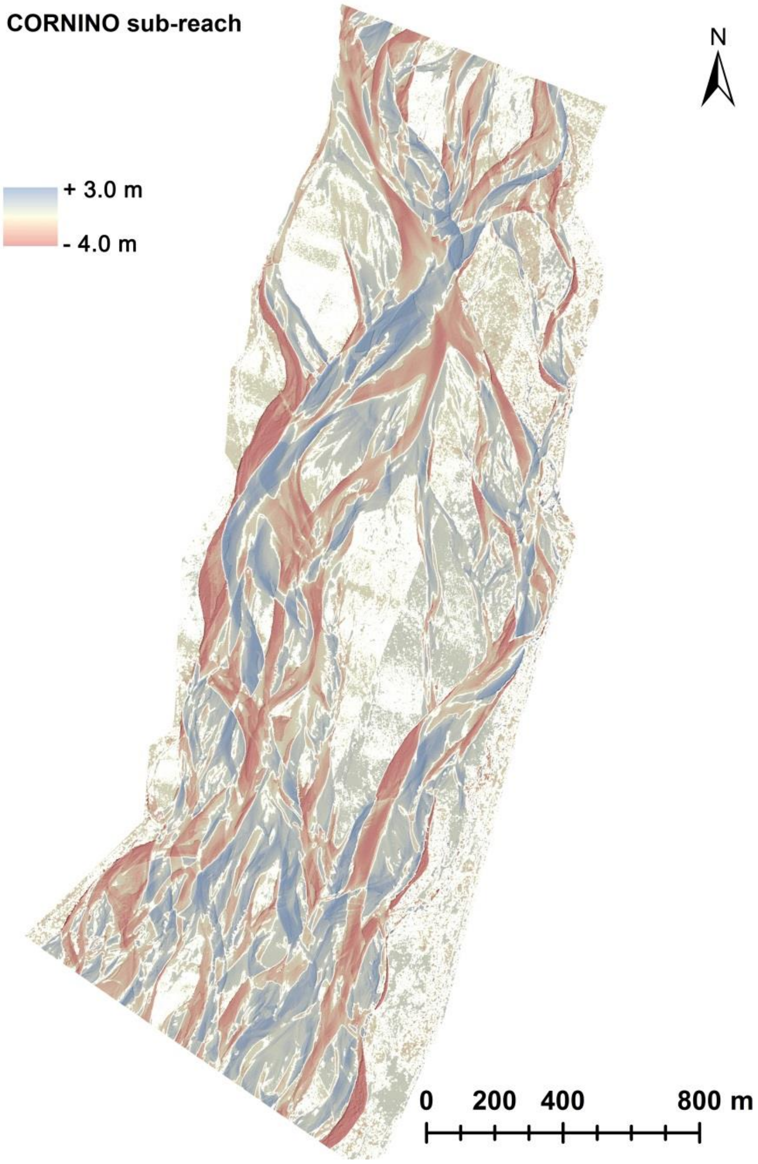

Figure 74. *Depured difference of DEMs (DoD) of Cornino sub-reach.*

PrEDA tool can in this particular case, be very useful to analyse a very complex erosion and deposition pattern such as the one presented for this reach. Figure 75 shows different applications of PrEDA. Erosion and deposition patches from 50 m^2, 100 m^2, 200 m^2, 500 and

1000 m^2 of threshold area with ± 0.20 m, ± 0.50 m and ± 1.00 m depth of change were extracted. Figure 75 shows the two extremes of extracted patches at different depths, while Figure 76 shows the associated surface and volume for each patch with the most significant variations (> 1000 m^2 and > ± 1.00 m of depth for each patch).

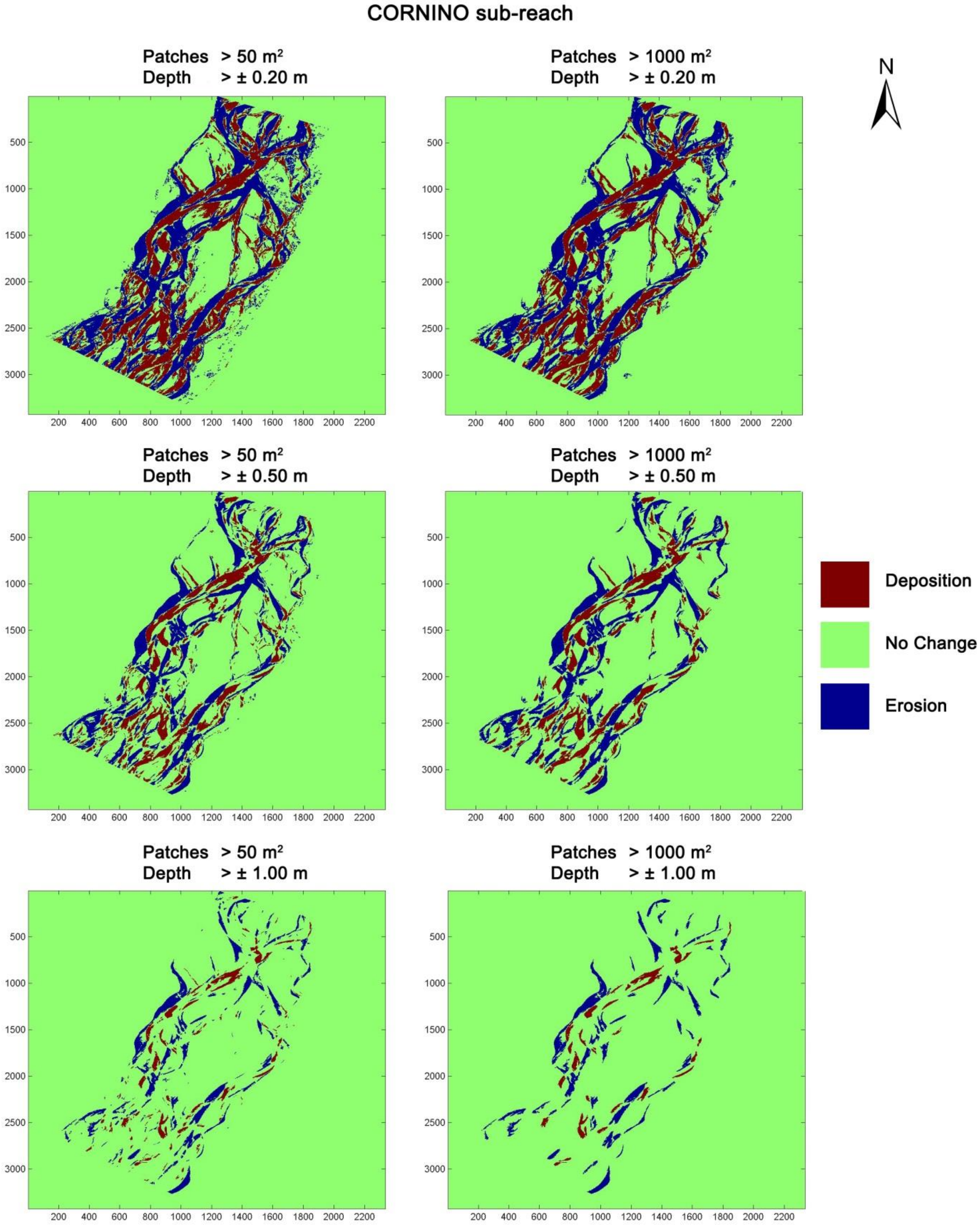

Figure 75. *Principal erosion-deposition extraction by PrEDA of Cornino sub-reach. Different minimum threshold of surface and depth of erosion or deposition characterizes the different sub-figures.*

Analysing Figure 75 we can note that the erosion and deposition is well distributed along the reach, which has favoured the birth of lots of new channels due to such a wide active area. Analysing the principal erosion and deposition we can confirm that erosion is also the predominant process for this reach. The most significant deposition (> 1000 m^2 and > ± 1.00 m - Figure 76) is represented by 26 patches with a more balanced ratio of surface/volume around 1:1.2 - 1:1.3, than the erosion. The most significant erosions are in 52 patches. Analysing Figure 76 we can note, as for the Brenta and Piave River, that the bigger the patches considered the greater the ratio surface/volume becomes, and up to around 1:2.

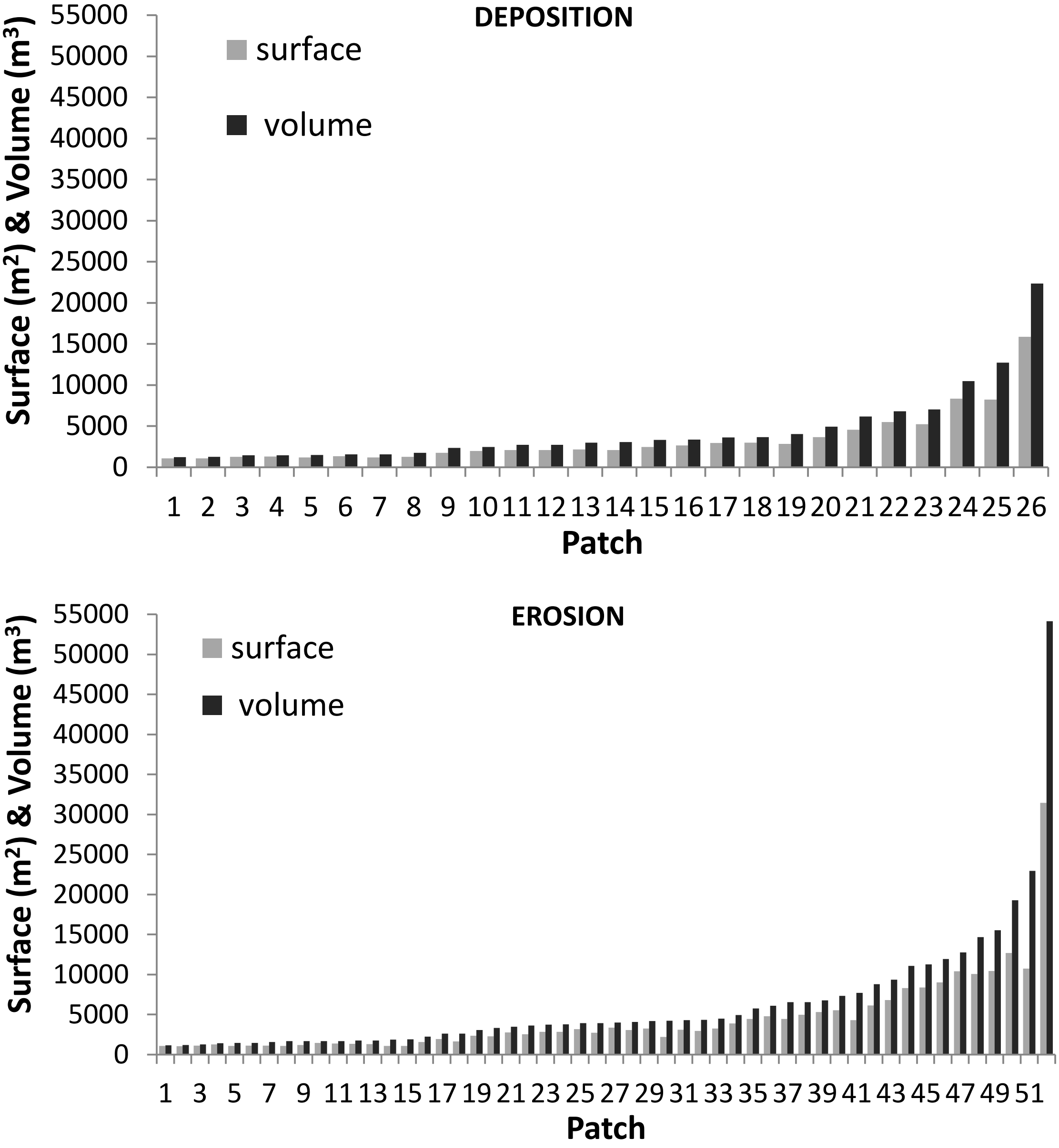

Figure 76. *Surface and volume of deposition and erosion among the different patches of Cornino sub-reach.*

Flagogna sub-reach

Figure 77 shows the effects of the November and December 2010 floods on Flagogna sub-reach (Tagliamento River). As for Cornino this reach has a braided morphology, but with half the extension of active channel. The erosion and deposition in this reach are equal to 399 098 m^3 and 520 334 m^3 respectively.

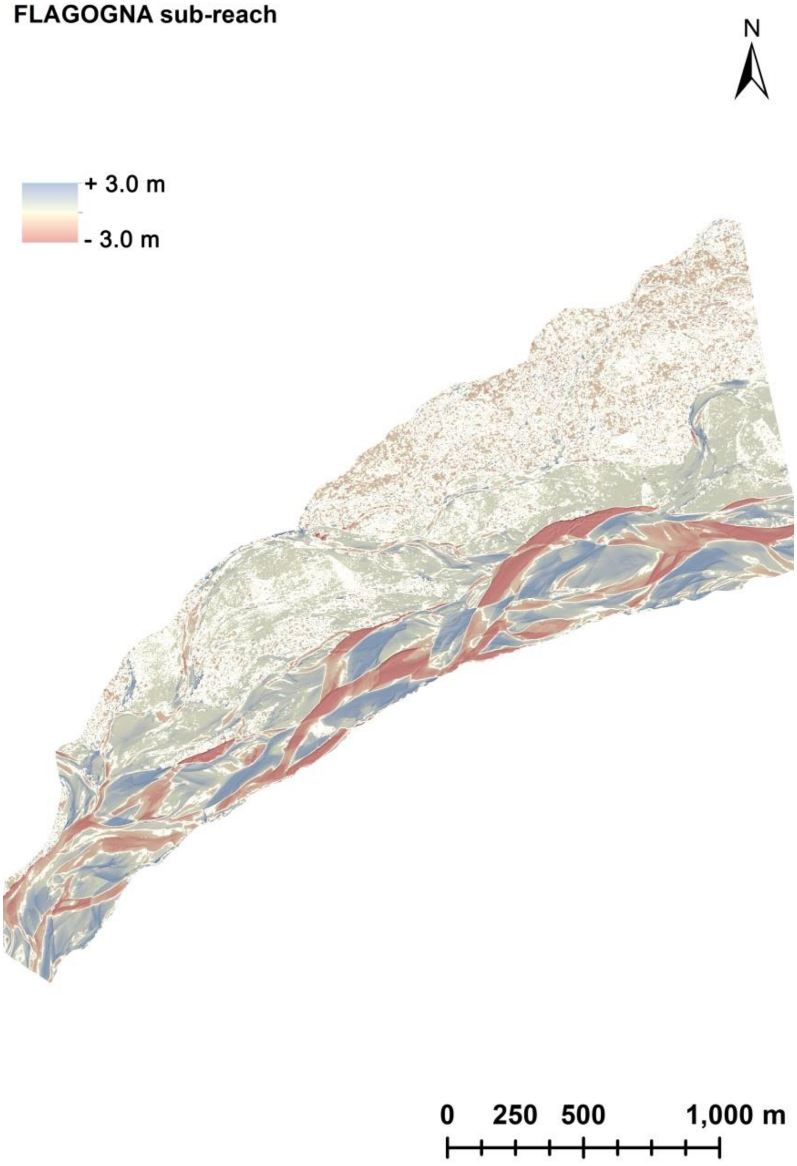

Figure 77. *Depured difference of DEMs (DoD) of Nove sub-reach.*

Figure 78 shows different applications of PrEDA. Erosion and deposition patches from 50 m^2, 100 m^2, 200 m^2, 500 and 1000 m^2 of threshold area with ± 0.20 m, ± 0.50 m and ± 1.00 m depth of change were extracted. Figure 78 shows the two extremes of extracted areas at different depths, while Figure 79 shows the associated surface and volume for each patch with the most significant variables (> 1000 m^2 and > ± 1.00 m of depth for each patch).

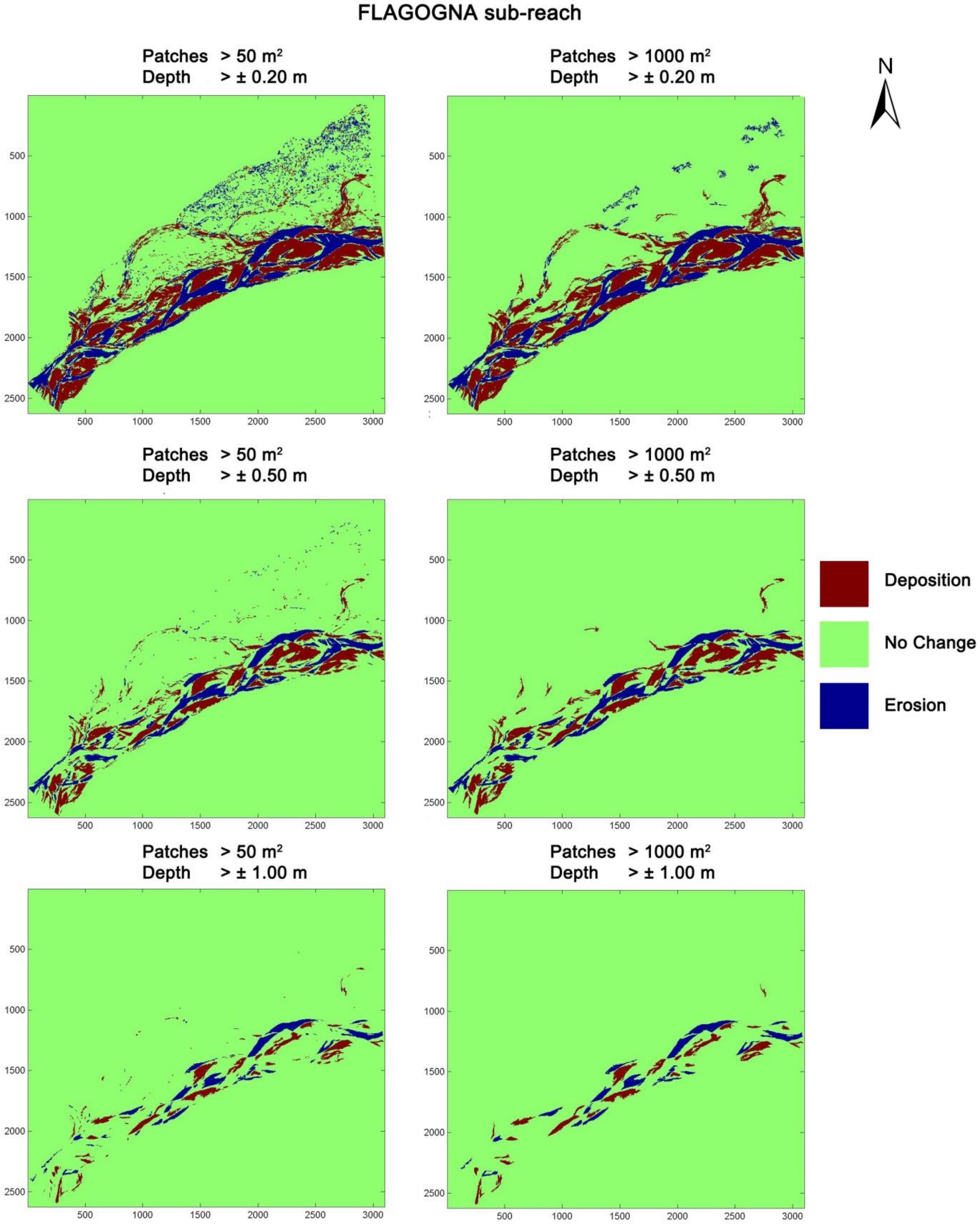

Figure 78. *Principal erosion-deposition extraction by PrEDA of Nove sub-reach. Different minimum threshold of surface and depth of erosion or deposition characterizes the different sub-figures.*

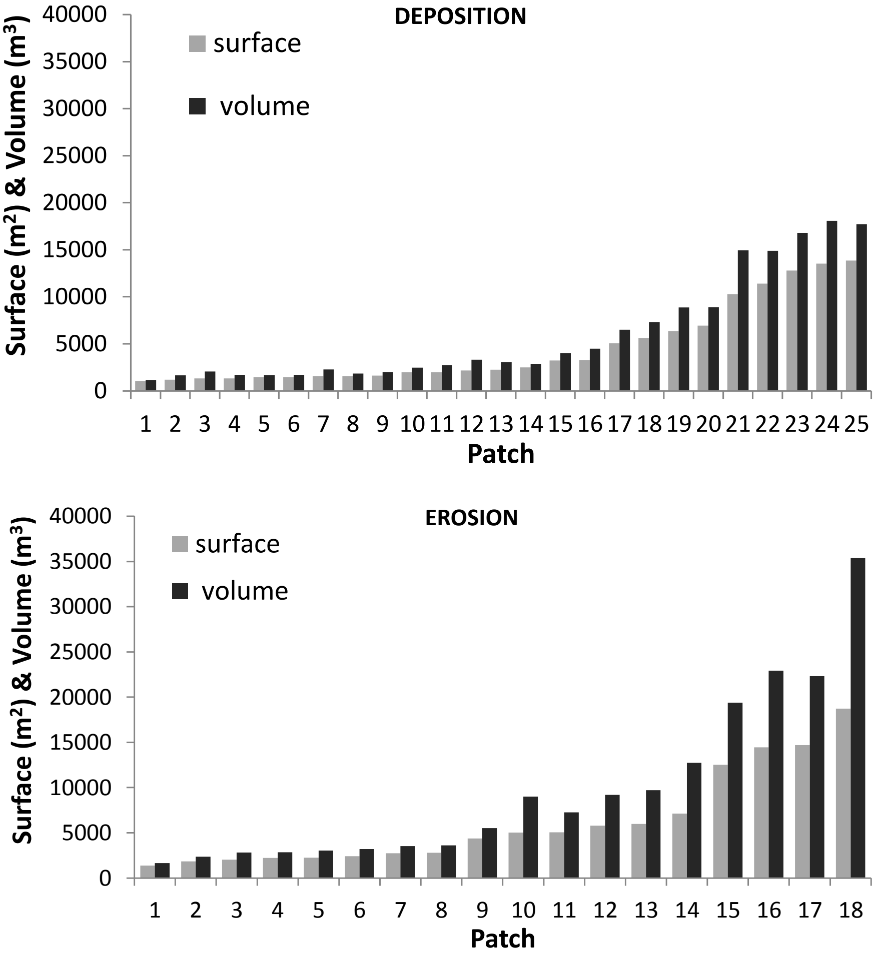

Figure 79. *Surface and volume of deposition and erosion among the different patches of Flagogna sub-reach.*

Analysing Figure 78 we can note that the deposition is slightly greater than the erosion, but more fragmented. The most significant deposition (> 1000 m^2 and > ± 1.00 m - Figure 76) is represented by 26 patches with a surface-volume ratio trend that becomes greater as the patch surface increases. The most significant erosions are in 18 patches. Analysing Figure 79 we can note, as for the Brenta and Piave River, that the bigger the patches considered the greater the ratio surface/volume becomes, and up to around 1:2.

12 Terrestrial Laser Scanner on Hydraulic Cross Section Scale

12.1 Terrestrial Laser Scanner Uncertainty Analysis

12.1.1 Registration errors

The registration phases, useful for georeferencing different scans together, have reported an average error (averaging all the samples) of 0.001 m, with a minimum error equal to 0.000 m, a maximum error of 0.006 m and a standard deviation of 0.001 m. With a maximum of four control targets for each experiment we have deleted the worst for each sample to decrease the final registration errors. In some cases not all four targets were available. As reported in Figure 80 the point intensity value for some targets has not allowed the centre to be found and consequently, the impossibility of using an alternative objective method to find the centre and use it during the registration.

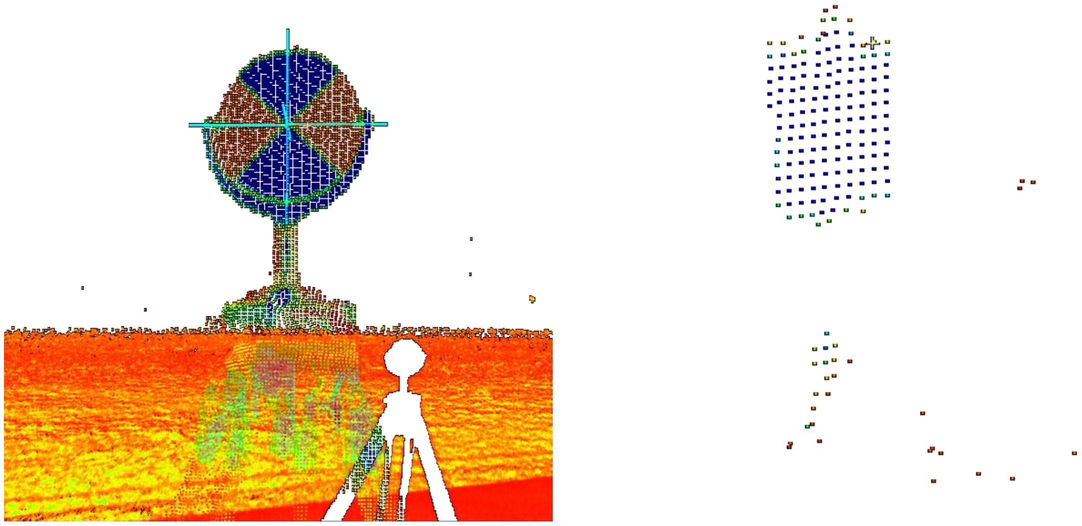

Figure 80. *Error in targets acquisition.*

For each kind of experiment, reported in Table 6, nine-ten scans repetition of the same surface have been done. Thanks to the application of "CeA tool" the average density and the right cell size to interpolate a DTM were calculated. The values reported in Table 8 represent the mean of ten scan repetitions. Among the different experiments we can note that more the range between the TLS and the patch increases, the quality of the final DTM decreases (increasing the cell size).

Table 6. *Right cell size calculation for each kind of experiment in function of the mean density.*

	EXPERIMENT	mean density pts/0.0025 m^2	mean density pts/0.01 m^2	mean density pts/m^2	min cell size m
GRAVEL EXP.	Range 10 m	10.8	43.0	4302.1	0.015
	Range 15 m	3.3	13.0	1304.2	0.028
	Range 20 m	1.3	5.1	505.0	0.045
	Moving TLS	8.4	33.6	3363.2	0.017
	Moving Targets	8.3	33.1	3312.5	0.017
	Moving Both	9.0	35.9	3592.0	0.017
FLAT EXP.	Vert. B/W poster Range 10 m dark	58.9	235.8	23578.5	0.007
	Vert. B/W poster Range 10 m light	58.7	234.7	23473.5	0.007
	Vert. B/W poster Range 15 m dark	26.0	103.8	10380.4	0.010
	Vert. B/W poster Range 20 m dark	14.8	59.3	5932.3	0.013
	Hor. B/W poster Range 10 m dark	10.0	40.0	4004.6	0.016
	Hor. B/W poster Range 15 m dark	1.8	7.1	709.6	0.038
	Hor. B/W poster Range 20 m dark	0.8	3.2	317.5	0.056
	Hor. B/W poster Moving Targets	24.9	99.5	9945.0	0.010
	Hor. Wood Range 10 m dark	14.4	57.5	5753.6	0.013
	Hor. Wood Range 15 m dark	3.6	14.4	1435.7	0.026
	Hor. Wood Range 20 m dark	0.7	2.8	279.4	0.060
SPHERES EXP.	Hor. Range 10 m	9.3	37.1	3705.8	0.016
	Hor. Range 15 m	2.7	10.9	1086.8	0.030
	Hor. Range 20 m	1.4	5.7	568.4	0.042
	Vert. Range 10 m	60.6	242.5	24247.5	0.006
	Vert. Range 15 m	26.9	107.6	10763.4	0.010
	Vert. Range 20 m	15.3	61.1	6114.7	0.013
FESHIE EXP.	Patches 1 moving	71.8	287.3	28731.5	0.017
	Patches 2 Range 5 m	58.3	233.3	23331.6	0.007
	Patches 2 Range 10 m	6.9	27.6	2755.1	0.019
	Patches 2 Range 15 m	2.2	8.9	891.3	0.034
	Patches 2 moving	10.1	40.4	4038.1	0.016
	Patches 2 Range 5 m	56.8	227.4	22739.9	0.007
	Patches 2 Range 10 m	8.2	32.9	3292.1	0.017
	Patches 2 Range 15 m	3.5	13.8	1380.7	0.027
	Patches 2 Range 20 m	1.2	4.7	467.7	0.046

In our case, considering the horizontal experiments at five meters of range, the right cell size, that guarantees at least one point for each cell, is 0.007 m. At ten meters the evaluated cell size is between 0.013 m and 0.019 m, fifteen meters between 0.026 m and 0.034 m and twenty meters between 0.042 m and 0.060 m. The range of values for 10 m are confirmed both for the range and moving experiments. It is interesting to note the difference in density between the horizontal and vertical experiments. From horizontal to vertical experiments, at the same range the points density increases 6 - 10 times (Table 6). In addition, comparing the wood scans with the black and white poster one (B/W poster) of the flat experiments, at the same range we can note that in the B/W poster experiments there are fewer points than the wood experiments (Figure 81); around 30% and 50% less at 10 m and 15 m range respectively. At 20 m of range it seems that the density becomes more comparable.

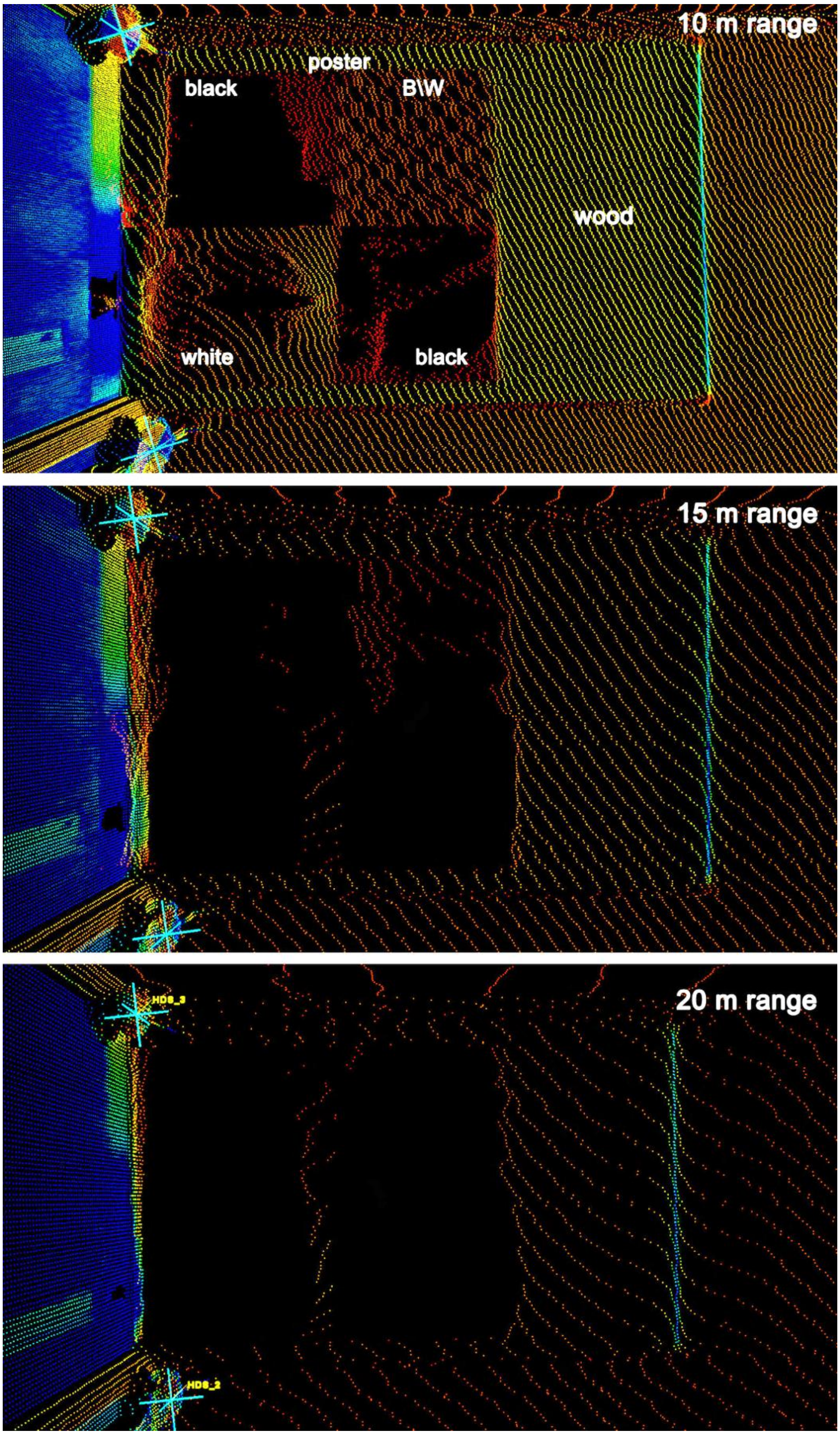

Figure 81. *Difference in density scanning different materials and colour at 10 m, 15m and 20 m from the scanner.*

12.1.2 Detrending methods comparison

The table below reports the roughness calculation using two detrending methods (described in section 9.1.2): the one implemented in CeA versus a moving window 3x3 cell. This comparison has been applied in the range and moving gravel experiments.

***Table 7**. Detrending method comparison between ToPCAT implemented in CeA versus a moving window 3x3 cell.*

RANGE EXPERIMENTS	**Average Roughness (m) ToPCAT detrending**			**Average Roughness (m) Moving wondow 3x3 detrending**		
GRAVEL SCANS	**10 m**	**15 m**	**20 m**	**10 m**	**15 m**	**20 m**
Scan1	0.006	0.004	0.003	0.007	0.005	0.004
Scan2	0.006	0.004	0.004	0.006	0.005	0.005
Scan3	0.005	0.004	0.004	0.006	0.005	0.004
Scan4	0.005	0.004	0.003	0.006	0.005	0.004
Scan5	0.006	0.004	0.004	0.006	0.005	0.004
Scan6	0.005	0.004	0.003	0.006	0.005	0.004
Scan7	0.005	0.004	0.003	0.006	0.005	0.004
Scan8	0.006	0.004	0.004	0.006	0.005	0.005
Scan9	0.006	0.004	0.003	0.007	0.005	0.004
Scan10	0.005	0.004	0.003	0.006	0.005	0.004
AVERAGE	**0.005**	**0.004**	**0.003**	**0.006**	**0.005**	**0.004**

MOVING EXPERIMENTS	**Average Roughness (m) ToPCAT detrending**			**Average Roughness (m) Moving wondow 3x3 detrending**		
GRAVEL SCANS	**mov. HDS**	**mov. TLS**	**mov. BOTH**	**mov. HDS**	**mov. TLS**	**mov. BOTH**
Scan1	0.005	0.005	0.005	0.005	0.005	0.006
Scan2	0.005	0.005	0.048	0.006	0.005	0.047
Scan3	0.005	0.004	0.005	0.005	0.005	0.006
Scan4	0.004	0.005	0.005	0.005	0.006	0.005
Scan5	0.004	0.005	0.005	0.005	0.006	0.006
Scan6	0.004	0.004	0.004	0.005	0.005	0.005
Scan7	0.005	0.005	0.005	0.005	0.006	0.005
Scan8	0.004	0.004	0.004	0.005	0.005	0.005
Scan9	0.004	0.004	0.004	0.005	0.005	0.005
AVERAGE	**0.005**	**0.005**	**0.010**	**0.005**	**0.005**	**0.010**

Observing the roughness results between the two detrending methods, it seems that no significant differences can be highlighted. Observing the range experiments it seems that the roughness computed with the “ToPCAT detrending method” of Brasington et al. (2012) is 1 mm lower than the moving window method.

12.1.3 Repeated scan uncertainty analysis

Thanks to the Cell Analyser toolbox applied on each scan, it is possible compare all the cells in common derived from each scan repetition on the same object, for each kind of experiment. All the statistics described in section 9.1.2 were calculated for each cell of each scan. The analyses were done with a cell size of analysis equal to 0.05 m. It is important to note that in this case the cell size is just an area of analysis. Indeed, from the point density analysis (derived by CeA and shown in table 6) we can evaluate the maximum threshold of detail representable, which is the minimum cell size allowed with its average density.

After applying CeA for each scan (note that we can do it simply by putting all the scans in the same folder, and CeA will elaborate them automatically), we can apply “Cell Analyser Error Dataset” that for each kind of experiment, among all the scans, finds the cells in common and computes the standard deviation from a scan defined as reference. The standard deviation of the same cell in common, from all the repetitions of each experiment, is defined as the error. Indeed, this represents the variability that we can find scanning the same surface (the same cell area) from different positions (Moving Experiments) or simply repeating the scan from the same position at a defined range (Range Experiments). Thanks to this tool, cells scanned 9 - 10 times were used to calculate their errors versus different factors described below.

Five main factors, with a total of 6911 cell samples, were collected: density, roughness, range, intensity and angle of incidence.

The point density per unit of surface is one of the main factors that control the level of DEM resolution. High density allows a more detailed elevation model.

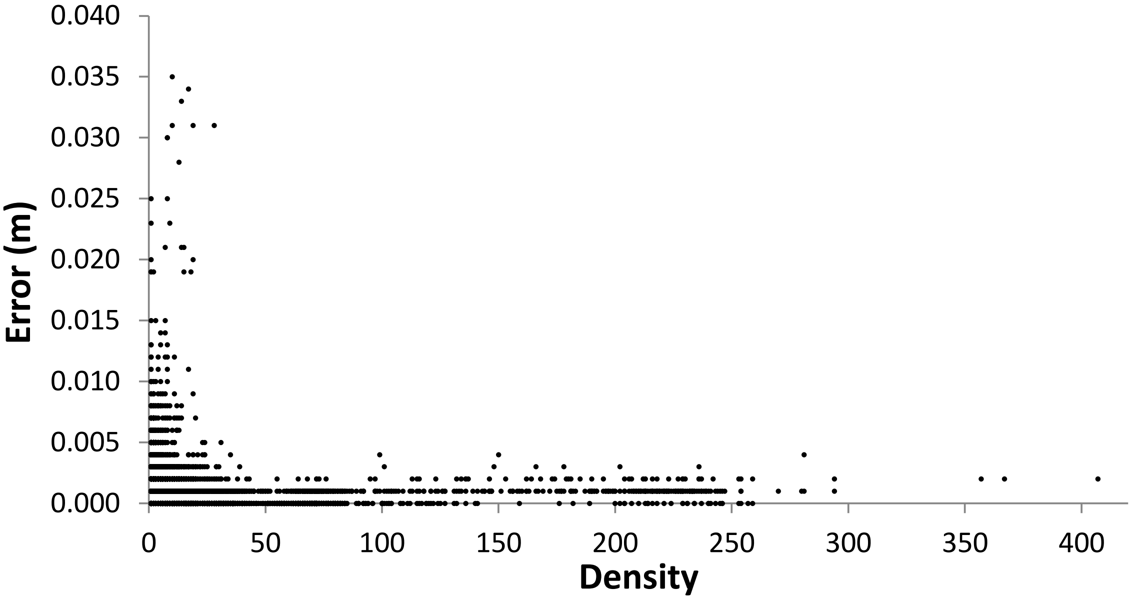

Figure 82. *Error variability accounting different scan repetition of the same patch versus density.*

Figure 82 shows the density for a cell of 0.05 m associated with the variability (error) of surveying the same cell 9 - 10 times with all the kinds of experiments. Note that the error is always lower than 0.005 m (for cell at 0.05 m) , with a point density greater than 30 points per cell. The maximum error registered is equal to 0.035 m.

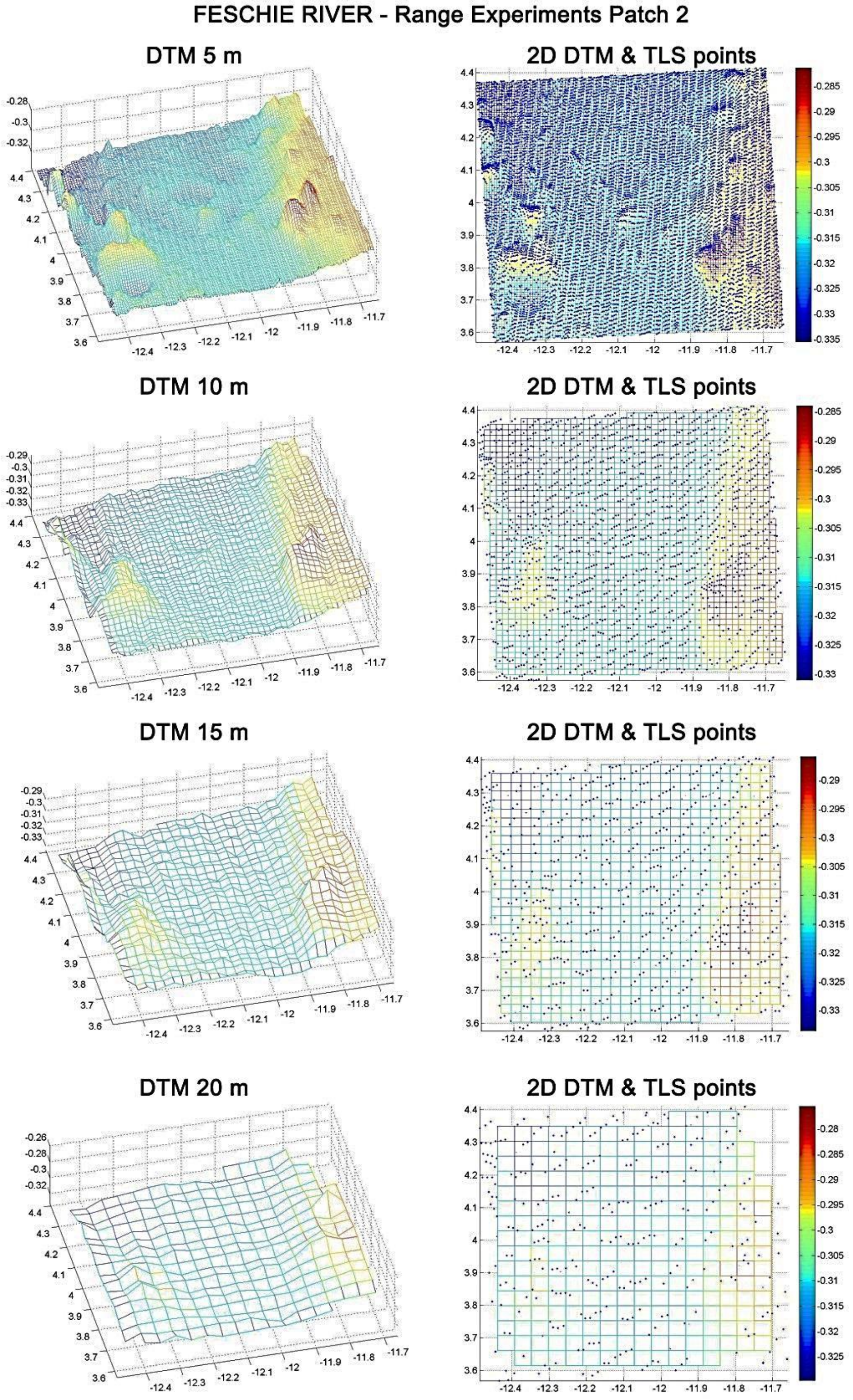

__Figure 83.__ Range effect on DTM building using TLS positioned at 5 m, 10 m, 15 m and 20 m on the Feshie river (patch 2). The figure also shows the loss of point density on the right hand side.

Figure 83 shows that the point density is influenced by range factor. The more the range increases, the lower the density becomes. Consequently, as shown in Figure 83, for Feshie River patch 2 the resolution decreases significantly: 5 m range with 0.007 m, 10 m range with 0.017 m, 15 m range with 0.027 m and 20 m range with 0.046 m (Table 6).

Therefore we are expecting that, if we relate the error to the range, it should be greater the more the range increases. Observing Figure 84, which combines all the experiments, it seems that this hypothesis is not verified. Indeed the range at 10 m has more cells with greater error than the ones with more range.

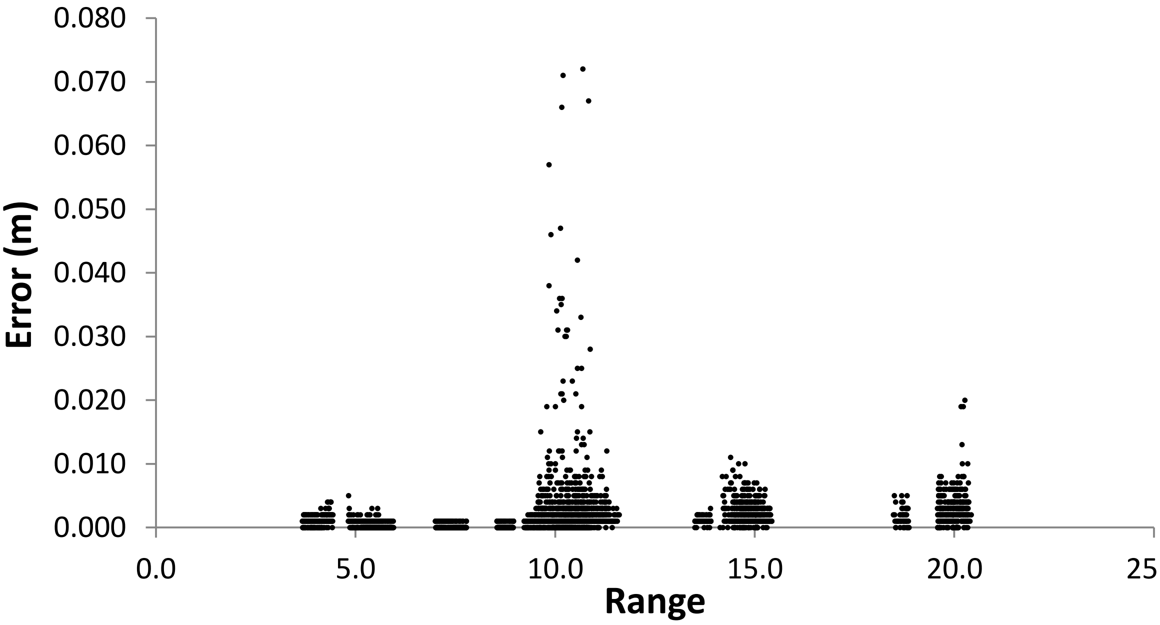

Figure 84. *Error variability accounting different scan repetition of the same patch versus range (m).*

Great variability at 10 m, in our case does not have to be interpreted badly, indeed the moving experiments have only been carried out at 10 m, while the range experiments at 5 m, 10 m, 15 m and at 20 m.

Figure 85 shows the DTM resulting from the moving TLS and target experiments of the gravel patch. Observing the different DTMs of the same patch, but acquired from different positions, it is evident that if we have just one scan to interpolate a DTM (each scan produces different points dislocation to interpolate the DTM), the final elevation models will differ from one another. In addition, observing Figure 85, it seems that the resulting DTMs have a “morphology” oriented with the scan source.

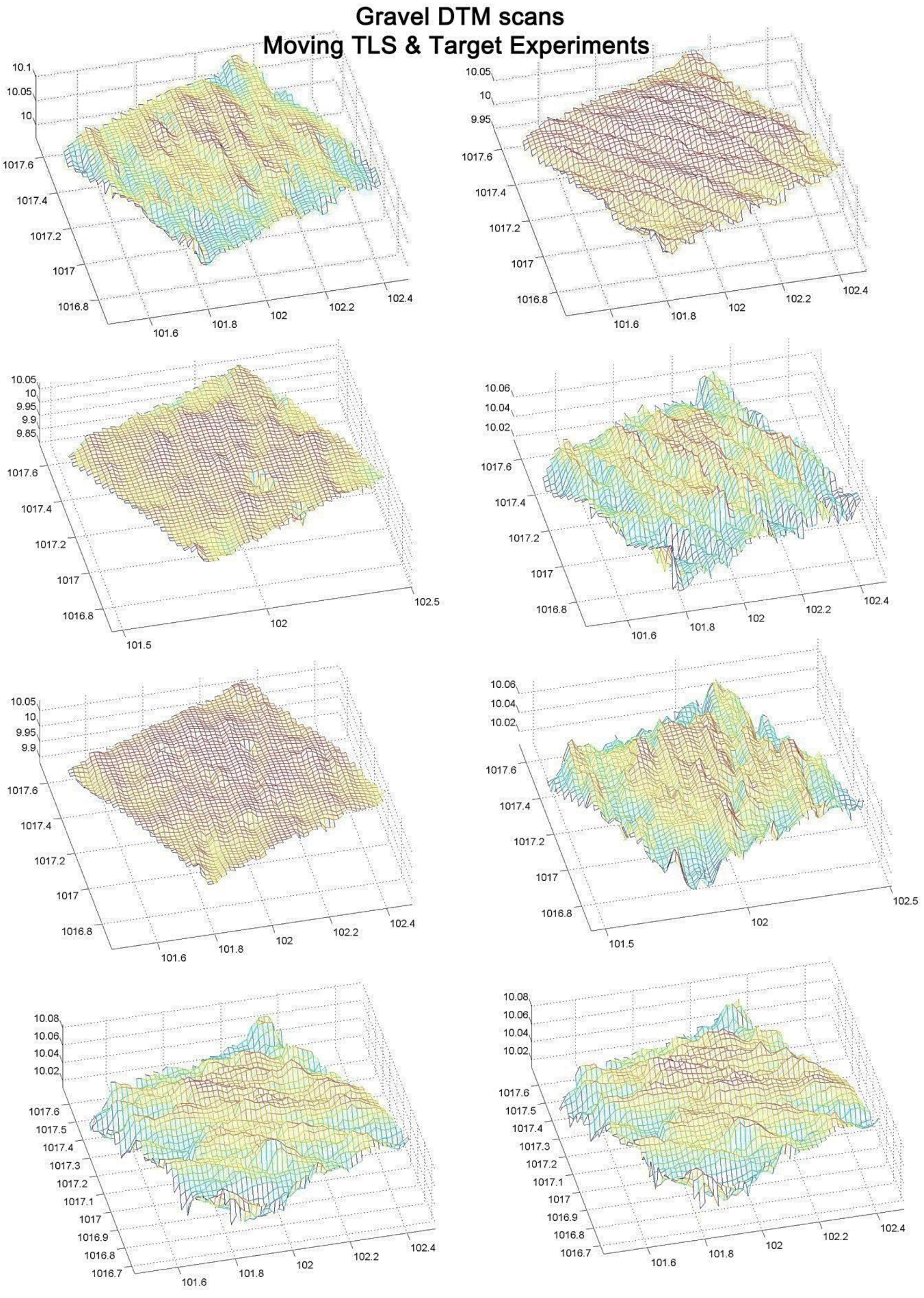

Figure 85. *Moving TLS and targets effect on DTM building. DTMs of the same patch made of gravel scanned from different TLS and target positions.*

To confirm that the moving experiments have more variability than the range one, Figure 86 and Figure 87 show the variability in elevation and density for the same cell scanned more times for the moving and range gravel experiments respectively.

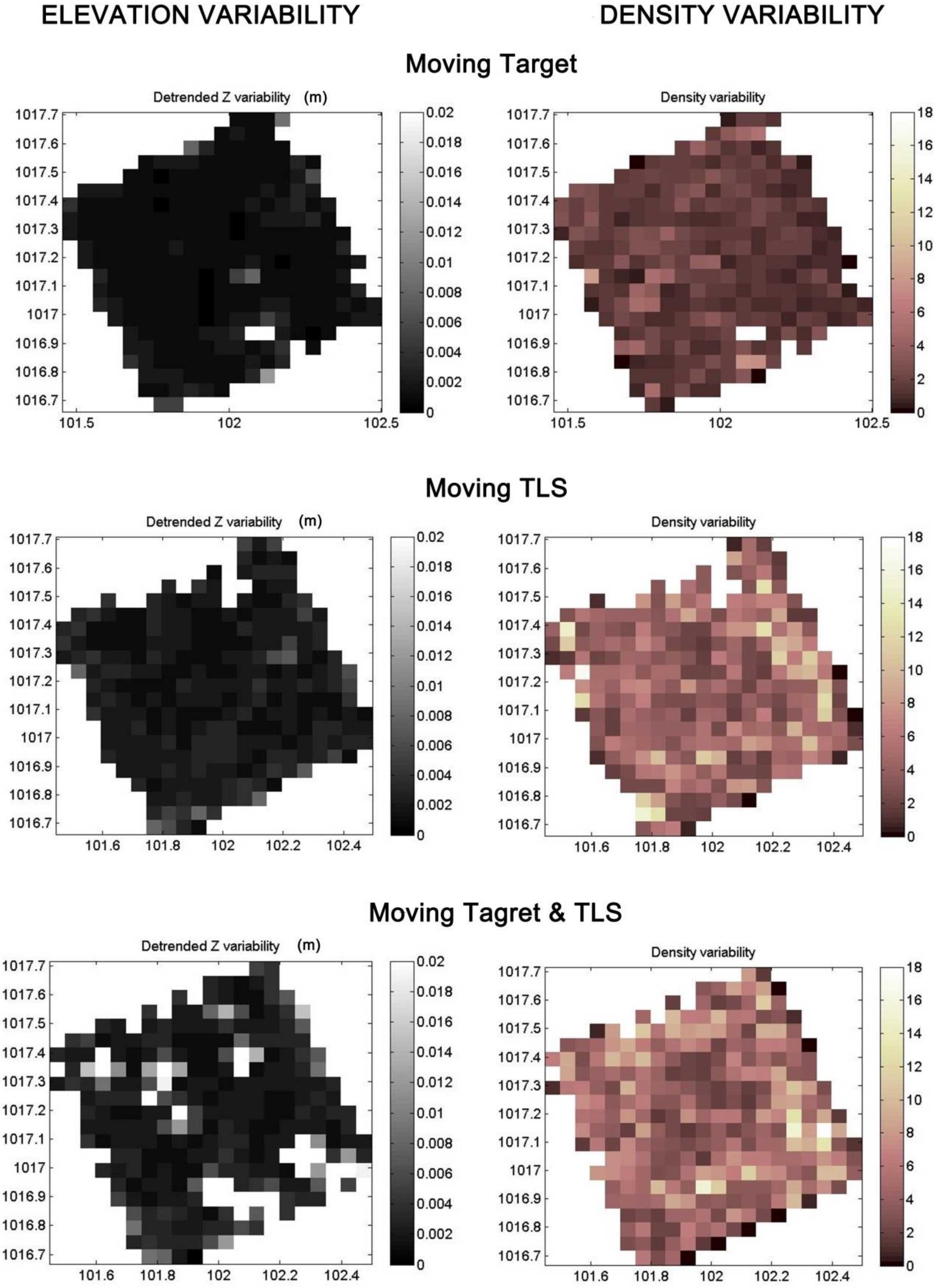

Figure 86. *Detrended elevation (Z) variability and density variability scanning the same gravel patch 10 times moving the TLS, the targets and both.*

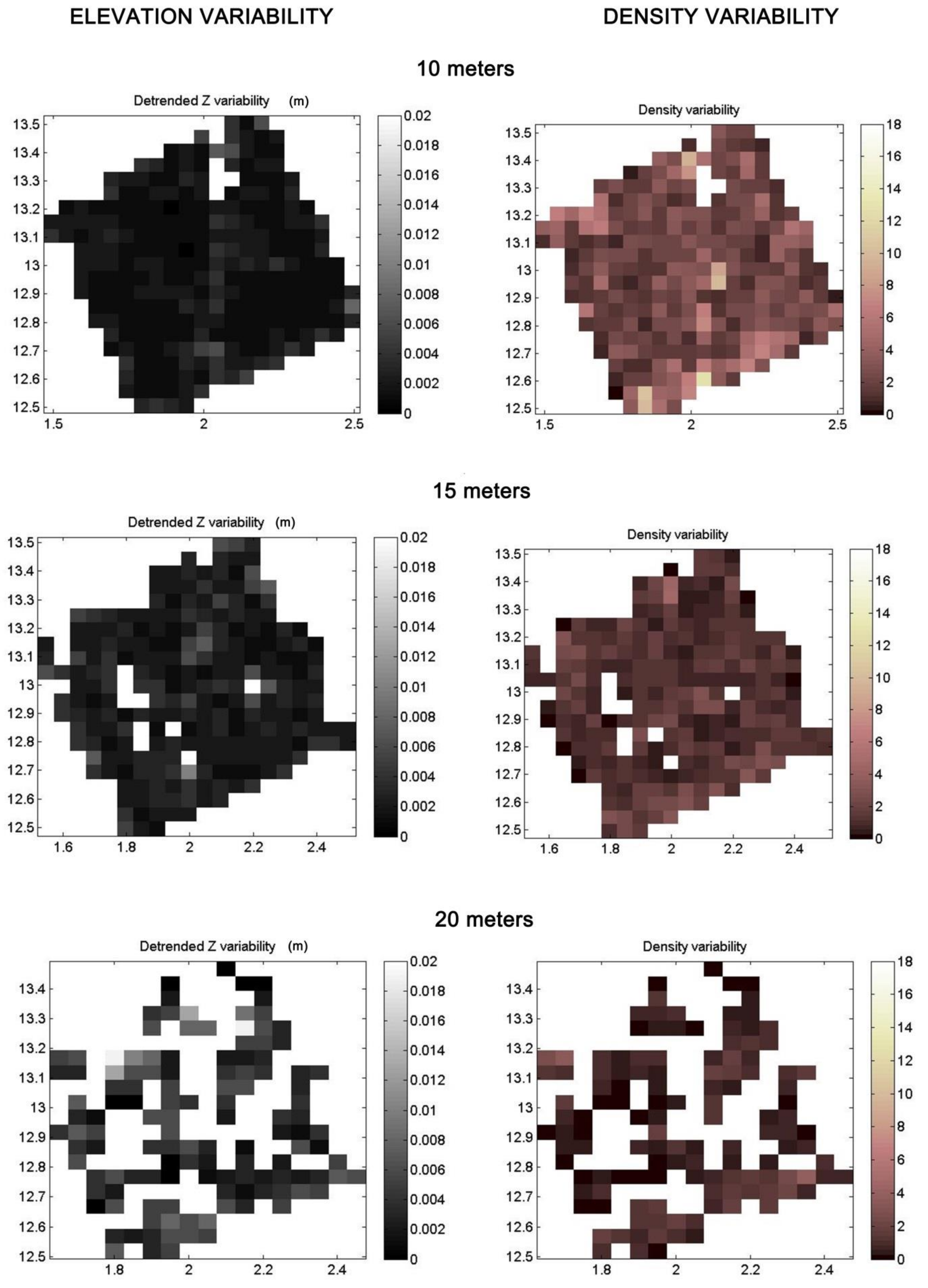

Figure 87. *Detrended elevation (Z) variability and density variability scanning the same patch 10 times (gravel experiments) from the same position.*

Also in this case the variability is the standard deviation of the elevation and density variation of the same cell among the different scans. It is interesting to note that the moving TLS and target experiments have the highest variability registered, whereas for the range experiments as the range increases the areas without points increase. To avoid areas without points it is necessary to increase the cell size (as reported in table 6 and shown in Figure 83). Considering the mobility the kind of experiments can be classed in relation to a "moving factor". Where:

0 = TLS and TARGET FIXED
1 = TLS or TARGET MOVED
2 = TLS and TARGET MOVED

This factor is graphed versus the error in Figure 88 to know if its influence the cell variability.

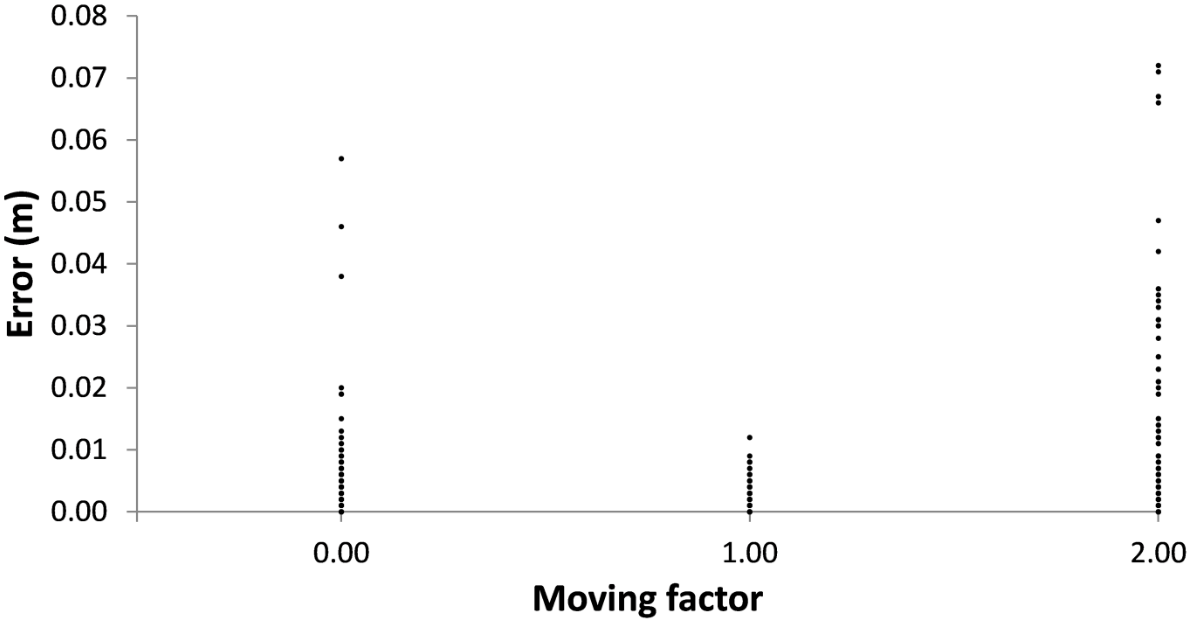

Figure 88. *Error variability without moving TLS or Targets (0), moving TLS or Targets (1) or both (2).*

Observing Figure 88, seems that the moving factor is one of the causes of great variability. Indeed we can observe that we have more error when we move both TLS and targets with respect to moving only one of these. It is interesting to note that some significant errors are also shown in the condition of fixed TLS and targets (every scan repetition made from the same position, with fixed targets, at a defined range). Therefore other causes can influence the variability besides the point density, range and moving factor.

Another source of error that can influence the importance of the uncertainty in the final digital elevation model is the roughness. This factor is the standard deviation of the points elevation computed cell by cell. The effective roughness of the survey area also influences the cell size to acquire. Indeed the more complex a surface is, if we wish to produce a reliable DEM, the more we need a small cell (high resolution). This is translatable as more point density.
Figure 93 shows the roughness for a cell of 0.05 m with the associated variability of surveying the same cell 9 - 10 times with all the kinds of experiments.

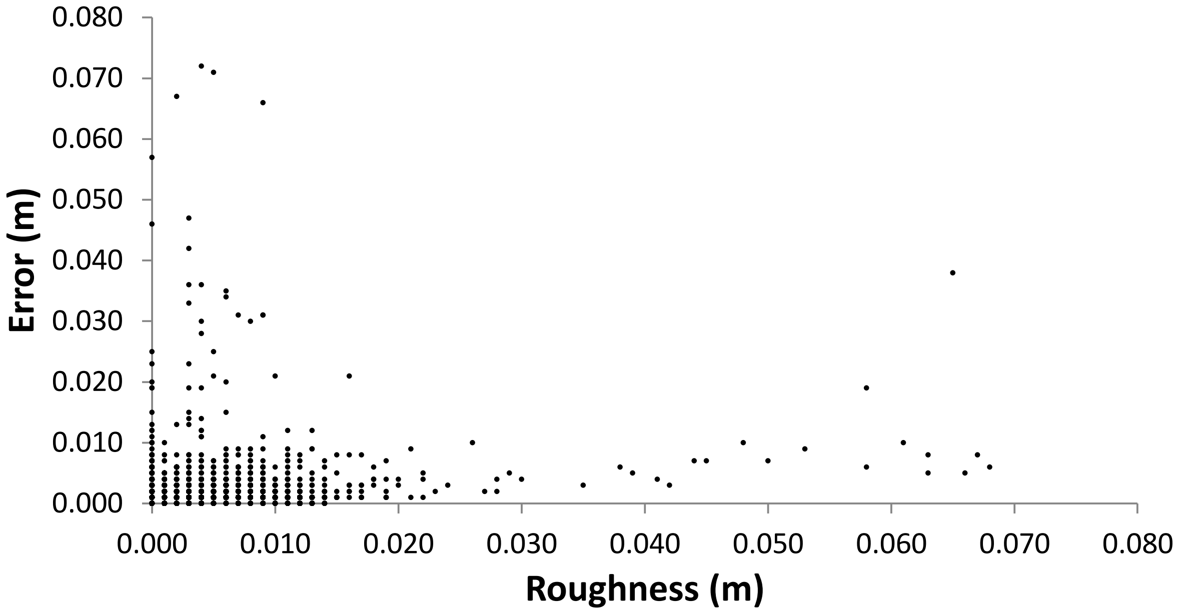

Figure 89. *Error variability accounting different scan repetition of the same patch versus roughness (m).*

Considering Figure 89, a not clear and logical relation seems to appear. Indeed with more roughness, we would expect more variability due to surveying the same patch from different position and different range. In other words, a very rough surface should show more variations than a flat surface. Indeed in topography, a flat surface (with low roughness in our case) requires fewer points to be represented with respect to a more complex surface (high roughness in our case). Therefore in this case a greater range, translatable as availability of less point density, does not significantly influence the error also increasing it or scanning from different positions. This situation is not completely verified in our experiments (Figure 89). We can recognize from 0.015 to 0.070 m of roughness a positive increase of error as expected, but there are some points in Figure 89 (representing the cell roughness) with a high error (up to 0.074 m) also from 0.00 to 0.015 m roughness, which is the flat condition. This means that the error has other influencing factors apart from density, range and roughness. It is important to take into account that the roughness, calculated as the standard deviation of the point elevation, changes with the cell size.

In Figure 90 different materials (laid out in horizontal position) and colours were scanned from different ranges (10 - 15 - 20 m). Black and white posters (B/W – Figure 34) made of paper and wood were compared.

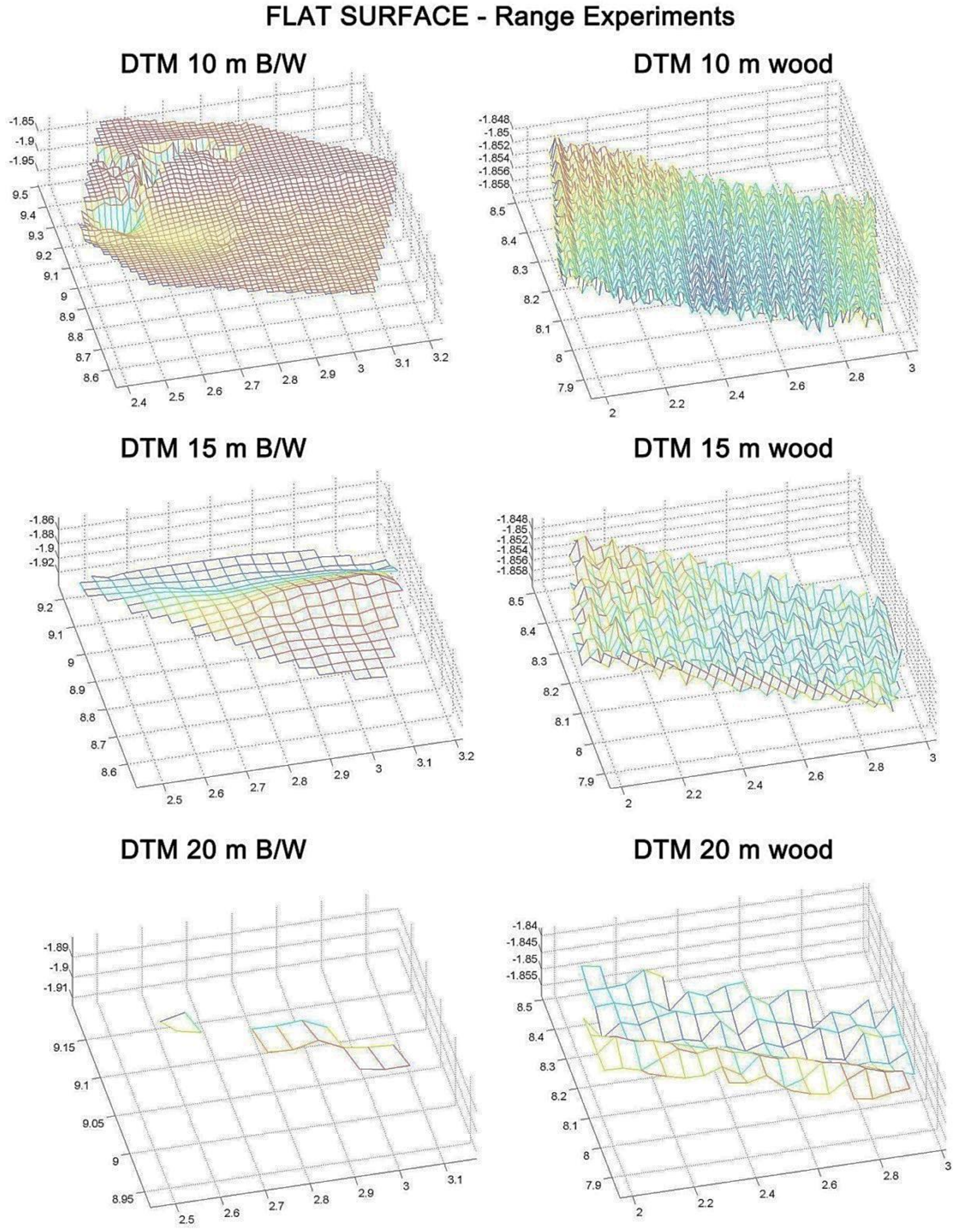

Figure 90. *Range effects on DTM building scanning different materials and colour: black and white flat surface and brown woody surface.*

All the surfaces are completely flat. In the wood scans the resulting DTM has very low variations in elevations ± 0.002 m (on the detrended raster) despite the range increasing. On the other hand the situation in the B/W poster is different. Considering the laser return it is evident that the B/W surface does not guarantee the same density as the wood surface, and the difference increases as the range becomes bigger. In addition, considering the B/W scan at 10 m, it seems that the black parts produce less returns than the white one; confirmed also in Figure 81. It is interesting to note that the difference from the black and white part is not just in density but a small implausible difference in elevation is also recognisable (Figure 90).

Therefore, it seems that the material and the colour influence the accurancy of the laser return. A factor that could consider the variation in reflectivity, is the laser intensity. Figure 91 shows the intensity associated with the variability by surveying the same cell more than once from the same or not the same position at defined range.

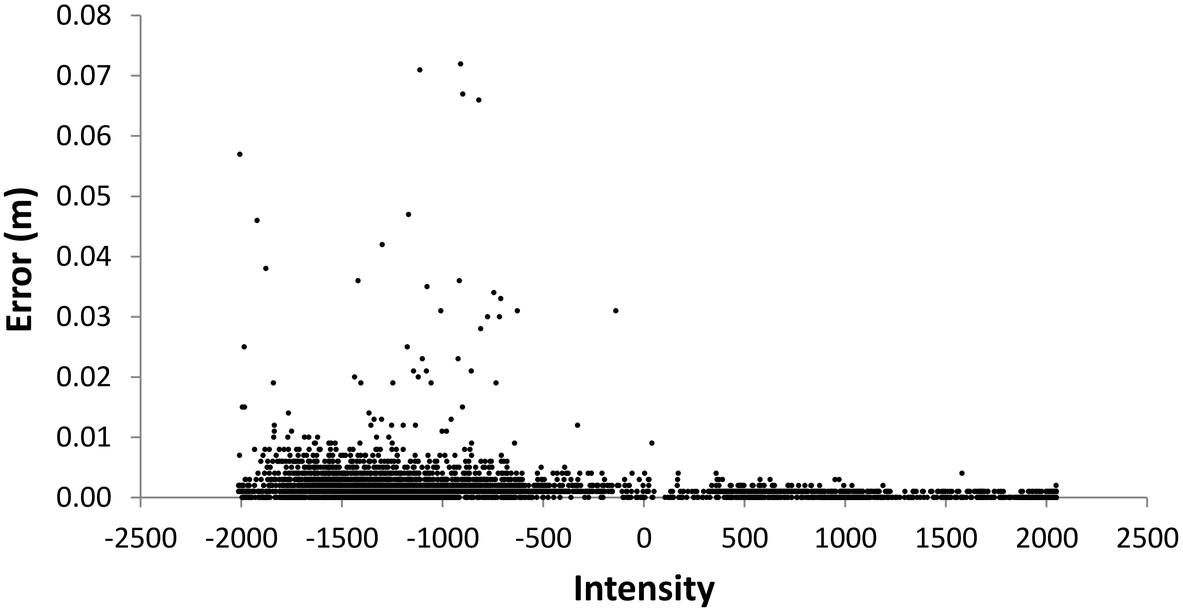

Figure 91. Error variability accounting different scan repetition of the same patch versus intensity.

Low intensity values are represented by dark or very "sink" surfaces, whereas high values represent clear surfaces with a good reflectivity versus the laser sources. Confirming as shown in the DTMs of Figure 90, the dark areas present more error than the clear ones (Figure 91). From -2000 to -500 of intensity, we registered errors up to 0.073 m and from -500 to 0 errors up to 0.032 m. On the other hand, from 0 to 2000 of intensity no errors greater than 0.005 m were registered.

Finally, another factor worth being considered: the angle of incidence of the laser to the scanned object (angle between the zenith and the laser beam). Figure 92, as for the previous factors considered, shows the relation between the error and the angle of incidence, using the dataset from all the kinds of experiments.

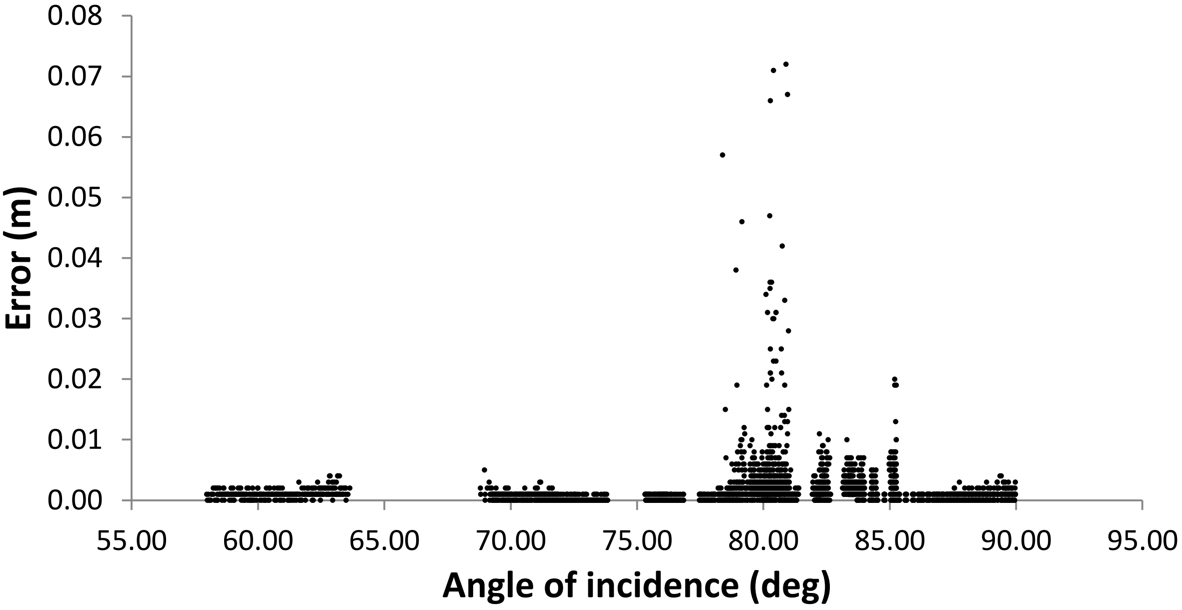

Figure 92. *Error variability accounting different scan repetitions of the same patch versus angle of incidence (deg).*

It is interesting to note that up to ~ 77 degrees the variability is lower than 0.005 m, while with an angle from ~ 77 to ~ 86 degrees the maximum registered error rises to 0.075 and no significant errors are registered from ~ 86 degrees. Trying to understand the reason for this, the angle of incidence was related to the range (Figure 93).

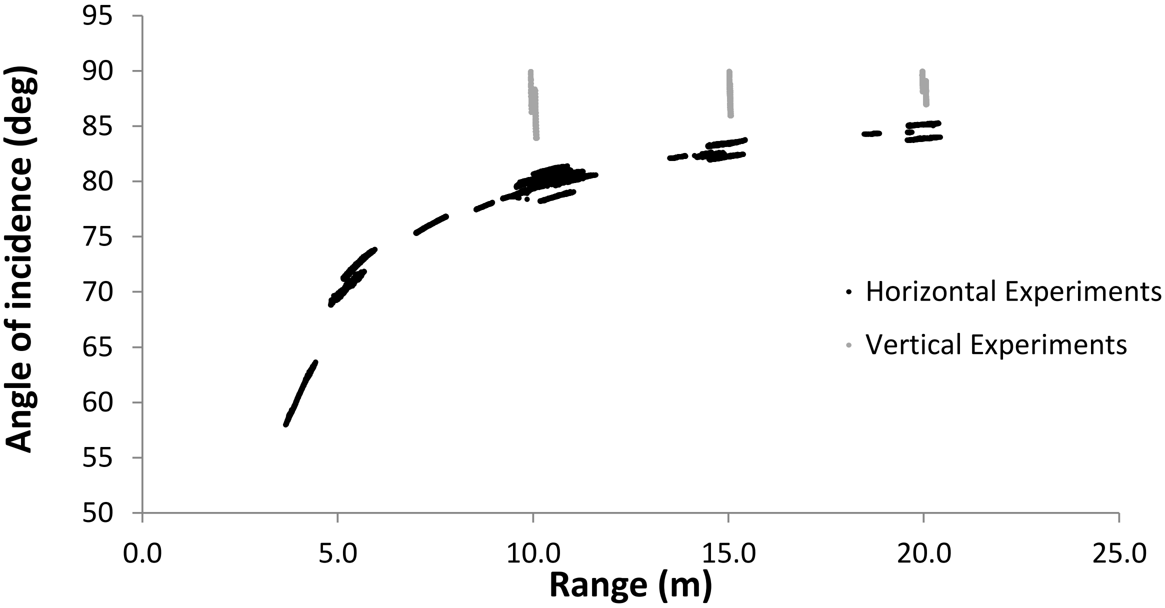

Figure 93. Angle of incidence versus three-dimensional range between TLS laser source and point acquired for horizontal and vertical experiments.

Figure 93 considers the horizontal and vertical experiments separately. It is interesting to note that for the horizontal experiments a clear relation exists between the angle of incidence and the range. Analysing this relation it seems that as the range increases in the horizontal experiments, its angle became more similar to the vertical one. If we delete the vertical experiments points from Figure 92 we can observe that the highest errors are only from the horizontal ones.

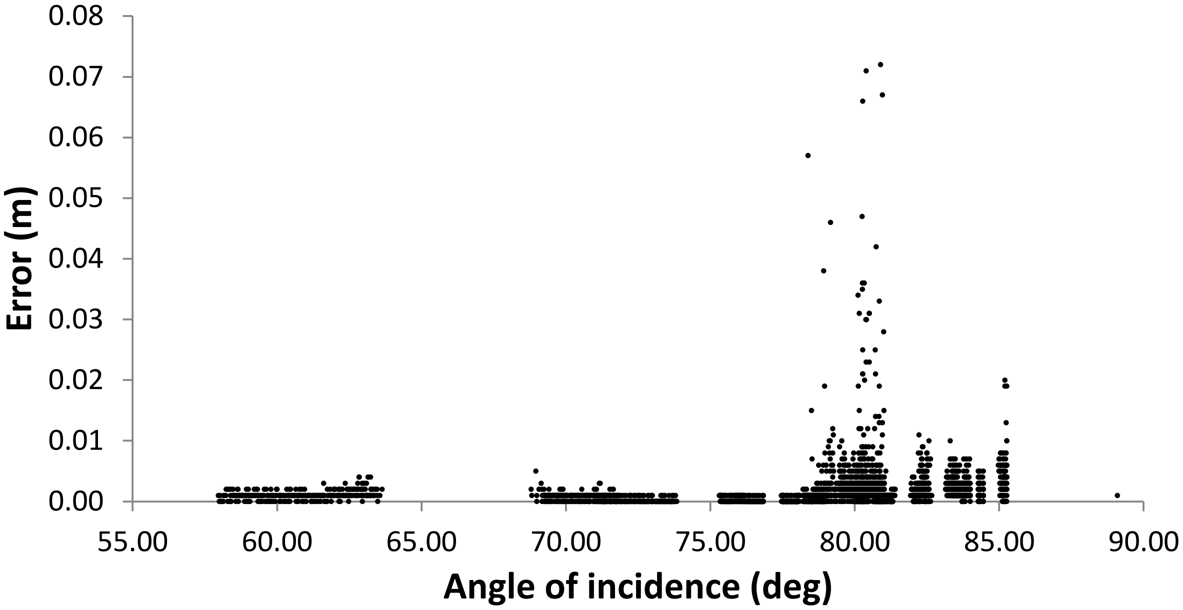

Figure 94. *Error variability accounting different scan repetition of the same patch versus angle of incidence (deg) without vertical experiments.*

Observing Figure 94, it seems that the angle of incidence has a significant effect on the error. To identify exactly what happens when we change the angle of incidence, a comparison of DTMs with the TLS points inside each cell for the spheres experiments scanned at different ranges and in horizontal and vertical position, is presented in Figure 95. As verified in Figure 83, the more the range increases, the lower the point density becomes, but this decrease in density with range is much greater when the scanned area has a horizontal with respect to a vertical dislocation. The difference in density from vertical to horizontal experiments at 10 m, 15 m and 20 m are equal to - 85%, - 75% and - 75% respectively. The mean densities of these and the other experiments are shown in Table 6. This difference in density means less detail and a worse quality in the final DTM. If we aim at representing with a digital model a spheres surface, at a defined range, the vertical experiments (as shown by the points dislocation in Figure 95) guarantee the least loss of real morphology.

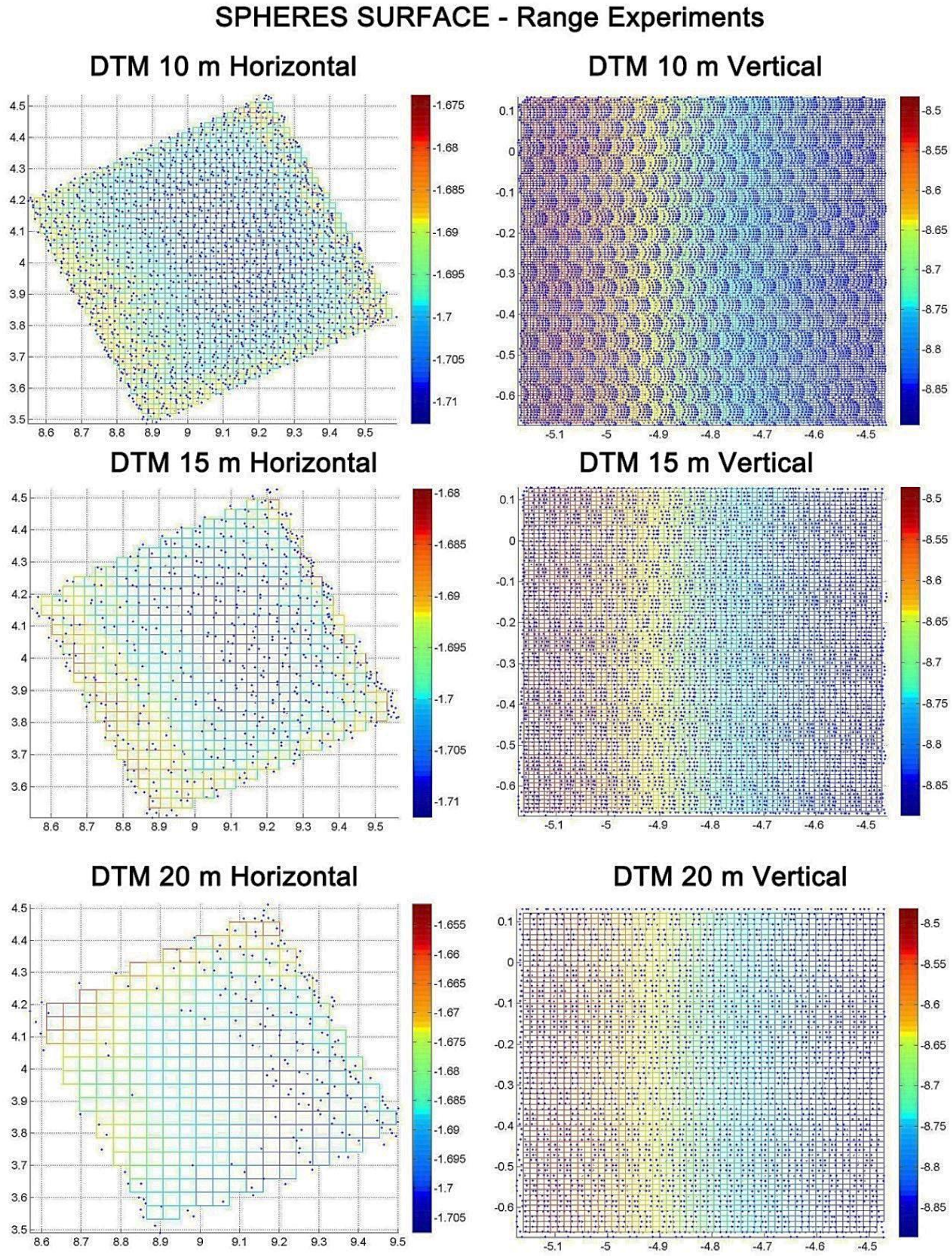

Figure 95. *Angle of incidence and range effect on DTMs building using TLS positioned at 10 m, 15 m and 20 m of a horizontal and vertical sphere surface (0.80 x 0.80 m).*

12.1.4 TLS uncertainty model for TLS analysis

Aiming at an objective quantification of a distributed uncertainty model, we need to evaluate which error factors could be used to implement it in *CeAfuzzy* (Matlab script; see 9.1.3 section). In the last section (sub-chapter 12.1.3) six potential error factors were considered: cell density, range 3D, moving factor, roughness, laser intensity and angle of incidence. Following the Wheaton *et al.* (2010) approach (explained in section 9.1.3), it is necessary to build up the fuzzy rules, combining non-related error factors. These components have to show a clear trend to allow a classification (low, medium and high in our case). Among the error factors considered, the density, intensity and angle of incidence have a clear error trend. The concomitance of more factors that act together over the range 3D, moving factor and roughness (with the analyses that have been carried out), it seems not to be possible to have a clear and usable trend. These concerns seem to have sense because, aiming at realizing detailed DTMs, an increase in range is equal to a decreasing point density. In addition, more and more the density per unit of surface increase, rough surfaces can be better interpolated, also avoiding the problem showed with the moving factor, that if we do not have enough density and a homogeneous point cover, the scan position significantly influences the final DTM (Figure 85). Therefore a homogeneous density per unit area is able to define the resolution of the final DTM. Taking into account the range, roughness and different scan positions, a homogeneous density can decrease their sources of errors. Although the density is probably one of the most influencing factors in DTMs building, the angle of incidence and laser intensity seem to play a fundamental role.

Combining the angle of incidence with a defined density we able (up to the surveyed range) to define if the surface of the scan is more versus a vertical or horizontal position. Indeed vertical positions of the surface of the scan have high density and high angle, that means less possible error than a surface in the same range, but horizontal (less density and smaller angle), as shown in Figure 95.

Considering also the colour and the material, the laser intensity could be used as the third error factor. Low intensity seems to provide worse data than surfaces that reflect points with high intensity.

Therefore TLS point density, angle of incidence and the laser return intensity have been used in this work to build up the uncertainty model. It is important to know that with “CeAFuzzy” we can also use different error factors and combine them as we want in the “fis” file (that combines the different factor classes to define a class of uncertainty).

The graphical representation of the used factors, their classes, and the classes of uncertainty are shown in Figure 96.

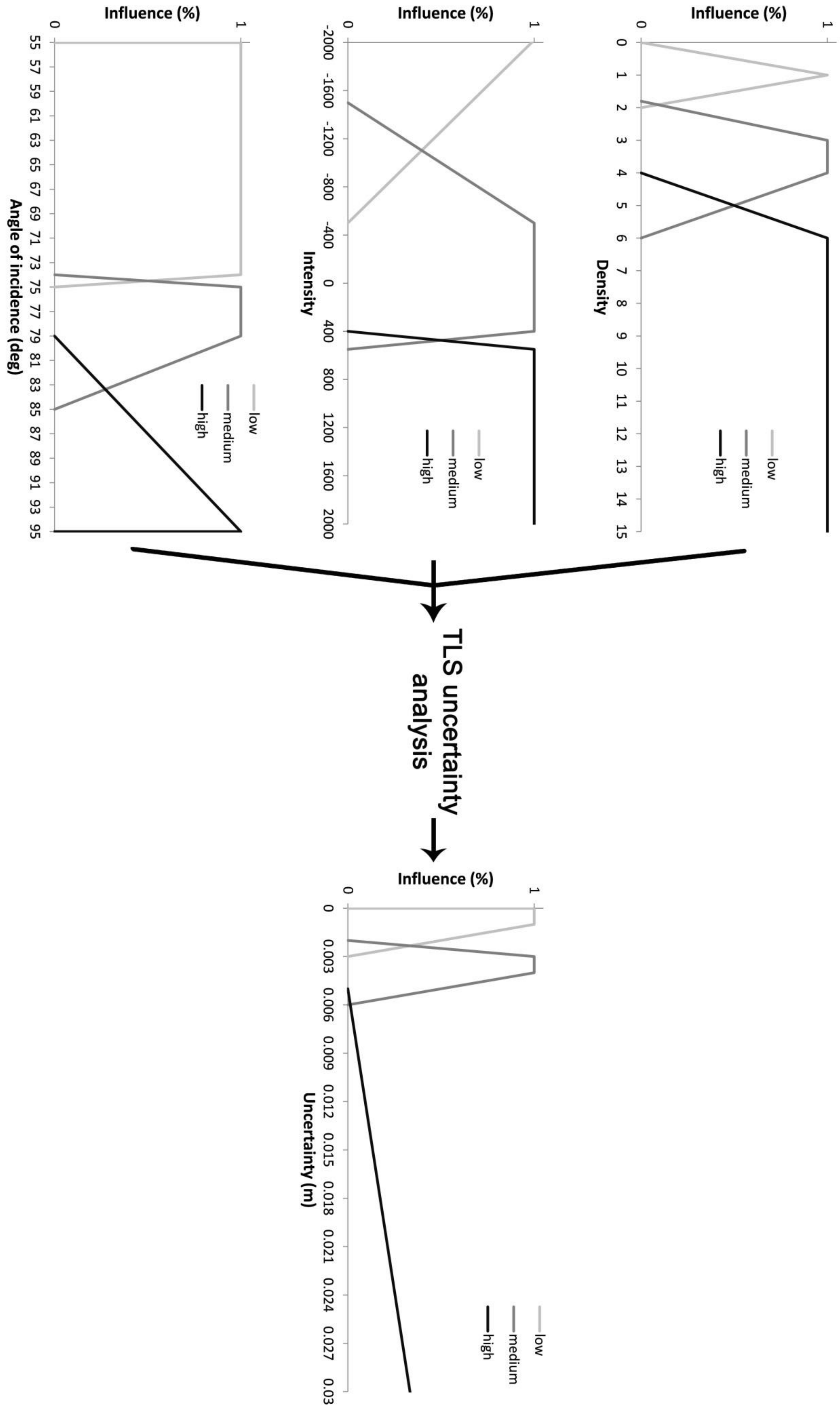

Figure 96. *Factors of uncertainty with the fuzzy level of influence used to define the uncertainty model.*

Different classes were defined trying to follow the trend observed in their relation (Figure 82, 91 and 94 for density, intensity and angle of incidence respectively) versus the error. It should be remembered that the classes also have to be calibrated depending on the instrument used; this operation is possible in the FIS editor of Matlab®. The used classes combinations of the error factors to associate their uncertainty class is shown in Table 8.

Table 8. *Fuzzy rules of the FIS file to combine different factors of uncertainty to define the uncertainty level.*

RULE	DENSITY	INTENSITY	ANGLE	UNCERTAINTY (m)
1	low	low	low	medium
2	low	low	medium	medium
3	low	low	high	high
4	low	medium	low	medium
5	low	medium	medium	medium
6	low	medium	high	high
7	low	high	low	medium
8	low	high	medium	medium
9	low	high	high	high
10	medium	low	low	medium
11	medium	low	medium	medium
12	medium	low	high	medium
13	medium	medium	low	low
14	medium	medium	medium	medium
15	medium	medium	high	medium
16	medium	high	low	low
17	medium	high	medium	medium
18	medium	high	high	medium
19	high	low	low	medium
20	high	low	medium	medium
21	high	low	high	medium
22	high	medium	low	low
23	high	medium	medium	low
24	high	medium	high	medium
25	high	high	low	low
26	high	high	medium	low
27	high	high	high	low

The number of rules to define is in relation to the number of factors and number of classes per each one. In our case 3 classes per 3 factors needs 27 possible combinations to define 3 possible uncertainty levels. The last rule (27th) for example is the case of vertical experiments, which is a case with high density, clear surface, high angle of incidence. In this case the associated level of uncertainty is low; justified by the observation made (Figure 95). In the case of the 3rd rule, low density associated with dark surfaces and high angle of incidence (range ≥ 10 m), a high level of uncertainty was assigned (considering our observations made in section 12.1.3).

At this point a model to evaluate a distributed uncertainty error is ready to be applied with "*CeAfuzzy*". Figure 98 shows an application of the projected uncertainty work flow.

The study area is the first patch of the Feshie River. Three applications were carried out on the same area, at different range (5 m, 10 m and 15 m) to analyse the different resulting DTMs and the corresponding uncertainty models. The figures show the correspondent 3D DTM with shadow effects, the 3D DTM with the cell grid highlighted, the 2D DTM with the TLS points overlapping and the uncertainty raster.

The first one (Figure 97) is the 1st Feshie patch scanned at 5 m of range. The cell size used for the interpolation is 0.007 m x 0.007 m. The values used to make the right resolution have been determined as a function of the point density. The results show a detailed DTM, a good point density but a not very good covering. This is attributable to a single scan that produces a single direction of the laser and in consequence, more “shadow zones” (no TLS points). Indeed the low errors in the uncertainty model are more oriented in correspondence to the laser beam returns and on the top of the pebbles. Among the pebbles and in the opposite side of the laser beam we registered the highest error values up to 0.005 m (white part). The minimum registered error in this scan is equal to 0.001 m. 38.4% of the cell has an error between 0.001 m and 0.004 m, whereas the remaining part has an error greater than 0.004 m.

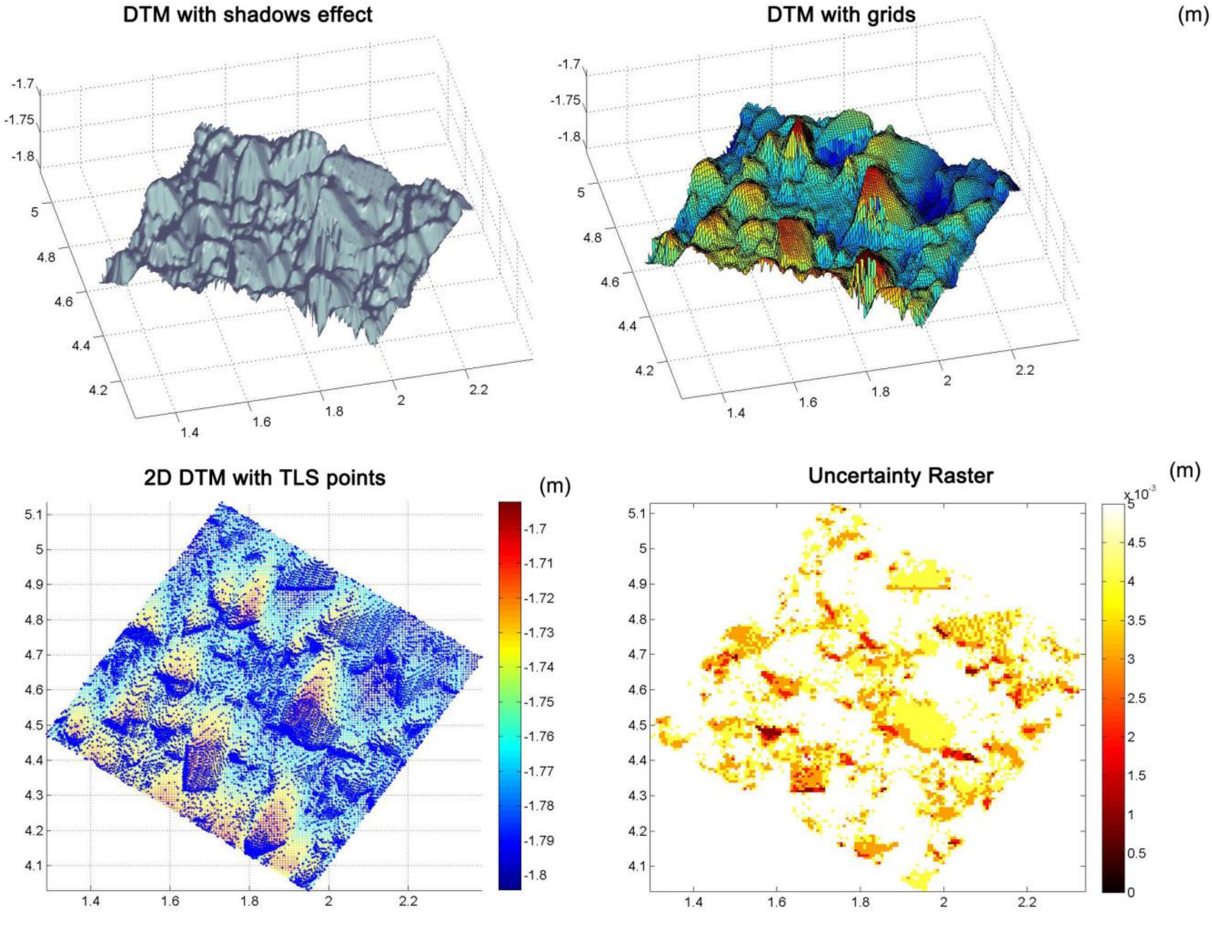

Figure 97. *DTMs at 0.007 m x 0.007 m of cell size, TLS points distribution and associated uncertainty raster of the patch 1 (Feshie River) scanned at 5 m of range.*

Analysing Figure 98, which represents the same area as the previous figure, but scanned at 10 m, we can note a significant loss of detail in the final DTM. The cell size used for the interpolation is 0.019 m x 0.019 m. The bigger cell size necessary to be representative with the correspondent point density has played an important role in the final resolution. For this reason the distributed error model shows cell with errors up to 0.035 m. The minimum registered error in this scan, is equal to 0.002 m. 29.73% of the cell has an error between 0.002 m and 0.035 m, whereas the remaining part has an error greater than 0.035 m. Also in this case the low error is in the more "laser exposed" surface, generally lower than 0.005 m. Higher error is more located in the less "laser exposed" zones.

Aiming at grain size analysis this range is not able to collect enough date usable to represent the grain particles with good detail.

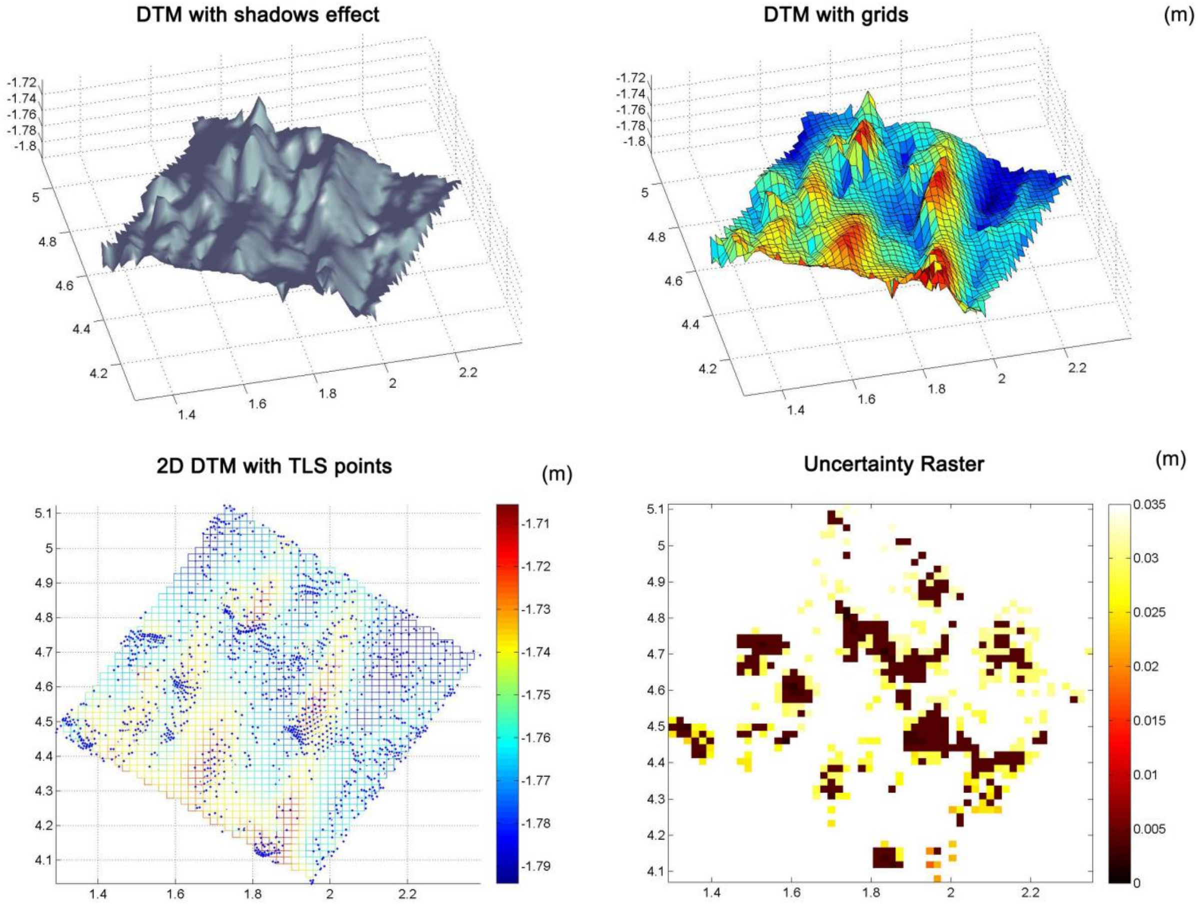

Figure 98. *DTMs at 0.019 m x 0.019 m of cell size, TLS points distribution and associated uncertainty raster of patch 1 (Feshie River) scanned at 10 m of range.*

Analysing Figure 99, that again represents the same area as the previous two figure but scanned at 15 m, we can note a complete loss of “sediment details” in the final DTM. The cell size used for the interpolation is equal to 0.034 m x 0.034 m. The minimum registered error in this scan, is 0.003 m. 24.38% of the cell has an error between 0.003 m and 0.043 m, whereas the remaining part has an error greater than 0.043 m. The point distribution is concentrated closer to the top of the pebbles. These zones indeed show a decrease in error around 0.005 m.

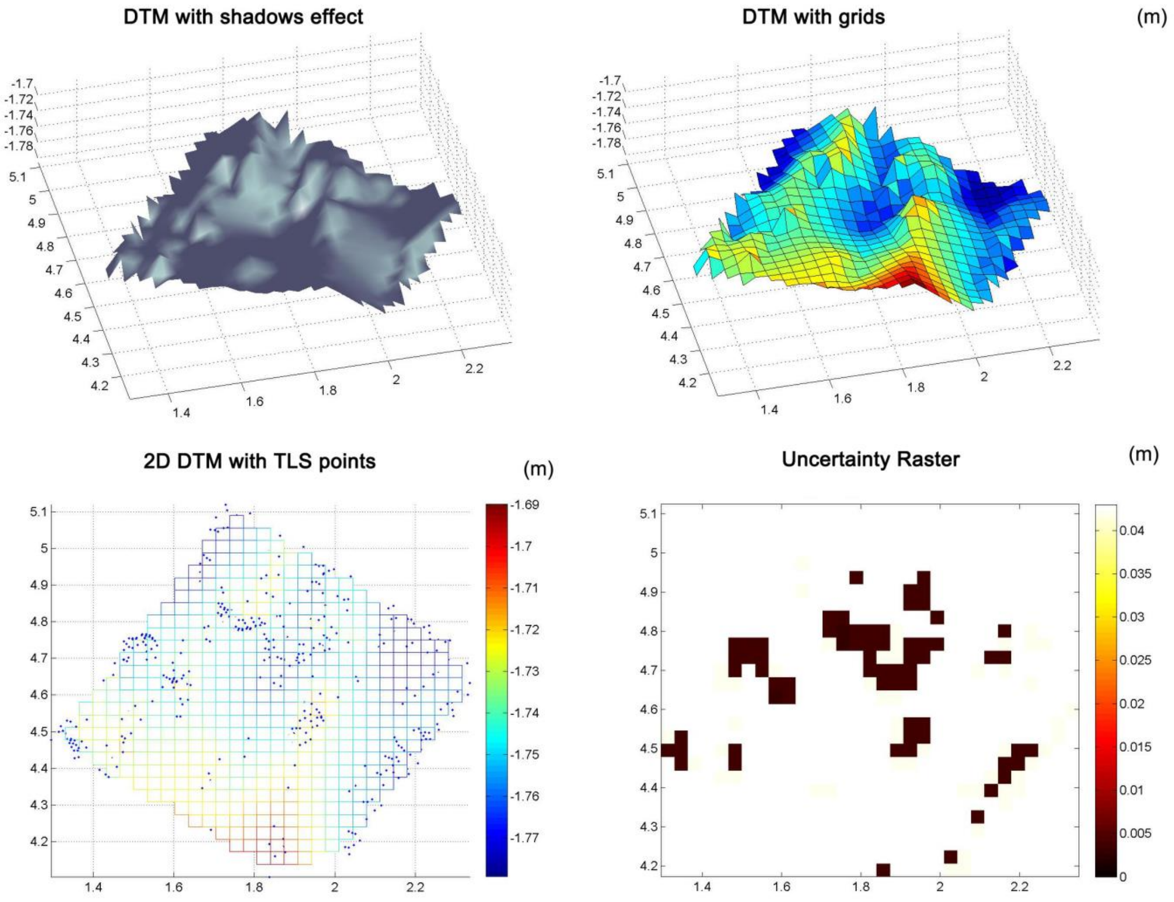

Figure 99. *DTMs at 0.034 m x 0.034 m of cell size, TLS points distribution and associated uncertainty raster of patch 1 (Feshie River) scanned at 15 m of range.*

12.2 *Fluvial point clouds classifications*

When we work with the TLS in a natural environment and aim at digital terrain models (DTMs) one of the preliminary steps before interpolating is filtering the vegetation. In Figure 100 we have an example on a reach of the Rio Cordon (tributary of the Piave River) of a very complex situation where a manual filtering could be very time-consuming.

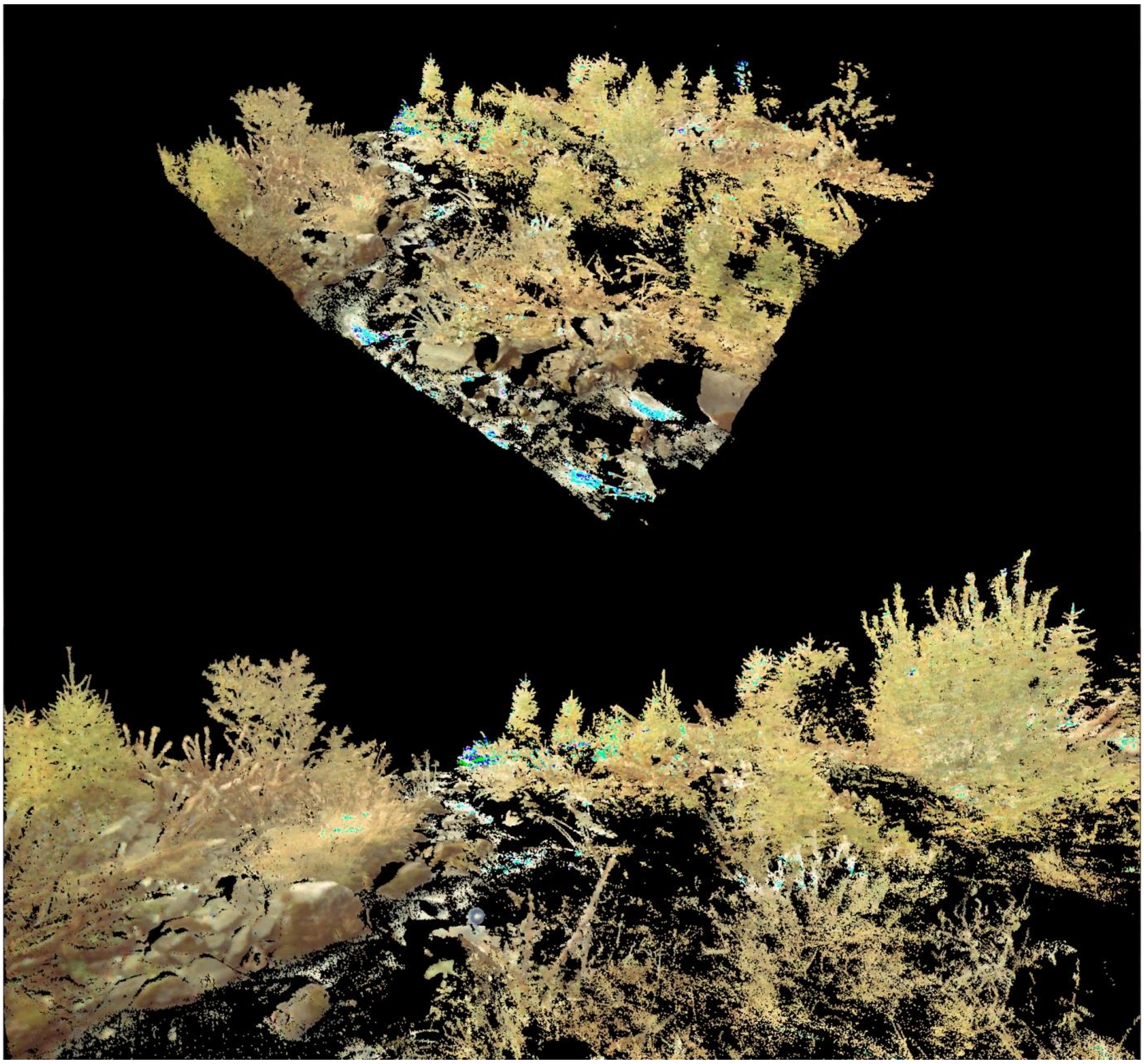

Figure 100. *TLS points coloud view of a strongly vegetated reach in the Rio Cordon (tributary of the Piave River).*

The filter presented in section 9.2 has been applied in different artificial and real surveyed clouds. This section presents the application in one of the most complex cases that we can work on.

12.2.1 Vegetation filter calibration in a real case study

Before running the filter some observations and calibration points are needed. Three internal filters are implemented and besides the outlier one they require some calibrations. The colour filter needs two cloud samples of vegetation and sediment respectively. These clouds have to be representative enough of the major part of vegetation and sediments in the study area (Figure 101).

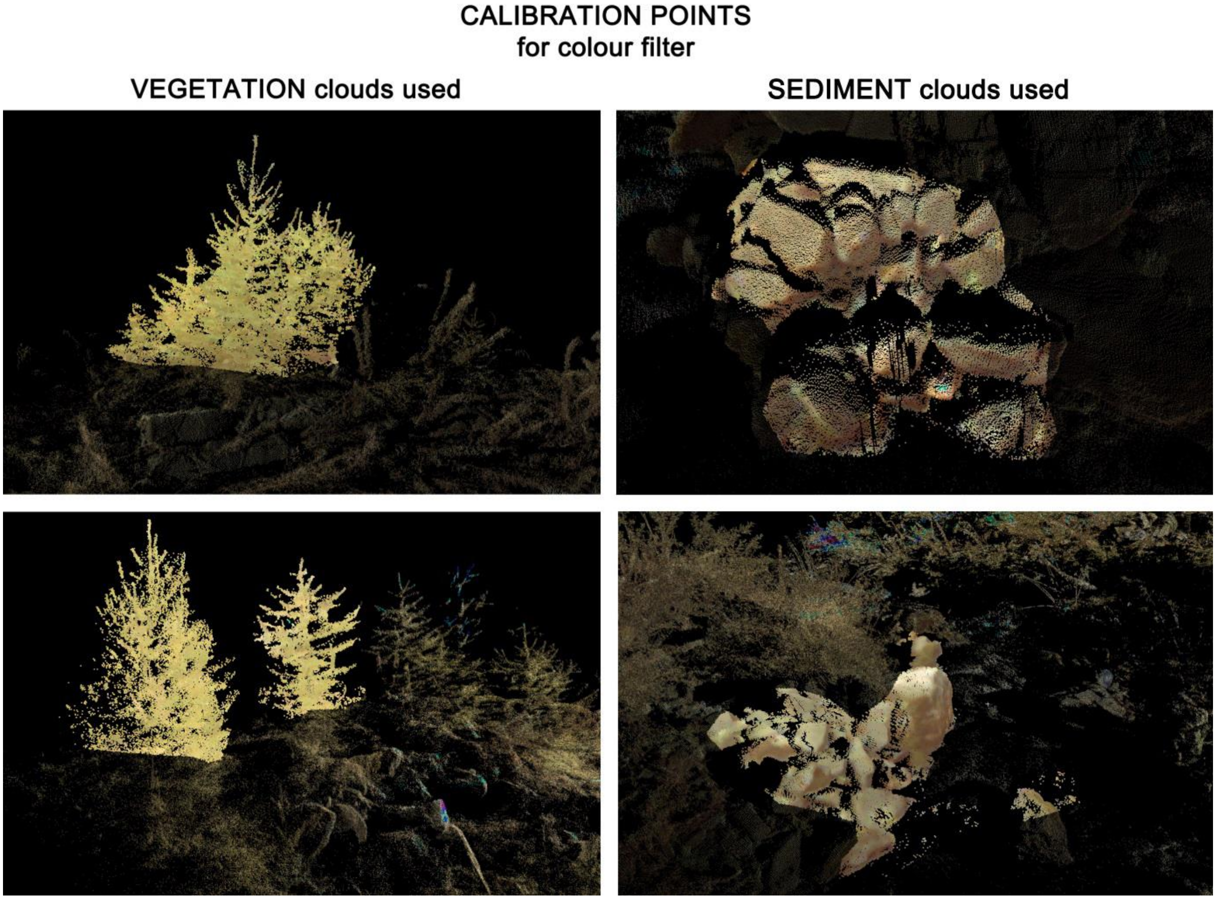

Figure 101. *Vegetation and sediment clouds calibration points used in the test area (Rio Cordon – tributary of the Piave River).*

At this point the code computes the vegetation and the sediment colour distribution for the three colour bands (Figure 102). The more separable the colour distributions are the better this filter works. As described in section 9.2, at least two colour bands have to reach separability (Figure 39) to be used. If we have these two bands, the code will check for each point if the corresponding colour intensities are inside the “sure” colour range detected for the vegetation. All the points that reach this situation will be deleted. In the case of the Rio Cordon the calibration points used are different enough to be used in the colour filter. In the case of no separability it is important to try to change the calibration points.

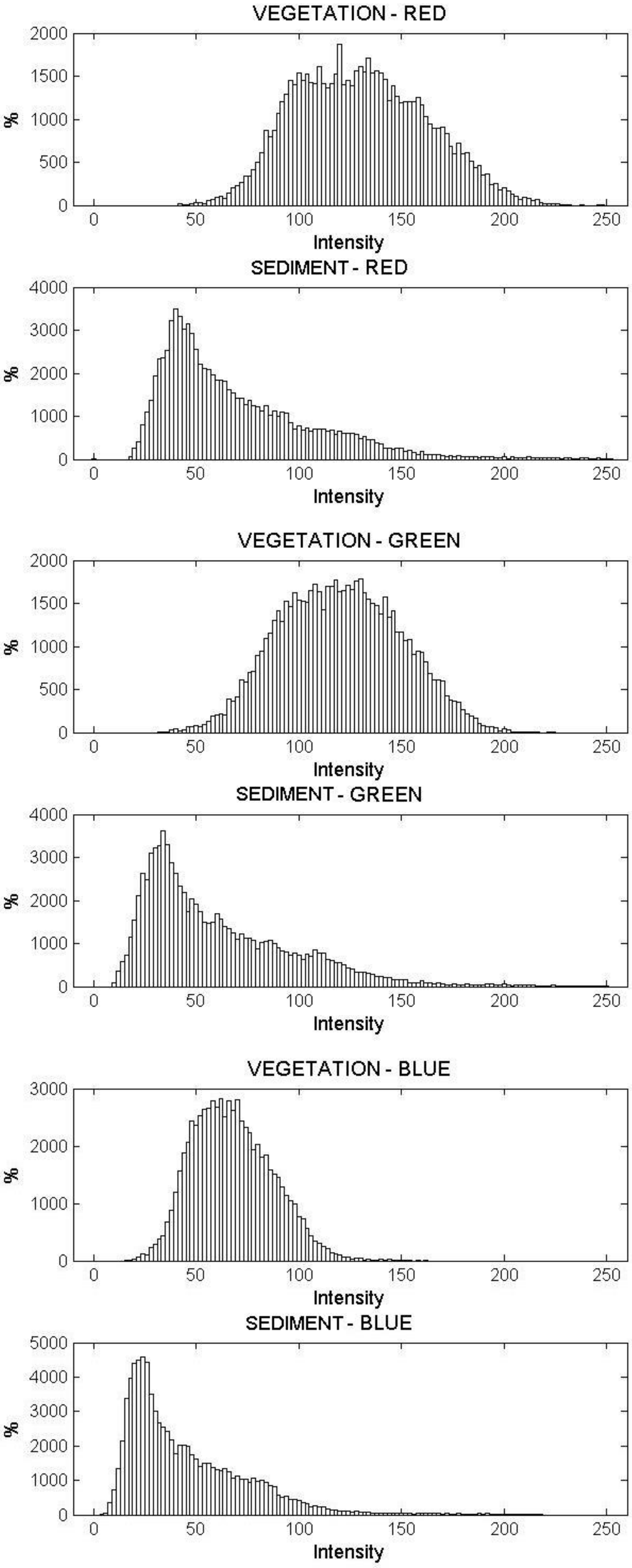

Figure 102. *Vegetation and sediment RGB colour distribution of the TLS calibration points.*

The colour distribution reported in Figure 102 shows that we are in the “B” case of Figure 39 (partial overlap between vegetation and sediment distribution).

Table 9 shows all the first sample of calibration parameters for the geometrical and colour filter (56 combinations were tested).

Table 9. *Different input parameters tested on vegeFILTER: cell of analysis to realize the TIN (CELL), the threshold vertical distance between the TIN and each point (DELTA), lowest number of points for each cell to average and use it as TIN vertex (nMIN), position of the moving window to averaging the lowest points (from) and the width of the colour bands (Pmin_R, Pmax_R, Pmin_G, Pmax_G, Pmin_B, Pmax_B).*

SAMPLE	CELL	DELTA	nMIN	from	FOLD	Pmin_R	Pmax_R	Pmin_G	Pmax_G	Pmin_B	Pmax_B
1	0.1	0.15	5	1	16	5	95	5	95	5	95
2	0.1	0.2	5	1	16	5	95	5	95	5	95
3	0.1	0.25	5	1	16	5	95	5	95	5	95
4	0.1	0.3	5	1	16	5	95	5	95	5	95
5	0.1	0.15	5	1	16	10	90	10	90	10	90
6	0.1	0.2	5	1	16	10	90	10	90	10	90
7	0.1	0.25	5	1	16	10	90	10	90	10	90
8	0.1	0.3	5	1	16	10	90	10	90	10	90
9	0.15	0.15	5	1	16	5	95	5	95	5	95
10	0.15	0.2	5	1	16	5	95	5	95	5	95
11	0.15	0.25	5	1	16	5	95	5	95	5	95
12	0.15	0.3	5	1	16	5	95	5	95	5	95
13	0.15	0.15	5	1	16	10	90	10	90	10	90
14	0.15	0.2	5	1	16	10	90	10	90	10	90
15	0.15	0.25	5	1	16	10	90	10	90	10	90
16	0.15	0.3	5	1	16	10	90	10	90	10	90
17	0.2	0.15	5	1	16	5	95	5	95	5	95
18	0.2	0.2	5	1	16	5	95	5	95	5	95
19	0.2	0.25	5	1	16	5	95	5	95	5	95
20	0.2	0.3	5	1	16	5	95	5	95	5	95
21	0.2	0.15	5	1	16	10	90	10	90	10	90
22	0.2	0.2	5	1	16	10	90	10	90	10	90
23	0.2	0.25	5	1	16	10	90	10	90	10	90
24	0.2	0.3	5	1	16	10	90	10	90	10	90
25	0.25	0.15	5	1	16	5	95	5	95	5	95
26	0.25	0.2	5	1	16	5	95	5	95	5	95
27	0.25	0.25	5	1	16	5	95	5	95	5	95
28	0.25	0.3	5	1	16	5	95	5	95	5	95
29	0.25	0.15	5	1	16	10	90	10	90	10	90
30	0.25	0.2	5	1	16	10	90	10	90	10	90
31	0.25	0.25	5	1	16	10	90	10	90	10	90
32	0.25	0.3	5	1	16	10	90	10	90	10	90
33	0.3	0.15	5	1	16	5	95	5	95	5	95
34	0.3	0.2	5	1	16	5	95	5	95	5	95
35	0.3	0.25	5	1	16	5	95	5	95	5	95
36	0.3	0.3	5	1	16	5	95	5	95	5	95
37	0.3	0.15	5	1	16	10	90	10	90	10	90
38	0.3	0.2	5	1	16	10	90	10	90	10	90
39	0.3	0.25	5	1	16	10	90	10	90	10	90
40	0.3	0.3	5	1	16	10	90	10	90	10	90
41	0.35	0.15	5	1	16	5	95	5	95	5	95
42	0.35	0.2	5	1	16	5	95	5	95	5	95
43	0.35	0.25	5	1	16	5	95	5	95	5	95
44	0.35	0.3	5	1	16	5	95	5	95	5	95
45	0.35	0.15	5	1	16	10	90	10	90	10	90
46	0.35	0.2	5	1	16	10	90	10	90	10	90
47	0.35	0.25	5	1	16	10	90	10	90	10	90
48	0.35	0.3	5	1	16	10	90	10	90	10	90
49	0.4	0.15	5	1	16	5	95	5	95	5	95
50	0.4	0.2	5	1	16	5	95	5	95	5	95
51	0.4	0.25	5	1	16	5	95	5	95	5	95
52	0.4	0.3	5	1	16	5	95	5	95	5	95
53	0.4	0.15	5	1	16	10	90	10	90	10	90
54	0.4	0.2	5	1	16	10	90	10	90	10	90
55	0.4	0.25	5	1	16	10	90	10	90	10	90
56	0.4	0.3	5	1	16	10	90	10	90	10	90

The cell size of analysis to create the TIN vertexes (see Figure 36) should have to be as a function of the granulometry; seven cell sizes from 0.1 to 0.4 m (that are around the D_{10} - D_{90} of the study area) were tested. The “delta” parameter (threshold vertical distance between the TIN and each point) defines the “cutting level” referred to each plane of the TIN; three deltas from 0.15 to 0.25 m were tested. At the end two different colour band ranges were tested: 5th - 95th and 10th - 90th percentage.

12.2.2 Best vegetation filter results

Starting with the filtering sessions, the total amount of TLS points in the test cloud is equal to 2381253. Figure 104 shows the number of filtered points using the different parameters of Table 8. We can note that the number of filtered points increases as the cell size becomes bigger and the delta distance and colour range decrease.

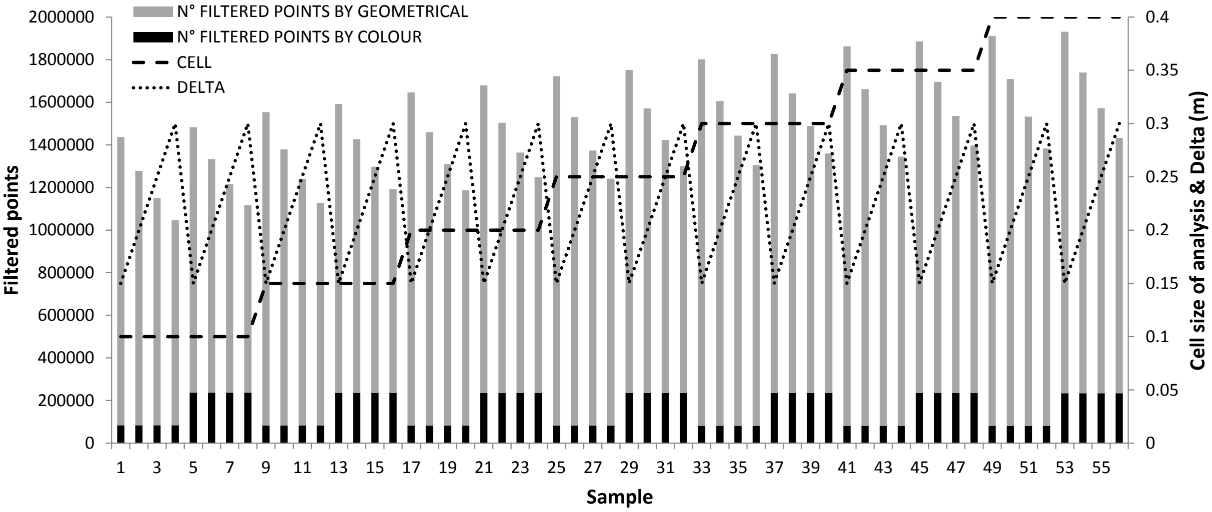

Figure 103. *Different number of filtered points by vegeFILTER by changing the cell of analysis to realize the TIN (CELL), the threshold vertical distance between the TIN and each point (DELTA) and the width of the colour bands (5th - 95th percentage or 10th - 90th).*

Comparing the cross sections and looking at the different filtering results, by using Cyclone 8® the best results seem be provided by the 47th sample. The parameters used in this sample guarantee the maximum vegetation cutting with the minimum loss of “morphology” (sediment and boulder cutting). The results of this application are reported in Figure 104 for the whole reach, while Figure 105 shows the cross sections comparison between the not- and filtered section. The parameters used in this test (for the geometrical filter) are a cell size of analysis equal to 0.35 m, a delta of 0.3 m and averaging the 5 lowest points to create the TIN vertex elevation. Regarding the colour filter in this test we have checked the overlap with the 10th and 90th percentage.

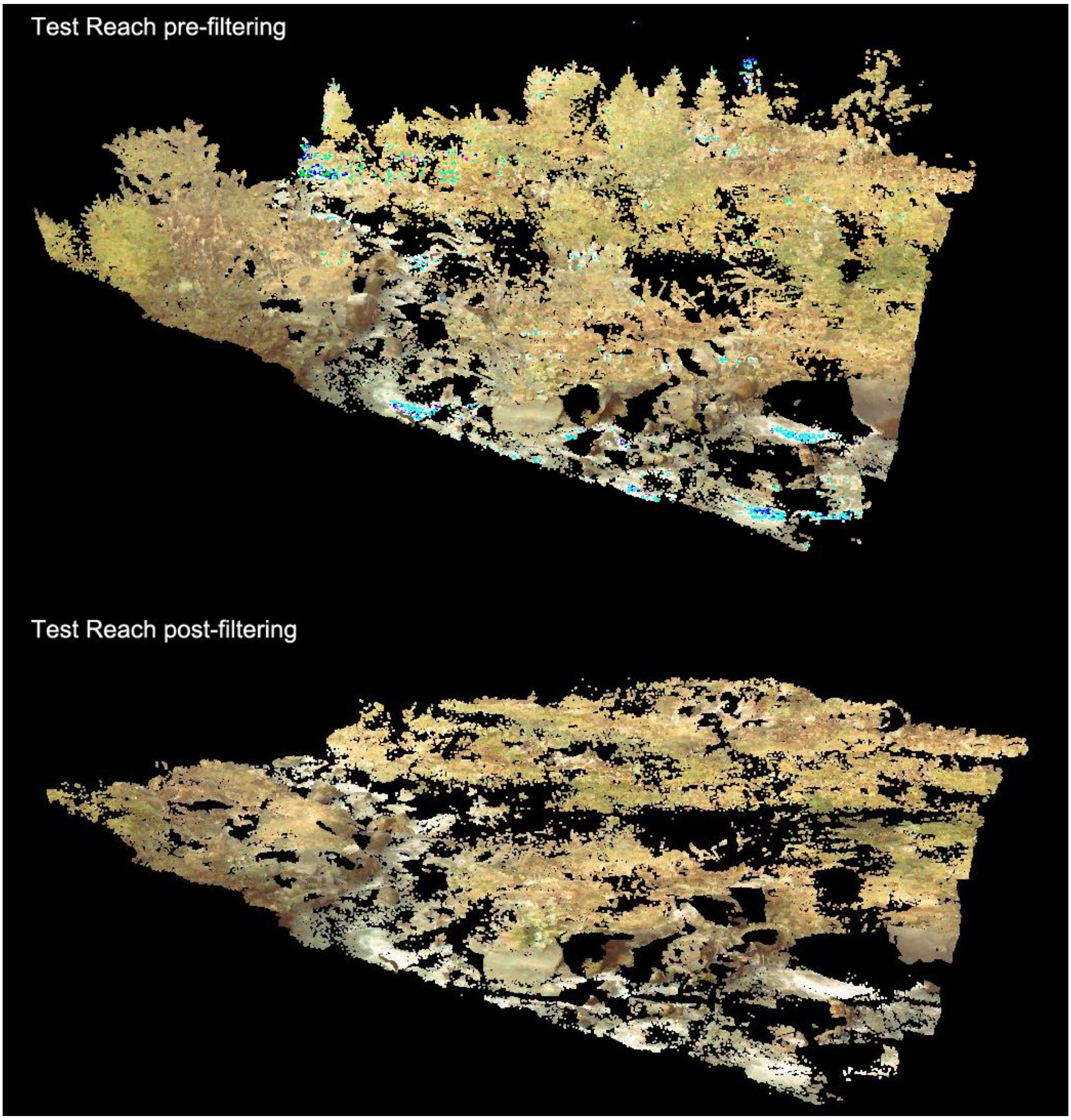

Figure 104. *Filtering results of the best set of parameters provided by the 47th sample.*

To evaluate the effect of the other input parameters in the final result, other 21 tests have been carried out by changing the number of points averaged to define the TIN vertex elevation, from 5 to 3 and the "*from*" parameters from 1 to 2 (that in this case exclude the lowest point inside the cell during TIN vertex computation).

In this reach with a density of 6644 m^2, these parameters do not produce significant changes, therefore the 47th test has been used as the best one. The density after filtering with the described parameters is 2319 m^2. With this density per square meter we are able to interpolate a DTM at 0.021 x 0.021 m of cell size. Comparing the cross sections, the filter seems to work well, it cuts the vegetation higher than 0.3 m, and leaves the morphology except for some tops of boulders (Figure 105).

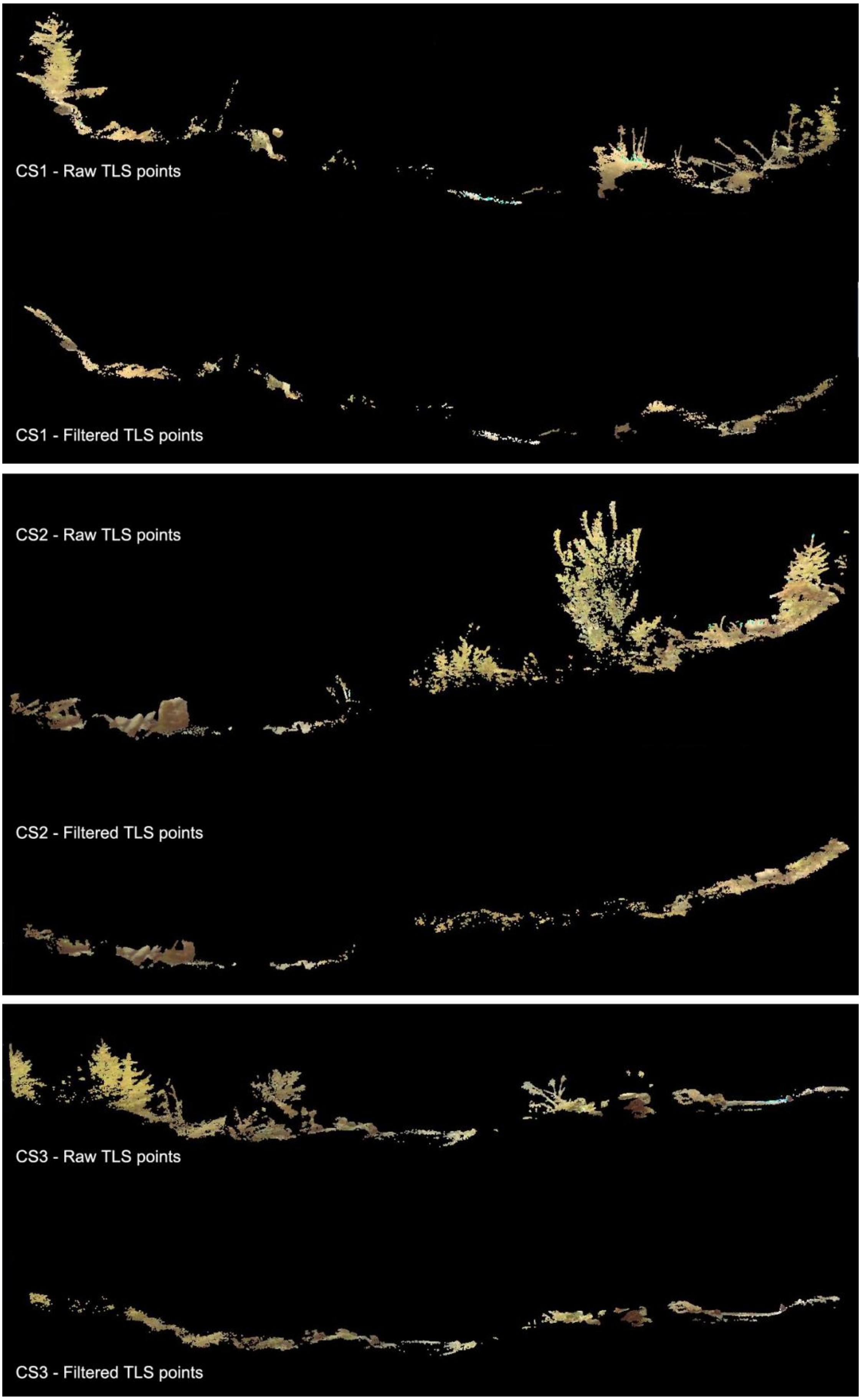

Figure 105. *Cross section comparison of the filtering results using the best set of parameters (47th sample).*

Section Four

Discussions and Final Remarks

13 *Driving Factors in Fluvial Dynamic of a Regulated Gravel Bed River*

13.1 Vertical and lateral adjustments along the middle portion of Brenta River over the last 30 years

The relationship between the vertical adjustment of the average elevation of cross-sections and the associated changes of active channel width was evaluated using ten historical cross-sections and considering two different periods: 1932-1997, and 1997-2010. Aerial photos of 1999 and 2010 were also used in order to improve the interpretation of the active channel width of cross-sections. In Figure 106, lateral and vertical adjustments of the active channel extent of 10 cross-sections are depicted. In the period 1932-1997, which corresponds to the incision/narrowing phase (except for section 1), vertical and lateral adjustments are not significantly correlated (R Spearman; p >>0.05). Channel incision and narrowing processes occurred at the same time in other Italian rivers as, for example, the Piave, the Po and the Tevere (Surian and Rinaldi, 2003). The weak correlation between vertical and planimetric adjustments over the last 30 years in the Brenta River could be related to the different temporal and spatial extent of the sediment dynamic processes. Similar processes occurred in the Piave River, which for instance experienced channel widening and incision at the same time from 1991 to 2006 (Comiti *et al.*, 2011).

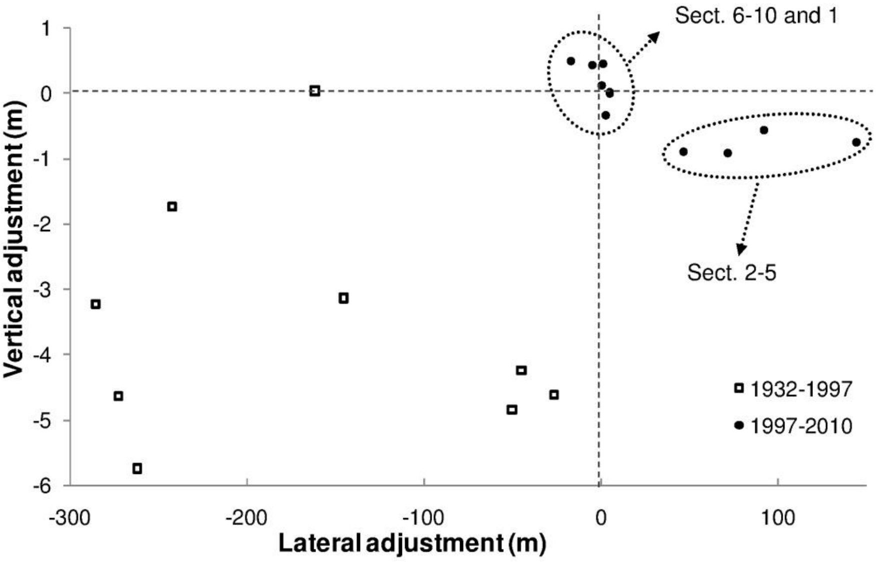

Figure 106. *Relationship between the changes of elevation of the bankfull stage and changes of active channel width evaluated at 10 historical cross-sections. The two reported series refer to the periods 1932-1997, and 1997-2010. Negative values mean narrowing or incision, while positive values correspond to widening or aggradation.*

The decoupled tendencies of vertical and lateral adjustment may be due to the fact that morphological variations can be very different at the sub-reach scale because of local constraints. Changes in active channel width were very different in the period 1997-2010, being the narrowing phase finished (Figure 106), and being some sections even widening (sections 2 to 5). Within the general widening trend over the recent 5 years, the upper reach part (except for section 1) experienced channel incision. This seems to be related to the paucity of sediment supply coming from upstream reaches due to the low connectivity with the mountain reach (Surian *et al.*, 2009a). In some portions of the upper reach (e.g. section 2), the severe incision (up to 5 m) has probably lead to reach a very coarse sub-layer, and the bed appears remarkably armoured (and possibly non completely alluvial), leading to a prevalent tendency to erode the banks rather than to further incise the channel. In the downstream reaches, where aggradation or equilibrium tendency are dominant, active channel is not widening, most likely due to two reasons: i) the longitudinal control works (built since the 1960s) greatly reduce the possibility of lateral migration of the river; ii) a mature riparian vegetation next to the active channel that stabilize the soil and reduce bank erosion.

13.2 Are flood events the main driving factor of channel changes and islands dynamics in the Brenta River?

Looking at the multi-temporal analysis of the active channel width conducted using aerial photos taken from 1981 to 2011, a certain correspondence between widening trends of the active channel and the occurrence of flood events appears to exist (Figure 107).

If the lateral annual adjustment (m year^{-1}) is related with the average of annual daily peak discharge over the photo period registered at the Barzizza gauging station for the analyzed photo period, a directly proportional relationship seem emerges (Figure 108), showing that at higher magnitude of flooding corresponds a stronger active channel widening. Minimum channel widening value of 1.5 m is obtained only with Qd_{mean} over 450 m^3 s^{-1}. Active channel narrowing is clearly due to the expansion of riparian vegetation in floodplains and islands during periods lacking major disturbing processes (r^2=0.87; Figure 107). Higher correlation is obtained (r^2 = 0.91) if the lateral adjustment rate is related to the number of the days per year where Q is greater than 450 m^3 s^{-1}, over the step time (Figure 109). For the period 1999-2003 (1407 days), 13 days with Qd over 450 m^3 s^{-1} were registered (3.4 days per year) and a widening of 7.4 meters per year was observed. A greater lateral adjustment rate of about 31.2 m year^{-1} was calculated for the step time 2010-2011 (225 days), with 6 days of Qd over the threshold value of 450 m^3 s^{-1} (Figure 109). Two major floods (RI> 10 years) occurred on each of these periods.

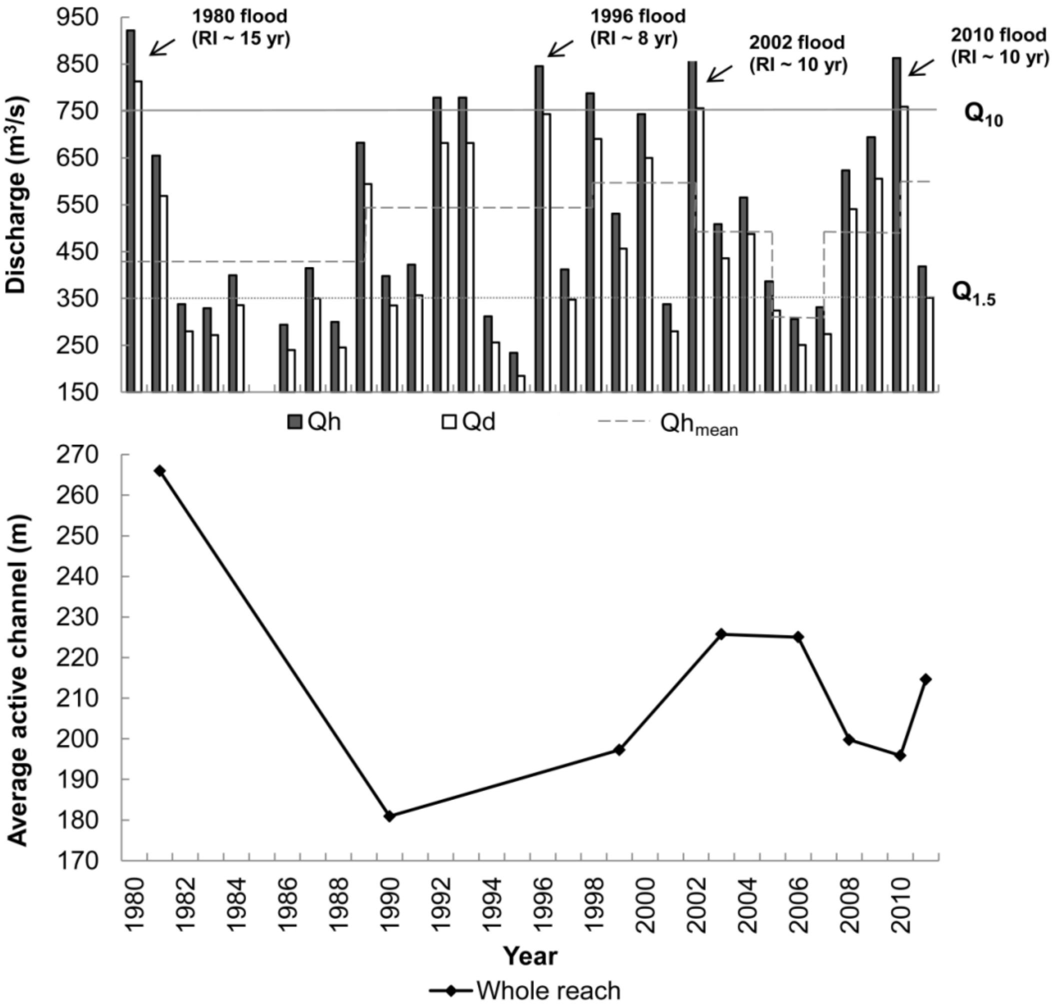

Figure 107. *Time evolution of the average active channel width and RI of flood events. (a) Bar chart represents the maximum hourly discharge registered in the year (Qh) and the maximum annual values of the mean daily water discharge (Q); dashed line (Qh_{mean}) represents the average of the annual Qh over a period between two aerial photo-interpretations. Flow discharges featuring RI = 1.5 years ($Q_{1.5}$), and RI = 10 years (Q_{10}) are also shown. (b) Adjustments of the average active channel width (whole reach and sub-reaches). Maximum annual peak discharges value was not available at the Barzizza gauging station for 1985*.

Overall, it appears that floods events with mean daily discharges (Q) around 750 m^3 s^{-1} (RI ~ 10 years) were able to cause evident widening of the bankfull section (>10-20 m). A similar flood magnitude has been reported by Comiti *et al*. (2011), that quantified in 10 years the RI flood needed to modify considerably the fluvial planimetric shape, especially floodplains and islands, in the Piave River. Further studies confirmed that island reduction processes take place due to flood events of considerable (>10 years) magnitude (Bertoldi *et al.,* 2009; Surian *et al.,* 2009b; Comiti *et al*., 2011; Vitti *et al*., 2011; Picco *et al*., 2012a.

Despite the fact that natural channel adjustments at the reach scale are mainly due to the occurrence of floods events, a fundamental role is also played by the individual characteristics of each small reach, which can strongly influence the change responses in the different portions of the river.

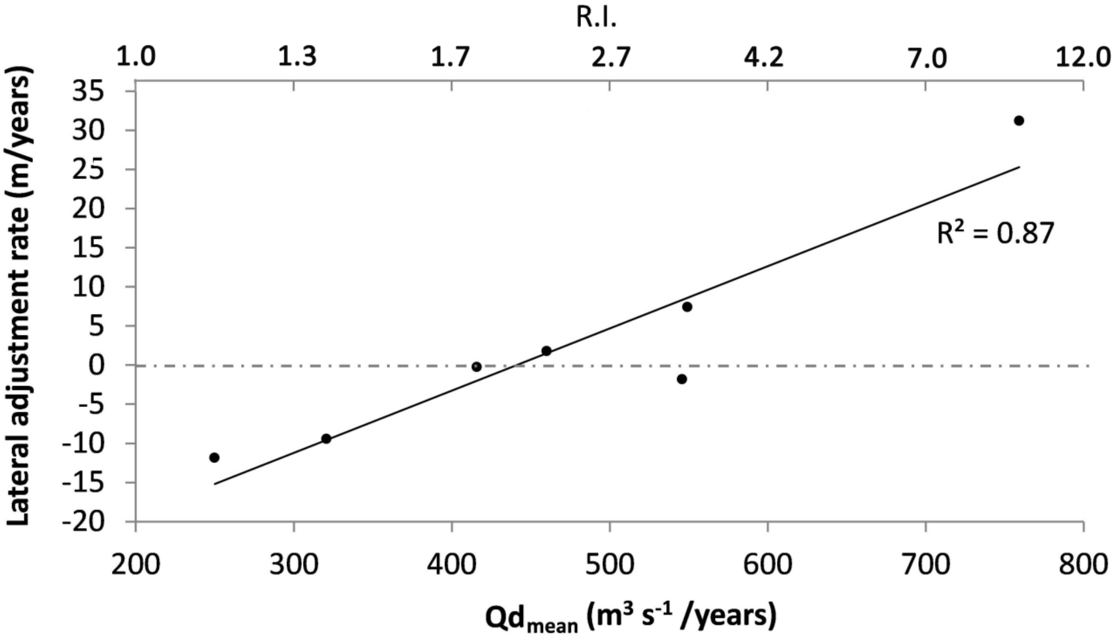

Figure 108. *Rate of active channel width variation (m year^{-1}) in relation to the average of annual daily peak discharge (Qd m^3 s^{-1}) over photo periods and the correspondent recurrence interval.*

Overall, differences in adjustment responses to the 2010-2011 flood events along the reach could be linked to different physical settings (especially bed slope), but also to the disturbance in sediment flux and sediment availability from upstream reaches. The higher erosional trend in the upper part of the study reach is likely due to the higher physical constrains which do not allow the channel to migrate. In fact, human structures aimed at protecting the nearby areas against floods (e.g., embankments, groins, and rip raps), are most likely to have reduced the active channel width, causing severe incision as partially confirmed by the recent multi-temporal analysis. The concentrated bank erosion could be enhanced by both the alteration of sediment flux due to the low connectivity with the upstream drainage basin already identified by Surian *et al.*, (2009b), and by the scarcity of vegetation growing on the banks. Sediment supply to the upstream reach is very low due to the presence of dams and torrent control works in the mountain basin. As a result, the connectivity with the upstream basin is virtually negligible for bedload and coarse sediment input to this sub-reach (cross-section 2). Moreover, a knickpoint in the longitudinal profile appears around cross section 3, located 4.4 km downstream section 1, indicating that this portion of the river is likely in a current transient condition to equilibrium. Channel incision in the upper part of the study reach is than likely continue until a further adjustment of slope, or until a further development of armour layer (Moretto *et al.*, 2013b).

The application of a 2D hydrodynamic and morphodinamic model for gravel bed rivers recently developed by Kaless (2012), to the Brenta River’s Nove sub-reach (around section 2), indicates that the most probable short-term evolution of the reach will depend on the floods magnitude. Ordinary events (discharges below 450 $m^3 s^{-1}$) will produce negligible changes within the channel bed. On the other hand, more infrequent floods (RI > 10 years), are expected to produce remarkable banks erosion. Widening is the main processes able to stabilize the channel owing to the reduction in shear stress and the delivery of sediment into the channel.

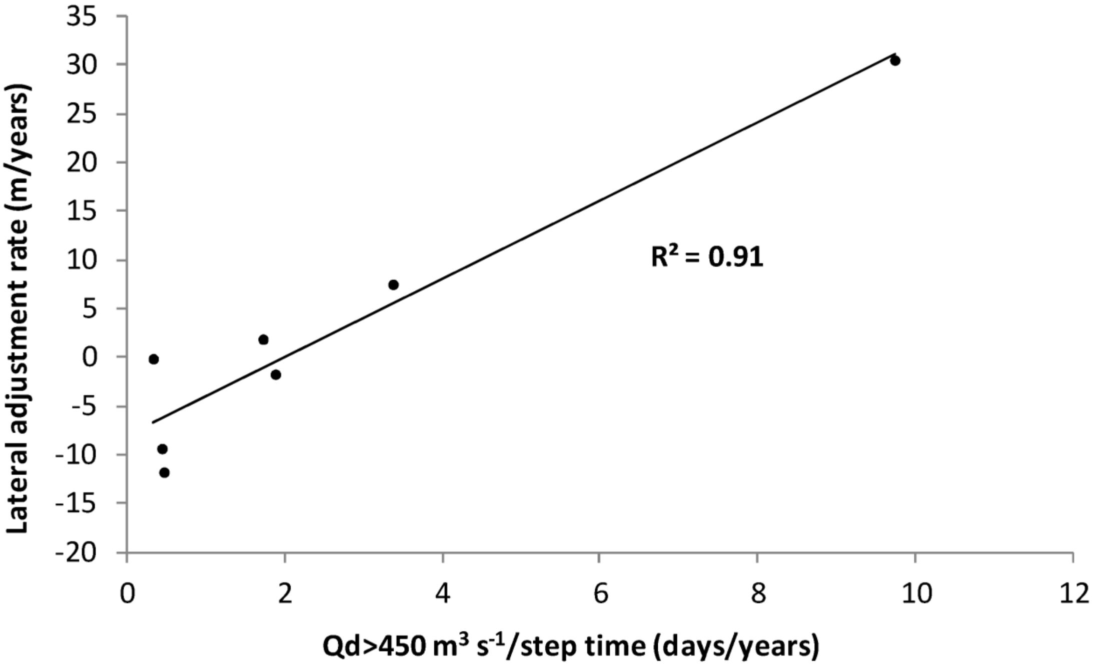

Figure 109. *Lateral adjustment rate versus the number of days per year with Qd over 450* $m^3 s^{-1}$ *for the photo period.*

In the middle portion of the study reach (around cross-section 5), the channel has recently been relatively stable, likely because in-channel mining hasn't longer been carried out since 1992-1994, and significant bank erosion has recently occurred in the upstream sub-reach, supplying eroded sediments and coarse material. In fact, the sub-reach around cross-section 6 appears to have been stable over the past few years, suggesting that major sediment supply is not to be expected in the further downstream reach. Indeed, gravel mining activities were not intensive in this part in the past, and enough volumes of coarse and fine sediments are available from bank erosion of the upper part of the study area.

Generally, it appears that portions of the study reach with lower human disturbances and structural constraints are currently widening, whereas reaches heavily constrained are still suffering considerable erosion processes. The dominance of erosional processes in the upstream and a general stability depositional phase on the downstream portion of the study reach is also reflected by the different islands dynamics. In the far downstream reach, (around section 7), the sediment deposition and the higher morphological stability creates suitable conditions for the stabilization of vegetation, while other active channel areas are more disturbed by floods and the islands are more affected by erosion processes. Beyond these aspects, it's worth considering the relevant influence of direct human actions (e.g. vegetation removal, local clearcuttings, bank protections, agricultural settlements, recreational areas) which are still present along the river corridor and can modify locally both the morphological and vegetation dynamics (Picco *et al.*, 2012a). The analyzed fluvial system is the result of centuries of alterations, as highlighted for other rivers of the Veneto Region (Comiti *et al.*, 2011). In the period 1990-2011, the fluvial dynamics of the Brenta River appears to be less affected by human alterations, due particularly to the decrease or almost the abandonment of mining activities within the channel.

13.3 Driving factors of channel evolution over the last 30 years and implications for channel recovery

The study reach of the Brenta River was characterized by a period of strong narrowing of the active channel (from 1981 to 1990) followed by a general stability and an initial, low recovery phase. A similar situation was found in the Piave River (Comiti *et al.*, 2011). Analyzing in detail this trend, five periods can be identified (1981-1990, 1990-2003, 2003-2008, 2008-2010 and 2010-2011). Comparing the surface extension of the active channel at the beginning and at the end of each series, it was possible to highlight and calculate erosion and deposition areas. In the first nine years (1981-1990), the active channel decreases of ~ 225 ha, equal to 19% of the total area, with a variation rate of 25 ha year^{-1} which represents the smaller historical extension. This period corresponds to a series of ordinary flood events (average annual hourly peak discharge 1981-1990 = 426 m^3 s^{-1}, maximum Qh = 682 m^3 s^{-1}) and still relevant human impacts. The 1990s coincide with the end of the narrowing phase, commonly associated, for Italian rivers, to sediment mining activities (Surian *et al.*, 2009b). Some differences are noticeable with other Alpine regions where floodplain reforestation (following changes in the land use), along with sediment mining, is considered a major cause of channel erosion (Liébeault and Piégay, 2001, 2002; Rinaldi *et al.*, 2011). As showed by the most recent channel evolution of the Brenta River, Surian and Rinaldi (2004) identified a phase of channel widening in several Italian rivers and Surian *et al.*, (2009b) pointed out that such phase is often associated with aggradation, even if it can also occur without significant bed level changes. A similar phase in our study site can be recognized from 1990 to 2003. In this period, there was a partial recovery of the active channel width of ~ 135 ha (11% of total area, 11 ha year^{-1}), eventually due to flood events (e.g. 2002 and 1996) and/or a partial recovery of the natural dynamics (in relation with the decrease of gravel mining and human pressure). During these 12 years, in fact, we can observe an increase of the most intense flood events (average annual hourly peak discharge 1990-2003 = 572 m^3 s^{-1}, maximum Qh 1990-2003 = 860 m^3 s^{-1}and 6 floods with RI ≥ 5 year). During the third period (2003-2008), the trend changes one more time as demonstrated by the multi-temporal analysis of the aerial photos: the active channel surface reduces of ~ 70 ha (14 ha year^{-1}) which corresponds to about 6% of the total area. In this period, the flows decrease their intensity (average annual hourly peak discharge 2003-2008 = 425 m^3 s^{-1}, maximum Qh 2003-2008 = 618 m^3 s^{-1}), and no flood events with RI > 4 years occur.

Observing the fourth period (2008-2010), we can notice a new little expansion of 10 ha, that corresponds to about 1%, due to two subsequent floods of around 327 m^3 s^{-1} and 676 m^3 s^{-1}, in 2008 and 2009, respectively. During the last period (2010-2011) there was a consistent enlargement of about 41 ha, that correspond to about 3%, due to the significant 2010 flood (Qh = 863 m^3 s^{-1}; Qd = 759 m^3 s^{-1} with RI = 10 years). In correspondence to this enlargement, a low channel incision in the upper part of the study reach is recognizable. On the contrary, in the second half of the reach a relative phase of equilibrium or smooth aggradation can be distinguished (see section 10.2 and Figure 45). Contrary to the Piave River which is currently showing a certain morphological recovery (Comiti *et al.*, 2011); the Brenta River is not entirely in a morphological recovery trajectory. Even though in the downstream area of Bassano Del Grappa the abandonment of gravel mining activities has led to a decrease of erosion and narrowing processes starting from the early 1990s, a low morphological degradation of the river is still undergoing. The main recognizable driving factors seem to be: i) the very scarce availability of bedload transported sediment from upstream (as highlighted also in Surian and Cisotto, 2007); ii) the absence of tributaries which can supply sediment; iii) the higher bedload transport capacity consequent to the increase of slope registered from 1997 until so far (+ 0.3 ‰). In the downstream part, otherwise, the active channel results much more stable, either in width and elevation terms due to: i) the higher availability of sediment which derives from the upstream part as consequence of bank and bed erosion; ii) the lower slope (reduction of 0.6‰) of the active channel if compared to 1997 from section 6 ahead; iii) the greater presence of stable riparian vegetation; iv) the reduction of sediment mobility carried out by numerous infrastructures as bridges and dam structures (Carturo dam built up in the 1970s). The recent variations of morphology and vegetation are related to the episodic severe flood events, in association with the effects of human actions acting both at reach- (in the past) and basin-scale (nowadays).

In order to avoid the adverse effects associated with the morphological deterioration experienced by the river over the past, it seems that the management strategy should pursue channel aggradation and promote bankfull expansion. These objectives could be achieved through a proper management of sediment with measures oriented to: i) prevent the extraction of gravel from the active channel and, if possible, locate these activities upstream of the dams, favoring the transfer to downstream of trapped sediment in the reservoir (Palmieri *et al.*, 2001); ii) rethink about torrent control measurements, promoting open check-dams with hydrodynamic filtering mechanism (Conesa-Garcìa and Lenzi, 2010; D'Agostino *et al.*, 2004); iii) promote the formation of an erodible river corridor (Piégay *et al.,* 2005), avoiding to occupy areas within the levees with historical structures or agricultural activities; iv) go back to manage the forest in mountainous areas, so as to promote recruitment processes of sediment from the slope. The moderate recovery that the Brenta River is experiencing, especially in the second half of the downstream reach analyzed (Surian *et al.*, 2009b), is likely to continue and increase only if a combinations of the actions described above will be applied.

14 Erosion Deposition Assessing on Gravel Bed Rivers

14.1 Analysis of the proposed bathymetric method for geomorphic change detection

The proposed colour bathymetry method is a revised procedure for the production of high resolution DTMs on gravel-bed rivers, integrating LiDAR points with filtered bathymetric points estimated through a regression model implemented on wet areas with high heterogeneity.

The bathymetric points can be derived from a physical and empirical relationship between water depth and RGB bands of aerial images taken concurrently with LiDAR data.

The model calibration requires a dGPS survey of the water level, without needing direct water depth measurements. It is crucial to acquire dGPS points nearly contemporary to LiDAR and aerial images, as already pointed out by Legleiter (2011). In fact, the calibration of the model does not need direct field surveys of water depth because this is indirectly estimated. Depth estimation entailed the subtraction of the water level raster (water surface) from the corresponding dGPS elevation points (bottom surface) of the channel bed (Zwet). This method is an effective approach for the indirect estimation of water depth and a similar technique was used by Carbonneau *et al.,* (2006). Checking the results obtained from direct measurements of water depth, using gauge rods in correspondence to dGPS points, we noticed that the values obtained from the same points by indirect estimation account for an average error of 0.15 m. This error may also be due to the speed of the water flux during the direct sampling, that created some turbulence around the graduated bar.

Indirectly estimated depths, together with the corresponding RGB values, made up the dataset for the statistical calibration of the regression models. The statistical analysis showed that all three bands (R, G, B) and also some of the other constituent factors (interactions among bands and square and cubic terms) are significant (p-value < 0.05) to predict the water depth. This statistical significance was also confirmed by two different statistical regression methods (verification of p-value and AICc index). The “ad hoc” calibration for each study year was necessary because of the different water stage during the LiDAR survey.

This study has demonstrated that in a very heterogeneous wet area, with different depths and different colours on the channel bottom (due to the presence of periphyton), the tested physical models have a lower degree of significance than the empirical models. The empirical models use all the colour bands, and also take into consideration their interactions (non-independence from the explicative variables), the presence of which is demonstrated in Figure 49. All the estimated models (physical and empirical) have an r^2 lower than other similar studies (e.g. Carbonneau *et al.*, 2006; Legleiter *et al.*, 2011), but this is due to the very strong colour and depth variability. Despite a lower r^2, the final validations of the elevation models (shown in Figure 51 and Table 4) have demonstrated a bathymetric uncertainty comparable with the LiDAR data.

Table 5 shows that in the case of the Brenta River the optimal application range of the estimated bathymetric models is between 0.2 m and 1.0 m for 2010 and 2011, respectively. The error of estimated water depth increases, in the first 20 cm from the water surface, due to strong colour variations at the bottom (periphyton, exposed pebbles, woody debris, etc.). This error was eliminated by substituting those areas with LiDAR points, capable of penetrating this first water layer. The capacity of the LiDAR signal to produce a reliable estimate in the first 20 cm of the water column was confirmed by dGPS and LiDAR cross-section comparison (Figure 52).

Nevertheless, the possible sources of error in the proposed colour bathymetry can generate elevation models of wet areas with an error on our data of less than ± 0.22 m for 95% of the 2010 wet area and less than ± 0.26 m for 99%. For 2011 we obtained an error of less than ± 0.24 m for 80% of the wet area and less than ± 0.32 m for 89%. Hydraulic conditions differed between 2010 and 2011 (see section 11.1), and the number of calibration points can play a significant role especially in a very variable fluvial environment.

To confirm the importance of using a bathymetric method if the aim is to evaluate erosion – deposition patterns by applying numerical models or developing sediment budgets, table 4 reports the loss of volume without applying colour bathymetry. These volumes were derived by subtraction between HDTMs and DTMs (derived entirely from LiDAR). The minimum loss (possible erosion and/or deposition) of 529,813 m^3 is registered at Nove and the maximum of 4,743,783 m^3 in Fontaniva. Therefore the loss of potential erosion and deposition without applying a bathymetric method cannot be excluded to avoid obtaining results far from the reality.

A comparison of the 2011 raw HDTM and the HDTM derived from the profiles of Friola wet areas is shown in Figure 110. Four types of errors were identified on raw HDTM: light reflection, water turbulence, periphyton and exposed sediment (sources of errors highlighted also by Legleiter *et al.*, 2009). The light reflections and water turbulence (white pixels) produce strongly negative depth estimates and substantially different (about 1 - 2 m) from adjacent cells not affected by these problems. The exposed or nearly exposed periphyton (green and brown pixels) and exposed sediment (grey pixels) produce an underestimation or overestimation of water depth (about ± 0.40 - 0.60 cm of difference with respect to the adjacent cells). The correction method, which involves the use of a filter based on the curvature and removal of outliers (points with errors exceeding 95% confidence interval), has provided excellent results as evidenced by Figure 110. The proposed filtering approach of erroneous points due to the causes listed above is the new element of the proposed colour bathymetric methodology.

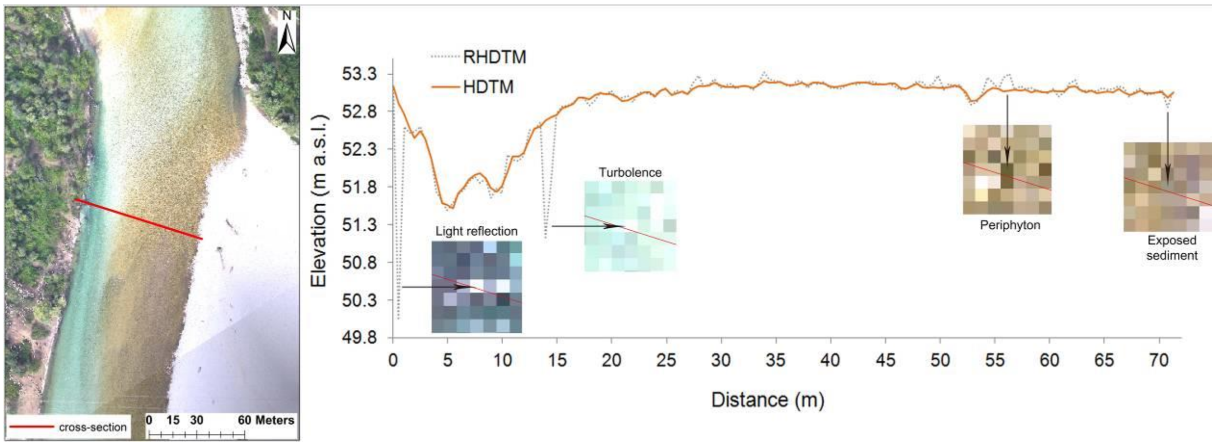

Figure 110. *Example of filtering process in a cross-section of Friola 2011 sub-reach.*

Shadows represent a disturbance factor difficult to correct and remove because they tend to cause an overestimation of the channel depth. However, their presence was minimal in the study sites, thanks to the image acquisition being done at midday. A further limitation is a water depth greater than 1.0 - 1.10 m, where the model tends to produce underestimations. This is partially due to the low availability of calibration points (for safety reasons) in the deepest areas of the water channel. Legleiter (2013) explained that depth estimates through aerial images become less reliable in deeper water due to the increase in saturation of the radiance signal.

In the HDTM profile there are some small areas lower than the dGPS profiles (Figure 52). This may be due, in part, to the presence of large boulders in the water channel that have altered the comparison between precise dGPS measurements and those derived from a mediated profile by HDTM cells of 0.5 x 0.5 m. These deviations are localized and on average included in the total average error detected in this reach (± 0.16 m). Consequently, the HDTMs produced can be considered a satisfactory topographical representation (considering the resolution of the final elevation models) for a homogeneous study of morphological variations.

To provide some guidelines to project the “colour bathymetry survey” (as reported in Moretto *et al.,* 2013a and Moretto *et al.,* 2013c), the expected error associated with the depth and the calibration points was implemented in Figure 111. Four “error model” are reported, one for each river (interpolating the 2010 and 2011 error data reported in Table 5) and one that is the average “error trend” obtained by interpolating all “error data” from each river. To provide more solid general rules, suspicious points were deleted. Therefore for the 2010 Piave points above 0.8 m (Table 5) of water depth were not considered.

The lower error that was resulting seems be erroneous if compared with the other survey. The reason is due to the worst luminosity conditions of the aerial photos. The different calibration point number among the different years and surveys at different water level, seems to suggest some general rules: i) a minimum number of 250 calibration points for each water range level (with a step of 0.2 m) seems able to guarantee an average error lesser than ± 0.2 m, from 0 to 1.5 m of water depth; ii) between 1.5 m and 2 m of depth (the deepest range surveyed), the error is generally greater than ± 0.2 m and between ± 0.3 - 0.4 with at least 200 - 250 calibration points; iii) the different “error” trend among the analysed rivers suggest that the error is not only in function with the different depth and calibration points, but also with the “photo conditions” such as luminosity, hour of flight, etc. Indeed the high presence of shadows and the low luminosity due to the aerial survey at sunrise found on the Piave reaches in 2011, has caused a greater error than the other reaches. Therefore a preliminary analysis to know both, the range of depths and the possible “surfaces of noise” (sources of shadows, artificial structures next to the wet area, etc.) in the study reach is required.

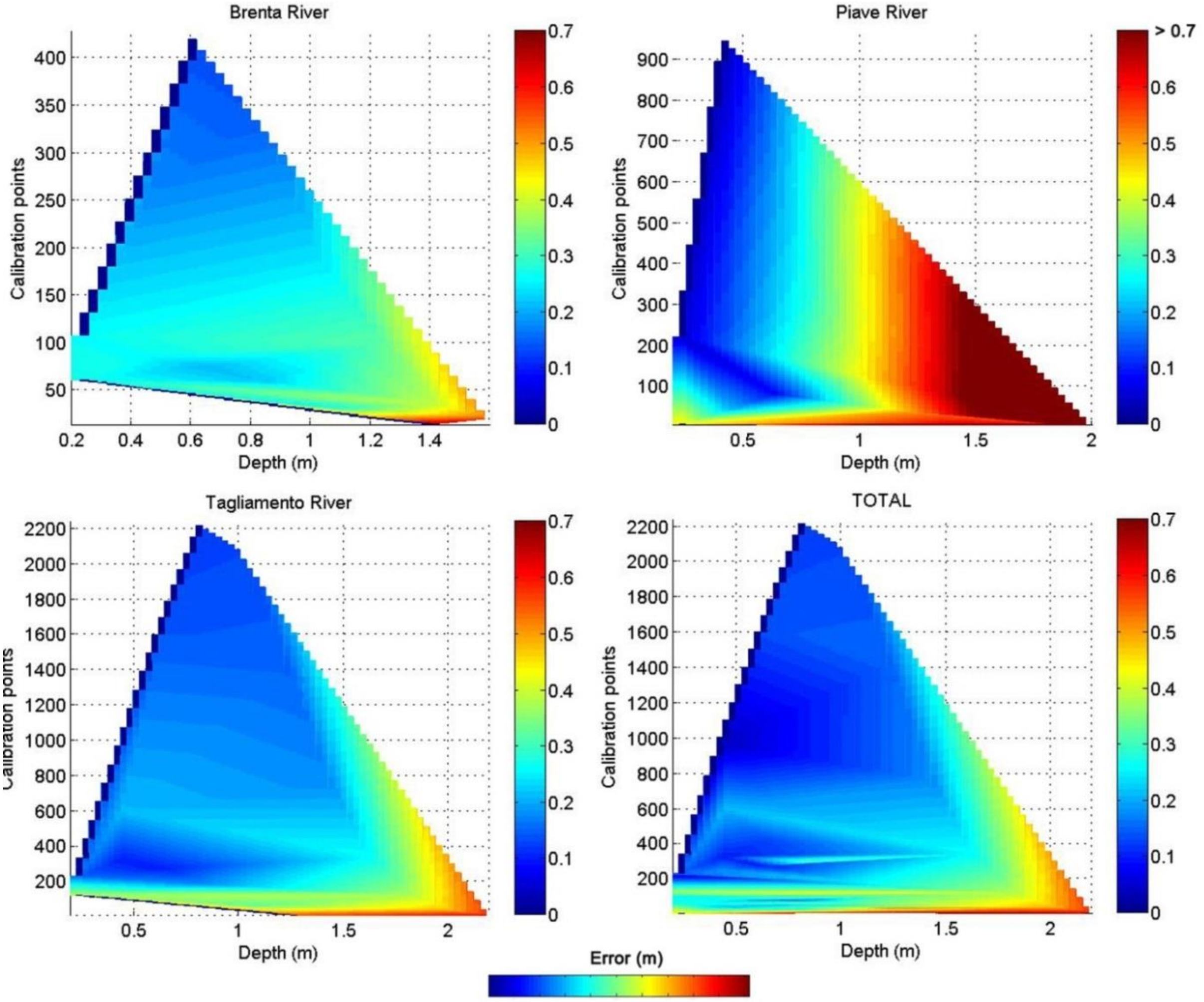

Figure 111. *Error expected (based on our surveys) at different water depth and number of calibration points.*

Other important rules to produce a reliable colour bathymetry are: i) commissioning LiDAR and aerial photos surveys with the lowest water depth and suspended sediment load; ii) flight time around midday, to avoid shadows which can introduce more errors on the colour models; iii) perfect photo-georeferenziation; iv) good water level estimation.

An example of difference of DEM (DoD), of Flagogna reach is reported in Figure 112), it is derived from 2011 and 2010 HDTMs difference. These changes are due to the flood events of November-December 2010 (RI ~ 10 years). The most part of the variations have occurred in the wet areas; as highlighted in (Moretto et *al*., 2012a, Moretto et *al*., 2012b and Moretto et *al*., 2013a). The results confirm that if we aim at geomorphic changes evaluation in environments with a significant presence of the wet areas, bathymetric techniques are required for not provide far results from the reality.

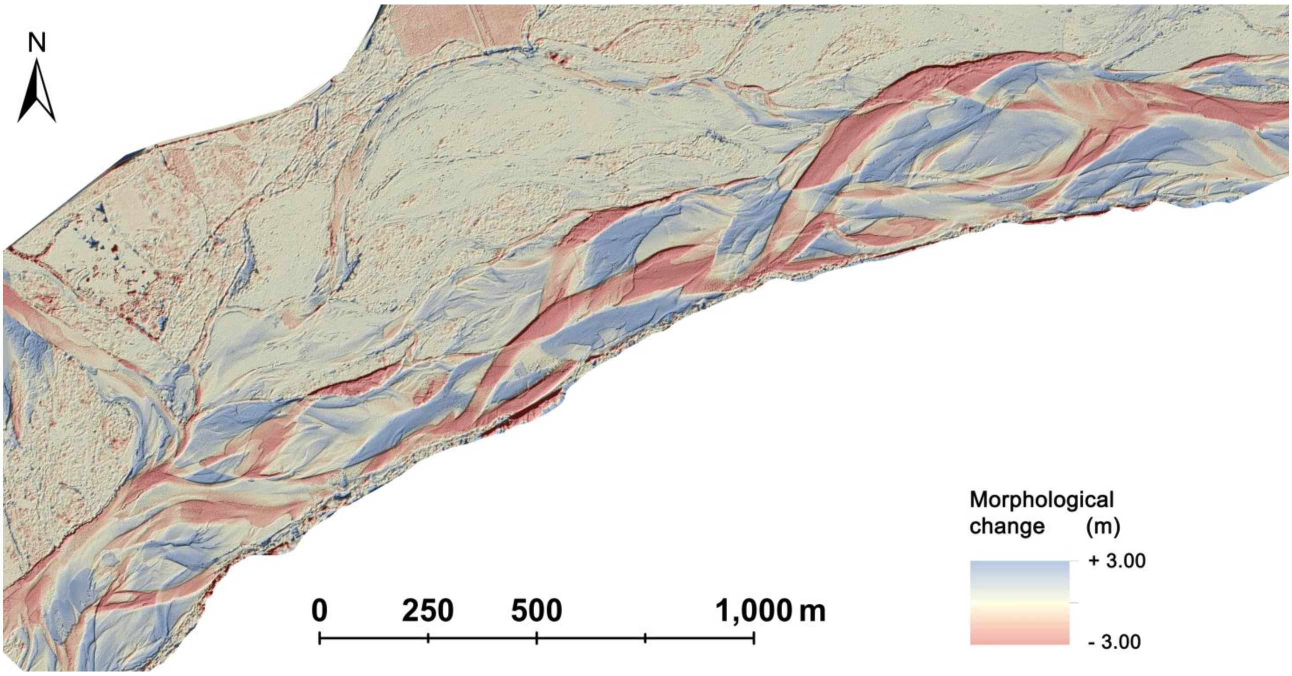

Figure 112. *Difference of DEMs (DoD) of Flagogna reach (Tagliamento River).*

14.2 Geomorphic changes after November and December 2010 floods: Brenta, Piave and Tagliamento River comparison

Considering the results obtained from the principal erosion-deposition analysis, we can compare the total amount and the single principal patches of variation among the Brenta, Piave and Tagliamento Rivers. Figure 113 shows the comparison of the total depurated erosion and deposition by using the Wheaton et al. (2010) approach, applied in Delai et al. (2013). Except for Flagogna sub-reach the erosion is always higher than the deposition. Friola and Belluno have similar amounts of erosion and deposition, while considering only the trend, also Cornino has a similar volumetric behaviour. Fontaniva and Praloran have a more balanced ratio of erosion and deposition, while Nove is more shifted to an erosion process. Flagogna sub-reach has an inverse trend with respect to the other reaches, where the erosion process is dominant. The higher volumetric changes registered in the Tagliamento River are also due to the greater area of these study reaches (Figure 113). It is interesting to confirm that in all of the three considered rivers, going from the up-stream to the down-stream reach, the deposition increases, while the erosion is always more marked in the up-stream reach.

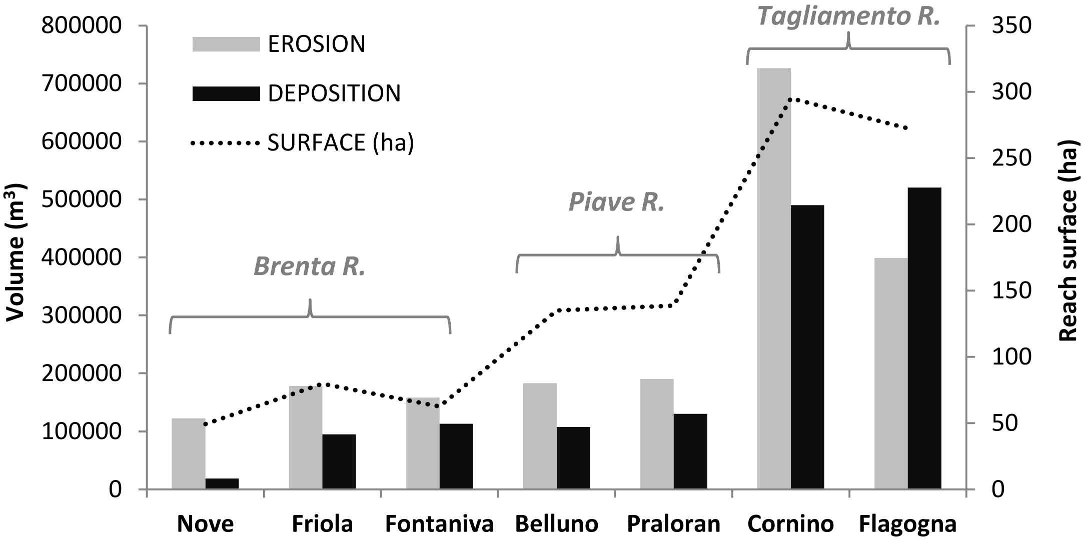

__Figure 113.__ Erosion – Deposition comparison with the associated reach surfaces among the Brenta, Piave and Tagliamento River.

The cubic meters related to surface of all the principal patches of variation greater than 1000 m^2 and deeper than ± 1.00 m of all the considered reaches were analyzed. Thanks to the PrEDA script developed, the data of all the principal patches were automatically extracted to realize the surface – volume relation. Figure 114 shows the surface-volume relation for the erosion. Each point represents a principal eroded patch (> 1000 m^2 and > - 1.00 m). The biggest patches registered, greater than 18000 m^2 in surface and 30000 m^3 volume, were reported from Cornino and Flagogna reach (Tagliamento River) and from Friola reach (Brenta River).

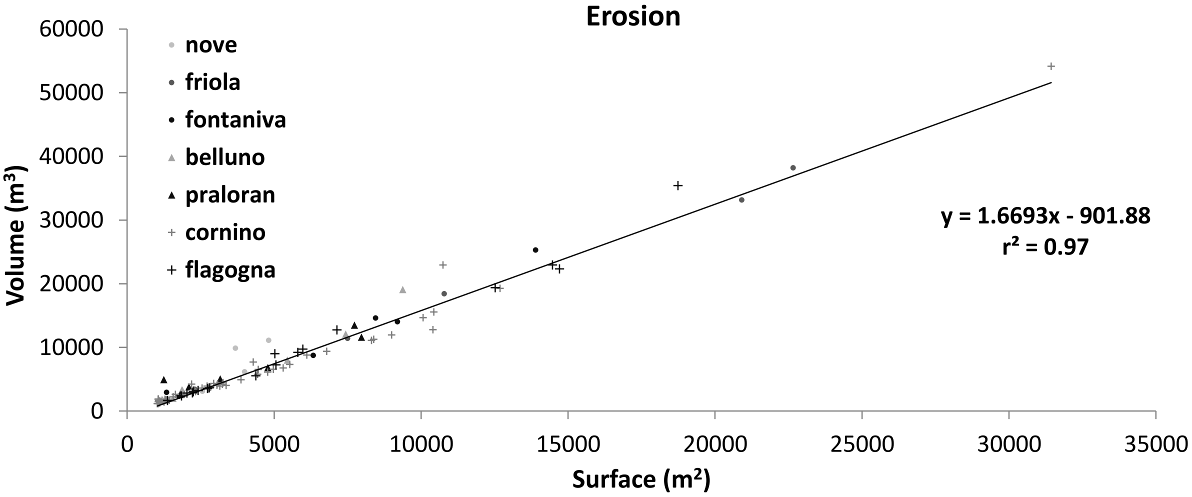

__Figure 114.__ Surface – Volume relation of the principal patches eroded (> 1000 m^2 and > - 1.00 m) among the Brenta, Piave and Tagliamento River.

In Figure 115 a similar relation is shown using the deposition. In this relation the biggest deposed patches are also represented this time from the Tagliamento, but also Friola reach, showing wide areas (Figure 59). It is interesting to note a defined linear relation between the surface and volume for the erosion (Figure 114) and also for the deposition (Figure 115). Analysing the angular coefficient we can note that at the same unit value of erosion, corresponds a greater volume than deposition. Indeed interpolating a linear relation with the erosion, an angular coefficient of 1.67 results, which means for one square meter of a significant patch, an average depth of erosion equal to 1.67 m. All the rivers seem to be well in accordance with this ratio, having a r^2 equal to 0.97. A similar relation was found for the deposition, but with a lower relation than the erosion. The angular coefficient is equal to 1.37, that means for one square meter of a significant deposed patch, an average depth of 1.37 m. All the rivers again seem to be well in accordance with this ratio, with a strong relation equal to 0.99 of r^2.

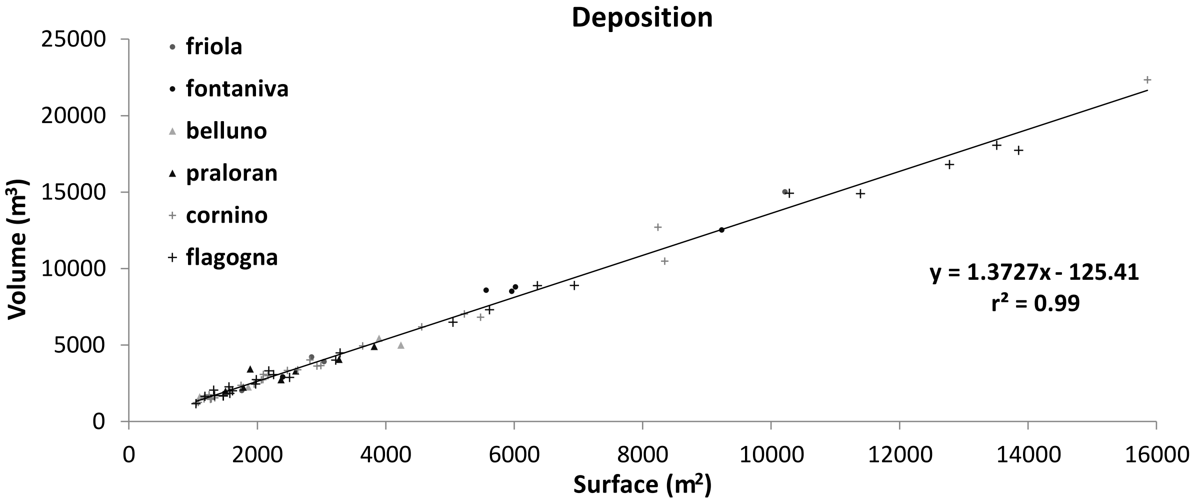

Figure 115. *Surface – Volume relation of the principal patches deposed (> 1000 m^2 and > + 1.00 m) among the Brenta, Piave and Tagliamento River.*

14.3 Influencing factors over intense flood events in a human impacted gravel bed river: the case study of the Brenta River

The morphological evolution of the Brenta River over the last 30 years has been strongly influenced by human impacts and flood events (Moretto *et al.*, 2013b). Lateral annual adjustment is directly correlated with the mean annual peak discharge (Moretto *et al.*, 2012a, 2013b), thus a higher magnitude of flooding corresponds to greater active channel widening. Substantial increases in channel width and reductions of riparian vegetation occur with flood events with an RI of more than 5 years, as already highlighted by other works concerning similar fluvial environments (e.g. Bertoldi *et al.*, 2009; Comiti *et al.*, 2011; Picco *et al.*, 2012a, 2012b; Kaless *et al.*, 2013). The flood events of November-December 2010 (RI = 8-10 years) have caused an expansion of the active channel average width by about 10% (from 196 m to 215 m) with the consequent removal of 10 ha of riparian vegetation (11% less) in the study reach (for more detailed information see Moretto *et al.*, 2012a, 2012b). The sediment processes can be analysed in detail at sub-reach level thanks to the HDTMs developed with the proposed methodology.

A severe flood event seems to generate riffle-pool migrations in the case with no nearby -natural or -artificial constrictions (e.g. P1 of Friola and Fontaniva 2010), while a pool enlargement along the channel when they are beside a constriction (e.g. P4 of Nove and P3 – P4 of Friola 2011). The location and geometry of the new bed forms seem to be related to the natural (vegetated bar) and anthropic (embankments and bridges) constrictions. Comparing the 2010 and 2011 pools it can also be noted that after a severe flood event, they are generally longer and the migrations are more concentrated beside the more compact lateral sides (Figure 62). The embankments and fluvial islands seem to have played an important role in the bed-form dynamics during the floods. Indeed, the pools of each 2011 sub-reach are located mainly next to more compact lateral surface with embankments and/or vegetated bars. On the other hand, riffles are mainly located over old pools and where no significant “constrictions” were present on either side of the wet areas.

The different behaviour of the three sub-reaches seems to be attributable to their diverse morphological characteristics (natural and imposed) and the availability of sediment from the upstream reach (Moretto *et al.*, 2012a, 2012b, 2013b). The first sub-reach is the most studied and the most affected by erosion processes (sub-chapter 11.1.3 and Moretto *et al.*, 2012a).

The conditions of Nove sub-reach can be summarized as follows: i) past and present heavy incision of the active channel with modifications in section shape and from the river basin; ii) very little sediment supply from upstream reaches; iii) almost total absence of vegetation on the floodplain; iv) increase of local slope.

In the second sub-reach, Friola, the Brenta River has a lower slope and is less constrained laterally than in the upstream area, as confirmed by the presence of a large island and a secondary channel to the right. During severe floods, therefore, the main channel can migrate forming new deposition bars. On the other hand the dynamics of Fontaniva are related to: i) greater availability of eroded sediments coming from the upper sub-reaches; ii) more balanced erosion deposition pattern (Moretto *et al.*, 2012a, 2012b, 2013b); iii) increase in the average elevation of the active channel in the last 30 years; iv) presence of extended and stable vegetation in the floodplain area which is increasingly affected by flood events; v) reduction of local slope; vi) presence of infrastructures (2 bridges). The slope reduction, together with the increase in average elevation of the active channel in the last 30 years (Moretto *et al.*, 2012a, 2012b, 2013b), determine a greater spatial mobility of the flood flow than in the past (with RI > 5 years), above all in external areas where dense and stable riparian vegetation is present. This means increased roughness and a river slowdown with the reduction of transport capacity.

The morphological changes that occurred in the Brenta River as a consequence of the flood events in 2010 (RI of about 8 and 10 years) are of great importance to evaluate the fluvial hydro-morphological quality, because they highlight the processes that are taking place, and provide insights into their future evolution as required by the EU Water Framework Directive. Nevertheless, for implementing evolutionary models and estimating sediment transport, a better assessment of the quantity of incoming and outbound sediment in the study reach and a detailed analysis of the transport rate in relation to the event magnitude are needed. Several works apply the morphological approach for estimating the sediment budget starting from transversal sections (i.e. Lane, 1998; Surian and Cisotto, 2007, Bertoldi *et al.*, 2010), nonetheless a much more accurate spatial definition can be obtained from remote sensing data (i.e. Hicks *et al.*, 2006; Hicks, 2012; Rennie, 2012; Milan and Heritage, 2012). The traditional methodologies of terrain change detection (e.g. with dGPS cross-sections) report a high precision punctual definition, however the determination of volume changes at reach scale may be improved with the assessment of DEMs differences (Lane *et al.*, 2003). The implementation of LiDAR data and colour bathymetry with the proposed methodology allowed us to obtain a terrain digital model with sufficient accuracy to derive patterns of sediment transfer, in particular within the water channels. The information obtained from such an analysis should be integrated with direct field measurements.

15 Terrestrial Laser Scanner on Hydraulic Cross Section Scale: Uncertainty Analysis

15.1 High resolution on DTMs with low uncertainty: a Protocol of Application

Aiming at DTMs building with as much resolution and least possible uncertainty the results obtained in the TLS uncertainty analysis can provide useful guidelines to achieve this goal. Three main objective factors were highlighted as able to influence the final uncertainty: the point density, angle of incidence and laser return intensity.

The point density is one of the factors that influences the final resolution (cell size) of the DTM (Wheaton *et al.* 2010). The elevation model resolution is the most important factor to choose when we plan a survey. Indeed, in function of the wanted cell size, a change the number of points required per square metre. The number of points per unit area is in function, as shown in Figure 83, with the range and/or the number of scan stations that cover that area. Figures 97, 98 and 99 show that as we lose details and consequently increase the distributed uncertainty more and more, the point density decreases. Although the number of points per unit area is a good indicator of DTMs quality, it is not enough. Indeed, as demonstrated with Figure 85, DTMs with roughly the same points number to interpolate, but surveyed from different positions, produce different DTMs. Therefore, aiming at a representative DTMs also with high resolution, we need to be careful with the homogeneity of the point distribution. As the roughness increases, we need to scan from more sides to create reliable elevation models. Aiming at reliable elevation models in gravel bed rivers, a good survey scheme to guarantee uniform points covering is proposed in Figure 116. The proposed survey method aims at scanning following an “equilateral triangle” as the scheme of the TLS scan station positioning. This scheme guarantees a good point covering inside the “triangle” by using three scan positions. The distances between each scan have to be as similar as possible, in function of the wanted number of points (to realize the desired resolution) and the instrument survey parameters used. This survey scheme could be a good compromise between good points covering and time-consuming in the field. Indeed, as shown on the right hand side of Figure 116, each “node” can be in common with more “triangles” optimizing the number of scans to do. The target positions that allow scan georeferentiation could follow the proposed scheme to allow an optimization of the surveying time and the errors derived from the registration processes, which can increase with a not good target dislocation (not uniform inside the survey area).

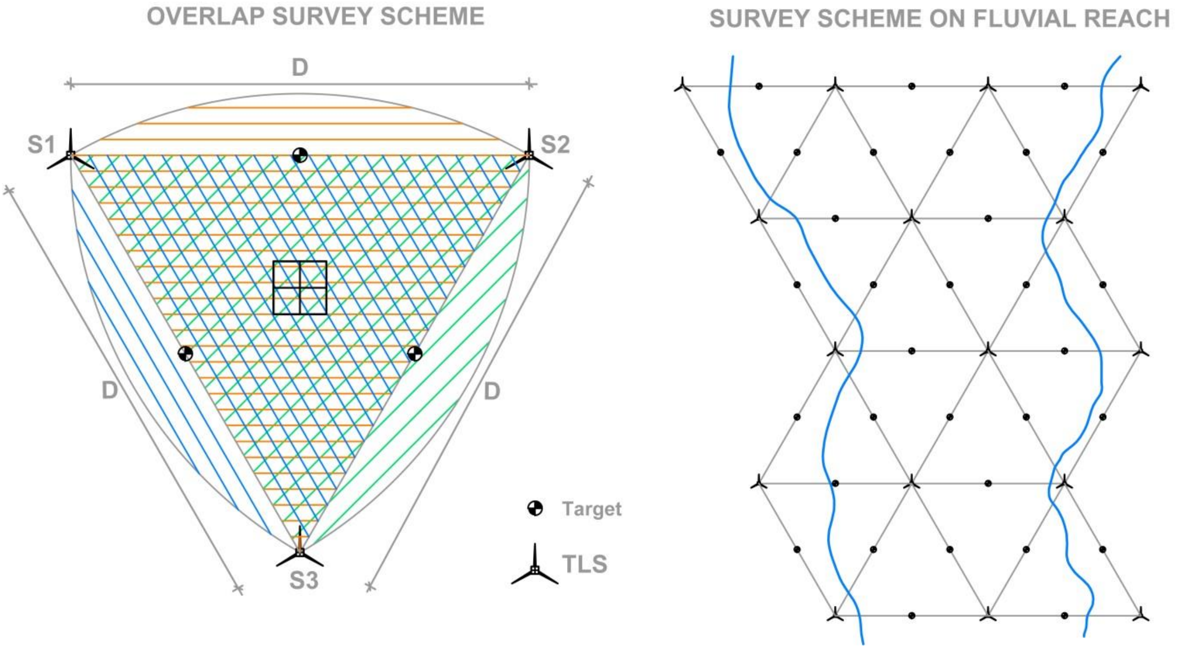

Figure 116. *Proposed survey method with equilateral triangle scheme.*

Having decided the cell size and knowing the instrument we have enough information to know how many points our instrument collects per unit area positioned at specified range. Our densities collected at specified range, material, and angle of incidence using a Leica HDS 6200 are shown in Table 6. A specified point density is not enough to collect a "highly detailed" dataset able to guarantee low uncertainty in the final elevation model. Indeed, apart from density per unit area, the second factor highlighted in the results that needs to be considered when planning a survey, is the angle of incidence.

In Figure 93, we found that the more the range increases, the angle of incidence follows the same trend. Considering not vertical surfaces, increasing the angle of incidence could be a problem because the more this angle and the roughness increase, the "shadow" effects become bigger (Figure 117). Therefore the angle of incidence associated with the surface roughness can significantly increase the final uncertainty.

Aiming at taking into account the principal sources of error in the "survey plan", a scheme could be adopted as reported in Figure 116, with a specified "station spacing" in function of the wanted resolution and the angle of incidence. Our experiments show that below 78° incidence angle (Figure 94), the errors associated with a sedimentological value D_{50} equal to 50-60 mm are lower than 0.005 m. In our case a scanner source positioned at 1.80 m height on a flat surface, corresponds to a range lower than 10 m (as shown in Figure 93).

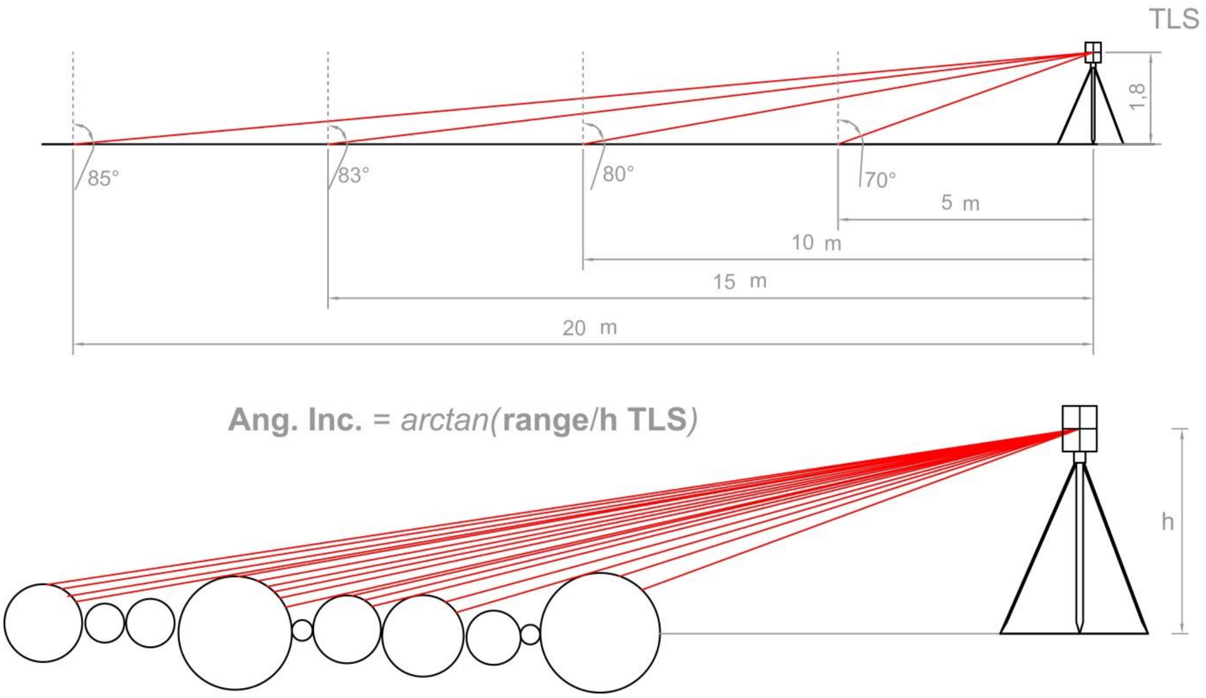

Figure 117. *Angle of incidence problem.*

A homogeneous point density from at least three scan positions, a specified threshold of point density considering also the angle of incidence, can guarantee good results, but two more factors need to be considered: the laser intensity and the presence of vegetation in the study area. Different materials, as shown in Figure 81, produce different laser returns that means different point density and point quality. Low laser intensity (Figure 91) found in dark materials, can produce more error than high intensity materials. Therefore, in the presence of a dark surface and/or moist surfaces, it is suggested to use a lower distance between each scan than for clear and/or dry surfaces.

The resolution to realize the wanted DTM needs a specified point density that has to take into account all the factors described, but all of these points must be "ground points". Surveying in the field, it is very difficult not be in the presence of vegetation or other things that will be acquired during the scanning phase. To realize reliable DTMs, also in these conditions, we must filter all not ground points from the clouds. The vegetation filter developed in this work, described in section 9.2 could be a help to filter the vegetation in a semi-automatic way (further explanation is given in sub-chapters 12.2 and 15.2).

After the "field" phase, which provides raw point clouds, we enter the "pre-elaboration" phase. This phase, if we are working with a Leica instrument for example, involves the data input, cloud registration (georeferencing) and data output of the registered point cloud by using Cyclone® software. This work, as described in section 9.1, adds a new "tool box" that could provide a good help to analyse the collected point cloud and quantify distributed uncertainty models. Thanks to this tool, we are able to calculate the range 2D - 3D and the angle of incidence on each TLS point. In addition the Matlab script “detrends” the point cloud and analyses cell by cell its density, point distribution, roughness, average intensity and other statistical parameters described in section 9.1. Point cloud interpolation and point cloud comparison are additional tools provided. Finally it is possible to calibrate an uncertainty model, based on the fuzzy analysis (see sub-chapter 9.1.3), which provides the distributed uncertainty model. The proposed model in sub-chapter 12.1.4 takes into account the density, the angle of incidence and the laser intensity, with defined error classes (Figure 96) and fuzzy rules (Table 8) to define the desired uncertainty model. The interesting thing is that the proposed model is not fixed, but by using Matlab fis editor and the “CeAfuzzy” code proposed, it is possible change or add all the factors used (collected for each TLS point) and/or fix the fuzzy rules and the classes of error. This is very important because it allows the operator to adapt the uncertainty model to the specific studied case.

Therefore the survey protocol that this work proposes to scan at high level of detail with as little uncertainty is possible, is listed below:

1. *Choose the reach of interest;*
2. *In function of the aim define the cell size of the final elevation model;*
3. *In function of the cell size, instrument, grain size and morphology, decide the distance to realize the “equilateral triangle” scheme to guarantee: the minimum number of points per unit area decided by the cell size, a homogeneous point covering, an angle of incidence less than 78° – 80° and low intensity effects as minimum as possible.*
4. *Scan the area;*
5. *Ranges and angle of incidence calculation for each scan with “RANGE_ANGLE” Matlab® code;*
6. *Scans registering and point cloud export with Cyclone®;*
7. *If required filter the vegetation with “vegeFILTER” Matlab® code;*
8. *Apply Cell Analyzer (CeA - Matlab® script) and check the right cell size;*
9. *Verify and/or fix the fuzzy rules (“fis” file). If “control patches” are available “CeAerror_dataset” Matlab® code can help in this process as shown in 12.1.3 section;*
10. *Apply CeA Fuzzy Matlab® code to have the distributed error model;*
11. *Interpolator applying to make the 2D and 3D elevation model.*

All the tools necessary to make the uncertainty are provided as an “uncertainty tool kit” with a user manual to make this work flow easy.

The proposed protocol of survey and data elaboration using a TLS could be a valid support to realize detailed DTMs with low uncertainty and low time consumption. The new tool proposed helps to reach these aims in a more automated way. The limits of the proposed tool are elaborating a very big point cloud dataset. Indeed Matlab® has a data upload limit. This problem has been in part solved in the proposed codes, indeed the code needs just to have enough memory to load the cloud; then it splits the cloud in a smaller set of clouds and uploads each time only the cloud needed in the computing. The proposed code with a dataset which has seven pieces of information (e.g. X, Y, Z, intensity, R, G, B) for each point is able to upload until 25 million points. Working with datasets bigger than the Matlab limits is possible by splitting the cloud in more parts as much as the program is able to upload. Once this operation is done, to automate the clouds elaborations, a loop has been implemented in the code that subsequently elaborates all the clouds if they are present in the same folder with the program.

In the future, converting the code in C++ could be a solution to allow the elaboration of a point cloud dataset bigger than the Matlab limit without splitting the operations.

The computing time is in function of the cell size, it increases as the cell size of analysis becomes smaller. To make the code faster, parallel computing options have been introduced. This option, as described in section 9.1.3, is able to open more Matlab sections, in function of the available RAM memory, and make them work together decreasing the computing time.

15.2 Fluvial point clouds vegetation filtering: Potentials and Limits

Working in a natural environment with the Terrestrial Laser Scanner the presence of vegetation in the study area can be a significant problem when aiming at a digital terrain model (such as shown in Figure 100). With this work A new tool to filter the vegetation in a semi-automatic way was presented in sub-chapter 9.2. The three internal filters have shown good potential (as presented in sub-chapter 12.2) but the method of points collection influences the goodness of their work. Indeed, aiming at a good performance of the colour filter, using more clouds derived from different scans, it is important to collect clouds with light conditions as similar as possible. If the final cloud has too many different vegetation and gravel colours we will be in the third case of Figure 39, where there is no separability or too restricted between the colour distributions. In this case this filter does not work. This filter is calibrated choosing a good set of vegetation and gravel calibration points and setting the percentage that defines the “distribution separability” (Figure 39).

The work of the geometrical filter is influenced by imposed parameters of calibration: cell size of analysis to build up the delta distance, the number of points to mediate necessary to generate the TIN vertex elevation and the possibility to not average some of the lowest points inside the cell of analysis (for more detail see section 9.2). The homogeneity of TLS points, apart from decreasing the uncertainty, as discussed in the previous sub-chapter, is also important for a good work of the geometrical filter. Indeed in the case study presented in sub-chapter 12.2, a cell size of analysis equal to 0.35 x 0.35 m was used. This cell size has demonstrated the best performance among the 56 tested. In theory, having a good point homogeneity and enough density, a small cell size is able to generate, with this code, a TIN that better follows the ground surface than a bigger cell. In the case study the smallest cell size tested (0.10 x 0.10 m) has not produced good performances. The reason is due to a not good homogeneity of the point cloud distributions, which involves zones with vegetation points and no ground points below, as shown in Figure 118.

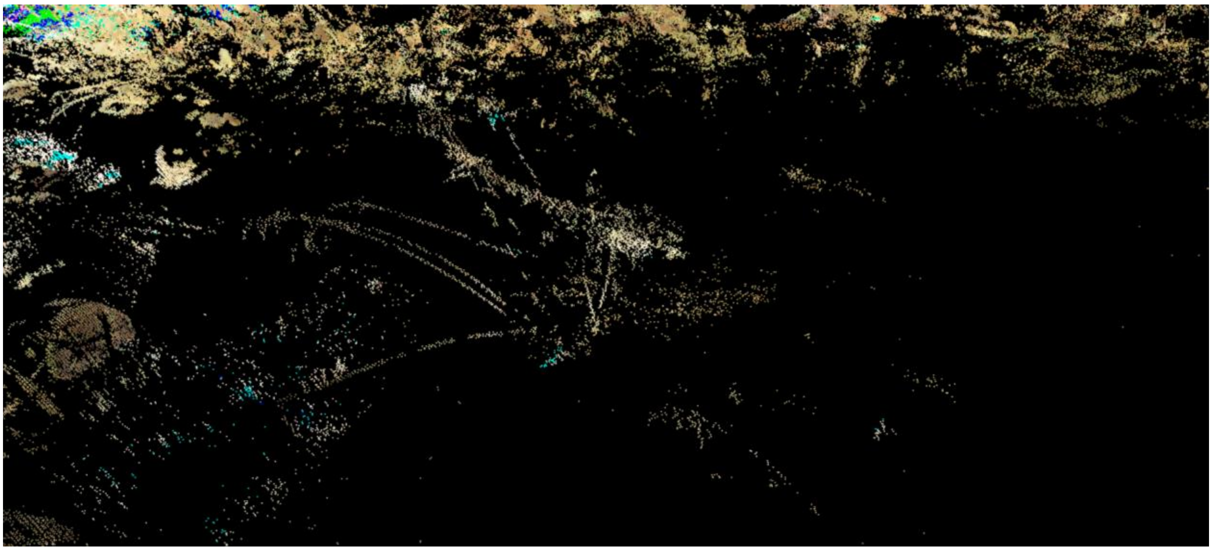

Figure 118. *Not homogeneous TLS point cloud with vegetation and no ground below.*

In these zones a small cell size is not able to filter those points, while a bigger one has more possibility of including on each cell, ground points useful to create a reliable “ground reference plane”. Although increasing the cell size could in part solve the inhomogeneity problem, in the presence of boulders, as in the case study, it increases the possibility of cutting off some ground elements.

If we follow a survey protocol as presented in the previous sub-chapter with a high point density, we have collected a homogeneous point cloud. In this case a more detailed cell size as shown in Figure 119 avoids the sediment cutting and allows a better filtering. The best cell size found with a homogeneous and an average point density equal to 5031 pts/m^2 and considering the grain size parameters D_{16}=37 mm, D_{50}=119 mm, D_{84}=357mm (Rainato et al. 2013), is equal to 0.075 x 0.075 m^2. This cell size is able to generate a TIN that follows the ground surface in a good manner. The delta associated with this cell size is the best found with the 56 preliminary tests, equal to 0.35 m and averaging the 5 lowest points to create the TIN vertex for each cell size of analysis.

Therefore, VegeFILTER seems to be a valid support in semi-automatic point cloud filtering. Its limit, as for the uncertainty analysis tool presented in the previous sub-chapters, is presented by the number of maximum points that Matlab is able to upload at the same time. This threshold is around 25 million points with seven pieces of information for each point (X, Y, Z, intensity, R, G, B). To avoid this problem we can split the cloud, with maximum 25 million points on each text file, then unify them using Cyclone® or ArcGIS®.

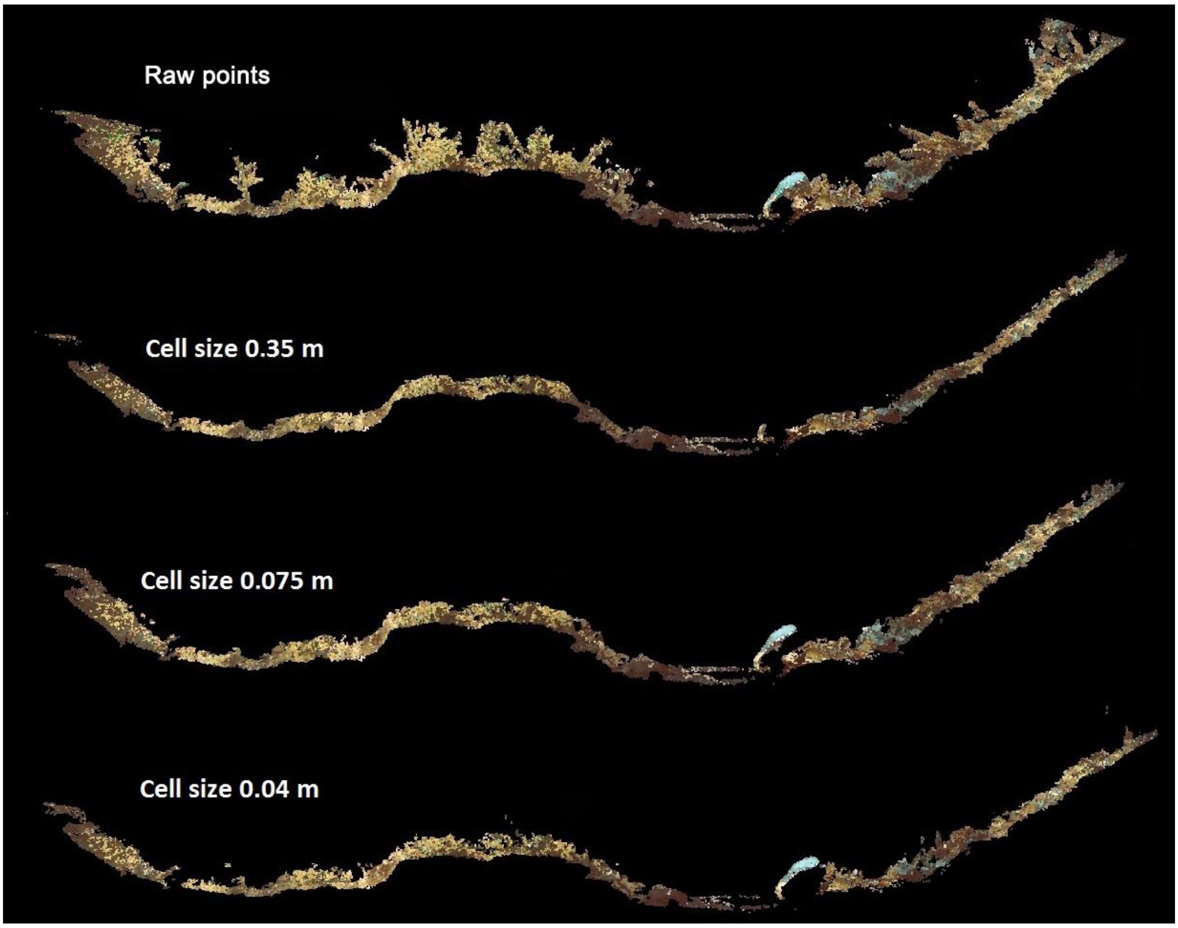

Figure 119. *Filter application on a very homogeneous case.*

In the future a code also able to classify the large wood debris could be developed to allow interesting analysis, and provide more accurate details on the debris transported by gravel bed rivers.

16 Final Remarks

One of the main problems in fluvial geomorphology is to identify the dominant process responsible for the creation of a particular form. If we really aim to connect a process with a change it is necessary to reconstruct it at a specific time and temporal scale. The observations as they happened can resolve controversies over, for instance, which process or event (e.g. discharge) is dominant (Richards, 1982).

The dynamics of a river reach can be conceived in terms of interacting waves of discharge and sediment, moving at different velocities through the catchment; as happens during a flood event. The behaviour observed in the fluvial reaches reflects the position in the catchment, and the local interaction of externally imposed discharge fluctuation with internally driven controls on sediment supply. Understanding the behaviour of a reach cannot be divorced from consideration of its position in the catchment (Lane and Richards, 1997). An implication is that the response of a system to an imposed process event, depends on the “conditioning” effects of previous events (Newson, 1980), which define the context that determines the system response. This conditioning has a spatial and temporal scale, both because processes patterns depend on a three-dimensional initial morphological condition and the spatial distribution of transportable sediment, and because the effects are closely related to the time taken for the event to propagate through the system.

Recognizing the process responsible for the creation of a particular form is not a simple analysis, it can be more difficult or impossible if the data available have too low resolution or too high uncertainty in relation to the spatial and temporal scale assessed.

For these reasons, this work has focused on analysing and optimizing different data, and collection methods derived from different time, space and resolution scales, with a good equilibrium between results, low uncertainty and time taken.

The specific objectives listed in the Introduction have allowed the limits and potentials to be known and to provide some optimizations from the small to big spatial scale and from the short- to long-term analysis.

Three main approaches were applied in this work: planimetric, volumetric and high resolution. The best spatial and temporal range of their application is shown in Figure 120.

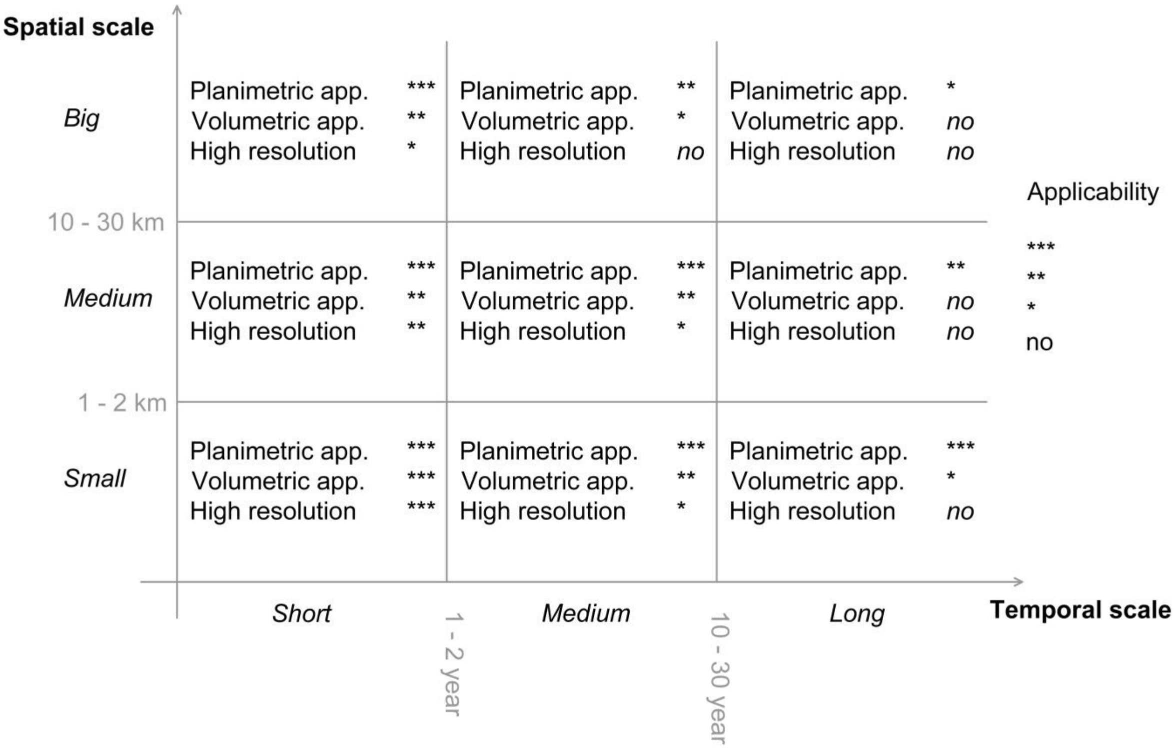

Spatial scale	Short	Medium	Long
Big	Planimetric app. *** Volumetric app. ** High resolution *	Planimetric app. ** Volumetric app. * High resolution *no*	Planimetric app. * Volumetric app. *no* High resolution *no*
Medium	Planimetric app. *** Volumetric app. ** High resolution **	Planimetric app. *** Volumetric app. ** High resolution *	Planimetric app. ** Volumetric app. *no* High resolution *no*
Small	Planimetric app. *** Volumetric app. *** High resolution ***	Planimetric app. *** Volumetric app. ** High resolution *	Planimetric app. *** Volumetric app. * High resolution *no*

Figure 120. *Table of approach application in function of time and space.*

Aiming at surface analysis, multitemporal changes among different land uses, the planimetric approach could be used. This method starts from a historical dataset of aerial photos that need to be interpreted to extract different land uses. The two critical phases and principal source of errors are the geo-rectification and photointerpretation. The photo georeferencing error is mainly related to the number, quality and dislocation of defined “control” points (recognized in the photo or on a map of reference and in the photo to fix). This error can be assessed with the root mean square errors (RMSE), as reported in sub-chapter 7.1.3. The photointerpretation error is instead mainly related to the photo resolution and operator precision. These errors can be assessed with the aerial survey details (flight parameters and photo-camera used) and with the Mount et al. (2003) method. Having assessed these sources of error, the multitemporal analysis can be considered a reliable methodology to evaluate changes in surfaces among different land uses with different temporal and spatial scales.

The medium and short-term morphological dynamics of the study reach of Brenta River, evaluated with the methodology discussed above, are remarkably complex due to the occurrence of spatially variable natural processes and human disturbances. During the study period a widening phase of the active channel has been observed, along with a reduction in island extension from 1990 to 2003 and from 2008 to 2011. On the other hand, from 1981 to 1990 and from 2003 to 2008, the river experienced channel narrowing and island expansion. However, due to the relevant spatial variability of morphological patterns, slope, and extent of human structures and disturbances, these dynamics and temporal trends are quite different along the study reach, which results in a different morphological evolution in terms of channel width and island extent. Also, the channel slope increased in the upper portion of the study reach from 0.495% to 0.526% and decreased in the lower portion from 0.429% to 0.374%. Overall, it seems that the evolution trends of these two portions, as introduced above, depend on sediment supply from upstream reaches and from the types and level of local human disturbances and infrastructure.

Alteration in sediment supply that drives recent channel and islands changes is related to the extraction of sediment, indeed since mining in the river bed was abandoned (1990s), the Brenta River has partially recovered its morphology. However, this trend is not yet stable and not distributed along the whole study reach. In the upstream area there are still incision and widening processes of the active channel as a result of bank erosion. Recent changes in the active channel size are related to the rates of flood events. The analysis of the relation between active channel adjustments and the occurrence of floods highlights that severe flood events (RI >8-10 years) caused substantial morphological modifications and erosion tends to reduce along downstream reaches.

Considering the volumetric data in gravel bed rivers, the methods with the volumetric approach and with high resolution can be used in relation to the degree of detail desired, the spatial and temporal scales.

The first thing to consider, in choosing the best method and technology to use, is the accepted error. Indeed, if we accept an average vertical error of around ± 0.20 m, the LiDAR technology, joined with the colour bathymetry (in the presence of wet areas) could be used to survey the fluvial system with a relatively low cost and time-consuming.

Not using a bathymetric laser in the presence of wet areas, can be a not negligible factor. To minimize the error introduced with those areas, is necessary to plan the LiDAR survey with the lowest hydrometric conditions. If the maximum water depth present in the surveyed reach does not exceed 1.5 m, having aerial photos contemporary with the LiDAR data and in-channel dGPS points, the proposed colour bathymetry presented in sub-chapter 8.1 could be applied.

This methodology allows high-resolution DTMs to be produced of wet areas with an associated uncertainty that has proved to be comparable to the LiDAR data. The bathymetric model calibration requires only a dGPS survey in the wet areas contemporary to the aerial image acquisition. The photo georeferencing has to be as precise as possible, to associate the right RGB cell to each dGPS point.

Statistical analyses have demonstrated that all three colour bands (R, G, B) are significantly correlated with water depth and the more explicative capacity of empirical than physical models. In addition the presence of the interaction between the colour bands cannot be neglected.

Error sources (reflections, turbulences, severe colour variations at the bottom, shadows, suspended transport, exposed sediment, etc.) were mostly intercepted through the two proposed filters regarding the curvature assessment and eliminating the implausible upper and lower limits in the bathymetric raster.

The different number of calibration points acquired (Brenta: 399 in 2010 and 1421 in 2011; Piave: 337 in 2010 and 2301 in 2011; Tagliamento: 1107 in 2010 and 9366 in 2011) also at different water level, has shown that the error of the colour bathymetry is significantly related to the water stage. A minimum number of 200 - 250 calibration points for each water range level (with a step of 0.2 m) seems to be the threshold to guarantee an average error lower than ± 0.2 m from 0 to 1.5 m of water depth.

The validation of the Hybrid Digital Terrain Models (HDTM) resulted as satisfactory for distributed evaluations of morphological variations.

The major limitations of this method are related to the presence of vegetation in the study area, that needs to be filtered. If the laser beams can pass through the vegetation, we are able to filter them by using specific filters, such as the one implemented with Terrascan software®. For the reason that we need to delete some points from the “raw” point cloud, we have to indicate the right number of ground points wanted on the filtered point cloud to the company that carries out the survey. The more density and complexity of the study area increase, the more detailed the survey has to be.

The flood events of November-December 2010 (RI= 8 and 10 years), have caused significant morphological changes in the different sub-reaches of the North-East Italian rivers (Brenta, Piave and Tagliamento).

The rasters of difference (DoD) highlight that a common consequence of these flood events is that the deposition and erosion are more concentrated in the wet areas. Therefore, aiming at quantifying erosion-deposition patterns, applying numerical models or developing sediment budgets, the bathymetric methods are fundamental to have realistic evaluations. The different behaviour registered among the sub-reaches, also thanks to the PrEDA script developed, seems to be attributable to their diverse morphological characteristics (natural and imposed) and the availability of sediment from the upstream reach.

Looking to average errors in the final DTM lower than ± 0.20 m, and a highly-detailed cell resolution in the dry areas, the TLS can be a good solution to survey relatively big areas with a very high point density per unit area and a low time required. As for the no bathymetric LiDAR, aiming at the same resolution in the wet area, we have to refer to some bathymetric sensors introduced in chapter 4. Using the TLS in gravel bed rivers, as for the LiDAR, the first question to answer for planning the survey, is the cell resolution required. Indeed, if the goal is a DTM with a spatial resolution usable to for conducting a sedimentological analysis (e.g. 0.01 x 0.01 m), three main factors were found that deserve to be carefully considered: the point density, angle of incidence and laser intensity.

A precise protocol of TLS application needs to be followed. A way could be the one presented in this thesis (sub-chapter 15.1), where the main steps are divided into four parts: survey planning, data acquisition, data processing and validation. In the first step, it is important to define the distances between the TLS scans, to have a homogeneous point covering that can guarantee enough resolution in the final DTM to reach the aimed goals. Considering the presence of vegetation and wet areas is essential. During the “field phases”, besides the parameters decided in the “planning phase”, the triangular survey scheme proposed in sub-chapter 15.1 is suggested to optimize the goodness of the point homogeneity and the time required. Implementation of the projected vegetation filter could solve a lot of time-consuming problems in the point processing phase. The new tool utilities, presented in sub-chapter 9.2, to evaluate distributed uncertainty model in the final DTMs could be a valid support to evaluate the goodness of the work in detail and identify and quantify the different sources of error.

The presented approaches can be complementary one another for some kind of analysis. Surface data indeed, can be extracted also from the application of volumetrical and high resolution approaches. Therefore, to reach results with a good equilibrium between low uncertainty and time taken, it is important to choose the right technology in relation to the required spatial resolution and accepted uncertainty. Is important to apply a precise protocol of application for each approach, which is also able to evaluate the sources of errors and the final uncertainty. The spatial and temporal scales play another important role in defining the right technology to use in relation to the data availability, financial budget and time.

The geomorphic approaches presented provide adequate topographical description of the rivers to explore channel adjustments due to natural and human causes at different spatial and temporal scales. The proposed study represents a valuable tool for any fluvial engineering, river topography description, river management, ecology and restoration purposes.

References

Antonarakis AS, Richards KS, Brasington J. 2008. Object-based land cover classification using airborne LiDAR. *Remote Sensing of Envirnoment* **112**: 2988-2998.

Arscott DB, Tockner K, Ward JV. 2000. Aquatic habitat diversity along the corridor of an Alpine floodplain river (Fiume Tagliamento, Italy). *Archiv für Hydrobiologie* **149**: 679-704.

Ashmore PE, Church MJ. 1998. Sediment transport and river morphology: a paradigm for study. In Kingleman PC, Bechta RL, Komar PD, and Bradley JB (eds) *Gravel Bed Rivers in the Environment.* Highland Ranch, CO, *Water Resources Publications*: 115-148.

Ball JE and Luk KC. 1998. Modeling Spatial Variability of Rainfall Over A Catchment. *Journal of Hydrologic Engineering*. **3**: 122-130.

Bandemer H, Gottwald S. 1995. Fuzzy Sets, Fuzzy Logic, Fuzzy Methods: with Applications. John Wiley and Sons: Chichester.

Barbara T, Rumsby, Mark G, Macklin. 2006. Channel and floodplain response to recent abrupt climate change: The tyne basin, Northern England. *Earth Surface Processes and Landforms* **19**: 499–515.

Bathurst JC. 1987. 'Measuring and modelling bedload transport in channels with coarse bed materials'. in Richards KS (Ed.). *River Channels: Environment and Process*. Blackwell Oxford: 272–294.

Bertoldi W, Gurnell A, Surian N, Tockner K, Ziliani L, Zolezzi G. 2009. Understanding reference processes: linkages between river flows, sediment dynamics and vegetated landforms along the Tagliamento River, Italy. River Research and Applications 25: 501-516.

Bertoldi W, Zanoni L, Tubino M, 2010. Assessment of morphological changes induced by flow and flood pulses in a gravel bed braided river: the Tagliamento River (Italy). Geomorphology 114: 348–360.

Besl PJ and McKay ND. 1992. A method for registration of 3-d shapes. *IEEE Transactions Pattern Analysis and Machine Intelligence* **14**: 239-256.

Braatne JH, Rood SB, Simons RK, Gom LA, Canali GE. 2003. Ecology of riparian vegetation of the Hells Canyon corridor of the Snake River: field data, analysis and modeling of plantresponses to inundation and regulated flows. *Technical Report Appendix* E. **3**: 3-3. Idaho Power Company. Boise, Idaho, USA.

Brasington J, Langham J, Rumsby B. 2003. Methodological sensitivity of morphometric estimates of coarse fluvial sediment transport. *Geomorphology* **53**(3–4): 299–316. DOI: 10.1016/ S0169-555X(02)00320-3.

Brasington J, Vericat D, and Rychkov I. 2012. Modeling river bed morphology, roughness, and surface sedimentology using high resolution terrestrial laser scanning. *Water Resource Research* **48**: W11519, doi:10.1029/2012WR012223.

Buckley SJ, Howell JA, Enge HD and Kurz TH. 2008. Terrestrial laser scanning in geology: data acquisition, processing and accuracy considerations. *Journal of the Geological Society* **165**: 625-638.

Buffington JM. 1995. Effects of hydraulic roughness and sediment supply on surface textures of gravel-bedded rivers. *Thesis, Seatle, University of Washington*: 184 p.

Buffington JM. 2012. Change in channel morphology over human time scales. In Church M., Biron P.M., and Roy A.G. (eds) *Gravel-bed Rivers: Processes, Tool, Environments*. Wiley-Blackwell: 435-463.

Burnham KP, Anderson DR. 2002. Model Selection and Multimodel Inference: A Practical Information-Theoretic Approach, 2nd ed. *Springer* **16**: pp. 488.

Carbonneau PE, Lane SN, Bergeron NE. 2006. Feature based image processing methods applied to bathymetric measurements from airborne remote sensing in fluvial environments. *Earth Surface Processes and Landforms* **31**: 1413–1423.

Castiglioni, GB, Pellegrini GB. 2001. Note illustrative della carta geomorfologica della Pianura Padana. *Suppl. Geogr. Fis. Dinam. Quat.*: IV: 207.

Cavalli M. 2006. “Caratterizzazione idrologica e morfologica dei bacini montani mediante metodologie di rilievo innovative”. *Relazione 1° anno Scuola di Dottorato T.A.R.S.* Università degli Studi di Padova.

Chappell A, Heritage GL, Fuller IC, Large ARG, Milan DJ. 2003. Geostatistical analysis of ground-survey elevation data to elucidate spatial and temporal river channel change. *Earth Surface Processes and Landforms* **28**(4): 349–370. DOI: 10.1002/esp.444.

Chen S, Nikolaidis E, Cudney HH, Rosca R, Haftka RT. 1999. Comparison of Probabilistic and Fuzzy Set Methods for Designing under Uncertainty. AIAA-99-1579, *American Institute of Aeronautics and Astronautics.*

Church M. and Jones D. 1982. Channel bars in gravel-bed rivers. *Gravel-bed Rivers. Fluvial Processes, Engineering and Management.* R.D. Hey, J.C. Bathurst and C.R.Thorne (Eds), Chichester, United Kingdom, John Wiley and Sons: 291-338.

Comiti F, Da Canal M, Surian N, Mao L, Picco L, Lenzi MA. 2011. Channel adjustments and vegetation cover dynamics in a large gravel bed river over the last 200 years. *Geomorphology* **125**: 147-159.

Conesa-Garcìa C, Lenzi MA (Eds.), 2010. Check Dams, Morphological Adjustments and Erosion Control in Torrential Streams. Nova Science Publishers, New York, pp. 298.

D’Agostino V, Dalla Fontana G, Ferro V, Milano V, Pagliara S. 2004. Briglie aperte. In Opere di sistemazione idraulico-forestali a basso impatto ambientale, Ferro V, Dalla Fontana G, Pagliara S, Puglisi S, Scotton P (eds). McGraw-Hill: Milano: 283–384.

Delai F, Moretto J, Picco L, Rigon E, Ravazzolo D, Lenzi MA. 2013. Analysis of Morphological Processes in a Disturbed Gravel-bed River (Piave River): Integration of LiDAR Data and Colour Bathymetry. *Journal of Civil Engineering and Architecture*, USA JCEA-E 20130528-4. (In press)

Dierssen HM, Zimmerman RC, Leathers RA, Downes TV, Davis CO. 2003. Ocean color remote sensing of seagrass and bathymetry in the Bahamas Banks by high-resolution airborne imagery. *Limnology and Oceanography* **48**(1, part 2): 444–455.

Dixon LFJ, Barker R, Bray M, Farres P, Hooke J, Inkpen R, Merel A, Payne D, Shelford A. 1998. Analytical photogrammetry for geomorphological research. In Lane S.N., Richards K.S., Chandler J.H. (eds). *Landform Monitoring, Modelling and Analysis,* John Wiley & Sons: Chichester; Chapter **4**: 63–94.

Einstein H, and Shen SW. 1964. A study of meandering in straight alluvial channels. *Journal of Geophysics Research*. **69**: 5239-5247.

Ferguson RI, Werritty A. 1983. Bar development and channel changes in the gravelly River Feshie. Schotland. *Special Publ. of the Int. Ass. Sedim*. **6**.

Fonstad MA, Marcus WA. 2005. Remote sensing of stream depths with hydraulically assisted bathymetry (HAB) models. *Geomorphology* **72**(4): 320–329.

Franceschi M, Teza G, Preto N, Pesci A, Galgaro A and Girardi S. 2009. Discrimination between marls and limestones using intensity data from terrestrial laser scanner. ISPRS *Journal of Photogrammetry and Remote Sensing*. **64**: 522-528.

Franke R. 1982. Smooth Interpolation of Scattered Data by Local Thin Plate Splines. *Journal of Computation and Mathematics with Applications*. **8**: 273-281.

Fryer JG, 1983. A simple system for photogrammetric mapping in shallow-water. *Photogrammetric Record* **11**: 203–208.

Fryirs KA, Brierley GJ. 2013 *Geomorphic analysis of river systems. An approach to reading the landscape.* Wiley-Blackwell

Gilvear DJ, Heal KV, Stephen, A. 2002. Hydrology and the ecological quality of Scottish river ecosystems. *Science of the total environment*, **294**(1), 131-159.

Giuliacci M, Abelli S, Dipierro G. 2001. Il clima dell'Italia nell'ultimo ventennio, Alpha test, Milano pp. 344.

Globevnik L, Mikoš M. 2009. Boundary conditions of morphodynamic processes in the Mura River in Slovenia. *Catena* **79**: 265-276.

Guarnieri A, Vettore A, Pirotti F, Menenti M, Marani M. 2009. Retrieval of small-relief marsh morphology from terrestrial laser scanner, optimal spatial filtering, and laser return intensity. *Geomorphology* **113**(1): 12-20.

Gurnell AM. 1997. Channel changes of the river Dee meanders, 1946–1992, from the analysis of air photographs. *Regulated Rivers: Research and Management* **13**: 13–26.

Gurnell AM, Petts GE. 2002. Island-dominated landscapes of large floodplain rivers, a European perspective. Freshwater Biology **47**: 581–600.

Gurnell AM, Surian N, Zanoni L. 2009. Multi-thread river channels: a perspective on changing European alpine river systems. *Aquatic Sciences* **71**: 253-265.

Heritage GL, Fuller IC, Charlton ME, Brewer PA, Passmore DP. 1998. CDW photogrammetry of low relief fluvial features: accuracy and implications for reach-scale sediment budgeting. *Earth Surface Processes and Landforms* **23**: 1219–1233.

Heritage, GL and Milan, DJ. 2009. Terrestrial Laser Scanning of grain roughness in a gravel-bed river. *Geomorphology* **113**: 4-11.

Hey RD, and Thorne CR. 1986. Stable channels with mobile gravel beds. *Journal of Hydraulics Engineering* **112**(8): 671-689.

Hicks DM, Duncan MJ, Walsh JM, Westaway RM, Lane SN. 2002. New views of the morphodynamics of large braided rivers from high-resolution topographic surveys and time-lapse video. *IAHS Publication* **276**: 373–380.

Hicks DM, Duncan MJ, Shankar U, Wild M and Walsh JR. 2003. “Project Aqua: Lower Waitaki River geomorphology and sediment transport”. *NIWA Client Report CHC01/115*, National Institute of Water and Atmospheric research, Christchurch: 195 p.

Hicks DM, Shankar U, Duncan MJ, Rebuffe M, Abele J, 2006. Use of remote sensing technologies to assess impacts of hydro-operations on a large, braided, gravel-bed river: Waitaki River, New Zealand. In Sambrook Smith GH, Best JL, Bristow CS, Petts GE, (eds) Braided Rivers, Processes, Deposits, Ecology and Management. *International Association of Sedimentologists, Special Publication* **36**, Oxford, Blackwell: 311-326.

Hicks DM. 2012. Remotely sensed topographic change in gravel riverbeds with flowing channels. In Church M., Biron P.M., and Roy A.G. (eds) *Gravel-bed Rivers: Processes, Tool, Environments*. Wiley-Blackwell: 303-314.

Hilldale RC, Raff D. 2008. Assessing the ability of airborne LiDAR to map river bathymetry. *Earth Surface Processes and Landforms* **33**: 773-783.

Hodge RA, Brasington J, Richards KS. 2009. Analysing laser-scanned digital terrain models of gravel bed surfaces: linking morphology to sediment transport processes and hydraulics. *Sedimentology* **56**: 2024-2043.

Hodge RA. 2010. Using simulated Terrestrial Laser Scanning to analyse errors in high-resolution scan data of irregular surfaces. *Photogrammetry and Remote Sensing* **65**: 227-240.

Horn BKP. 1987. Closed-825 Form Solution of Absolute Orientation Using Unit Quaternions. *Journal of the Optical Society of America* A **4**(4): 629-642.

Hughes ML, McDowell PF, Marcus WA. 2006. Accuracy assessment of georectified aerial photographs: implications for measuring lateral channel movement in a GIS. *Geomorphology* **74**: 1–16.

Jang JSR, Gulley N. 2007. Fuzzy Logic Toolbox 2: User Guide, Matlab, Matlab, Natick, MA, 299 pp.

Kaless G. 2012. Stability analysis of gravel bed rivers: caomparison between natural rivers and disturbed rivers due to human activities. PhD Thesis; University of Padova, Italy, pp. 275.

Kaless G. 2013. Stability analysis of gravel-bed rivers: comparison between natural rivers and disturbed rivers due to human activities. *PhD Thesis. University of Padua*. 299 p.

Kaless G, Mao L, Lenzi MA. 2011. Regime theories in gravel bed rivers; preliminary comparison between disturbed rivers due to antrophic activities (Northeastern Italy) and natural rivers (Patagonia, Argentina). Proceedings of the Intermediate Congress of the Italian Association of Agricultural Engineering; Belgirate, Italy; September 22-24, 2011; pp. 8.

Keller EA, Melhorn WN. 1973. Bedforms and fluvial processes in alluvial stream channels: selected observations, in M. Morisawa (Ed.) Fluvial geomorphology: SUNY-Binghamton NY, Proc. Fourth Annual Geomorphology Symposium. *Geomorphology*: 253-283.

Kinzel PJ, Wright CW, Nelson JM, Burman AR. 2007. Evaluation of an experimental LiDAR for surveying a shallow, braided, sand-bedded river. *Journal of Hydraulic Engineering* **133**: 838–842.

Kinzel PJ, Legleiter CJ, and Nelson JM, 2012. Mapping River Bathymetry with a Small Footprint Green LiDAR: Applications and Challenges. *Journal of the American Water Resources Association* (JAWRA) 1-22. DOI: 10.1111.

Klir GJ, Yuan B. 1995. Fuzzy Sets and Fuzzy Logic: Theory and Applications. Prentice Hall: Upper Saddle River, NJ.

Kondolf GM. 1997. Hungry water: effects of dams and gravel mining on river channels. *Environ. Mgmt*, 21-4-1997: 533-551.

Kruizinga S, Yperlaan GJ. 1978. Spatial Interpolation of Daily Total of Rainfall. *Journal of Hydrology*. **36**: 65-73.

Lane SN. 1998. The use of digital terrain modelling in the understanding of dynamic river channel systems. In Lane S.N., Richards K., Chandler J. (eds.), Landform Monitoring, Modelling and Analysis. Wiley, Chichester; pp. 311–342.

Lane SN, Richards KS, Chandler JH. 1994. Developments in monitoring and terrain modelling of small-scale riverbed topography. *Earth Surface Processes and Landforms* **19**: 349–368.

Lane SN, Richards KS and Chandler JH. 1996. 'Discharge and sediment supply controls on erosion and deposition in a dynamic alluvial channel'. *Geomorphology*. **15**: 1–15.

Lane SN, Richards KS. 1997. Linking river channel form and process: time, space and causality revisited. *Earth Surface Processes and Landforms* **22**(3): 249-260.

Lane SN, Westaway RM, Hicks DM. 2003. Estimation of erosion and deposition volumes in a large, gravel-bed, braided river using synoptic remote sensing. *Earth Surface Processes and Landforms* **28**(3):249–271. DOI: 10.1002/esp.483.

Lane SN, Tayefi V, Reid SC, Yu D, Hardy RJ. 2007. Interactions between sediment delivery, channel change, climate change and flood risk in a temperate upland environment. *Earth Surface Processes and Landforms* **32**: 429–446.

Lane SN, Widdison PE, Thomas RE, Ashworth PJ, Best JL, Lunt IA, Sambrook Smith GH, Simpson CJ. 2010. Quantification of braided river channel change using archival digital image analysis. *Earth Surface Processes and Landforms* **35**: 971–985. DOI: 10.1002/esp.2015.

Langbein WB, Leopold LB. 1968. River channel bars and dunes: Theory of kinematic waves. *Geological Survey Professional Paper* **422**-L, 23p.

Legleiter CJ. 2011. Remote measurement of river morphology via fusion of LiDAR topography and spectrally based bathymetry. *Earth Surface Processes and Landforms* **37**: 499-518.

Legleiter CJ, 2013. Mapping river depth from publicly available aerial images. *River Research and Applications* **29**: 760–780. doi: 10.1002/rra.2560

Legleiter CJ, Roberts DA, Marcus WA, Fonstad MA. 2004. Passive remote sensing of river channel morphology and in-stream habitat: physical basis and feasibility. *Remote Sensing of Environment* **93**: 493 –510.

Legleiter CJ, Roberts DA, Lawrence RL. 2009. Spectrally based remote sensing of river bathymetry. *Earth Surface Processes and Landforms* **34**: 1039–1059.

Legleiter CJ, Roberts DA. 2009. A forward image model for passive optical remote sensing of river bathymetry. *Remote Sensing of Environment* **113**: 1025–1045.

Legleiter CJ, Kinzel PJ, Overstreet BT. 2011. Evaluating the potential for remote bathymetric mapping of a turbid, sand-bed river: 1. Field spectroscopy and radiative transfer modeling. *Water Resource Research*. **47**. W09531, doi:10.1029/2011WR010591.

Lenzi MA, D'Agostino V, Sonda D. 2000. Ricostruzione morfologica e recupero ambientale dei torrenti. *Editoriale Bios*. Cosenza, Italia.

Lenzi MA, Mao L, Comiti F, Rigon E, Picco L, Vitti P, Moretto J., Sigolo C. 2010. Scientific contribution by the Research Unit Land and Agro-forest Department, to the research activities carried out in the framework of the CARIPARO Project "Linking geomorphological processes and vegetation dynamics in gravel-bed rivers", from September 2009 to October 2010. *Research and Technical Report; Department of Land and Agro-forest Environment, University of Padova, Padova , Italy,* pp. 102.

Leopold LB, Wolman MG, Miller JP. 1964. Fluvial Processes in Geomorphology, W. H. Freeman and Company, San Francisco. 522p.

Leopold LB. 1982. Water surface topography in river channels and implications for meander development. In *Gravel-bed Rivers*. R. D. Hey, J. C. Bathurst and C. R. Thorne (Eds.), John Wiley $ Sons, 359-388.

Lichti DD. 2005. Spectral filtering and classification of terrestrial laser scanner point clouds. *The Photogrammetric Record*. **20**: 218-240.

Lichti DD, Gordon SJ, Stewart MP. 2002. Ground-Based Laser Scanners: Operations, Systems and Applications. *Geomatica*. **56:** 21 - 33.

Lichti DD, Jamtsho S. 2006. Angular Resolution of Terrestrial Laser Scanners. *The Photogrammetric Record* **21**: 141-160.

Lichti DD, Pfeifer N, Maas HG. 2008. Editorial: ISPRS Journal of Photogrammetry and Remote Sensing theme issue "Terrestrial Laser Scanning". ISPRS Journal of Photogrammetry and Remote Sensing **63**: 1-3.

Lichti DD, Skaloud J. 2010. Registration and Calibration. In Airborne and Terrestrial Laser Scanning, edited by G. Vosselman and H.-G. Maas. *Whittles Publishing, Caithness*. UK, 83-133.

Liébault F, Piégay H. 2001. Assessment of channel changes due to long-term bedload supply decrease, Roubion River, France. *Geomorphology* **36**: 167–186.

Liebault R, Piegay H. 2002. “Causes of 20th century channel narrowing in mountain and piedmont rivers and streams of southeastern France”. *Earth Surface Processes and Landforms* **27**: 425–44.

Linton DL. 1949. Some Schottish river captures re-examined: 1. The diversion of the upper Geldte. *Scott. Geogr. Mag.* **65**: 123-32.

Lodwick WA, Santos J. 2003. Constructing consistent fuzzy surfaces from fuzzy data. *Fuzzy Sets and Systems* **135**: 259–277. DOI: 10.1016/S0165-0114(02)00139-2.

Lyon JG, Lunetta RS, Williams DC. 1992. Airborne multispectral scanner data for evaluating bottom sediment types and water depths of the St. Marys river, Michigan. *Photogrammetric Engineering and Remote Sensing* **58**: 951–956.

Lyon JG, Hutchinson WS. 1995. Application of a radiometric model for evaluation of water depths and verification of results with airborne scanner data. *Photogrammetric Engineering and Remote Sensing **61***: 161–166.

Macklin MG, Rumsby BT. 2007. Changing climate and extreme floods in the British uplands. *Transactions of the Institute of British Geographers* **32**: 168–186. doi: 10.1111/j.1475-5661.2007.00248.x

Marcus WA. 2012. Remote sensing of the hydraulic environments in gravel-bed rivers. In Church M., Biron P.M., and Roy A.G. (eds) *Gravel-bed Rivers: Processes, Tool, Environments*. Wiley-Blackwell, pp. 261-285.

Marcus WA, Fonstad MA. 2008. Optical remote mapping of rivers at sub-meter resolutions and watershed extents. Earth Surface Processes and Landforms **33**: 4–24.

Marcus WA, Legleiter CJ, Aspinall RJ, Boardman JW, Crabtree RL. 2003. High spatial resolution hyperspectral mapping of in-stream habitats, depths, and woody debris in mountain streams. *Geomorphology* **55**: 363–380.

McKean JA, Nagel D, Tonina D, Bailey P, Wright CW, Bohn C, Nayegandhi A. 2009. Remote Sensing of Channels and Riparian Zones With a Narrow-Beam Aquatic-Terrestrial LiDAR. *Remote Sensing* **1**(4):1065-1096.

Milan DJ, Heritage GL, Hetherington D. 2007. Application of a 3D laser scanner in the assessment of erosion and deposition volumes and channel change in a proglacial river. *Earth Surface Processes and Landforms* **32**: 1657–1674.

Milan DJ, Heritage GL, Large ARG, Fuller IC. 2011. Filtering spatial error from DEMs: Implications for morphological change estimation. *Geomorphology* **125**: 160-171.

Milan DJ, Heritage GL, 2012. LiDAR and ADCP use in gravel-bed rivers: Advances since GBR6. In Church M, Biron PM, and Roy AG. (eds.) Gravel-bed Rivers: Processes, Tool, Environments. Wiley-Blackwell, pp. 286-302

Mitas L, Mitasova H. 1988. General Variational Approach to the Interpolation Problem. *Journal of Computation and Mathematics with Applications*. **16**: 983-992.

Montane JM, Torres R. 2006. Accuracy assessment of LiDAR saltmarsh topographic data using RTK GPS. Photogrammetric engineering and remote sensing, **72**(8): 961-967.

Montgomery DR, Buffington JM. 1997. Channel-reach morphology in mountain drainage basins, Geol. Soc. Am. Bull., **109**: 596–611, doi:10.1130/0016-7606(1997)109<0596:CRMIMD>2.3.CO;2.

Moretto J, Rigon E, Mao L, Picco L, Delai F, Lenzi MA. 2012a. Assessing short term erosion-deposition processes of the Brenta River using LiDAR survey. *WIT Transactions on Engineering Sciences* **73**: 149-160; doi: 102495/DEB120131.

Moretto J, Rigon E, Mao L, Picco L, Delai F, Lenzi MA. 2012b. Medium-and short-term channel and island evolution in a disturbed gravel bed river (Brenta River, Italy). *Journal of Agricultural Engineering* **43**(4); 176-188; doi: 10.4081/jae.2012.e27.

Moretto J, Delai F, Picco L, Lenzi MA, 2013a. Integration of colour bathymetry, LiDAR and dGPS surveys for assessing fluvial changes after flood events in the Tagliamento River (Italy). *Agricultural Sciences* 4(8A): 21-29; doi: 10.4236/as.2013.48A004

Moretto J, Rigon E, Mao L, Picco L, Delai F, Lenzi MA. 2013b. Channel adjustment and island dynamics in the Brenta River (Italy) over the last 30 years. *River Research and Applications;* doi: 10.1002/rra.2676

Moretto J, Delai F, Lenzi MA. 2013c Hybrid DTMs derived by LiDAR and Colour bathymetry for assessing fluvial geomorphic changes after flood events in gravel-bed rivers, Italy. International Jurnal of Safety and Security Engeneering, 3(2): 1–13.

Mount NJ, Louis J, Teeuw RM, Zukowskyj PM, Stott T. 2003. Estimation of error in bankfull width comparison from temporally sequenced and corrected aerial photographs. *Geomorphology* **56**: 65–77.

Muste M, Kim D, Merwade V. 2012. Modern digital instruments and techniques for Hydrodynamic and morphologic characterization of river channels.In Church M., Biron P.M., and Roy A.G. (eds) *Gravel-bed Rivers: Processes, Tool, Environment*s. Wiley-Blackwell, pp. 315-341.

Newson MD. 1980. ‘The geomorphological effectiveness of floods – a contribution stimulated by two recent events in mid-Wales’. *Earth Surface Processes* **5**: 1–16.

Nield JM, Wiggs GFS. 2011. The application of terrestrial laser scanning to Aeolian saltation cloud measurement and its response to changing surface moisture. *Earth Surface Processes and Landforms* **36**: 273–278.

Oliver MA. 1990. Kriging: A Method of Interpolation for Geographical Information Systems. *International Journal of Geographic Information Systems* **4**: 313-332.

Palmieri A, Shah F, Dinar A. 2001. Economics of reservoir sedimentation and sustainable management of dams. Journal of Environmental Management 61: 149–163.

Panissod F, Bailly JS, Durrieu S, Jacome A, Mathys N, Cavalli M, Puech C. 2009. Qualifiction de modeles numeriques de terrain LiDAR pour l'etude de l'erosion: Application aux badlands de draix. *Revue Francaise de Photogrammetrie et de Teledetection* **192**: 50-57.

Parker G, Sutherland AJ. 1990. Fluvial armor, Journal of Hydraulic Research. **28**(5): 529-544.

Petrie G, Toth CK. 2008. Introduction to laser ranging, profiling, and scanning. *Topographic Laser Ranging and Scanning: principles and processing*. edited by: Shan, J. and Toth, C. K., CRC Press, Taylor & Francis, 590 pp.

Picco L. 2010. Long period morphological dynamics in regulated braided gravel-bed rivers: comparison between Piave River (Italy) and Waitaki River (New Zealand). *PhD Thesis*. University of Padua. 190 p.

Picco L, Mao L, Rigon E, Moretto J, Ravazzolo D, Delai F, Lenzi MA. 2012a. Medium term fluvial island evolution in relation with floods events in the Piave River. *WIT Transactions on Engineering Sciences* **73**: 161-172; doi: 10.2495/DEB120141; ISSN 1743-3522.

Picco L, Mao L, Rigon E, Moretto J, Ravazzolo D, Delai F, Lenzi MA. 2012b. Riparian forest structure, vegetation cover and flood events in the Piave River. *WIT Transactions on Engineering Sciences* **73**: 137-147; doi: 10.2495/DEB120121; ISSN 1743-3522.

Picco L, Mao L, Cavalli E, Buzzi E, Rigon E, Moretto J, Delai F, Ravazzolo D, Lenzi MA. 2012c. Using a Terrestrial Laser Scanner to assess the morphological dynamics of a gravel-bed river. *IAHS-AISH Publication, Issue* **356**: 428-437.

Piegay H, Darby S, Mosselman E, Surian N. 2005. A review of techniques available for delimiting the erodible river corridor: a sustainable approach to managing bank erosion. River Research and Applications 21: 773–789.

Piégay H, Grant G, Nakamura F, Trustrum N. 2006. Braided rivers management: from assessment of river behaviour to improved sustainable development. In: (eds.); *Braided rivers: process, deposits, ecology and management*, Wiley- Blackwell: 257-275.

Poff NL, Olden J D, Merritt DM, and Pepin DM. 2007. Homogenization of regional river dynamics by dams and global biodiversity implications. *Proceedings of the National Academy of Sciences* **104**: 5732–5737.

Press WH. 1988. Numerical Recipes in C. *The Art of Scientific Computing*. New York Cambridge University Press.

Rainato R, Picco L, Lenzi MA, Mao L, Rigon E, Delai F, Moretto J, Cesca A, Vianello A 2013. Monitoring and analysis of the sediment transport event of November 2012 in the Rio Cordon Station. Quaderni di Idronomia Montana (in press).

Rennie CD. 2012. Mapping water and sediment flux distributions in gravel-bed rivers using ADCPs. In Church M., Biron P.M., and Roy A.G. (eds) *Gravel-bed Rivers: Processes, Tool, Environments.* Wiley-Blackwell, pp. 342-350.

Richards KS. 1982. Rivers: Form and Process in Alluvial Channels, Methuen, London, 361 pp.

Rinaldi M, Piégay H, Surian N. 2011. Geomorphological approaches for river management and restoration in Italian and French rivers. in Stream Restoration in Dynamic Fluvial Systems: Scientific Approaches, Analyses, and Tools, Geophys. Monogr. Ser., vol. 194, edited by A. Simon, S. J. Bennett and J. M. Castro, pp. 95–113, AGU, Washington, D. C., doi:10.1029/2010GM000984.

Rinner K. 1969. Problems of two medium photogrammetry. *Photogrammetric Engineering* **35**: 275.

Robins NS. 1990. Hydrogeology of Scotland. London: HMSO.

Royle AG, Clausen FL and Frederiksen P. 1981. Practical Universal Kriging and Automatic Contouring. *Geoprocessing* **1**: 377-394.

Rumsby B, McVey R, Brasington J. 2001. The Potential for high resolution fluvial archives in braided rivers: quantifying historic reach-scale channel and floodplain development in the River Feshie, Scotland. In Maddy D, Macklin MG, Woodard JC (eds). *River Basin Sediment Systems: Archives of Environmental Change*. Steenwijik, The Netherlands, pp. 445–467.

Soudarissanane S, Lindenbergh R, Menenti M, Teunissen P. 2010. Scanning geometry: Influencing factor on the quality of terrestrial laser scanning points. *Photogrammetry and Remote Sensing* **66**: 389-399.

Stover SC, Montgomery DR. 2001. Channel change and flooding, Skokomish River, Washington. *Journal of Hydrology* **243**: 272-286.

Surian N. 1998. “Studio finalizzato alla definizione geomorfologica della fascia di pertinenza fluviale del Fiume Piave tra Perarolo e Falzè e del torrente Cordevole tra Mas e Santa Giustina”. Autorità di bacino dei fiumi Isonzo, Tagliamento, Livenza, Piave, Brenta-Bacchiglione. Studi finalizzati alla redazione del piano di bacino del Fiume Piave, 38 pp. più appendici e cartografia.

Surian N. 1999. Channel changes due to river regulation: the case of the Piave River, Italy. *Earth Surface Processes and Landforms* **24**: 1135–1151.

Surian N. 2002. Downstream variation in grain size along an Alpine river: analysis of controls and processes. Geomorphology, 43(1), 137-149.

Surian N, Rinaldi M. 2003. Morphological response to river engineering and management in alluvial channels in Italy. *Geomorphology* **50**: 307–326.

Surian N, Rinaldi M. 2004. Channel adjustments in response to human alteration of sediment fluxes: examples from Italian rivers. In: Golosov V, Belyaev V, Walling DE. (Eds.), Sediment Transfer Through the Fluvial System, IAHS Publication N. 288. , pp. 276–282.

Surian N, Cisotto A. 2007. Channel adjustments, bedload transport and sediment sources in a gravel-bed river, Brenta River, Italy. *Earth Surface Processes and Landforms* **32**: 1641-1656.

Surian N, Mao L, Giacomin M, Ziliani L. 2009a. Morphological effects of different channel-forming discharges in a gravel-bed river. *Earth surface processes and landforms* **34**: 1093-1107.

Surian N, Ziliani L, Comiti F, Lenzi MA, Mao L. 2009b. Channel adjustments and alteration of sediment fluxes in gravel-bed rivers of north-eastern Italy: Potentials and limitations for channel recovery. *River Research and Applications* **25**: 551-567.

Taylor J. 1997. An Introduction to Error Analysis: the Study of Uncertainties in Physical Measurements. (2nd eds) *University Science Books*: Sausalito, CA.

Thompson A. 1986. Secondary flows and the pool–riffle unit – a case-study of the processes of meander development. *Earth Surface Processes and Landforms* **11**(6): 631–641.

Tockner K, Malard F, Ward JV. 2000. “An extension of the Flood Pulse Concept”. Hydrol. Process. **14**: 2861-2883.

Tockner K, Ward JV, Arscott DB. 2003 The Tagliamento River: a model ecosystem of European importance. Aquatic Sciences **65**: 239–253.

Tung YK. 1983. Point Rainfall Estimation for a Mountainous Region. *Journal of Hydraulic Engineering* **109**: 1386-1393.

Vitti P, Picco L, Mao L, Sitzia T, Comiti F, Rigon E, Lenzi MA. 2011. Linking riparian forest structure and fluvio-morphological characteristics in a gravel bed river (Piave river-Italian Alps). Poster presented at the International Workshop Advances in River Science, 18-21 April 2011, Swansea, UK.

Vosselman G, Mass HG. 2010. Airborne and Terrestrial Laser Scanning, Whittles Publishing, Scotland, UK.

Ward JV, Tockner K, Edwards PJ, Kollmann J, Bretschko G, Gurnell AM, Petts GE, Rossaro B. 1999. A reference river system for the alps: the Fiume Tagliamento. *Regulated rivers: Research & Management* **15**: 63-75.

Watson DF, Philip GM. 1985. A Refinement of Inverse Distance Weighted Interpolation. *Geo-Processing* **2**: 315-327.

Wehr A, Lohr U. 1999. Airborne laser scanning – an introduction and overview. ISPRS Journal of Photogrammetry and Remote Sensing **54**: 68–82.

Werritty A. 1984. Stream response to flash floods in upland Scotland [in:] TP Bust and DE Walling (eds.). Catchment experiments in fluvial geomorphology. *Geobooks*. Norwich.

Westaway RM, Lane SN, Hicks DM. 2003. Remote survey of largescale braided, gravel-bed rivers using digital photogrammetry and image analysis. *International Journal of Remote Sensing* **24**(4): 795– 815. DOI: 10.1080/01431160110113070.

Wheaton JM. 2008. Uncertainty in morphological sediment budgeting of rivers. *Unpublished PhD.* University of Southampton. Southampton. 412 p. Available at: http://www.joewheaton.org/Home/ research/projects-1/phdthesis.

Wheaton JM, Brasington J, Darby SE, Sear DA. 2010. Accounting for uncertainty in DEMs from repeat topographic surveys: improved sediment budgets. *Earth Surf. Process. Landforms* **35**: 136–156.

Winterbottom SJ, Gilvear DJ. 1997. Quantification of channel bed morphology in gravel-bed rivers using airborne multispectral imagery and aerial photography. *Regulated Rivers: Research and Management* **13**: 489–499.

Winterbottom SJ. 2000. Medium and short-term channel planform changes on the Rivers Tay and Tummel, Scotland. *Geormorphology* **34**: 195–208.

Yang CT. 1971. Potential energy and stream morphology. *Water Resources Research* **7**: 311-322.

Young JAT. 1976. The terraces of glen Feshie, Inversess-shire. Trans. Roy. Soc. Edinburgh **69**.

Zanoni L, Gurnell A, Drake N, Surian N. 2008. Island dynamics in a braided river from analysis of historical maps and air photographs. *River Research and Applications* **24**: 1141-1159.

Aknoledgements

Un ringraziamento molto sentito è dovuto al Professor Mario Aristide Lenzi che mi ha dato la possibilità di fare questa interessantissima esperienza di dottorato e per tutti i suoi preziosi consigli.

Un ringraziamento al Professor Luca Mao che mi ha sempre suggerito ottimi spunti da seguire e da usare per assemblare il mio lavoro di dottorato.

I gratefully acknowledge to James Brasington Professor for providing me the possibility of a great experience with the TLS and the data elaboration in England and in Scotland.

Un grande ringraziamento a tutti i miei colleghi PhD Emanuel Rigon, PhD Lorenzo Picco, Dott. Fabio Delai, Dott. Diego Ravazzolo e Dott. Riccardo Rainato per tutto il loro supporto, le avventurose missioni, i convegni e le mangiate fatte assieme in questi tre anni.

Un grande ringraziamento al Professor Gabriel Kaless, per tutto il suo supporto e alla indimenticabile esperienza passata assieme in Patagonia prima di intraprendere questo percorso di dottorato.

Un ringraziamento molto speciale alla mia ragazza Stefania che in questi tre anni mi è sempre stata molto vicina e mi ha regalato degli indimenticabili momenti assieme.

In fine un ringraziamento molto speciale va ai miei genitori Mauro e Diega e ai miei fratelli Danny e Michael che mi sono sempre stati vicini e mi hanno sempre supportato in tutti i momenti di necessità.

Thank you very much to all!!!